

CRANFIELD UNIVERSITY

ANTHONY TREMLETT

**Optimal Time and Handling Methods for
Motorsport Differentials**

School of Engineering

PhD THESIS

CRANFIELD UNIVERSITY

SCHOOL OF ENGINEERING
Department of Automotive Engineering

PhD Thesis

Academic Year: 2013-2014

ANTHONY TREMLETT

Optimal Time and Handling Methods for Motorsport Differentials

Supervisors: Professor Francis Assadian,
Dr David Purdy, Professor Nicholas Vaughan

December 2014

This thesis is submitted in partial fulfilment of the requirements
for the degree of Doctor of Philosophy.

© Cranfield University 2014. All rights reserved. No part of this publication
may be reproduced without the written permission of the copyright owner.

Abstract

In the motorsport environment, where traction at one wheel is often compromised due to high cornering accelerations, Limited Slip Differentials (LSD) offer significant improvements in traction and vehicle stability. LSDs achieve these performance benefits through the transfer of torque from the faster to slower rotating driving wheel. In the majority of racing formulae, modern devices have evolved to become highly adjustable, allowing this torque bias to alter both ultimate vehicle performance and handling balance through specific corner entry, apex and corner exit phases.

This work investigates methods to optimise LSD setup parameters, both for minimum lap time and desirable handling characteristics. The first stage of addressing this objective involved the creation of a range of contemporary motorsport LSD models. These included a plate or Salisbury type, a Viscous Coupling (VC) and a Viscous Combined Plate (VCP). A differential test rig was developed to validate these models.

The parameter optimisation is addressed in two main parts. Firstly, a Quasi Steady State (QSS) time optimal method is used to maximise the vehicle's GG acceleration envelope using a direct, nonlinear program (NLP). A limitation of this approach however, is that system transients are neglected. This is addressed through the development of an alternative indirect, nonlinear optimal control (NOC) method. Both methods were able to find LSD setup parameters which minimised lap time, providing significant improvements over traditional open and locked devices. The NOC method however, was able to give greater insight into how a locked device ultimately limits the vehicle yaw response during quick direction changes.

The time optimal analysis was extended to investigate aspects of vehicle stability and agility. These factors are known to have a major influence on driveability and thus, how much of the theoretical performance limit the driver can extract. A more unified GG diagram framework was implemented, to characterise both the vehicle's acceleration limits, and how its stability and agility changes leading up to this limit.

The work has generated a number of novel contributions in this research field. Firstly, the creation and validation of a range of state-of-the-art motorsport LSD models. Secondly, the methodologies used to optimise LSD setup parameters, the results from which, have themselves provided the basis of a novel, vehicle speed dependent LSD device. Finally, a more practical and intuitive way to evaluate vehicle stability and agility at different cornering phases. This has laid the foundations of a procedure which not only maximises the vehicle's acceleration limits, but also allows its response to be tailored to suit individual driver preferences.

Acknowledgements

I would like to pay special thanks to my supervisors, Professor Francis Assadian, Dr David Purdy and Professor Nick Vaughan. The passion and enthusiasm they have for their subject is infectious and made me feel very lucky to have them as supervisors. Their support and guidance to develop my own research ideas was also hugely fulfilling and something I shall remember for the rest of my days. It is only sad that the late David Crolla, instrumental in the early stages of this work is not here to witness its completion.

This work has been supported technically and financially by Xtrac Ltd. The R&D facilities that they provided have significantly raised the level of research and made it much easier to apply the results in an industrial context. Particular thanks goes to Adrian Moore, Technical Director and Martin Halley, Chief Engineer, for their support and understanding of the pressures faced by a part time student.

Sincerest thanks must also go to Dr Damien Brayshaw, Dr Matteo Massaro, Dr Efstathios Velenis and the rest of the Vehicle Dynamics Group at Cranfield (past and present) who's depth of knowledge and insight into vehicle dynamics has made the process that much more enjoyable.

The following people have shown an interest in my work and have provided much help, support and encouragement along the way: Ian Dickason, Dr Marko Tirovic, Dr Shaun Forth, Dr Daniel Auger, Dr Stefano Longo, Simon Cumberpatch, Craig Porley, Ian Foster, Oliver Grant and Dan Fox.

There are difficult times in any project, but huge thanks should also go to Christina McKevitt for her moral support and patience during the thesis writing stage. She is a very special girl indeed.

The final dedication must go to my family and late father Brian Tremlett. Without their support, guidance and inspiration this work would simply not have been possible. They have made me what I am, so it is to them I owe the greatest debt of gratitude.

Contents

Abstract	i
Acknowledgements	ii
Contents	iii
List of Figures	vii
List of Tables	xi
Nomenclature	xii
1 Introduction	1
1.1 Context	1
1.2 Open-Locked Differential Compromise	3
1.3 Time Optimal Methods	4
1.3.1 Quasi Steady State (QSS)	4
1.3.2 Transient Nonlinear Optimal Control (TNOC)	6
1.3.2.1 Indirect Methods	8
1.3.2.2 Direct Methods	9
1.3.2.3 Nonlinear Model Predictive Control (NMPC)	13
1.4 Handling Considerations	14
1.4.1 Vehicle Stability	15
1.4.2 Vehicle Agility	19
1.5 Aims and Objectives	20
1.6 Thesis Structure	20
2 Differential Technology and Handling Review	22
2.1 Passive Limited Slip Differentials (PLSD)	22
2.1.1 Plate Type (Salisbury)	24
2.1.2 Viscous Coupling (VC)	26
2.1.3 Viscous Combined Plate (VCP)	27
2.2 Active Limited Slip Differential (ALSD)	27
2.3 Torque Vectoring Differentials (TVD)	29
2.4 Differential Handling Influence	31
2.5 Differential Simulation Models	34
2.6 Review Summary	37
2.7 Contribution	37

3	Differential Modelling and Validation	38
3.1	Plate Differential (Salisbury) Model	38
3.1.1	Preload Locking Gradient (∇_{pp})	42
3.1.2	Ramp Locking Gradient (∇_r)	45
3.1.3	Clutch Plate Friction Coefficient Calculation	48
3.1.4	Example Plate LSD Performance Map	50
3.2	Quasi Transient Differential Test Rig (QTDTR)	52
3.2.1	Instrumentation and User-Interface	55
3.3	Steady State Validation	55
3.3.1	Friction Faces and Ramp Angle	57
3.3.2	Positive and Negative Preload	58
3.4	Transient Validation	62
3.4.1	Step Input	62
3.4.2	Drive - Coast Ramp Input	64
3.5	Viscous Coupling (VC)	66
3.5.1	Fluid Viscosity Variation	66
3.5.2	Shear Torque Calculation	67
3.5.3	Transient VC Validation	69
3.6	Viscous Combined Plate (VCP)	71
3.6.1	VCP Validation	72
3.7	Conclusions	73
4	Vehicle Modelling and Validation	75
4.1	Vehicle Model Structure	75
4.1.1	Chassis Equations of Motion	76
4.1.2	Load Transfer	78
4.1.3	Engine	79
4.1.4	Gearbox	79
4.1.5	Brakes	79
4.1.6	Differential Operating States	80
4.1.6.1	Open State	81
4.1.6.2	Limited Slip State	81
4.1.6.3	Locked State	82
4.1.7	Plate/VCP Limited Slip and Locked Operation	82
4.1.8	Equations of Wheel Motion	83
4.1.9	Tyre Model	84
4.1.9.1	Slip Angle and Slip Ratio Calculation	86
4.1.10	Aerodynamic Loads	86
4.1.11	Driver Model	87
4.2	Vehicle Model Verification	88
4.2.1	Racing Line Reconstruction	88
4.2.2	Lap Replay	91
4.2.3	Differential Validation	93
4.3	Conclusions	97

5	QSS Time Optimal Solutions	98
5.1	Generating the GG Diagram	98
5.2	Initial Results	103
5.3	Generating the Time Optimal Solution	106
5.4	Parameter Sensitivity - Plate LSD	108
5.4.1	Ramp Angles	108
5.4.2	Friction Faces	111
5.4.3	Positive and Negative Preload	113
5.5	Parameter Sensitivity - VC	115
5.6	Parameter Sensitivity - VCP	118
5.7	LSD Optimisation	119
5.7.1	Optimal Passive LSD characteristics	121
5.8	Conclusions	125
6	Extensions to the QSS Method	126
6.1	The Feasibility Region	126
6.2	Feasibility Results - LSD Yaw Moment	129
6.2.1	Torque Sensing Plate LSD	129
6.2.2	Speed Sensing VC	131
6.2.3	Speed and Torque Sensing VCP	133
6.3	The Stability vs Agility Balance	135
6.3.1	Vehicle Model Linearisation	135
6.3.2	Eigenvalue Analysis	138
6.3.3	Yaw Rate Analysis	141
6.3.4	Understeer Angle	144
6.4	Setup Change Example	146
6.4.1	Stability and Agility	147
6.5	Handling Optimal Methods	149
6.6	Conclusions	153
7	Dynamic Time Optimal Solutions	155
7.1	Optimal Control Method	155
7.1.1	Model Revisions	156
7.1.2	Inequality Constraints	157
7.1.3	Solution of Equations	159
7.1.4	Tyre Wear	162
7.2	Simulation Results	163
7.2.1	90° bend	163
7.2.2	Lane Change	167
7.3	Optimal Passive LSD	172
7.3.1	Road Friction	173
7.4	Conclusions	175
8	Conclusions and Further Work	177
8.1	Differential Modelling	177
8.2	QSS Time Optimal Methods	178
8.3	Dynamic Time Optimal Methods	179
8.4	QSS Handling Methods	180
8.5	Contribution	181

CONTENTS

8.6 Future Work	181
Publications	183
References	184
Appendices	
A QTDTR Sensor Calibration Certificates	193
B Plate LSD Step Response Data	197
C Clutch Pack Transducer	198
D Vehicle Parameters	203
E Vehicle Model Linearisation	205
F Simplified Pacejka Tyre Model	209

List of Figures

1.1	GG - speed contour diagram schematic	5
1.2	QSS example speed profile	6
1.3	Direct single shooting discretisation	11
1.4	Direct single shooting method	11
1.5	Direct collocation discretisation	12
1.6	Direct multiple shooting discretisation	12
1.7	NMPC schematic	13
1.8	Optimal and realisable lap time schematic	14
1.9	Stability and control derivative concept	16
1.10	Side slip - yaw rate phase portrait example [55]	18
2.1	Xtrac plate type Limited Slip Differential (sectional view)	25
2.2	Xtrac plate type Limited Slip Differential (exploded view)	25
2.3	Viscous Coupling (VC) unit (exploded view)	26
2.4	Xtrac Viscous Combined Plate (VCP) LSD example (sectional view)	27
2.5	WRC active centre differential example [121] (sectional view)	28
2.6	Formula 1 active LSD driver controls	29
2.7	AYC differential section view and schematic (superimposed/clutch type)	30
2.8	Stationary clutch/brake type TVD	31
2.9	a) Understeer gradient comparison between open and ALSD (FWD car, 40m constant radius test) b) step steer response at 75km/h [50]	32
2.10	a) Steady state cornering characteristics of a TVD b) double lane change manoeuvre at initial speed of 60km/h [86]	33
2.11	Xtrac 516 Salisbury PLSD Locking Model Validation [24]	35
2.12	ALSD (GKN ETM) model validation results of clutch engagement and disengagement at a 25rpm slip speed [44]	36
3.1	a) FWD powertrain schematic - on throttle conditions b) FWD powertrain schematic - off throttle conditions	38
3.2	Description of the three phases of locking torque (on-throttle drive side only)	40
3.3	Pinion mate thrust loads	42
3.4	Pinion mate frictional contact geometry	43
3.5	Ramp-crossspin free body diagram and clutch surface geometry	46
3.6	Friction characteristic of single molybdenum friction disc with increasing speed, $F_{cref} = 7\text{kN}$ clamp load, bulk oil temperature 80°C , SAE 75W90 oil	49
3.7	Friction characteristic of single molybdenum friction disc with increasing load, $\omega_d = 40\text{rpm}$, SAE 75W90 oil	50

3.8	Example plate LSD torque bias performance map with input torque and differential speed	51
3.9	Xtrac Quasi Transient Differential Test Rig	52
3.10	Xtrac Quasi Transient Differential Test Rig	53
3.11	QTDTR schematic	54
3.12	DTR Test Executive GUI	56
3.13	Friction face and ramp angle steady state validation, bulk oil temperature 80°C, 40rpm differential speed	58
3.14	Positive preload steady state validation	59
3.15	Negative preload steady state validation	61
3.16	Transient step response, drive ramp $\theta_r = 60$, friction faces $z_f = 12$, 40rpm differential speed, bulk oil temperature 80°C	63
3.17	Measured and predicted ramp clamping force	64
3.18	Drive and coast ramp response	65
3.19	a) silicon fluid viscosity variation with temperature b) silicon fluid viscosity with shear rate	67
3.20	VC disc and plate geometry	68
3.21	VC unit speed ramp validation, 80°C casing temperature	70
3.22	Example VCP torque bias map with input torque and differential speed	71
3.23	VCP steady state validation, bulk oil and VC casing temperature 80°C, 40rpm differential speed	73
4.1	7DOF vehicle model structure	76
4.2	3DOF planar model	77
4.3	Load transfer roll model	77
4.4	Total gear ratio function - example	80
4.5	FWD gearbox layout schematic (plate type LSD case)	81
4.6	Schematic showing limited slip and locked states of plate LSD	82
4.7	Wheel free body diagram	83
4.8	a) Pure lateral tyre force with slip angle b) pure longitudinal tyre force with longitudinal slip	85
4.9	a) Modulus of total tyre force as function of slip angle and slip ratio b) contour plot showing lines of constant tyre force	85
4.10	Preview steer driver model	87
4.11	Snetterton 300 longitudinal velocity profile	89
4.12	Snetterton 300 racing line reconstruction	89
4.13	Snetterton 300 racing line reconstruction - turns 1-7	90
4.14	Snetterton 300 racing line reconstruction - turns 9-10	90
4.15	Comparison of simulated and actual lateral (top) and longitudinal (bottom) acceleration data	91
4.16	Actual and simulated longitudinal velocity profiles	92
4.17	Steering (top), throttle (middle) and brake (bottom) histories	92
4.18	Differential Setup 1 - driven wheel speed difference	94
4.19	Differential Setup 2 - driven wheel speed difference	94
4.20	Differential Setup 1 - percentage lap time vs driven wheel speed difference	95
4.21	Differential Setup 2 - percentage lap time vs driven wheel speed difference	95
4.22	Differential Setup 1 - transmitted wheel torque	96
4.23	Differential Setup 1 - driven wheel speed difference	96

5.1	GG acceleration envelope example	99
5.2	GG diagram for RWD Touring Car	103
5.3	GG envelope for open and locked differentials	105
5.4	Snetterton 300 apex points	106
5.5	QSS speed, longitudinal acceleration and lateral acceleration time histories	107
5.6	Coast ramp lap time sensitivity	109
5.7	Drive ramp lap time sensitivity	109
5.8	Drive ramp lap time sensitivity	110
5.9	GG envelope variation with coast ramp angle	110
5.10	GG envelope variation with drive ramp angle	111
5.11	Friction face lap time sensitivity (drive)	112
5.12	Friction face lap time sensitivity (coast)	112
5.13	Positive preload lap time sensitivity	113
5.14	Negative preload lap time sensitivity	114
5.15	Negative preload lap time sensitivity	115
5.16	VC torque bias characteristics	116
5.17	VC lap time sensitivity	116
5.18	GG envelope variation with VC shear faces (20m/s)	117
5.19	GG envelope variation with VC shear faces (60m/s)	117
5.20	VCP lap time sensitivity	118
5.21	Active differential GG envelope	120
5.22	Active differential hydraulic pressure	121
5.23	a) QSS optimal torque bias profile at 20m/s b) QSS optimal torque bias profile at 60m/s	122
5.24	Optimal passive torque sensing characteristics	123
5.25	Optimal torque sensitive bias profile schematic	124
6.1	GG feasibility point grid example	127
6.2	Differential yaw moment contours - plate LSD (20m/s)	130
6.3	Differential yaw moment contours - plate LSD (60m/s)	131
6.4	Differential yaw moment contours - VC LSD (20m/s)	132
6.5	Differential yaw moment contours - VC LSD (60m/s)	132
6.6	Differential yaw moment contours - VCP LSD (20m/s)	134
6.7	Differential yaw moment contours - VCP LSD (60m/s)	134
6.8	Linearised lateral tyre force	136
6.9	Eigenvalue contour throughout GG envelope at 20m/s	138
6.10	Eigenvalue contour throughout GG envelope at 60m/s	139
6.11	Eigenvalue skid pan comparison	140
6.12	Normalised yaw rate bandwidth at 20m/s	142
6.13	Normalised yaw rate bandwidth at 60m/s	142
6.14	Yaw rate response bode plot at 20m/s	143
6.15	Yaw rate response bode plot at 60m/s	144
6.16	Understeer angle contour (20m/s)	145
6.17	Understeer angle contour (60m/s)	146
6.18	a) GG edge contour with cornering phases points b) cornering phases on 90° bend	147
6.19	GG acceleration point grid	150
6.20	Active LSD yaw moment contours (20m/s)	151

LIST OF FIGURES

6.21	Active LSD pressure contour (20m/s)	151
6.22	Active LSD yaw moment contours (60m/s)	152
6.23	Active LSD pressure contour (60m/s)	153
7.1	Curvilinear track coordinates	157
7.2	Vehicle trajectory - 90° bend	163
7.3	Total driven wheel tyre wear (longitudinal direction only)	164
7.4	Vehicle control history - 80m bend	165
7.5	Rear wheel speed and torque - 90° bend	166
7.6	90° bend - slipping/locked status	166
7.7	Locked - optimal LSD time difference	167
7.8	Lane change vehicle trajectory curvature	168
7.9	Vehicle control history - lane change	169
7.10	Rear wheel speed and torque - 90° bend	170
7.11	Total driven wheel tyre wear	171
7.12	Driven wheel slip ratios	171
7.13	Passive torque sensing LSD data fit	172
7.14	Vehicle control history - 80m bend	174
7.15	Passive torque sensing LSD data fit - variable road friction	175
A.1	QTDTR torque and speed sensor calibration certificate - page 1	193
A.2	QTDTR torque and speed sensor calibration certificate - page 2	194
A.3	QTDTR torque and speed sensor calibration certificate - page 3	195
A.4	QTDTR rack load cell calibration certificate	196
B.1	Transient step response data	197
C.1	Transducer plate installation within LSD cassette assembly	198
C.2	Strain gauged transducer - top and bottom views	199
C.3	Strain gauged transducer - bridge configuration	199
C.4	Transducer calibration, 80°C differential casing temperature	200
C.5	Transducer pressure plate	201
C.6	Transducer calibration tooling	202
F.1	Normalised longitudinal tyre forces	211
F.2	Normalised lateral tyre forces	212

List of Tables

3.1	Plate differential setup parameters	51
3.2	Molybdenum friction disc parameters	52
3.3	Plate differential setup parameters - ramp and friction face validation	57
3.4	Ramp and friction face validation errors	58
3.5	Positive preload detent adjustment	59
3.6	Positive preload validation errors	60
3.7	Negative preload detent adjustment	61
3.8	Plate differential setup parameters - negative preload validation	61
3.9	Negative preload validation errors	62
3.10	VC setup and fluid parameters	70
3.11	Plate differential setup parameters, VCP validation	72
3.12	VCP validation errors	72
4.1	Plate differential parameters - Setup 1	93
5.1	GG optimisation state vector variables	100
5.2	Area of constant velocity GG contours (open-locked comparison)	104
5.3	QSS lap time comparison	107
5.4	Active LSD lap time comparison	119
5.5	Area of constant velocity GG contours (locked-active comparison)	120
5.6	Fitted plate differential setup parameters	122
6.1	GG optimisation state vector variables	128
6.2	Plate differential parameters	129
6.3	VC setup and fluid parameters	131
6.4	QSS and simulation model eigenvalue summary	140
6.5	Plate differential setup parameters	146
6.6	Eigenvalue and yaw rate bandwidth setup comparison (20m/s)	148
6.7	Eigenvalue and yaw rate bandwidth setup comparison (60m/s)	148
7.1	Vehicle and track inequality constraint values	158
7.2	Manoeuvre time summary - 90° bend	163
7.3	Manoeuvre time summary - lane change	167
7.4	Fitted plate differential setup parameters	172
7.5	Plate differential setup parameters - variable road friction	173
D.1	FWD Touring Car vehicle parameters	203
D.2	RWD Touring Car vehicle parameters	204
F.1	Simplified Pacejka model coefficients	209

Nomenclature

Abbreviations

AD	Algorithmic differentiation
ALSD	Active limited slip differential
AWD	All wheel drive
AYC	Active yaw control
BTCC	British Touring Car Championship
BVP	Boundary value problem
CAD	Computer aided design
CG	Centre of gravity
DOF	Degree of freedom
FWD	Front wheel drive
IVP	Initial value problem
KKT	Karush-Kuhn-Tucker
LSD	Limited slip differential
LTV	Linear time varying
LVFA	Low velocity friction apparatus
NLP	Nonlinear programming
NMPC	Nonlinear model predictive control
NMSE	Normalised mean square error
PI	Proportional Integral
PLSD	Passive limited slip differential
QP	Quadratic programming
QSS	Quasi steady state

QTDTR	Quasi transient differential test rig
RMS	Root mean square
RWD	Rear wheel drive
SAE	Society of Automotive Engineers
SISO	Single input single output system
SQP	Sequential quadratic programming
TNOC	Transient nonlinear optimal control
TVD	Torque vectoring differential
VC	Viscous coupling
VCP	Viscous combined plate
WRC	World Rally Championship

Greek Symbols

α_p	Side gear - pinion mate pressure angle (deg)
α_n	Slip angle of wheel n (rad)
β	Side slip angle (rad)
$\dot{\gamma}_b$	Silicon fluid critical shear rate (/s)
$\dot{\gamma}$	Silicon fluid shear rate (/s)
γ_t	Wheel torque control parameter
δ_{rw}	Road wheel steering angle (rad)
ΔT	Differential bias torque (Nm)
δ_k	Kinematic steer angle (rad)
δ_p	Pinion mate pitch cone angle (deg)
δ_{ua}	Understeer angle (rad)
θ_r	Ramp angle (deg)
θ_{rc}	Coast ramp angle (deg)
θ_{rd}	Drive ramp angle (deg)
θ_{s0}	Reference silicon fluid temperature (K)
θ_s	Silicon fluid temperature (K)

NOMENCLATURE

κ_n	Longitudinal slip of wheel n
λ_e	Eigenvalues of linearised vehicle model
λ	Vector of Lagrange multipliers
μ_{pm}	Friction coefficient of pinion mate - ramp contact
μ_p	Clutch disc friction coefficient
μ_r	Ramp-crosspin contact friction coefficient
ν	Silicon fluid viscosity (mm^2/s)
$\nu_{\theta_{s0}}$	Base silicon fluid viscosity at θ_{s0} (mm^2/s)
ρ_a	Air density (kg/m^3)
ρ_v	Shear fluid density (kg/m^3)
τ	Plate LSD time constant (s)
τ_z	Suspension time constant (s)
ϕ	Roll angle (deg)
ψ_d	Angle of vehicle relative to track centreline (rad)
ψ_t	Tangent angle of vehicle path (rad)
ψ_v	Vehicle heading angle (rad)
$\dot{\omega}_e$	Rotational acceleration of engine (rad/s^2)
ω_d	Differential wheel speed (rad/s)
ω_f	Front axle speed (rad/s)
ω_n	Rotational speed of wheel n (rad/s)
ω_r	Rear axle speed (rad/s)
ω_a	Rotational axle speed (locked differential only) (rad/s)
ω_e	Rotational engine speed (rad/s)
∇_{pp}	Positive preload gradient
∇_r	Ramp locking gradient

Latin Symbols

a	Distance from front wheel centre to CG (m)
A_b	Abradability factor ($\text{kg}/\text{m}^2 \text{ kJ}$)

A_f	Frontal area of vehicle (m^2)
a_x	Total longitudinal acceleration (m/s^2)
a_y	Total lateral acceleration (m/s^2)
A_{sv}	Silicon fluid empirical constant
a_{xi}	Longitudinal acceleration point within feasibility region (m/s^2)
a_{yi}	Lateral acceleration point within feasibility region (m/s^2)
b	Distance from rear wheel centre to CG (m)
B_f	Brake balance factor
C_d	Drag coefficient
c_s	Silicon fluid specific heat capacity (J/kg K)
$c_{1..7}$	Clutch friction empirical constants
$C_{\alpha 0}$	Linearised tyre cornering stiffness coefficient (N/rad)
$C_{\kappa 0}$	Linearised tyre longitudinal stiffness coefficient (N)
c_{eq}	Equality constraints of QSS optimisation
C_f	Front cornering stiffness (N/rad)
c_{ineq}	Inequality constraints of QSS optimisation
C_r	Rear cornering stiffness (N/rad)
d_{m1}	Mean pitch cone diameter of pinion mate (m)
d_{m2}	Mean pitch cone diameter of side gear (m)
e_i	Path error (m)
e_v	Velocity error (m/s)
e_ψ	Attitude angle error (rad)
$f_{\delta_{rw}}^r$	Normalised yaw rate bandwidth
F_{drag}	Longitudinal drag force (N)
F_d	Tangential ramp force - per side (N)
F_{ramp}	Clutch pack clamp force - per side (N)
F_{xn}	Longitudinal tyre force, tyre fixed reference frame (N)
F_{yn}	Lateral tyre force, tyre fixed reference frame (N)

NOMENCLATURE

F_{zn}	Normal load on tyre n (N)
g	Acceleration due to gravity (m/s^2)
G_r	Combined gearbox and final drive ratio
$G_{r1..6}$	Gear ratios between 1st and 6th gear
H	Hamiltonian function
H_a	Active differential hydraulic piston area (m/s^2)
h_g	Height of sprung mass CG (m)
H_p	Active differential hydraulic pressure (bar)
h_{rc}	Roll centre height at CG (m)
h_{rf}	Front roll centre height (m)
h_{rr}	Rear roll centre height (m)
I_{zz}	Vehicle yaw inertia (kg m^2)
J	Performance index / objective function
J_e	Engine inertia (kg m^2)
J_w	Wheel inertia (including hub, brake disc and wheel)(kg m^2)
K_a	Silicon fluid empirical constant
k_b	Preload spring stiffness (kN/mm)
k_t	Track curvature ($/\text{m}$)
K_{us}	Understeer gradient (deg/g)
l	Wheelbase (m)
m	Total vehicle mass (kg)
m_s	Silicon fluid mass (kg)
m_{sf}	Silicon fluid viscosity-shear rate slope
n	Subscript denoting each wheel corner where $n=1..4$, front left(1), front right(2), rear left(3), rear right(4)
n_c	Number of preload adjustment detents
n_{ct}	Total number of preload adjustment detents
N_{diff}	LSD yaw moment (Nm)
p_i	Inequality constraint penalty function ($i = 1..q$)

Q	Heat generation by silicon fluid (kJ)
r	Yaw velocity/rate (rad/s)
\dot{r}	Yaw acceleration (rad/s ²)
r_t	Path radius (m)
r_{c1}	Inner clutch plate diameter (m)
r_{c2}	Outer clutch disc diameter (m)
r_{p1}	Inner diameter of pinion mate contact (m)
r_{p2}	Outer diameter of pinion mate contact (m)
R_{rr}	Effective ramp contact radius (m)
R_{sf}	Front relative roll stiffness factor
R_{sr}	Rear relative roll stiffness factor
r_s	Radius of pinion mate contact face (m)
s_t	Position of vehicle along the track centreline (m)
s_v	Lateral offset of vehicle from track centreline (m), shear surface separation distance (m)
S_m	Stability margin (Nm/rad)
T_d	Differential input torque (Nm)
T_e	Engine torque (Nm)
t_f	Final manoeuvre time (s), front vehicle track (m)
t_l	Distance from track centreline to left hand track boundary (m)
T_p	Positive preload torque (Nm)
T_r	Ramp locking torque (Nm)
t_r	Distance from track centreline to right hand track boundary (m), rear vehicle track (m)
T_{bf}	Total front brake torque (Nm)
T_{bmax}	Total maximum brake torque available (Nm)
T_{bn}	Brake torque at wheel n (Nm)
T_{br}	Total rear brake torque (Nm)
t_{hp}	Preload adjuster thread pitch (mm)

NOMENCLATURE

T_{np}	Negative preload offset (Nm)
T_n	Torque transmitted to wheel n (Nm)
T_{pg}	Transition preload gain factor
T_{pp}	Static preload torque (Nm)
T_{tr}	Transition region torque bias (Nm)
T_{vcp}	VCP bias torque (Nm)
T_{vc}	VC bias torque (Nm)
U	Longitudinal velocity (m/s)
\dot{U}	Longitudinal acceleration (m/s ²)
\mathbf{u}	Vector of continuous control variables
U_n	Longitudinal velocity at wheel centre n (m/s)
U_v	Shear surface tangential speed (m/s)
$U_{g1..6}$	Threshold speed to change into 1st-6th gears (m/s)
u_{tb}	Throttle position parameter
V	Side slip velocity (m/s)
\dot{V}	Side slip acceleration (m/s ²)
V_n	Lateral velocity at wheel centre n (m/s)
W_a	Vehicle agility weighting factor
W_f	Longitudinal tyre frictional work (kJ)
W_r	Tyre wear rate (kg/m ²)
W_s	Vehicle stability weighting factor
\mathbf{x}	Vector of continuous vehicle system state variables
z_f	Number of friction faces
z_s	Number of shear surfaces

Chapter 1

Introduction

1.1 Context

Differentials are well established as an efficient means of transferring torque to wheels rotating at different speeds. Provided there is a sufficient level of grip at each wheel, the open differential has proven to be a perfectly satisfactory device [62]. However, in the motorsport environment, where traction at one wheel is often compromised due to high cornering accelerations, Limited Slip Differentials (LSD) have been shown to offer significant improvements in traction and vehicle stability [50, 66, 62]. LSDs can be implemented both in the lateral sense, to distribute torque between left and right driving wheels in a two-wheeled drive (2WD) vehicle, and between front and rear axles in an all-wheel drive (AWD) application. The focus in this thesis will be on the lateral 2WD application and its ability to generate yaw moments through differences in longitudinal tyre forces.

There has been a trend in motorsport towards passive LSD devices, since regulations in many racing formulae have prohibited the use of active control systems, on cost grounds [28]. Regulations dictate that this torque bias is controlled passively, either through proportionality with differential input torque or the driven wheel speed difference. Even at top level motorsport, in Formula 1, only semi-active devices are allowed. These use predetermined control algorithms based on a limited number of vehicle parameters including lateral and longitudinal acceleration and vehicle speed. Their use in Formula 1 has highlighted their ability to change vehicle handling balance during particular cornering phases, namely corner entry, apex and the corner exit. These are typically adjusted by the driver during a race distance to counter changes in handling due to tyre degradation and a depleting fuel load. Modern passive LSDs, widespread through other motorsport categories, have also evolved to be highly adjustable, although not in real time by the driver. They too, have the capability to change handling balance, by adjusting a number of setup parameters before each test session or race. The way in which these setup parameters influence vehicle handling are not well documented in literature, and in particular, their influence on low, mid and high speed corners is similarly not well understood. This is one of the unexplored areas that this research addresses.

This work is carried out with the support of Xtrac Limited [121], who design and manufacture transmissions for the automotive and motorsport industries. In such a competitive environment, there is technological and commercial benefit in being able to offer tailored designs which will maximise vehicle performance. The time optimal methods described by Brayshaw [10] and Kelly [47] demonstrate the most obvious performance criteria to use when optimising differential setup parameters. This is based solely on the resulting lap time of the vehicle when it is at its acceleration limits. Lap simulation packages have been developed for this purpose, and are used widely by researchers when optimising other vehicle parameters including weight and roll stiffness distribution [10, 15, 47, 114]. While this brings considerable insight, the time optimal solution only represents the raw performance potential of the vehicle, not the driver's ability to use it. A key factor in determining how close a driver can get to this limit, is the perceived balance between vehicle stability and agility. A vehicle which has been setup to achieve the right handling balance in the driver's view, will allow the driver to attack the circuit, more able to exploit the vehicle performance envelope. This is demonstrated in a quote from Formula 1 driver, Jean-Eric Vergne, after a disappointing race at the Interlagos circuit:

“ Catastrophic starts for both Toro Rossos today and after that, I had a car that was very difficult to drive. It's the first time we ran here in the dry, but the balance of my car just wouldn't allow me to push ”.

Jean-Eric Vergne, Brazilian GP, 2013

In qualitative terms, getting the balance right, normally means limiting the unwanted instability brought on by excessive oversteer during the braking phase of corner, without detrimentally affecting the agility of the vehicle (with excessive understeer), during the corner exit phase. It is not sufficient therefore, to focus simply on lap time, or even the balance of the vehicle at the limit. An understanding of how the vehicle balance changes up to the limit is required to help determine whether a driver might be able to extract the most from a particular setup. This is one of the areas where this research aims to make a contribution, in presenting a new way to evaluate vehicle stability and agility throughout a vehicle's operating envelope. This is described with a view to developing the way in which optimal LSD torque bias characteristics can be determined.

Wider afield in the automotive sector, the use of LSDs is generally restricted to the luxury and performance vehicle market, due to the additional costs associated with their implementation. This can also be explained by the increasing availability of brake based traction control systems [111, 112]. These help alleviate some of the traditional open differential limitations, by braking the slipping wheel and artificially increasing overall traction at the driven axle. Understandably, literature has shown a greater emphasis on vehicle safety than ultimate performance. The majority of work has therefore focused on improving LSD model fidelity for more efficient control system implementation, and understanding those factors which limit actuator bandwidth [44, 23, 50] in active LSD architectures. These have a significant impact, both on the control authority of the device for yaw moment generation, and how well torque biasing systems integrate with other active control systems including traction control, anti-lock brakes (ABS) and yaw stability control. The fidelity of LSD models is relevant to this research which aims to validate differentials models in isolation on a

bespoke differential test rig (see Chapter 3), but also against in-car test data. Few existing LSD models have been validated with regard to the torque transfer that they generate. The few that have, show substantial errors (30-40%) in locking torque calculation [24, 44] and bring into question the validity of any subsequent traction and handling assessments. This is discussed in greater detail in Section 2.5.

In light of the issues documented in this section, this thesis presents a range of comprehensive, high fidelity, adjustable motorsport differentials models, which are validated against test rig and vehicle track data. These form the basis of an exploration into the influence of differential setup parameters on handling and on ultimate vehicle performance. Several methods to predict the time optimal solution are presented, and used to conduct lap time sensitivity studies, for typical differential setup parameters. These methods are extended into a novel, unified framework which predicts both the time optimal solution and a more practical way to show how the stability-agility balance of the vehicle changes, both below and leading right up to the limit. This can be more easily related to the manoeuvre type being considered and provides a foundation to optimise vehicle handling balance for varying driver preferences.

The remainder of this chapter is designed to introduce the reader to important concepts in the study of motorsport differential devices. The two extremes of LSD operation (open and locked) are discussed and the behaviour of the theoretical optimal LSD device outlined. Current time optimal methodologies are then presented, as a prelude to literature which deals with the characterisation of vehicle stability and agility. This material is presented so that the aims and objectives defined in Section 1.5 can be more easily understood. The remaining literature review material focusing on the differential hardware is discussed in Chapter 2. The findings from both chapters are summarised at the end of Chapter 2 in Section 2.6.

1.2 Open-Locked Differential Compromise

The need for a differential arises from the speed difference established between the inner and outer wheels of any vehicle travelling around a corner. Due to the different radius each wheel follows, a speed difference is generated which is proportional to both the track width of the vehicle and the radius of turn. As a result, any driven axle needs to be able to deliver equal amounts of torque to wheels rotating at different speeds. The open differential has successfully achieved this aim since its invention in 1827 [12] and provided there is a sufficient level of traction at both wheels, is a perfectly satisfactory device. However, when typically, an inner wheel starts to slip due to lateral load transfer or poor road conditions, its fundamental limitation is evident. As the open differential can only ever deliver equal torque to each wheel, the total traction is always limited to twice that at the slipping wheel.

The extreme solution to the traction limited open differential, is to lock both driven wheels together so they are constrained to rotate at the same speed. This is commonly known as a locked or ‘spool’ differential [25, 62] and has proved popular in off-road and oval-based racing applications. Although traction is maximised, the loss of inner

to outer wheel speed independence has been shown to be severely detrimental to handling, tyre degradation and driveline reliability [62, 97, 119]. The limited slip differential provides a compromise between these two extremes, by biasing torque from the faster to slower rotating driven wheel.

Summarising the arguments presented above, it can be concluded that the ideal differential, is one that:

- (i) Transfers engine torque to the driven wheels, whilst still allowing wheel speed independence during cornering.
- (ii) Maximises traction when the grip at one wheel has been compromised, due to lateral load transfer effects, curb strikes or poor road conditions.
- (iii) Minimises the unnecessary tyre scrub associated with a locked differential, which can significantly increase tyre wear.
- (iv) Efficiently utilises differential yaw moments to enhance performance. These might involve understeer moments during braking to help stabilise the vehicle, or oversteer moments under acceleration to increase vehicle agility.

The reader should note that the characteristics presented above consider the sole case of a track based vehicle driving on tarmac surfaces. These conditions will be assumed for all the studies presented in this thesis.

1.3 Time Optimal Methods

The following section is designed to present current state-of-the-art time optimal methods, which have previously been used to show the influence of vehicle parameters on lap time. This is a prelude to a discussion on approaches taken to characterise vehicle stability and agility. Lap simulation methods described in literature generally fall under three main classifications: steady state, quasi steady state (QSS) and transient. Only current QSS and transient methods will be described, due to the inherent over simplification of steady state methods.

1.3.1 Quasi Steady State (QSS)

Although QSS lap simulation programs are established technologies in motorsport [47, 119], there is not yet a definitive method for their implementation. This is mainly due to their primary developers being racing teams and software companies, not willing to release information to their direct competitors. They have proved popular, since they can provide an adequate level of vehicle realism, with minimal computational effort. This means that programs can complete track-side simulations in a matter of minutes, providing instant feedback as to a particular setup decision. They can also be used to perform lap time sensitivity studies, to assist development at the design stage.

There are a number of inherent assumptions which must be understood when using any QSS program:

- (i) The real life, transient lap, can be broken down into a number of segments, and approximated with a series of dynamic equilibrium problems. The associated assumption is that the vehicle states can transition instantaneously from segment to segment, and that this is an acceptable realisation of vehicle behaviour.
- (ii) The vehicle is considered to be in quasi steady state. This means both lateral and longitudinal acceleration remains constant throughout the length of each segment.
- (iii) The influence of any inertial or energy dissipating elements, like yaw inertia, tyre temperature or suspension dampers are considered to be negligible.
- (iv) The racing line is pre-defined and cannot be changed during the simulation process.

The noteworthy examples in literature which do discuss QSS implementation can be classed into two main types. Firstly, the work of Siegler [94] and Kelly [47] describe methods which use the racing line path curvature as a basis, and solve the vehicle equations of motion interactively around the path, to yield vehicle state and control histories. An alternative approach presented by Candelpergher [14], Blasco-Figueora [8] and Brayshaw [10], reduces some of the computational burden during iterative phases, by generating an offline ‘GG’ speed diagram. This essentially characterises the vehicle acceleration limits at a number of vehicle speeds. An example is shown in Figure 1.1, for a typical race vehicle with aerodynamic downforce.

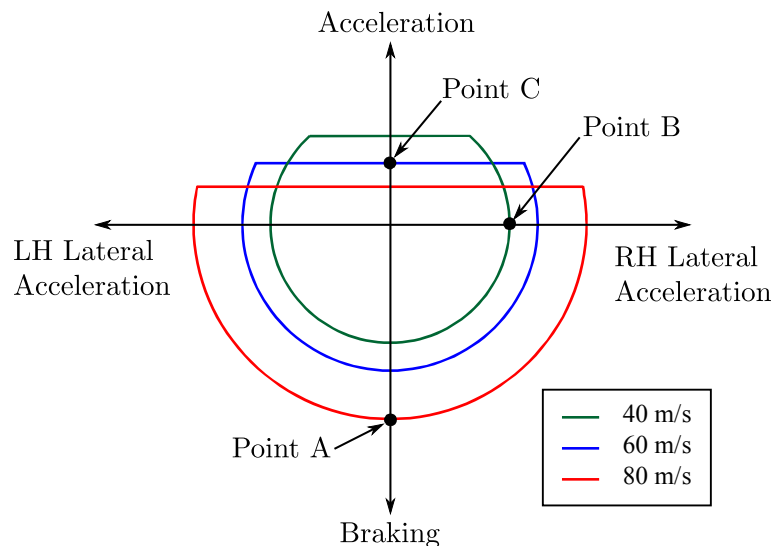


Figure 1.1: GG - speed contour diagram schematic

The speed profiles of both types of QSS simulation are progressively built up in the acceleration and braking phases, by first establishing boundary conditions at the apexes of the racing line. These apexes are usually taken to be the points of maximum path curvature. Since the curvature at the apex is known, the maximum vehicle speed is calculated by considering the vehicle in pure steady state cornering, i.e. with

100% lateral tyre force utilisation and zero longitudinal acceleration. This can be conceptualised as an interpolation between the GG speed contours at the point of maximum lateral acceleration, or point ‘B’ in Figure 1.1. Moving away from each of the apex points, will reduce the associated path curvature. The spare lateral capacity of the tyres is then used to establish a non-zero longitudinal acceleration potential. This can be likened to interpolating from point ‘B’ to point ‘C’ under acceleration, and point ‘A’ under braking. The speed profile of the entire lap is built up this way, until the braking phase of one apex crosses over with the acceleration phase of the next. An example is shown in Figure 1.2.

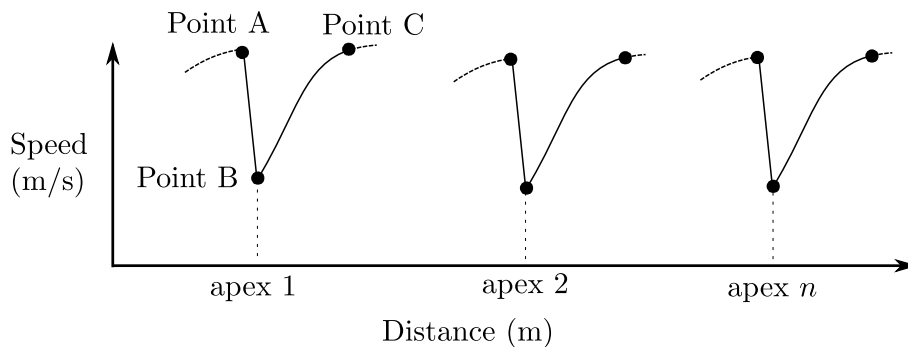


Figure 1.2: QSS example speed profile.

The concept of the GG diagram is a powerful tool for demonstrating the vehicle performance limits, and provides an intuitive framework to quantify the influence of any vehicle setup changes. An increase in the GG envelope indicates that there is potential to reduce an associated lap time, the magnitude of which, will depend on the track configuration and its specific combination of low to high speed corners. Part of the work presented in this thesis, aims to extend this concept, into a unified framework which allows both ultimate performance potential at the limit, and sub-limit vehicle handling balance to be evaluated.

1.3.2 Transient Nonlinear Optimal Control (TNOC)

Although the QSS methods described in Section 1.3.1 are widespread throughout the motorsport industry, the inability to study factors which influence transient behaviour, and variations in racing line, are major weaknesses in many researcher’s view [15, 47, 102]. In light of this, some have developed quasi-transient methods [72, 114], which allow the inclusion of a number of transient parameters including yaw acceleration, vertical suspension damping ratio and tyre temperature. The approach taken by Völkl [114] uses a pre-defined racing line, and an initial QSS solution as the input to a time varying dynamic model. The dynamics are then recorded over the lap distance, and reused in subsequent QSS simulations until the QSS and dynamic results converge. None of these approaches however, allowed the racing line to be optimised.

The vast majority of researchers however, have preferred to include the full system dynamics, by formulating the minimum time problem as one of nonlinear optimal control. Detailed proofs of optimal control problem formulation are given by Bryson

and Ho [11], but the relevant material is summarised here. The goal of any optimal control problem, is to allow continuous control of a dynamic system:

$$\dot{\mathbf{x}} = \mathbf{f}[\mathbf{x}(t), \mathbf{u}(t)] \quad (1.1)$$

with initial conditions:

$$\mathbf{x}(t_0) = \mathbf{x}_0 \quad (1.2)$$

whilst minimising or maximising a specific performance index:

$$J = \phi[\mathbf{x}(t_f)] + \int_{t_0}^{t_f} L[\mathbf{x}(t), \mathbf{u}(t)] dt \quad (1.3)$$

Where ϕ describes a cost functional depending on the final time system states $\mathbf{x}(t_f)$, and L , a cost functional reliant on both the states $\mathbf{x}(t)$, and control inputs $\mathbf{u}(t)$, from start time t_0 , to the end time t_f . The set of differential equations in 1.1 and the initial conditions in Equation 1.2 essentially constitute a set of equality constraints which must be satisfied at all times. These are included through the use of Lagrange multipliers $\boldsymbol{\lambda}(t)$, and are adjoined to the performance index. The resulting *augmented* performance index \bar{J} , is then simplified by the using the Hamiltonian function $H(t)$:

$$\bar{J} = \phi[\mathbf{x}(t_f)] - \boldsymbol{\lambda}^T(t_f)\mathbf{x}(t_f) + \int_{t_0}^{t_f} [H(t) + \dot{\boldsymbol{\lambda}}^T(t)\mathbf{x}(t)] dt + \boldsymbol{\lambda}^T(t_0)\mathbf{x}_0(t_0) \quad (1.4)$$

where the Hamiltonian is defined by:

$$H(t) = L[\mathbf{x}(t), \mathbf{u}(t)] + \boldsymbol{\lambda}^T(t)\mathbf{f}[\mathbf{x}(t), \mathbf{u}(t)] \quad (1.5)$$

For the performance index to reach an extremum, the gradient at the stationary point must be zero. By taking partial derivatives with respect to $\mathbf{x}(t)$ and $\mathbf{u}(t)$, and considering the change from a small change $\delta\mathbf{u}(t)$ in the input, the change in the performance index $\delta\bar{J}$, can then be defined as:

$$\delta\bar{J} = \left[\left(\frac{\partial\phi}{\partial\mathbf{x}} - \boldsymbol{\lambda}^T \right) \delta\mathbf{x} \right]_{t=t_f} + [\boldsymbol{\lambda}^T \delta\mathbf{x}]_{t=t_0} + \int_{t_0}^{t_f} \left[\left(\frac{\partial H}{\partial\mathbf{x}} + \dot{\boldsymbol{\lambda}}^T \right) \delta\mathbf{x} + \left(\frac{\partial H}{\partial\mathbf{u}} \right) \delta\mathbf{u} \right] \delta t \quad (1.6)$$

Since the initial state values are fixed, the second term on the right hand side is equal to zero. To yield further simplifications, specific values can be chosen for the Lagrange multipliers:

$$\dot{\boldsymbol{\lambda}}^T = -\frac{\partial H}{\partial\mathbf{x}} \quad (1.7)$$

$$\boldsymbol{\lambda}^T = \frac{\partial\phi}{\partial\mathbf{x}}(\mathbf{x}(t_f)) \quad (1.8)$$

This allows Equation 1.6 to be expressed as:

$$\delta \bar{J} = \int_{t_0}^{t_f} \left[\left(\frac{\partial H}{\partial \mathbf{u}} \right) \delta \mathbf{u} \right] \delta t = 0 \quad (1.9)$$

However, Equation 1.9 can only be satisfied if:

$$\frac{\partial H}{\partial \mathbf{u}} = 0 \quad (1.10)$$

Equations 1.7, 1.8 and 1.10 constitute the Euler-Lagrange equations, which formally define the necessary conditions for optimality. Thus, in order to find the optimal control history $\mathbf{u}(t)$ which produces a stationary point in the performance index J , these equations must be solved for the entire state trajectory. This involves solving a number of differential equations, namely: the model (Eq. 1.1), co-state (Eq.1.7) and optimality equations (Eq.1.9), and the initial and end boundary conditions in Eq.1.2 and Eq.1.8. These split boundary conditions form a two point, boundary value problem (BVP), which has traditionally been solved in two main ways: indirect or direct methods.

1.3.2.1 Indirect Methods

The main attribute of indirect methods, is that the optimality conditions are applied explicitly. The resulting equations are normally solved by applying Pontryagin's minimum principle [78], which formally requires the value of the Hamiltonian function to reach a minimum, when the optimal control inputs have been found. In practice, this is achieved by making an initial approximation of the solution, adjusting the control inputs, then re-evaluating the optimality conditions until the true optimal solution is found. Fujioka and Kimura [32] were the first to use indirect methods on a simple 3 degree of freedom (DOF) planar vehicle model, travelling around a simple hairpin manoeuvre. This used a Sequential Conjugate Gradient Restoration Algorithm (SCGRA) to optimise a vehicle with different driving and steering configurations along a predefined path. Hendrikx et al. [40] then developed this 3DOF model by adding an engine torque curve, nonlinear tyre characteristics and a steady state approximation of aerodynamic forces and load transfer.

More recently, Best and Gordon [5] describe a generalised indirect optimal control technique which involves a similar iterative re-simulation of the vehicle states. This was conducted with a 2DOF model, with load transfer and nonlinear tyres, to find optimal control inputs and vehicle yaw inertia. This work was later developed into a 'dual mode' approach [4, 6], which allowed more complex vehicle models to be tackled by first approximating a solution with a simpler nonlinear particle model. This is applied both to the application of lap simulation and later, to obstacle avoidance.

In pursuit of a real-time method for yaw control system implementation, Tsiotras and Velenis [107, 109] develop a semi-analytical method. This used a predefined racing line, and allowed the vehicle model to deal with uncertainties in operating environment, by adopting a receding horizon strategy. It is noted in their previous works [106, 108], that direct methods are computationally intensive and too sensitive to initial conditions for

real-time implementation.

One of the main limitations with indirect methods is that symbolic differentiation of the system equations is required. With a complicated vehicle model, including characteristics most conveniently specified with lookup tables (engine characteristics for example), this becomes increasingly difficult. Another consideration is that most methods require a reasonable initial estimate of the solution. In the case of the minimum time problem, the physical properties of the dynamic system (the vehicle) are well known, allowing a good initial estimate of the state trajectory and control history. However, no information on the co-state trajectory is generally available. This issue is usually overcome by employing a more robust, but slower to converge method, like a steepest descent algorithm [48], which is more able to cope with an inaccurate initial estimation. Once a feasible solution is found, Quasi-Linearisation [48] or indirect shooting methods [79] can be used, which converge much faster on the optimal solution. Quasi-Linearisation relies on using a Taylor series expansion of the nonlinear equations, about nominal values of the system states and Lagrange multipliers. This allows the original nonlinear problem to be transformed into a series of linear equations, more easily solved using the superposition principle. Conversely, the more popular indirect shooting method relies on converting the two point BVP into a more standard initial value problem (IVP) form. This is achieved by making an estimate of the initial conditions, and integrating the equations of motion forward in time, whilst evaluating any constraint violations. The initial estimate is then revised until all constraints are satisfied.

An important final consideration is that indirect solutions must have a continuous control history. This was highlighted as a concern by Thommyppillai [102] and Casanova [15], due to the rapid acceleration - braking transition typical of a race vehicle throttle/brake trace. Although this was thought to limit the quality of the resulting control histories, the results presented in Chapter 7 seem to disagree with these findings.

1.3.2.2 Direct Methods

Another branch of optimal control problems do not use the necessary conditions for optimality explicitly. Instead, the original continuous problem is solved with a discrete approximation. The control history is broken up into a number of discretisation points or ‘nodes’, which determine the points on the state trajectory where the control input can be manipulated to minimise the associated performance index. The intermediate points in-between nodes, are then found by interpolation, to provide a continuous control history. The resulting performance index and constraints can then be expressed directly as functions of the control parameters, and solved using nonlinear programming (NLP) techniques. The resulting NLP problem control history can be described by the vector of discrete control inputs \mathbf{u}_n , which minimises a nonlinear multi-variable objective function subject to equality and inequality constraints [68]:

$$\text{minimise objective function} = J(\mathbf{u}_n) \quad \text{for } \mathbf{u}_n \in \mathbb{R}^n \quad (1.11)$$

$$\text{subject to } c_i(\mathbf{u}_n) = 0, \quad i = 1, \dots, p_e \quad (1.12)$$

$$c_i(\mathbf{u}_n) \leq 0, \quad i = p_e + 1, \dots, p \quad (1.13)$$

where $J(\mathbf{u}_n)$ is the objective function, $c_i(\mathbf{u}_n) = 0$, $i = 1, \dots, p_e$, the equality constraints and $c_i(\mathbf{u}_n) \leq 0$, $i = p_e + 1, \dots, p$, the inequality constraints. The process of altering the control inputs, to minimise the objective function, is normally implemented by ensuring the first order necessary conditions or Karush-Kuhn-Tucker (KKT) conditions are met [68], where:

$$\frac{\partial \mathcal{L}(\mathbf{u}_n^*, \boldsymbol{\lambda}^*)}{\partial \mathbf{u}_n} = 0 \quad (1.14)$$

$$c_i(\mathbf{u}_n) = 0, \quad i = 1, \dots, p_e \quad (1.15)$$

$$c_i(\mathbf{u}_n) \leq 0, \quad i = p_e + 1, \dots, p \quad (1.16)$$

$$\lambda_i \leq 0, \quad i = p_e + 1, \dots, p \quad (1.17)$$

$$\lambda_i c_i(\mathbf{u}_n^*) = 0, \quad i = 1, \dots, p \quad (1.18)$$

The Lagrange multipliers λ , have again been used to adjoin the constraints to the objective function to form the Lagrangian function:

$$\mathcal{L}(\mathbf{u}_n, \boldsymbol{\lambda}) = J(\mathbf{u}_n) - \sum_{i=1, \dots, p} \lambda_i c_i(\mathbf{u}_n) \quad (1.19)$$

where \mathbf{u}_n^* and $\boldsymbol{\lambda}^*$ are the control and Lagrange multiplier vectors at the stationary point described by Equation 1.14. Allen [2] was among the first to apply a direct, *single shooting* algorithm to the race vehicle minimum time problem. This involved varying control inputs at each node point, and re-evaluating the objective function, by performing a one-pass integration along the state trajectory. This is shown diagrammatically in Figures 1.3 and 1.4. This information was used in subsequent iterations of the discrete control history, until the sequence converged to a solution. Allen only considered relatively short manoeuvres, for a simple 3DOF vehicle model, and ran into difficulties when trying to extend the method for longer manoeuvres (a complete lap for example). This so called *journey sensitivity* is typical of direct-shooting methods, and demonstrates that early control decisions can impact significantly on later constraint violations. This can effect the rate of converge, or even if convergence is possible at all.

An alternative approach to overcome journey sensitivity issues is to use a direct collocation procedure [7]. The main difference to shooting methods, is that it also requires discretisation of the state trajectory (see Figure 1.5). This allows more decoupling between control inputs and states, since each control variable can only alter the systems states at neighbouring points, not along the whole state history. The obvious by-product of this methodology however, is that the size of the optimisation is increased quite dramatically, and by implication, the time to convergence. If the right algorithm is chosen however, which takes advantage of the sparsity of derivative information, then collocation methods can prove very efficient [7, 15]. At the time of writing, Limebeer and Perantoni [73] have implemented these methods for parameter optimisation of a contemporary Formula 1 car.

Other researchers however, have opted to use a multiple-shooting approach [7, 9], which essentially breaks down the problem into a series of smaller single shooting problems.

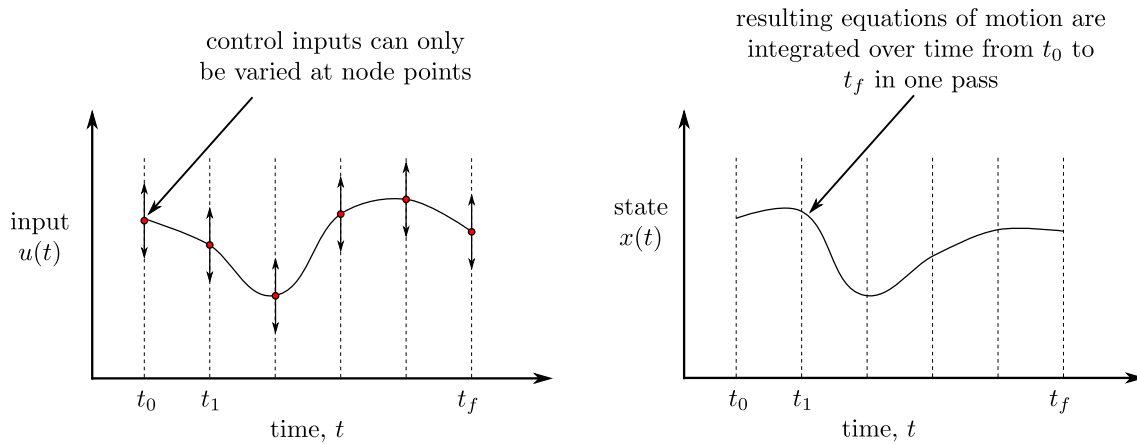


Figure 1.3: Direct single shooting discretisation

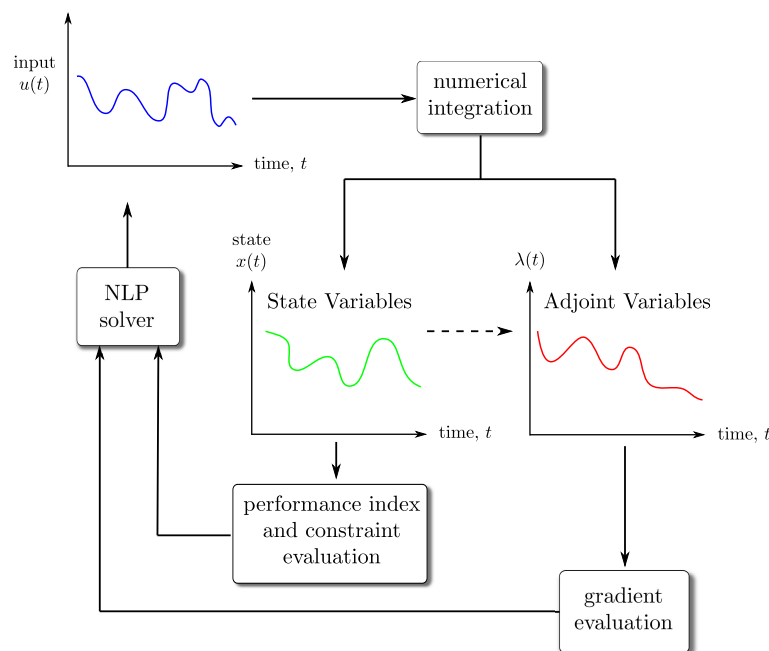


Figure 1.4: Direct single shooting method [16]

The state trajectory is divided up into a number of segments, and the system equations of motion integrated over time, in each respective segment. To ensure continuity between sections, the error between the end and start of the next respective section are driven to zero as part of the process. This is generally thought to reduce the journey sensitivity issues associated with single shooting, whilst achieving rates of convergence closer to collocation [7, 15, 102]. This process is shown diagrammatically in Figure 1.6. Casanova implemented a multiple shooting method with a Sequential Quadratic Programming (SQP) algorithm. This combines the use of a quadratic approximation of the objective function with a line search globalisation strategy. At each iteration, the KKT conditions are reviewed and a merit function used to find the next feasible step. This process is repeated until convergence. Casanova [15] produced a full lap simulation package, using a 7DOF vehicle model, with aerodynamic downforce, a Magic Formula tyre model [69] and a passive, Salisbury type differential. Kelly [47] used a similar strategy and vehicle model, but focused on increasing robustness, by employing

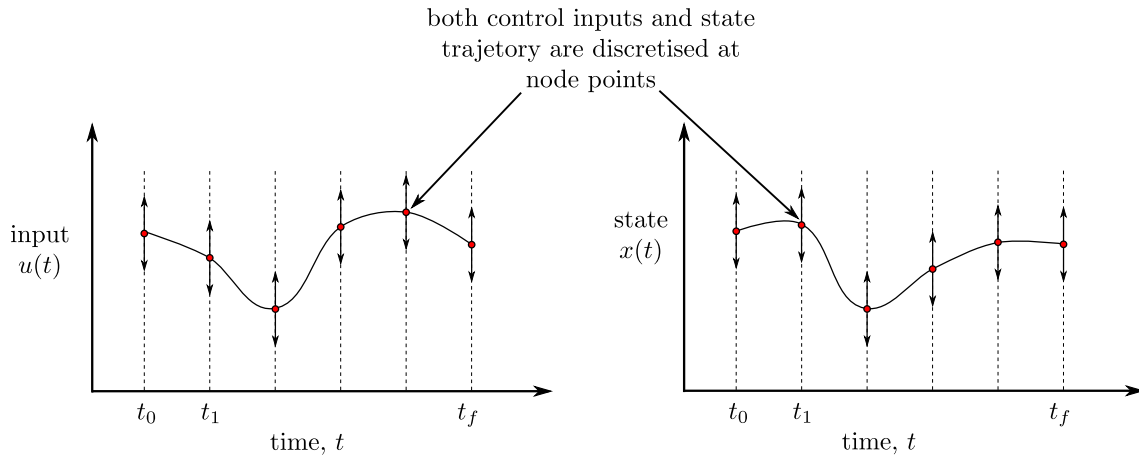


Figure 1.5: Direct collocation discretisation

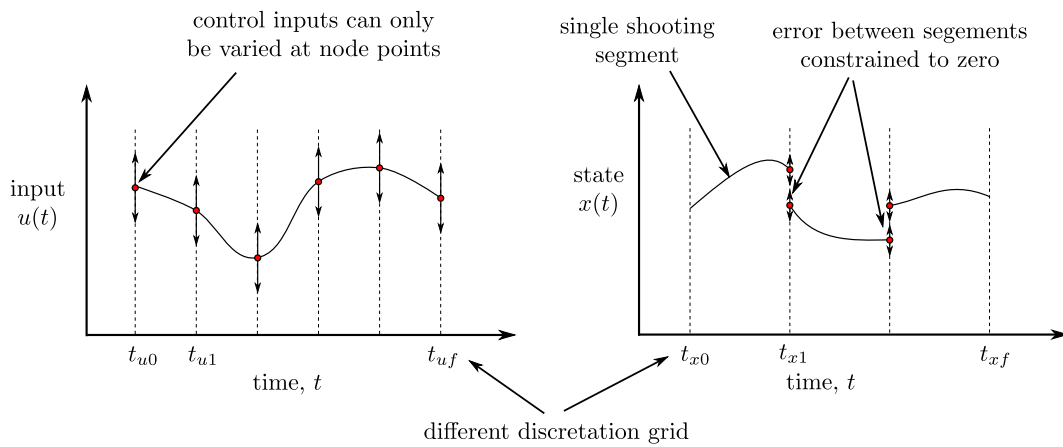


Figure 1.6: Direct multiple shooting discretisation

additional constraints to reduce the solution space. This was achieved through the use of Feasible Sequential Quadratic Programming (FSQP) which, in contrast to SQP methods, does not allow any iterations during the optimisation process to violate the constraints. This is useful in regions along the state trajectory, where the vehicle is likely to be highly unstable (under braking for example), and more likely to create convergence issues.

The inherent limitation of all direct methods, is that results will only be an approximation of the true optimal result. Convergence to a global minimum is also not guaranteed. Stryk and Bulirsch [110] discuss this limitation with respect to the particular case of optimal control problems in the aerospace industry. They used direct methods to solve a number of different optimal control problems and found their accuracy to be within one percent. Although this sounds reasonable, this equates to nearly a second of a typical racing lap time. The resolution of lap simulation programs needs to be in the thousandths of seconds to give the user confidence that the results are representative.

1.3.2.3 Nonlinear Model Predictive Control (NMPC)

Among the first to apply Nonlinear Model Predictive Control (NMPC) or receding horizon control to the minimum time problem was Prokop [80]. In certain aspects, NMPC is similar to the direct methods already discussed, since the control and states histories are again discretised. Rather than evaluating multiple sections of these histories concurrently, NMPC sweeps through discrete time points, and uses a finite preview horizon to make predictions about the future response of the vehicle. This provides an alternative way of overcoming the journey sensitivity issues of some direct NLP methods. A schematic of the process is shown in Figure 1.7.

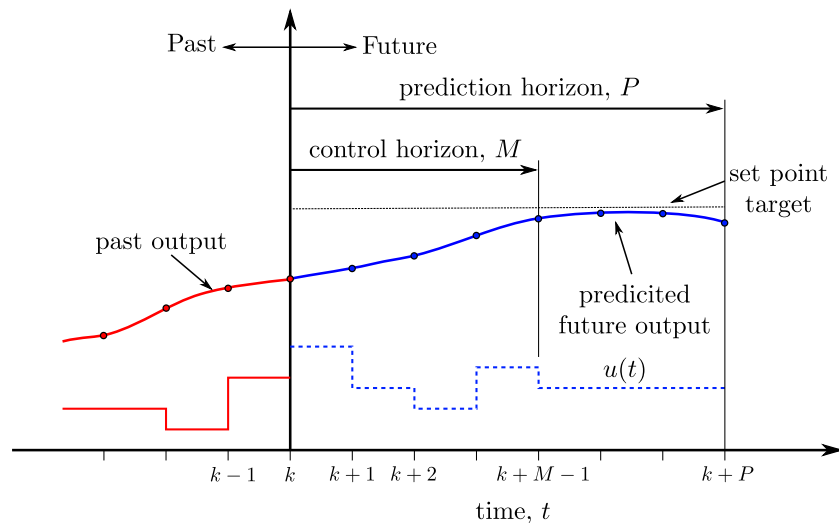


Figure 1.7: NMPC schematic

In the context of this work, the most relevant contribution, is that of Timings and Cole [103]. They focused on making the process more computationally efficient, by linearising the vehicle model and using traditional, but fast, Quadratic Programming (QP) methods. A single track, 5DOF nonlinear vehicle model was used, which also included a second order, low pass filter to represent the limited bandwidth of a human driver's neuromuscular system. NMPC was used to provide a predictive estimate of the vehicle trajectory through lane change and 90° bend manoeuvres. This allowed the on-line adaption of steering and throttle controls to make the optimisation process more robust to external disturbances. The authors compare optimal control history results from a 90° bend manoeuvre, using both NMPC and the direct NLP approach of Casanova and Kelly. The results are very comparable, but it is noted that NLP is marginally better at exploiting tyre saturation limits. Timings and Cole have most recently extended their work to include an indication of the vehicle 'driveability' [104]. This is achieved by using a tube-based control philosophy to account for external disturbances in the vehicle road surface and chassis handling characteristics. The root mean square (RMS) of the driver steering velocity is used to quantify how easy a vehicle is to drive. This idea is central to the work presented in this thesis, as will be shown in subsequent sections.

1.4 Handling Considerations

The time optimal methods described in Section 1.3 can all be used to carry out sensitivity studies, varying vehicle parameters like weight distribution, roll stiffness or differential torque bias, to give the associated impact on lap time [10, 15, 47]. This process was carried out more efficiently by Best [5], Brayshaw [10] and Perantoni [73] who included a limited number of variable vehicle parameters in the optimisation process itself. Either method however, can be used to give a theoretical optimum setup which yields the minimum lap time. This is represented diagrammatically, in Figure 1.8 as the *open-loop vehicle performance limit*. Experience has shown however, that the optimal setup, does not always result in a quicker vehicle on track. This is one of the reasons why many racing teams have developed their own driver-in-the-loop simulators, to allow the highly subjective measure of driver confidence to be practically tested. The higher the confidence, the more likely the driver will be to really push the vehicle limits and achieve a faster lap time. Conceptually, we can represent this by considering a realisable lap time, which is a function of both the driver skill and confidence with a particular setup configuration. A schematic of the process it outlined in Figure 1.8. The key question that arises when evaluating any vehicle setup, is whether changes in the optimum lap time will be followed by similar changes in the realisable lap time.

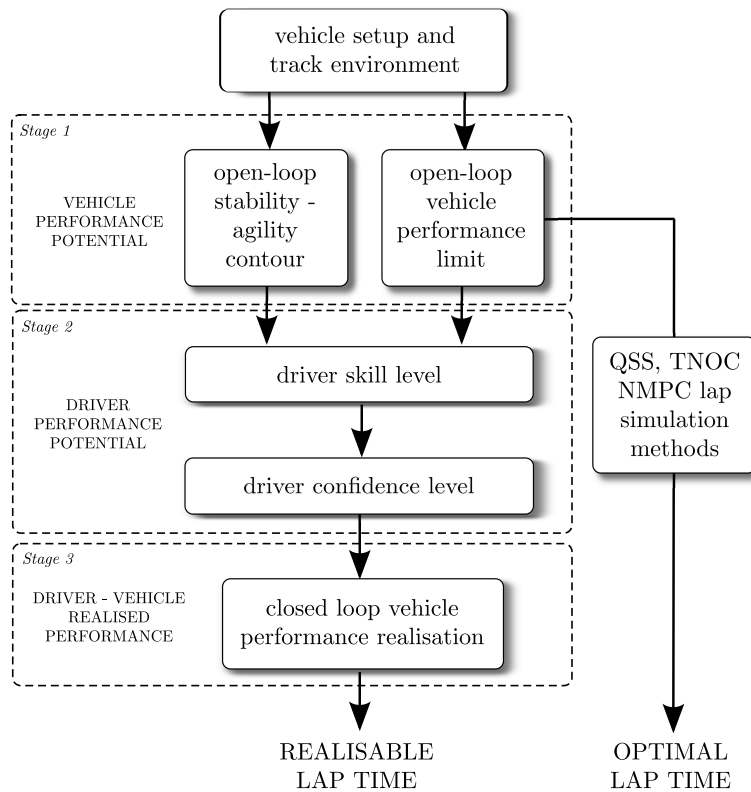


Figure 1.8: Optimal and realisable lap time schematic

In some cases, the answer to this question is relatively straight forward; an increase in engine power or downforce for example, is almost guaranteed to reduce both lap time measures. However, as will be shown in this thesis, some parameter changes, for the LSD case in particular, have a relatively minor impact on the optimal lap time, but a much more significant impact on the stability and agility of the vehicle. These changes are characterised as the *open loop stability-agility contour* in Figure 1.8, and will affect how much of the optimal lap time is realisable by the driver. In summary, a setup change which yields minimal *optimal* lap time improvement, may make the vehicle more driveable and result in a more significant *realisable* lap time improvement.

The stability - agility contour previously discussed, is an attempt to define what drivers normally refer to as ‘balance’. To some extent, this can mean different things to different drivers, but it is generally accepted that the balance between stability and agility, and oversteer and understeer are important elements. In qualitative terms, getting the balance right, normally means preventing the unwanted instability brought on by excessive oversteer during the braking phase of corner, without detrimentally affecting the agility of the vehicle (with excessive understeer), during the corner exit phase. In the context of this work, methods to try and quantify balance have focused on open-loop characterisation of the stability-agility contour. Understeer/oversteer characteristics are addressed, but it is shown that, under braking particularly, it is common for a vehicle to operate in an open loop unstable region [47]. Skilled drivers are known to pilot such systems for brief periods, and benefit from doing so, due to the system’s increased response. Focusing purely on achieving a neutral understeer/oversteer handling balance then, will not allow the driver to fully exploit the vehicle limits.

The investigations of Brayshaw [10] and Kelly [47] included an assessment of vehicle stability using an understeer coefficient and stability derivatives [62]. These considered the limit case, where the vehicle was at its maximum allowable combination of longitudinal and lateral accelerations. While this brings considerable insight, much of a driver’s handling perception is determined by how the vehicle behaves leading up to this limit. It is not sufficient therefore, to focus simply on minimum lap time, or even the balance of the vehicle at the limit. An understanding of how the vehicle balance changes up to the limit is required, to help determine whether a driver might be able to extract the most from a particular setup. This is one of the areas that this research starts to address in Chapter 6. The remainder of this section is devoted to describing how the stability-agility balance has previously been characterised.

1.4.1 Vehicle Stability

The first notion of vehicle stability was captured in the work of Segel [89], who helped develop the fundamental concept of the understeer gradient (K_{us}) and the associated stability margin (S_m) under steady state cornering conditions:

$$K_{us} = \frac{mS_m}{lC_fC_r} \quad (1.20)$$

$$\text{where } S_m = (bC_r - aC_f) \quad (1.21)$$

where a , b , are the distances of the CG from the front and rear of the vehicle, l the wheelbase, and m the vehicle mass. This was based on a traditional 2DOF bicycle model with linear cornering stiffnesses (C_f , C_r) and assumes slip angles are small. The stability margin is essentially a measure of the resultant yaw moment acting on the vehicle. If the sign is positive, higher lateral tyre forces at the rear are present giving rise to understeer. Similarly, if the sign is negative, then oversteer behaviour dominates. In the racing environment, stability assessments are required near or even past the lateral force saturation limit, so it is crucial that cornering stiffnesses take into account load transfer and combined longitudinal and lateral slip conditions [69]. With the particular case of the limited slip differential, it is also important to include the additional yaw moment generation from the difference in longitudinal tyre forces of the driven wheels.

A way of developing this steady state stability concept into one that is closer to a full dynamic description, is to consider the influence of resultant unbalanced forces due to perturbations in the vehicle states. Segel [89] and Milliken [62] were the first to propose this methodology and borrowed techniques from the aerospace industry. These relied on the evaluation of the change in yaw moment ΔN , due to perturbations in steer angle $\Delta\delta$, side slip $\Delta\beta$, and yaw rate Δr (see Figure 1.9). These were formalised into a series of stability and control derivatives [62, 81], which provided useful metrics with more meaningful physical interpretations.

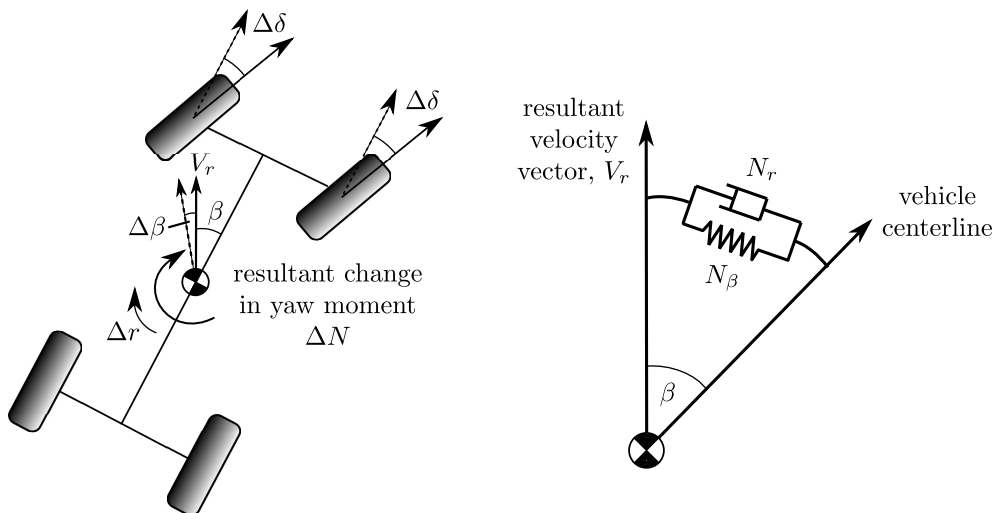


Figure 1.9: Stability and control derivative concept

Yaw Stiffness, $N_\beta \left(\frac{\Delta N}{\Delta \beta} \right)$ - this is the vehicle response to a disturbance in side slip angle, and can be likened to a spring which acts between the vehicle centreline and resultant velocity vector (see Figure 1.9). When N_β is positive, a restoring or understeer moment is generated, which attempts to reduce side slip angle. When the sign turns negative, the resulting yaw moment encourages higher side slip angles, hence oversteer behaviour.

Yaw Damping, $N_r \left(\frac{\Delta N}{\Delta r} \right)$ - this is the vehicle response to a disturbance in yaw velocity (rate), and can be likened to a damper which acts between the vehicle centreline and resultant velocity vector (see Figure 1.9). The sign is always negative, and analogous to an angular viscous damper, always trying to decrease yaw velocity.

Control Derivative, $N_\delta \left(\frac{\Delta N}{\Delta \delta} \right)$ - this is the vehicle response to a disturbance in steering angle, and can be considered the ‘control power’ or ‘turn-in’, available to the driver to steer the vehicle. This is always positive, and falls to zero when the steered axle is at its adhesion limit.

Another well established method, is to evaluate the system eigenvalues of a linear, typically 2DOF (side slip - yaw) bicycle model, or a more complicated nonlinear model which has been linearised about multiple operating points [20]. Sharp [91] describes this linearisation procedure for a simple 3DOF planar vehicle model, through the use of a multibody simulation package called AutoSim [88]. The system eigenvalues were used to show how the stability of yaw, lateral and roll motions changed with speed for the straight ahead, or *free response* condition. Several other authors have applied similar techniques to show yaw and side slip stability under steady state cornering conditions [10, 20]. Steady state cornering however, is difficult to apply to the limit conditions often associated with motorsport. To the authors knowledge, the use of eigenvalue stability analysis for accelerating or decelerating (linear time varying, LTV) vehicles is not in general, well documented. Notable examples include assessments of motorbike stability [26, 90] and in the context of jack-knifing articulated vehicles [35]. So called *frozen time* eigenvalue analysis can be conducted by computing the system eigenvalues at a number of instants within the range of operating time. These could be points in time where longitudinal and lateral accelerations are considered constant or in quasi steady state, and where the vehicle states are assumed to be varying only very slowly. Inferences drawn on system stability using linearised frozen time models however, should only be used with caution. This has been shown to be especially relevant when eigenvalues are near or cross the imaginary axis [95]. In this work, frozen time eigenvalue analysis is used to predict stability characteristics throughout the GG vehicle performance envelope (see Chapter 6).

More recently, the study of vehicle stability has focused on providing a more complete description of nonlinear system stability, by using phase plane analysis and bifurcation theory [41, 122, 52]. This allows all possible solutions of the nonlinear system equations (starting from a non-zero initial state), to be visualised on a two-dimensional phase plane plot. This is only valid however, around a set operating or equilibrium point. In the vehicle dynamics application, it is common to plot side slip angle against yaw rate for a set speed and steering angle. An example is shown in Figure 1.10.

The continuous dynamics system, $\dot{\mathbf{x}} = \mathbf{f}(\mathbf{x}, t)$ is said to be asymptotically stable if two conditions are met [96]:

- (i) the initial system states $\mathbf{x}(t_0)$, start from within a circle of sufficient radius e , and remain within a circle of arbitrary radius E , for all time.

$$\|\mathbf{x}(t) - \mathbf{x}_e\| < E, \quad \forall t \geq t_0 \quad \text{if} \quad \|\mathbf{x}(t_0) - \mathbf{x}_e\| < e \quad (1.22)$$

- (ii) the state trajectory converges on the equilibrium point states \mathbf{x}_e , as time tends to infinity.

$$\lim_{t \rightarrow \infty} \|\mathbf{x}(t) - \mathbf{x}_e\| = 0, \quad \text{if} \quad \|\mathbf{x}(t_0) - \mathbf{x}_e\| < e \quad (1.23)$$

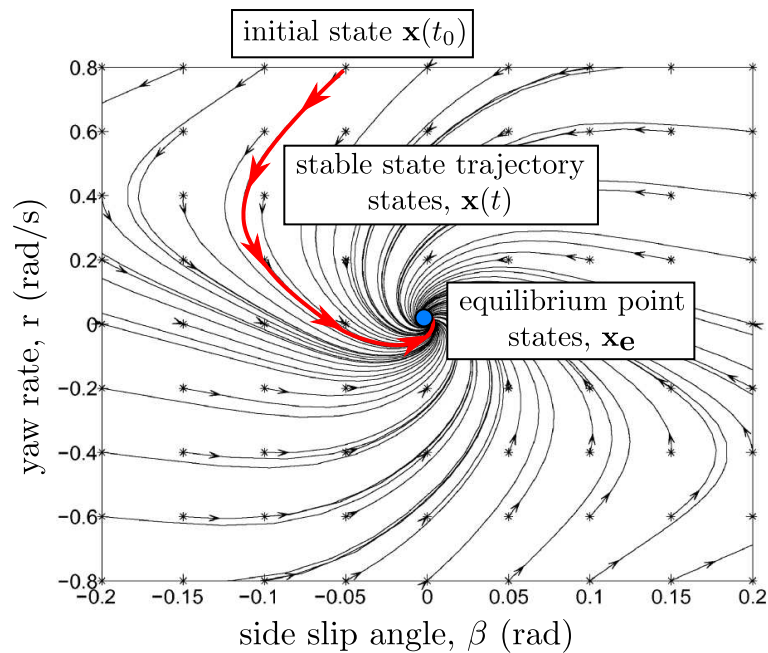


Figure 1.10: Side slip - yaw rate phase portrait example [55]

If condition 1.22 does not hold then the system is unstable. It is also important to note that these nonlinear system concepts only refer to *local* stability, about the equilibrium point. If condition 1.22 holds for any initial state ($\mathbf{x}(t_0) \in \mathbb{R}^n$), then the system is said to be *globally* stable.

The nonlinear description of stability can be related back to the linear eigenvalue analysis of Sharp [91], by considering the equilibrium point of the phase plot. This operating point, relates to a linearisation point of a nonlinear model, with its own associated eigenvalue and stability properties. In the linear system case however, asymptotic stability implies global stability, so there is no need to differentiate between these two forms.

1.4.2 Vehicle Agility

Historically, methods to define the agility of a vehicle are not detailed in literature as rigorously as stability criteria. The terms agility, controllability and manoeuvrability are sometimes used interchangeably, confusing their real meaning. In the formal sense, a linear system is said to be controllable if, by changing its inputs, the initial system states can be transformed to *any* other state, in a finite time [30]. In the vehicle dynamics sense, this concept is most closely related to vehicle manoeuvrability, which is the ability to change the resultant magnitude and direction of the velocity vector. Vehicle agility however, refers to the driver's ability to rotate the vehicle about its centre of gravity, and is independent of acceleration or braking control inputs. This can be thought of as a control power, or directional authority.

Although not the only metric used for directional authority, the yaw rate response has proved a popular measure for objective handling evaluations and in some cases, correlated well with subjective driver evaluations [116, 1]. Much of the literature that surrounds this area originates from the mainstream automotive industry, where there are significant commercial and safety based requirements, to relate driver assessments to objective handling metrics. In the vehicle agility sense, there is no methodology which has been widely adopted, but a number of standards have been produced to augment this procedure. ISO7401 [43] details a step steer response test in which the steady state yaw rate gain and response time, help to characterise an aspect of vehicle agility. The standard also details a procedure for generating a frequency response bode plot from sinusoidal steer tests. This helps to give a more complete picture of transient response, as well as an open-loop measure of the vehicle's bandwidth in yaw. Mimuro [63] uses similar techniques, but formalises steady state gain, natural frequency, damping ratio and phase delay into a spider style diagram for practical evaluation. The yaw rate gain is interpreted as a heading easiness, the natural frequency as a heading responsiveness and the damping ratio as directional damping. Unfortunately, literature which explains the influence of each of these factors on driver perception is sparse.

Although the control derivative metric detailed in Section 1.4.1 was derived from similar aerospace methods, more modern techniques have also been demonstrated by Yi [122]. In his evaluation of agility in an aggressive pendulum turn manoeuvre, two agility metrics are used: lateral acceleration jerk (or the derivative of the acceleration vector), and a normalised relative acceleration. This is simply the ratio of lateral acceleration to a peak value calculated from the lateral tyre force potential. These are used in combination to represent an overall metric of vehicle agility.

The stability and agility metrics described, can all characterise varying aspects of the vehicle handling balance. The key issue however, is how the driver perceives these differences to get an overall sense of driveability. The scope of this task is vast, and clearly different drivers will have varying skill levels and associated preferences. In this work, methods are presented for characterising the vehicle stability - agility balance, and a way in which to change these to suit driver preferences. The definition of these driver preferences however, is outside the scope of this work.

1.5 Aims and Objectives

The aim of this research is to develop methods to optimise the torque biasing characteristics of motorsport limited slip differentials. The supporting objectives of this research are:

1. Create, test and validate adjustable torque and speed sensing LSD models as a basis for exploration into vehicle handling influence. This includes the development of a differential test rig to validate the LSD in isolation.
2. Validate LSD models within the parent vehicle model system. This will involve validation against in-car data, to show the models are capable of capturing transient differential behaviour.
3. Use time optimal methods to show the influence of typical torque and speed sensing LSD setup parameters on lap time. These include drive and coast ramp angles, positive and negative preload and Viscous Coupling (VC) rating.
4. Investigate alternative methodologies to show the influence of typical LSD setup parameters on the vehicle stability and agility.
5. Use quasi steady state and dynamic parameter optimisation methods to establish time optimal differential torque bias solutions. Investigate how these optimal solutions can be implemented on both passive and active LSD devices.

1.6 Thesis Structure

Chapter 2 presents the remaining literature which is relevant to the work presented in this thesis. This includes a review of differential types found both in motorsport and in the wider mainstream automotive industry. Previous studies which have focused on LSD handling influence are also discussed. The chapter concludes with a summary of findings from the material presented in both Chapters 1 and 2.

Chapter 3 details the model formulation of an adjustable, torque sensing, plate type Salisbury LSD and a speed sensing VC unit. A novel VCP LSD model is also presented, which combines both torque and speed sensing properties. These models are validated on a differential test rig under steady state and transient conditions.

Chapter 4 describes the creation of a 7DOF vehicle model which is used for the majority of handling assessments presented in this thesis. The vehicle model is validated against in-car data from a FWD saloon racing vehicle, around a qualifying lap of the Snetterton race circuit.

Chapter 5 presents a nonlinear constrained optimisation method to find the vehicle GG envelope. This method is developed to improve robustness and to include a range of LSD models. The optimisation scheme then forms the basis of a QSS lap simulation program, used to perform several parameter sensitivity studies on a range of LSD setup parameters. The chapter concludes by presenting the optimal torque biasing profile throughout the vehicle speed range and uses this to propose a novel LSD device.

Chapter 6 builds on the QSS GG diagram method, by linearising the vehicle model about multiple operating points, and investigating how the stability and agility of the vehicle changes throughout the GG envelope. To demonstrate the influence of LSD setup on particular regions in the GG envelope, stability and agility contours are then defined for a number of LSD configurations.

Chapter 7 presents a nonlinear optimal control solution to the minimum time problem, for a fully dynamic, nonlinear vehicle model. The optimal torque bias profile for a series of manoeuvres is found and compared to previous QSS solutions. The influence of tyre road friction and wear considerations are also included in the analysis.

Chapter 8 summarises the main conclusions from the research and outlines suggestions for future work.

Chapter 2

Differential Technology and Handling Review

In pursuit of the aims and objectives defined in Section 1.5, this chapter presents the current body of knowledge that surrounds state-of-the-art differential hardware. Several differential types are presented and used to demonstrate differences between passive and active LSDs, and the greater control authority offered by Torque Vectoring Differentials (TVD). The way in which each device creates a torque transfer is discussed, along with their potential to alter vehicle handling balance. The chapter concludes with a discussion of how previous researchers have modelled differential behaviour.

2.1 Passive Limited Slip Differentials (PLSD)

Section 1.2 demonstrated that the ultimate differential is one that allows the transmission of torque to two wheels rotating at different speeds, but also limits the amount of longitudinal slip under conditions where traction is compromised. The following sections are designed to review how existing LSDs try to achieve this aim in generating a bias torque, and how this bias torque is characterised. An initial evaluation of their influence on handling is also given, which is later developed in more detail in Section 2.4.

All LSDs rely on being able to bias torque from a faster to slower rotating wheel, which, provided there is adequate grip to support the additional torque, can be hugely beneficial. Several authors have demonstrated improvements in overall traction under straight-line acceleration [50, 51, 97] and over split- μ conditions (lower grip level at one wheel). During cornering conditions, the inherent nature of the torque transfer means that a PLSD will generally produce an opposing yaw moment during corner entry, promoting understeer behaviour at relatively low lateral acceleration levels (0-0.6g)[25, 97, 119]. Although detrimental in some cases, this opposing yaw moment has also been used to stabilise the car under extreme braking [17, 66], where longitudinal weight transfer effects can promote corner entry oversteer. Without a means of active control however, this provides only a very basic level of yaw correction. The amount of torque transfer a PLSD can support is critical in determining its effects on vehicle handling. Since the magnitude of the torque bias is determined by the mechanical properties of the differential and not environmental factors like the grip available at the tyre, their setup and adjustability are crucial. This helps explain why much differential

development has focused on defining differential torque bias characteristics. Chockolek [18] and Hass [34] provide a fundamental basis for locking torque characterisation by defining this torque biasing ability as a *bias ratio* or *percentage locking*:

$$\text{Torque Bias Ratio} = \frac{T_1}{T_2} : 1 \quad (2.1)$$

$$\text{Percentage Locking} = \frac{(T_1 - T_2)}{(T_1 + T_2)} \times 100 \quad (2.2)$$

Where T_1 and T_2 describe the torque that can be supported by each of the driven wheels. The terms ‘torque bias’ and ‘locking’ are used interchangeably in literature, and this convention shall be continued in this thesis. Bias ratios in the region of 1-6:1 are common [18, 62, 97] but are highly dependent on the method of locking torque generation. Similarly, 0% locking indicates that the differential is fully ‘open’, and 100% that the two wheels have locked together and are operating as a spool differential. The vast majority of literature shows that the way in which this torque bias is created and controlled can be classed into two main types [25, 59, 62, 97]:

Torque Sensitive - PLSDs which rely on their input torque to determine locking characteristics. These types, to a limited extent, will automatically re-apportion torque to the wheel with more grip. As such, they are more proactive in their operation and will prevent excessive longitudinal slip occurring in many cases. Two of the most common types include the plate type, or Salisbury differential [62, 97] which uses clutch plates to create a bias torque and the Torsen (I & II) [18, 97], which harnesses the friction generated from the axial thrust of helical worm gears. A more detailed explanation of the operation of a plate type differential is given in Section 2.1.1

Speed Sensitive - PLSDs which rely on a wheel speed difference to determine locking characteristics. When compared to torque sensing types, these are more reactive in operation, since sufficient longitudinal slip needs to occur first for any locking to take place. One of the most common is the Viscous Coupling (VC) which has proven to be more progressive in operation [97] since the locking relies on the shearing action of metal plates through a viscous fluid (typically silicon), and not a fluctuating input torque. Other types like the gerotor [71, 97] use the hydraulic pressure generated from a gerotor pump to clamp a traditional multiplate clutch, increasing its bias torque proportionally with wheel speed difference. In general, one can conclude that the use of a fluid element provides a greater degree of damping, but at the expense of responsiveness.

Less well documented in literature is the presence of a PLSD which controls locking torque through both speed and torque sensitive means. Smith [97] describes a Viscous Combined Plate (VCP) device, which uses a plate type differential to provide the majority of locking and a VC to smooth the delivery of locking torque. Their locking torque characterisation and influence on vehicle handling are not well documented in literature. A more detailed explanation of their operation is given in Section 2.1.3.

2.1.1 Plate Type (Salisbury)

One of the most common torque sensitive PLSDs is a plate type, or Salisbury differential [62, 97]. Like the majority of LSDs it uses a conventional bevel gear open differential to provide a means of wheel speed independence. It generates a torque bias through the use of a multiplate clutch, with alternate friction discs splined to left and right-hand outputs. A relative speed difference between the clutch plates coupled with an axial clamping load, generates a frictional torque that attempts to lock one output to the other. The extent of this locking is controlled by the magnitude of the axial load and the frictional properties of the clutch surfaces. Salisbury types have proved popular in motorsport since they are responsive, highly adjustable and cost efficient. Figures 2.1 and 2.2 show an example of an Xtrac [121] plate differential which is typical of many motorsport differentials racing today.

Inherent in its definition, the degree of torque bias the device can support is determined by its input torque. A final drive gear transmits the engine input torque to the differential body and through to a splined set of ramps which can move axially within the body. The ramps react against an angled set of crosspin faces which are constrained to the pinion mates and side gears, through to the left and right hand outputs. It is this reaction force that produces an axial component which clamps the clutch plates and provides a torque bias. There are a number of manufacturers which have developed variations on this theme, but Smith [97] and Milliken [62] identify that they are all tuned using three main elements:

- (i) **Ramp Angle** - The ramp angle controls the proportion of input torque which is translated into an axial clutch pack clamping force. These angles can be tuned for both drive and coast conditions (on and off throttle). Typically, the lower the angle, the greater the magnitude and rate of locking. Ramp angle configurations are normally quoted in the form 'D65/C30' for a 65° drive angle and a 30° coast angle.
- (ii) **Number of Friction Faces** - Friction discs are arranged symmetrically either side of the ramps and can be configured to give different numbers of active friction faces. Four, six, eight and sixteen are typical depending on packaging limitations.
- (iii) **Preload** - This is a residual clamping force (typically from a belleville spring), that provides a degree of torque bias when no input torque can be supported (e.g. when a wheel is off the ground). The preload applied can be both positive (increasing any locking) and negative, which serves as a load which must be overcome before any locking can be generated.

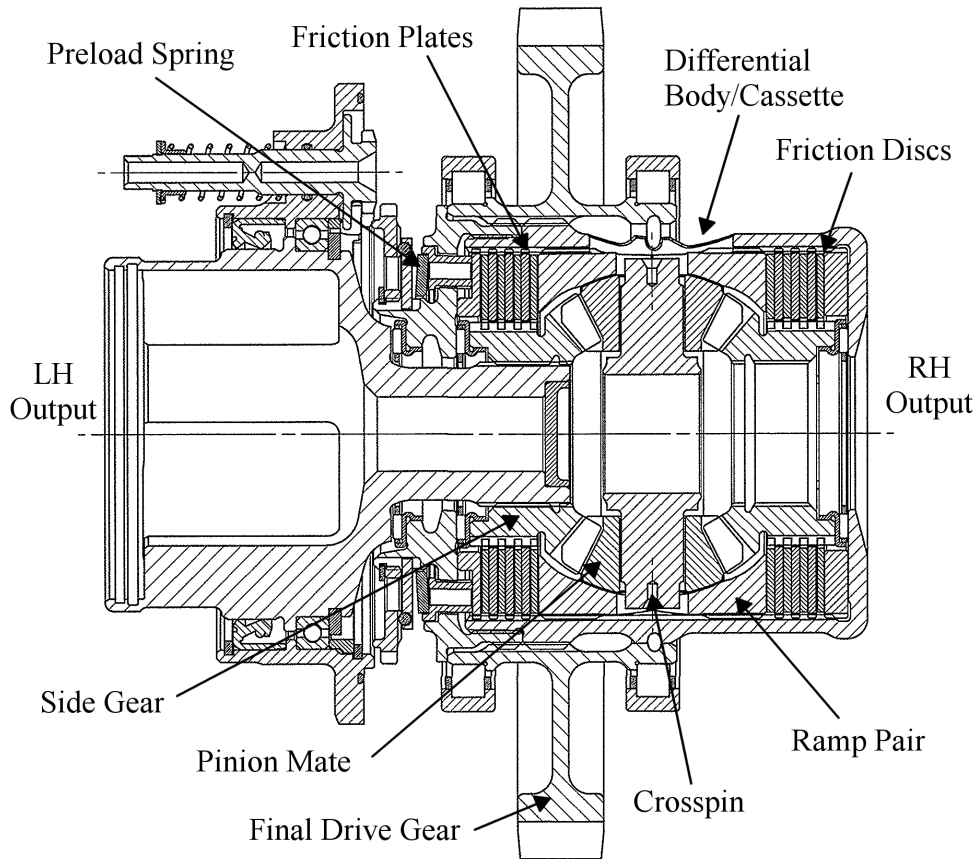


Figure 2.1: Xtrac plate type Limited Slip Differential (sectional view) [121]

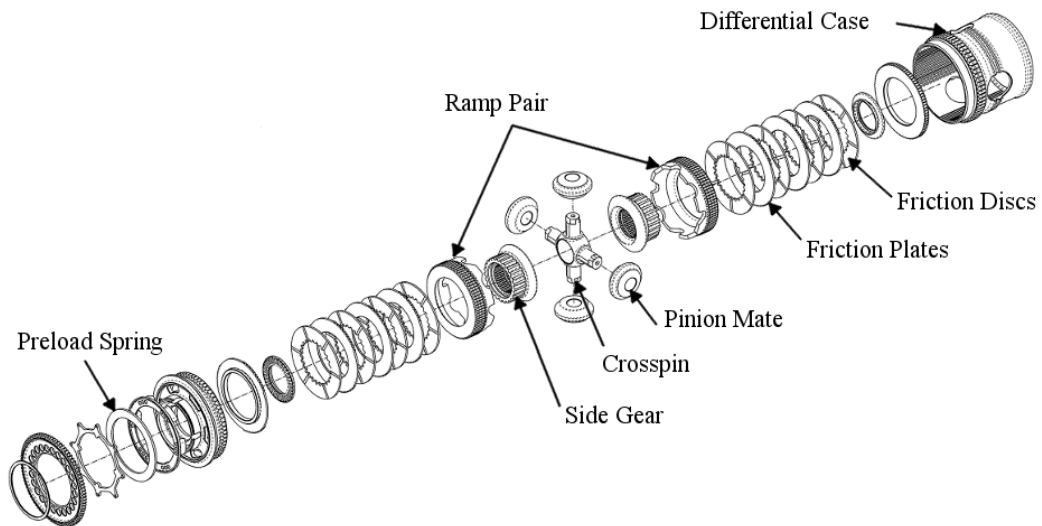


Figure 2.2: Xtrac plate type Limited Slip Differential (exploded view) [121]

2.1.2 Viscous Coupling (VC)

In contrast to the torque sensitive LSD described in Section 2.1.1, speed sensing differentials are not reliant on an input torque to generate a bias torque. Of the current types in use, viscous couplings used in conjunction with a conventional bevel gear open differential have proved popular, since they provide a reliable and cost efficient solution, which can be easily tuned to give a range of locking characteristics [65, 74]. Figure 2.3 shows a typical VC unit, in which a set of thin steel plates and discs are alternately splined to the VC housing and hub. The housing is filled with a viscous fluid (typically silicon), which is sheared under relative rotation of the housing and hub. This shearing action produces a viscous drag torque, which is proportional to the slip speed of the rotating elements.

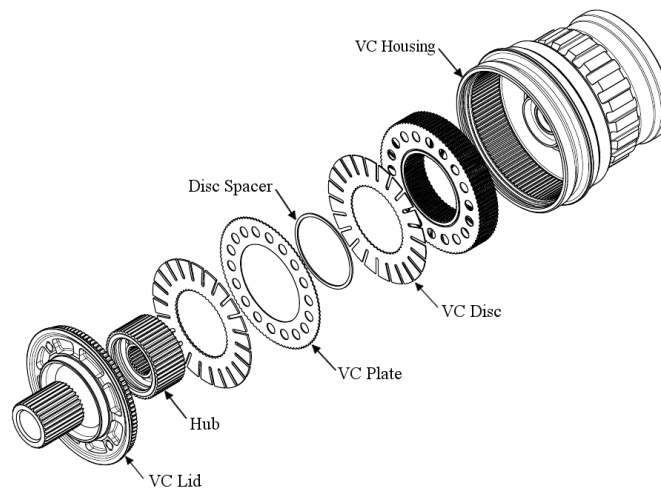


Figure 2.3: Viscous Coupling (VC) unit (exploded view) [121]

VC units can be tuned using the following elements [99, 100]:

- (i) **Number of Shear Faces** - In a similar manner to plate LSDs, the number of shear surfaces can be rearranged to increase or decrease the number of active surfaces shearing the fluid. Unlike plate LSDs, the shear surfaces are not designed to touch in service.
- (ii) **Disc Spacer Thickness** - This controls the separation distance between the shear discs and plates. The closer the shear surfaces, the greater the velocity gradient, and the greater the resulting shear torque.
- (iii) **Fluid Viscosity** - The viscosity of the shear fluid varies significantly with both shear rate and temperature. Base viscosities can be adjusted by altering the chemical composition of the shear fluid.
- (iv) **Plate and Disc Geometry** - The configuration of specific slots, holes and grooves in the shear surfaces has been shown to alter the torque biasing characteristics throughout a range of differential speeds and temperatures [65, 74, 100]. Perhaps more significantly, they also improve the service life of a VC unit, by limiting excessive temperature and pressure rises of the shear fluid.

2.1.3 Viscous Combined Plate (VCP)

Examples of passive LSDs which allow their torque bias to be controlled by both speed and torque sensitive means are rare. Smith [97] describes a Viscous Combined Plate (VCP) differential which combines a traditional plate LSD with a VC unit. Once such example is shown in Figure 2.4. The VC unit is coupled to the outputs of the torque sensing plate LSD with the use of a linking shaft and only influences the torque bias when there is a driven wheel speed difference. This is thought to combine the quick response of a plate LSD with the speed sensing VC element used to dampen any spikes in transfer torque (although this is not substantiated in literature). Perhaps the biggest performance potential the device holds is an increased ability to tune its characteristics for different corner phases. The torque sensing element will have more influence during corner entry and exit phases. The speed sensing element however will have a more significant effect at the corner apex. The implications of this are discussed in Chapter 6.

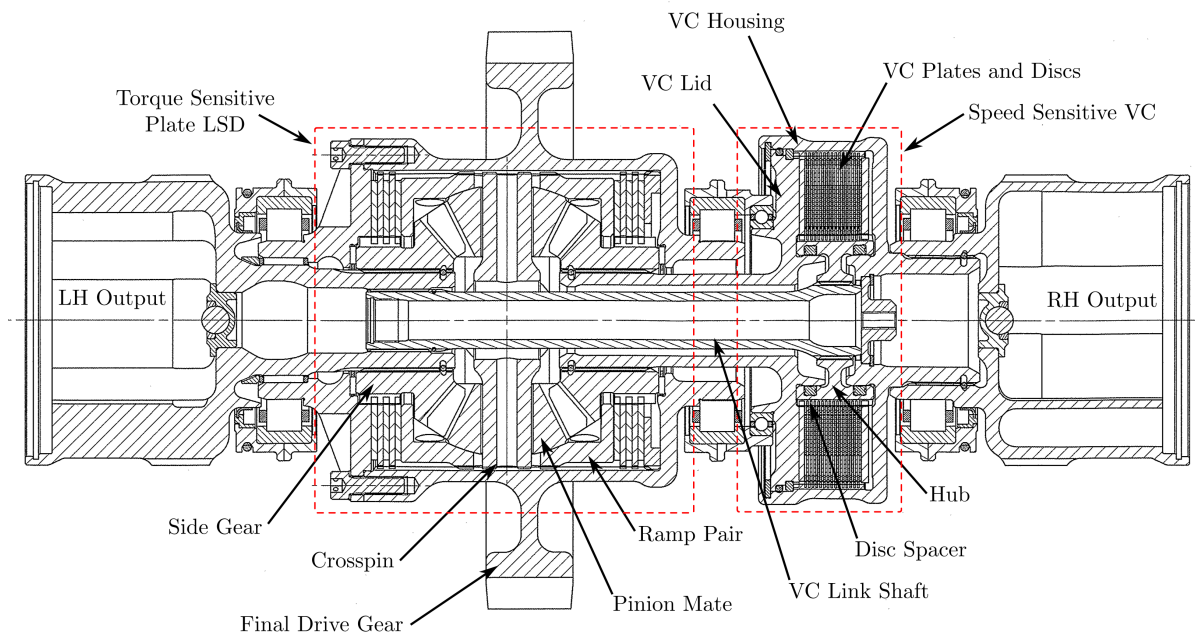


Figure 2.4: Xtrac [121] Viscous Combined Plate (VCP) LSD example (sectional view)

2.2 Active Limited Slip Differential (ALSD)

To increase the flexibility of PLSDs, a means of closed loop control allows both the precise point of application and the magnitude of the locking torque to be controlled as required. Their first documented use was on the Rally Cars of the late 1980s [119] and later found their way onto a limited number of production sports cars, in the early 1990s [84]. Initial research was aimed towards overcoming the corner entry understeer associated with PLSDs and formulating effective control system implementation. Holzwarth [42] and Teraoka [101] also demonstrated that ALSDs provided better integration with other control technologies in development during this

period, like ABS, Traction Control (TC) and yaw stability control systems [111, 112]. This research theme is still highly relevant today, driven by the need for constant road car safety improvements [39, 75].

The hardware associated with ALSDs is very similar to their passive counterparts. The most common examples still use a wet multiplate clutch as the basis for torque transfer, and can be actuated in a number of ways: electro-hydraulically, electromagnetically and by electric motor control. Hancock [36] and Stall [98] discuss the relative merits of each type of actuation. It is clear that for mainstream automotive applications, electric motor control provides a good compromise between performance and cost. Contrastingly, in the motorsport sector, as one would expect, there is a bias towards systems that provide ultimate performance and minimum weight. As a result, more expensive electro-hydraulic systems [119] are used, as they provide faster response times and can be packaged more easily for minimum weight. Only the very highest levels of motorsport can afford the use of such technology, which restricts their use to Formula 1 and up until 2010, the World Rally Championship (WRC). An example of an epicyclic WRC centre differential is shown in Figure 2.5. The torque bias between outputs is controlled by an external hydraulic system, which varies the pressure acting against a piston, and the resulting thrust load on a clutch pack.

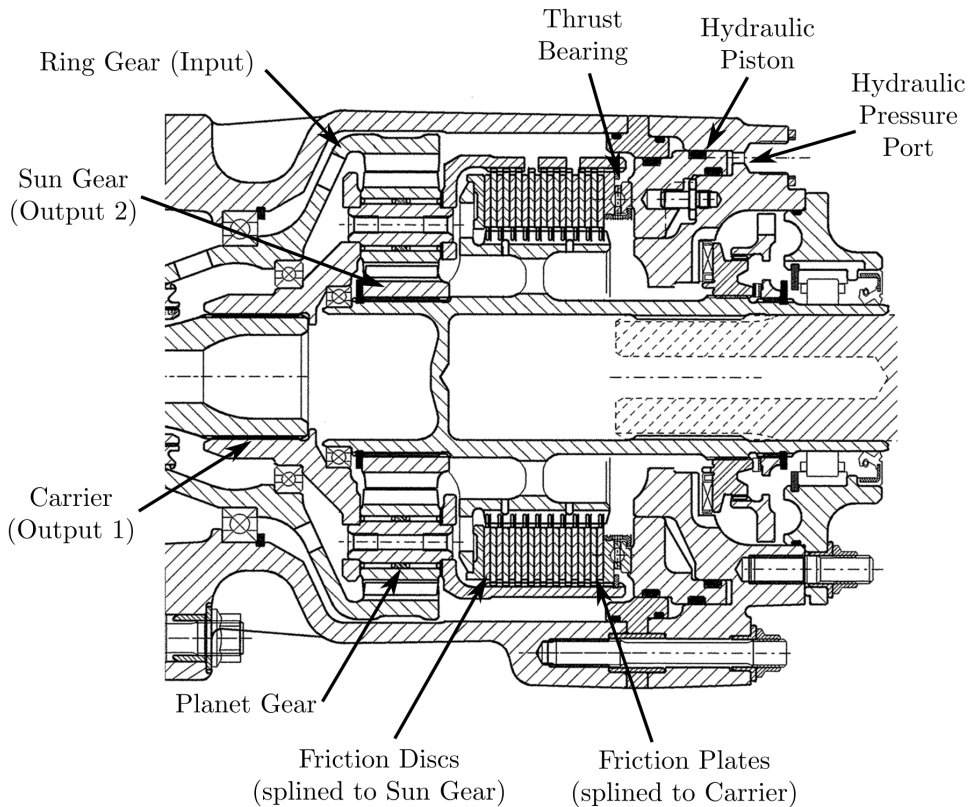


Figure 2.5: WRC active centre differential example [121] (sectional view)

In Formula 1, technical regulations [28] still dictate that these are semi-active, open loop devices, since some element of driver control must be retained. Differential control algorithms must use a limited number of vehicle data channels including, longitudinal and lateral acceleration, speed, engine rpm and race lap number. The driver is able

to switch between configuration maps during a race distance through steering wheel control dials. An example of a 2008 F1 steering wheel is shown in Figure 2.6. These typically allow a range of settings between fully open and fully locked and are normally split into entry, apex and corner exit controls. This allows the balance of the car to be modified as this changes with tyre degradation and fuel load. Much of the work presented in this thesis, is aimed at understanding how similar, corner-phase specific changes can be made with passive differentials.

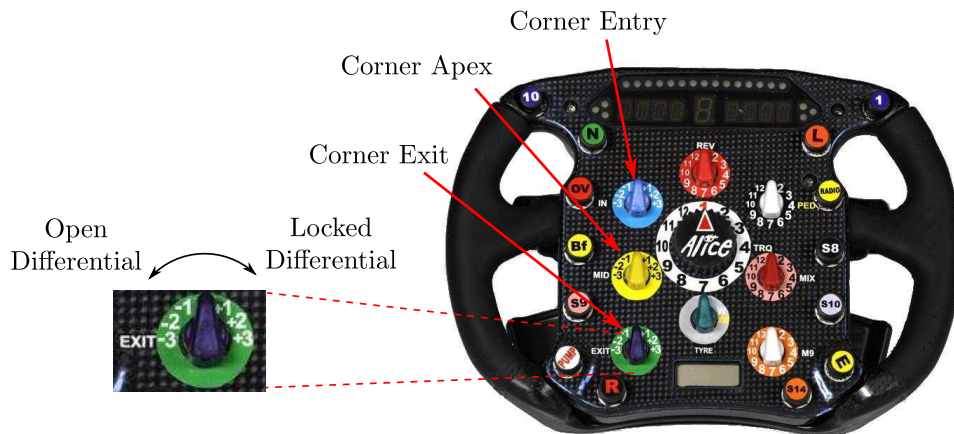


Figure 2.6: Formula 1 active LSD driver controls, [115]

2.3 Torque Vectoring Differentials (TVD)

Although the focus of this thesis is on the evaluation of passive LSDs, a brief discussion of the literature surrounding TVDs is also given, so the physical hardware required for their operation and potential benefits are understood.

Active LSDs offer a much greater flexibility and control authority than their passive counterparts, but they can only ever be used for enhanced stability and traction at the adhesion limit. Their yaw moment generation is also effectively limited by their input torque. To increase their potential into the realms of sub-limit control, the application, magnitude and critically the direction of the torque transfer is required. Differentials which fulfil these requirements are commonly referred to as Torque Vectoring Differentials (TVD).

One of the first uses of TVD technology was to steer military tracked vehicles and was used more out of necessity than for performance enhancement. Its documented use in motorsport begins in the 1980s, where active front, rear and centre differentials were used to make Rally Cars more responsive [119]. A handful of teams in Formula 1 used TVDs on both front and rear axles (to apportion drive and brake torque), but these devices were promptly banned in the 1990s [28]. Mitsubishi developed these concepts into a production car version with its Active Yaw Control (AYC) system [84]. A TVD was used as an integral part of an AWD powertrain consisting of passive front and centre differentials with the TVD supplying torque to the rear wheels. A section view

and schematic of the rear differential unit is shown in Figure 2.7 [85].

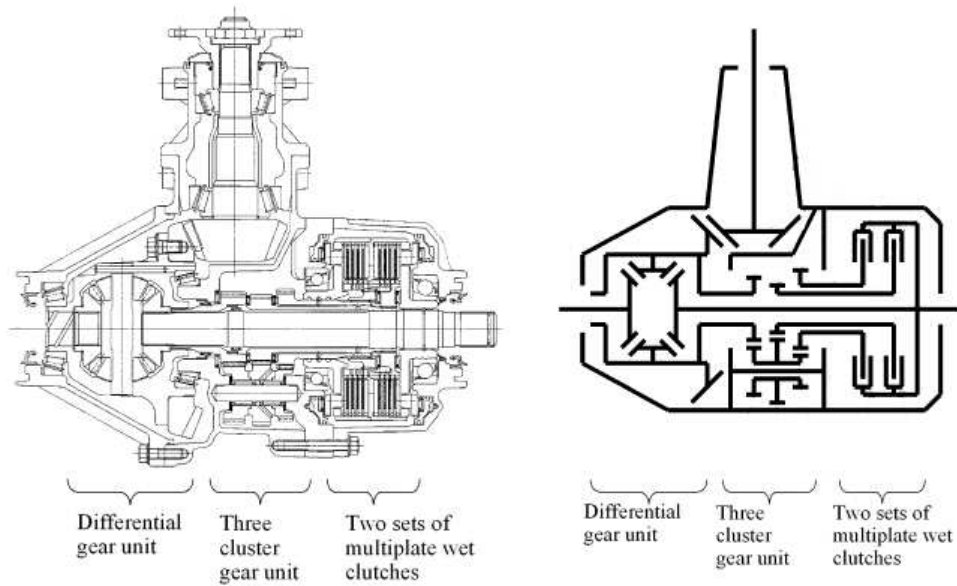


Figure 2.7: AYC differential section view and schematic (superimposed/clutch type) [85]

At its heart, a conventional spur or bevel gear open differential provides a means of wheel speed independence. An additional gear train is then used to divert a proportion of the input torque to speed up a set of shafts relative to the main differential housing. Typically, two clutches are then positioned or *superimposed*, on the torque path between these shafts and the two wheel outputs. Since these shafts are rotating faster than the two outputs, selective activation of either clutch will give a torque transfer in the desired direction.

Other manufacturers have introduced similar lateral torque vectoring devices which operate in a subtly different manner. Rather than transferring torque through clutches superimposed onto the torque path, it is directed through an epicyclic gear train by two *stationary* clutches or brakes. Figure 2.8 shows schematic diagrams of two such systems: the Honda ATTS [93] and Magna MDT-II [64]. They both operate by selectively locking either the carrier or sun inputs of an epicyclic gear train to the stationary body of the differential. The exact configuration of the epicyclic itself can take various forms, but all operate in a similar manner. The Ricardo TVD [117] is a combination of both superimposed and stationary clutch types. Each clutch is engaged pre-emptively before a torque transfer can take place, with the direction being controlled by a stationary clutch fixed to the differential casing.

There is no doubt that TVDs increase the vehicle performance capability, but high production costs currently preclude their use in the majority of production cars. Another important factor to consider is their additional weight, which can be anything from 15-30kg over their traditional LSD counterparts [36]. For the moment at least, TVD development is focused around reducing this weight deficit and continued improvement in actuator response and control systems integration. Sawase [87]

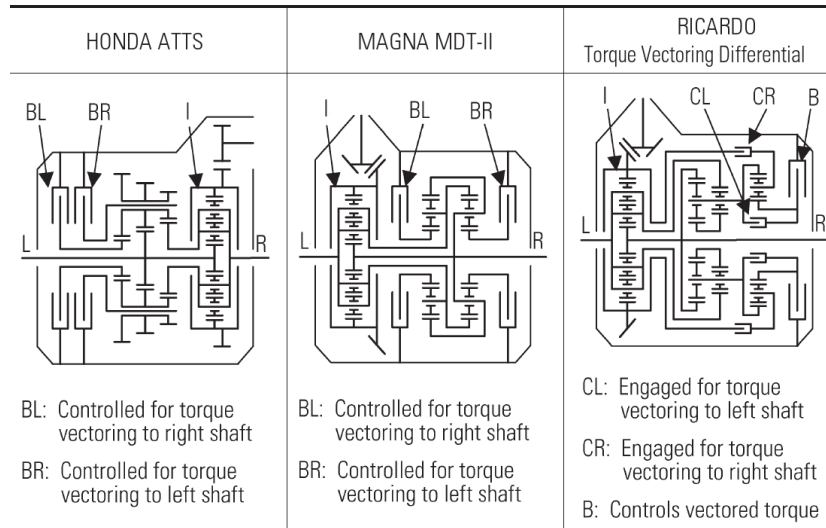


Figure 2.8: Stationary clutch/brake type TVD [87]

postulates that a hydraulic based torque transfer (instead of the use of clutches) may ultimately prove more efficient and controllable if cost reductions would ever allow their use in road cars.

2.4 Differential Handling Influence

Open Differential - as one might expect, since the open differential must deliver equal torque to each driving wheel, they have been shown to have a fairly benign impact on handling [66, 83, 97], up to the point of tyre saturation. When the traction at one driving wheel is compromised, its inherent limitation encourages the slipping wheel to slip even further. This not only limits total longitudinal traction, but also reduces the lateral force capability of the spinning tyre. This typically manifests itself as understeer on a FWD vehicle, and oversteer on RWD.

PLSD - Mastinu [59] presents one of the first comprehensive vehicle handling studies of torque and speed sensitive PLSDs in a RWD vehicle. In steady state cornering, both types were shown to promote understeer at low lateral accelerations (0-0.6g), since the torque bias occurs between the faster outer to inner wheel. Higher degrees of locking also demonstrated more pronounced understeer. These findings are in agreement with Cheli [17], Morselli [66] and Piyabongkarn [76] who have since used more complex vehicle models to replicate similar PLSD behaviour. Smith [97] reinforces this view with a more practical discussion of differential types within the motorsport industry. Mastinu [59] goes on to examine their effects at higher lateral accelerations where the influence of lateral weight transfer becomes more critical. As lateral acceleration increases, inside tyre traction reduces to the point of longitudinal saturation. At this point, there is a reversal in torque transfer direction, which is now transmitted from inner to outer wheel. This reverses the direction of the associated yaw moment, promoting a snap oversteer behaviour at the point of wheel slip. Mastinu underlines the importance of torque bias tuning and vehicle suspension setup, in avoiding this snap understeer-oversteer behaviour. He argues that this is undesirable from the point

of view of driver workload. Results presented in Chapter 7 show that while this may increase driver workload, this ultimately provides a faster vehicle.

In the particular case of a PLSD, it is also important to note that driving style will also influence differential behaviour. This is particularly relevant in motorsport, since it is common for drivers to adapt their racing line for specific corners. The classic racing line encourages drivers to decelerate the vehicle in a straight line before turning into a corner. The parabolic or trail-braking approach allows the driver to brake later, but decelerates the vehicle right up to the corner apex. This means that the choice of racing line also determines which region of the corner the resulting PLSD yaw moment will be most dominant.

ALSD - since the torque transfer direction of an ALSD is constrained in the same way as their passive counterparts, handling influences are very similar. However, a means of electronic control allows a far better compromise to be sought between the conditions under which a locking torque is generated, and how smoothly this is applied. Morselli [66] and Kopf [50] investigate their use in FWD and RWD vehicles and demonstrate that this added flexibility helps reduce PLSD understeer effects at low lateral accelerations. Under steady state cornering, the electro-hydraulic ALSD under test, remained fairly open and benign under these conditions. At higher lateral accelerations, more locking was required to prevent excessive longitudinal slip of the inside tyre, but allowed peak lateral accelerations to be extended by up to 1m/s^2 (Figure 2.9a). Transient step-steer tests also confirmed a smoother yaw response through higher side slip angle damping (Figure 2.9b). Although many authors have discussed the use of ALSDs in alleviating corner-entry understeer, other researchers have employed these stabilising yaw moments under more extreme conditions. Through the evaluation of ALSD control system architecture, Cheli [17] and Sasaki [83] develop vehicle stability methods which apply this understeering moment under heavy braking, corner entry conditions, where longitudinal weight transfer would normally promote dangerous oversteer characteristics. This has proven to be highly effective in making the car more predictable for the average driver.

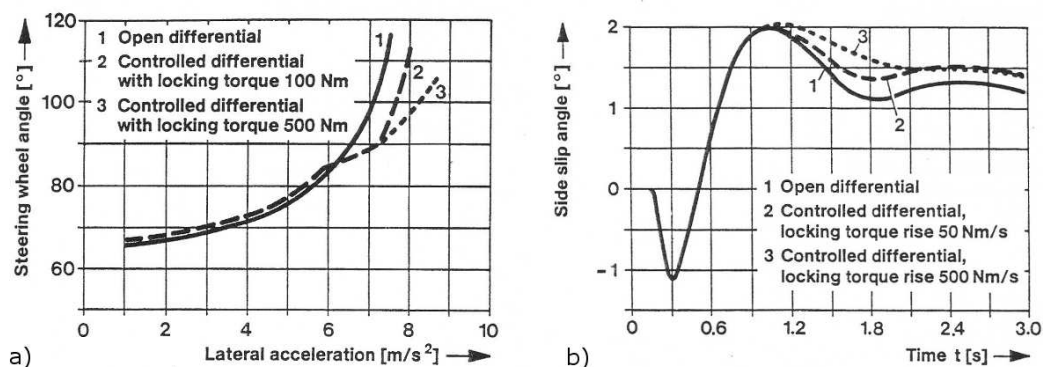


Figure 2.9: a) Understeer gradient comparison between open and ALSD (FWD car, 40m constant radius test) b) step steer response at 75km/h [50]

TVD - the evaluation of the effects of TVDs on handling characteristics is perhaps one of the most active research areas today. This in part, is due to the considerable yaw moment authority offered by TVDs when compared to ALSDs. They can control the point of application and the magnitude of the locking torque, but also its direction. This means they can provide both stabilising understeering moments at the vehicle limit, and sub-limit oversteer moments to improve vehicle agility. The first pioneering work conducted by Sawase [84, 86, 87] highlighted these benefits, by showing the increase in peak lateral acceleration an AWD saloon car could achieve under steady state cornering (Figure 2.10a). The resulting understeer gradient was shown to be more linear up to this limit, giving more predictable handling characteristics. Like ALSDs, control strategy forms an important part of their operation and Sawase develops early vehicle control algorithms into what is now known as the AYC system (see Section 2.3). This has been an important part of providing more robust control of tyre saturation levels and better integration with other vehicle safety systems. Sawase [86] demonstrates this most clearly in the yaw rate response of a vehicle equipped with AYC and a brake based stability system (Active Stability Control or ASC), during a double lane change manoeuvre (Figure 2.10b). Improved yaw rate response and a reduction in driver workload is seen as vehicle stability is maintained throughout. A more recent assessment is offered by Croft-White [19], who conducts similar simulation tests for an AWD rally application. Additional focus is given to the relative contribution of axle and centre differentials and the development of a control strategy which aims to minimise side slip angle. He shows similar improvements in peak lateral acceleration levels and a reduction in peak side slip angle of 40%, when compared to a baseline vehicle fitted with three open differentials. Axle differentials were also shown to be more effective at generating yaw moments than front-rear torque distribution through a centre differential.

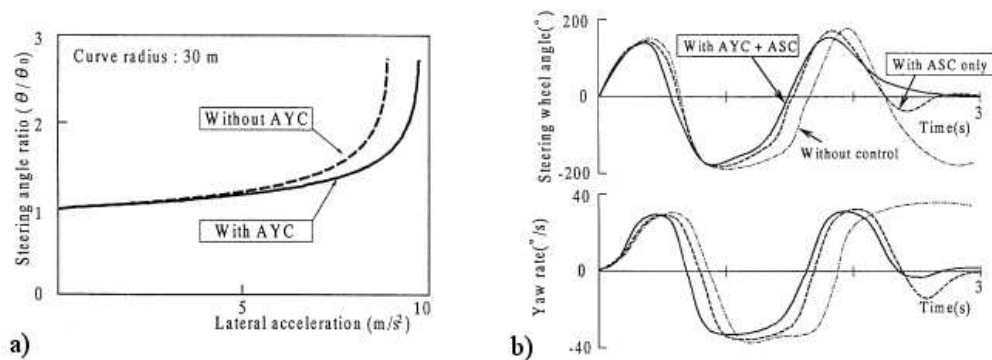


Figure 2.10: a) Steady state cornering characteristics of a TVD
 b) double lane change manoeuvre at initial speed of 60km/h [86]

Locked/Spool - although its application is limited, the locked or spool differential must be included in this discussion, since it represents one of the two extremes in operating condition of all LSD devices. In complete contrast to the benign characteristics of the open differential, they display a more pronounced handling response. Since the driving wheels are constrained to rotate at the same speed, the inner wheel is forced to slow down and the outer wheel to speed up, during typical cornering conditions. The resulting difference in longitudinal tyre slip creates a more severe understeer moment

that is proportional to the radius of turn and vehicle track width [25, 97, 119]. At higher lateral accelerations when the tyres are closer to saturation, spool differentials have also been known to promote oversteer in RWD vehicles [83], although its exact effects under these conditions is heavily dependant on tyre characteristics and the amount of lateral weight transfer. Outside vehicle handling evaluations, spool differentials have been shown to be highly effective in maximising traction in slow speed, low grip conditions [25, 62], where the loss of wheel speed independence is less detrimental to driver control.

2.5 Differential Simulation Models

A wide range of simulation models have traditionally been used in the analysis of differential behaviour, which can all be broadly grouped into steady state or dynamic models. One of the first analytical models formulated by Dixon [25], uses an idealised steady state torque transfer to inner and outer wheels to demonstrate how the understeer gradient of a linearised 2DOF model is affected. Casanova [15] is seen to develop these concepts into a torque sensitive, Salisbury type differential model. This is justifiably basic, since it was a small part of a much more complex laptime optimisation program. Nevertheless, the model included the effects of ramp angle and preload, with the bias torque modelled as a linear function of input torque. Brayshaw [10] extends this model by using uniform pressure clutch theory [38], to give a more physically significant relationship between the differential input torque, clutch clamp load and the resulting locking torque. The significance of a variable friction coefficient with relative rotation of the friction surfaces (termed the μ - v characteristic) was also included with a negative slope approximation. This model is used as a basis for optimising a vehicle's GG envelope and although open, PLSD and ALSD devices were compared, their dynamic effects were not explored in detail. Sasaki [83], Mastinu [59] and Cheli [17] all used similar steady state models in road car vehicle handling assessments.

Piyabongkarn [77] presents a dynamic model as part of an investigation into an AWD system. An active clutch plate differential and centre coupling are modelled as torsional spring-damper mechanisms to introduce a degree of compliance and damping to the system. Their formulation considered wheel and driveshaft inertia with power transmission from the engine assumed to be 100% efficient. The transitions of the differential between open and locked states are modelled as 'stage transitions', which instantaneously switch depending on a number of boundary conditions. Although this is likely to show some elements of true 'stick-slip' behaviour, a variable μ - v characteristic was not included in the formulation.

Deur, Hancock and Assadian [22, 36] present a kinematic analysis of a wider range of differentials including open, PLSD, ALSD and TVD types. A bond graph energy method is used to simplify the formulation of the equations of motion and provides a more structured framework for exploration. This kinematic analysis is later extended [23], in the development of dynamic models, which take into account differential and wheel inertias, as well as driveshaft compliance. These models are then used to calculate torque transfer, but also to predict low frequency 'shuffle modes' and higher frequency 'clutch mode' oscillations. These vibration modes were important considerations in

their investigation, which centred around stringent road car refinement targets for smooth torque bias delivery.

At the time of writing, only a limited number of authors have discussed the validation of these theoretical models. Dickason [24] attempts to validate a steady state model for an Xtrac plate type LSD. Experimental data is generated by a test rig designed to characterise the LSD in isolation. The torque bias was measured at a constant differential rpm, for discrete variations in input torque. The theoretical model was based on uniform pressure clutch theory, but extended to include the frictional contact between the crosspin and ramps. Dickason notes that the resulting locking torque is highly sensitive to both clutch plate and ramp-crosspin contact friction coefficients, and an evaluation of their accuracy forms a large part of the validation process. The coefficients used were taken from single plate friction tests conducted by James [45] and are consistent with other experimental data presented by Maki [53, 54]. The tests studied a number of friction materials including sintered bronze, molybdenum and carbon, with static and dynamic friction coefficients shown to lie between 0.08-0.12. Dickason identifies that this range in values produces a large variation in the resulting locking torque. His comparison of ‘static’ and ‘dynamic’ models against measured test data is shown in Figure 2.11. The resulting model accuracy is poor, with the locking magnitude underestimated by up to 40%. To account for this error, additional sources of internal friction which could provide an amount of residual locking are considered. A revised multiplate model [82] is proposed to account for spline friction, but did not improve fidelity to within an acceptable level. Inconsistencies in locking torque gradients between drive and coast ramps also suggests a more fundamental error in the clamping force calculation or frictional properties of the clutch material.

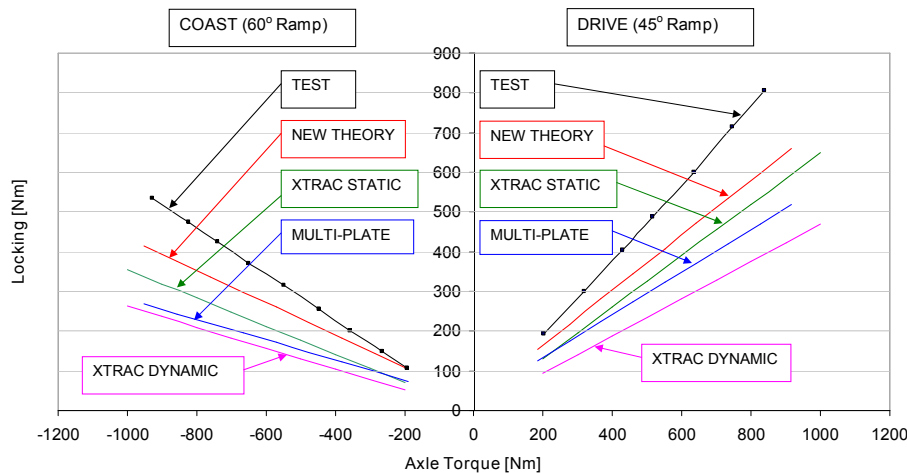


Figure 2.11: Xtrac 516 Salisbury PLSD Locking Model Validation [24]

Ivanovic et al [44] develops a similar differential test rig to validate a DC motor actuated ALSD (the GKN ETM [37]) model. The model was again based on uniform pressure clutch theory but was extended to include compliance and damping effects of a ball-and-ramp locking mechanism. A good qualitative correlation is shown between predicted and measured values, but a 20% error is seen in the steady state locking torque (T_c in Figure 2.12). This may be in part due to temperature effects on the

friction coefficient, which were considered as a source of error but not included in the published simulation model.

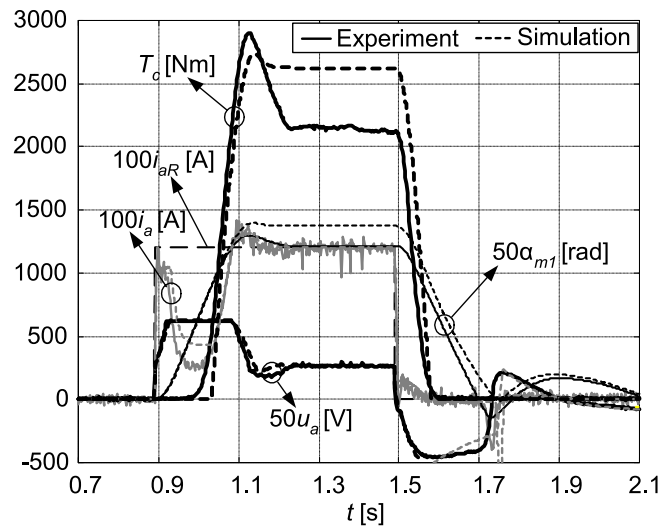


Figure 2.12: ALSD (GKN ETM) model validation results of clutch engagement and disengagement at a 25rpm slip speed [44]

It is clear that a number of factors influence differential friction characteristics and test rig validation of theoretical models has historically proven difficult. Nevertheless, errors in locking torque calculation will undoubtedly have an impact on yaw moment generation and the resulting vehicle handling behaviour observed. The fidelity of these models is therefore a worthy concern and the improvement of existing plate differential models forms a key theme to this research.

2.6 Review Summary

In accordance with the aims and objectives outlined in Section 1.5, the relevant findings from the literature review material presented in Chapters 1 and 2 are summarised below.

- i) PLSDs offer many traction and handling benefits when compared to open differentials. These are achieved by generating a bias torque from the faster to slower rotating driven wheel. The vast majority of literature deals with the study of these benefits in a traditional road car application. Previous works have used relatively simplistic models, which do not reflect the modern, highly adjustable devices currently found in motorsport. These are capable of altering the balance of the vehicle through corner entry, apex and corner exit phases. Few PLSD models have been validated against test rig or in-vehicle data, since the frictional properties of torque biasing elements have traditionally been difficult to predict. Those that have, demonstrate a 20-40% steady state error in the predicted locking torque.
- ii) QSS, TNOC and NMPC time optimal lap simulation methods have been used to show the influence of vehicle setup parameters on ultimate lap time. QSS methods have been more widely adopted due to their ease of implementation, robustness and quick solve times. A limited number of researchers have used more sophisticated TNOC methods which allow the system dynamics to be included. This is an important factor to consider in the optimisation of LSDs since the dynamic yaw response (or ‘turn-in’) is a behaviour drivers most readily associate with LSD setup.
- iii) Practical experience has shown that a time optimal setup doesn’t always result in a faster lap time. Vehicle stability and agility are key factors in determining how much of the ultimate performance can be extracted by a driver in the form of a realisable lap time. Some researchers have started to investigate the influence of LSD setup parameters on vehicle stability for a limited number of manoeuvres. New methods are required however, to show how the stability-agility balance of the vehicle changes throughout its performance envelope.

2.7 Contribution

Given the findings of the literature review in Section 2.6, this research aims to make a contribution to the understanding of performance differentials in three areas. Firstly, in the generation of a range of state-of-the-art motorsport LSD models, which will be validated against test-rig and in-car data. Secondly, new methodologies will be developed to optimise LSD setup parameters, providing guidance on the torque biasing characteristics of future motorsport LSDs. Finally, a more practical and intuitive way to evaluate vehicle stability and agility at different cornering phases will be proposed. The unification of the minimum lap time solution and driveability metrics into one methodology has not been considered by previous researchers. This forms a crucial part of determining how much performance potential a driver can extract from the vehicle.

Chapter 3

Differential Modelling and Validation

Chapters 1 and 2 discussed the relevant literature surrounding this research. This chapter moves on to present three models of common LSD types currently used in motorsport. Firstly, a torque sensing plate differential model, with tunable drive, coast and preload parameters. A speed sensing VC model is then developed, which relies on the characterisation of its shear fluid to determine changes in torque bias. These are then combined to form a speed and torque sensing device, in the form of a VCP differential. Finally, all LSD models are validated against data generated on a bespoke test rig, under both steady state and transient conditions.

3.1 Plate Differential (Salisbury) Model

One of the key elements in modelling a plate LSD, is the characterisation of its input torque under both on and off-throttle (i.e. drive or coast) conditions. To illustrate this, a simplified schematic of a FWD driveline under both conditions is shown in Figure 3.1.

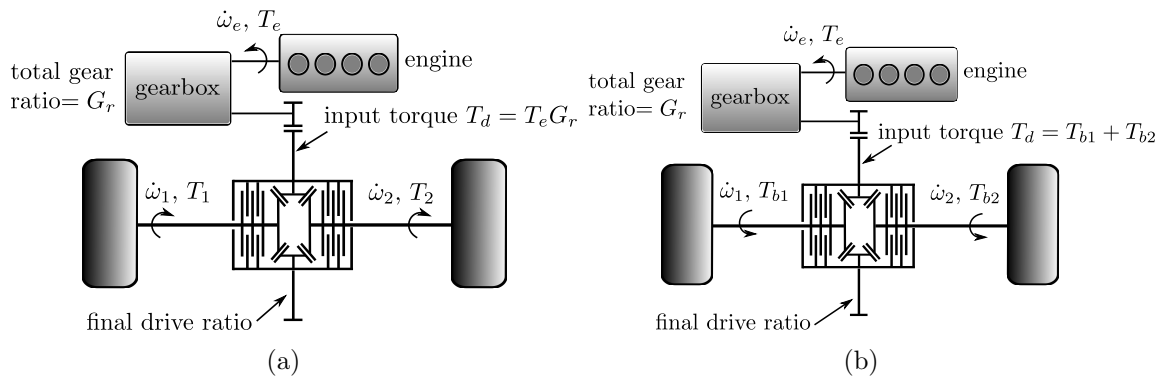


Figure 3.1: a) FWD powertrain schematic - on throttle conditions
b) FWD powertrain schematic - off throttle conditions

In Figure 3.1a, engine torque T_e is positive, driven wheel brake torque T_{b1} and T_{b2} are zero, and the resultant differential input torque T_d , is simply the engine torque

multiplied by the associated gearbox ratio gain, G_r :

$$\text{for } T_e > 0 \text{ and } T_{b1}, T_{b2} = 0 \quad (3.1)$$

$$\text{LSD Input Torque } T_d = T_e G_r \quad (3.2)$$

Under off-throttle, braking conditions (Figure 3.1b), it is not so apparent what the differential input torque will be, and is dependant on the engine overrun characteristics. If the wheels are decelerating faster relative to the engine, then the differential will transition to its coast side ramps and use the driven axle brake torque as its input. If the opposite is true, then engine overrun torque will be its input. Experimental race vehicle data presented in Chapter 4, suggested the first of these assumptions was true, and will be the adopted convention in this thesis, such that:

$$\text{for } T_e = 0 \text{ and } T_{b1}, T_{b2} > 0 \quad (3.3)$$

$$\text{LSD Input Torque } T_d = T_{b1} + T_{b2} \quad (3.4)$$

Modern uniform pressure clutch plate theory has been used as a basis for the majority of plate differential models [10, 24, 44]. These analyses can be extended and applied to the particular case of the Salisbury type differential presented in Section 2.1.1, by incorporating the effects of ramp angle (θ_r) and statically applied preload torques. Positive preload (T_{pp}), is commonly applied through the use of a belleville spring, and allows a degree of torque bias to take place when little differential input torque can be supported at one of the driven wheels (e.g. when a wheel is in mid-air due to a curb strike). The effects of negative preload (T_{np}) are less well documented in literature, but can be thought of as an initial force which must be overcome before the clutch plates can generate any locking. In the passive torque sensing differential application, this extends the region in which little or no torque bias takes place. In the vehicle dynamics sense, this corresponds to phases of a manoeuvre in which the driver is transitioning from braking to acceleration, typically at the apex of a corner.

Empirical rig testing carried out as part of this research has shown that the resulting torque bias characteristics can be characterised by three operating regimes, shown in Figure 3.2 and summarised below:

- i) *Linear Positive Preload* - locking torque (T_p) generated at low input torque levels, dominated by belleville spring force and the inherent friction of rotating elements within the differential housing (bearings, side gear, pinion mates).
- ii) *Non Linear Transition* - locking torque (T_{tr}) generated at low to mid input torque levels, governing the transition between positive preload and ramp regions.
- iii) *Linear Ramp Locking* - locking torque (T_r) generated at mid to high input torque levels, dominated by the separating forces of the ramps.

The reader should note that in all three regimes, the input torque T_d can take the form of engine torque under positive acceleration, or the driven axle brake torque T_{br} , under braking conditions.

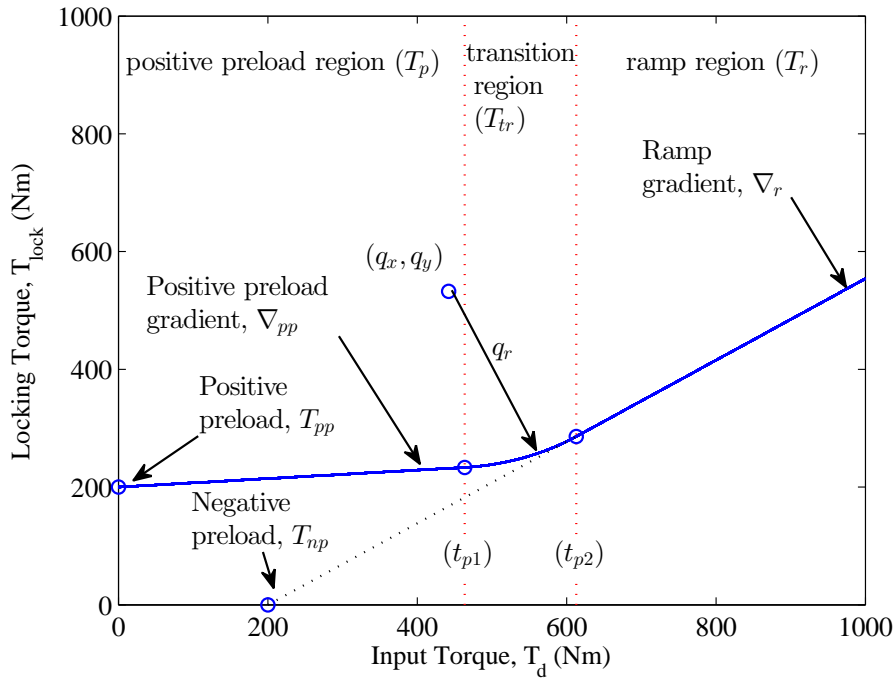


Figure 3.2: Description of the three phases of locking torque (on-throttle drive side shown only).

Figure 3.2 shows the three operating regimes for on-throttle, positive input torque. The first positive preload region can be defined by the linear expression:

$$T_p = \nabla_{pp} T_d + T_{pp} \quad \text{for } 0 \leq T_d \leq t_{p1} \quad (3.5)$$

Where the statically defined preload torque T_{pp} , is generated through the compression of a belleville spring (see Figure 2.1 and 2.2) acting against the plate pack. The positive preload gradient ∇_{pp} , is as a result of the inherent friction of rotating elements and separating forces of the pinion mates generating a small increase in torque bias as input torque levels rise. The calculation of this preload gradient is described in Section 3.1.1. Once the input torque has reached the first transition point t_{p1} , the locking torque transitions between preload and ramp locking regions. In this case, the resulting locking torque has been approximated by a constant radius profile, with centre q_x , q_y and radius q_r :

$$T_{tr} = q_y - \sqrt{q_r^2 - (T_d - q_x)^2} \quad \text{for } t_{p1} < T_d \leq t_{p2} \quad (3.6)$$

where q_r represents the radius of transition between positive preload and ramp locking regions. Through physical tests, q_r was found to be proportional to the magnitude of both positive and negative preload. This behaviour was included through the use of an empirical transition preload gain factor T_{pg} , such that:

$$q_r = T_{pg}(T_{pp} + T_{np}) \quad (3.7)$$

The radius centre points q_x and q_y can be defined explicitly by first considering the modification of the equations describing the preload (Equation 3.5) and ramp (Equation 3.12) locking regions. Offsetting both of these equations by q_r creates an intersection point which defines the transition radius centre. The two modified equations can be expressed as:

$$T_{p_{offset}} = \nabla_{pp} T_d + T_{pp} + q_r \sqrt{(\nabla_{pp}^2 + 1)} \quad (3.8)$$

$$T_{r_{offset}} = \nabla_r T_d + \nabla_r T_{np} + q_r \sqrt{(\nabla_r^2 + 1)} \quad (3.9)$$

where ∇_r is the ramp locking gradient (see Equation 3.12 and Section 3.1.2). Setting Equations 3.8 and 3.9 equal to each other and solving for T_d effectively gives the radius centre point q_x :

$$q_x = \frac{-\left(T_{pp} - \nabla_r T_{np} + q_r \sqrt{(\nabla_{pp}^2 + 1)} - q_r \sqrt{(\nabla_r^2 + 1)}\right)}{(\nabla_{pp} - \nabla_r)} \quad (3.10)$$

substituting Equation 3.10 into 3.9 and setting $T_{r_{offset}} = q_y$ gives the associated y-axis coordinate:

$$q_y = \nabla_{pp} q_x + T_{pp} + q_r \sqrt{(\nabla_{pp}^2 + 1)} \quad (3.11)$$

As input torque levels increase further, past the second transition point t_{p2} , the torque bias is dominated by the separating forces of the ramps. This force can be tuned by the specific ramp angle (θ_r) for positive or negative input torque, allowing the user to alter the torque bias significantly during acceleration and braking phases. The effects of negative preload are included as a linear y-axis offset, described by the equation.

$$T_r = \nabla_r T_d - \nabla_r T_{np} \quad \text{for } T_d > t_{p2} \quad (3.12)$$

where T_{np} is the negative preload torque described in terms of a required input torque to overcome the belleville spring force. The ramp gradient, ∇_r is a function of multiple parameters including the frictional and geometric properties of the clutch surfaces and the clamping load imparted onto the clutch pack. The derivation of this gradient is described in Section 3.1.2.

Finally, the locking torque in all three regions can be combined into a continuous function, to allow a smoother transition between different input torque regimes. As a result, the torque bias can be calculated as a function of input torque, without the need for lookup tables, where:

$$T_{lock} = T_p + (0.5 + 0.5 \sin(\tan^{-1}(T_d - T_{tp1})))((T_{tr} - T_p) + (0.5 + 0.5 \sin(\tan^{-1}(T_d - T_{tp2})))((T_r - T_{tr})) \quad (3.13)$$

3.1.1 Preload Locking Gradient (∇_{pp})

Positive preload is often applied to the plate pack to give some residual torque bias when the input torque is otherwise very low (e.g. during the transition between braking and on-throttle conditions). This is typically achieved through the use of a belleville spring and a screw thread winder mechanism (see Figure 2.1). The torque bias magnitude during this preload region, is to a large extent, determined by the belleville spring force. However, empirical testing has also shown that there is a slight increase in torque bias as input torque levels increase, due to the friction of internal components. This is characterised by the preload gradient ∇_{pp} , described in Equation 3.5. Dickason [24] proposed multiple sources for the friction, including the bevel gear mesh, side gear thrust bearing, and the pinion mate back face interaction against the inner ramp profile. In the model presented below, only the friction generated from the pinion mate - ramp contact is considered. This source of friction is known to be significant due to the high rate of wear normally seen on these surfaces.

Figure 3.3 shows the resultant gear thrust forces acting on a single pinion mate, as a result of input torque T_d . The geometry of the pinion mate - side gear mesh is also depicted in Figure 3.4.

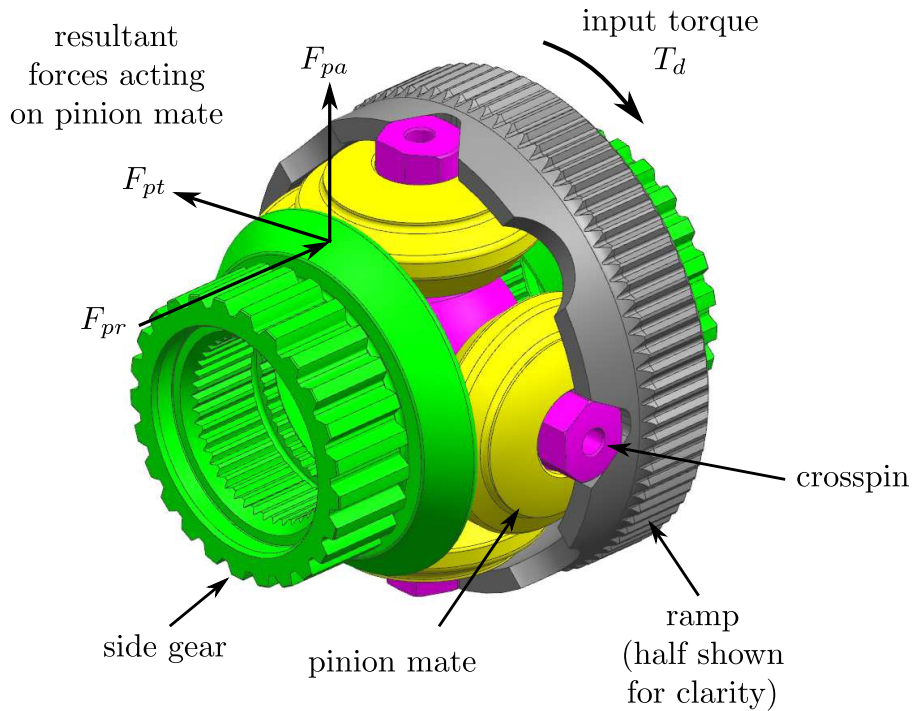


Figure 3.3: Pinion mate thrust loads

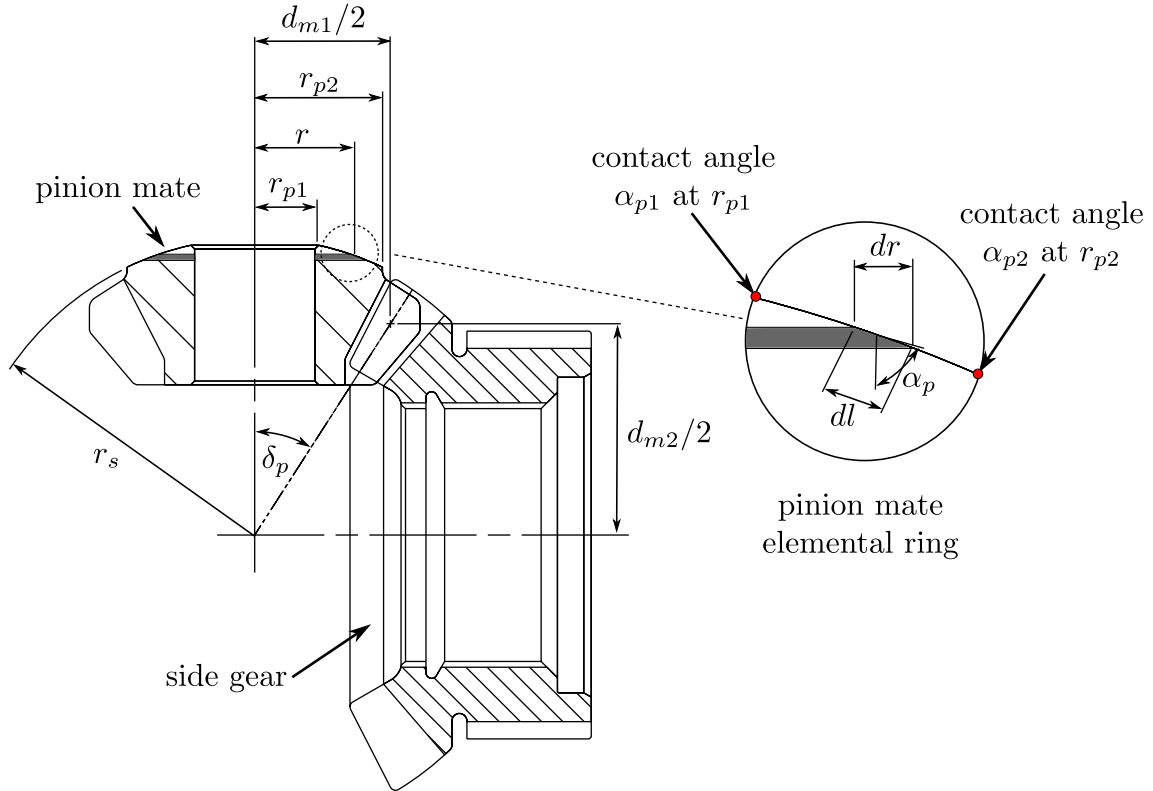


Figure 3.4: Pinion mate frictional contact geometry

The tangential force acting on a pinion mate can be defined as:

$$F_{pt} = \frac{2T_d}{d_{m2}} \quad (3.14)$$

Taking into consideration the straight cut, bevel gear tooth geometry, this tangential force can be resolved into the axial component F_{pa} , acting on the pinion mate:

$$F_{pa} = F_{pt} \tan(\alpha_p) \sin(\delta_p) \quad (3.15)$$

where α_p is the gear mesh pressure angle, and δ_p , the pinion mate pitch cone angle (see Figure 3.4). The frictional resistance due to the rotation of the pinion mate against the inner ramp edge can be derived by first considering the force acting normal to an elemental ring on the pinion mate back face, where:

$$dF_{pn} = 2\pi r p dl \quad (3.16)$$

The pressure p , is considered uniform across the surface. Since the surface is inclined at an angle α_p , dl can be written as $dl = dr/\sin(\alpha_p)$. Substituting this, and since $F = \mu R$, the elemental frictional force then becomes:

$$dF_{pf} = 2\pi r p \mu_{pm} \frac{dr}{\sin(\alpha_p)} \quad (3.17)$$

where μ_{pm} represents the coefficient of friction for the contact. This expression can be integrated with respect to r , between the inner and outer contact radii, r_{p1} and r_{p2} , to give the frictional torque acting about the pinion mate rotation axis:

$$M_p = 2\pi p \mu_{pm} \int_{r_{p1}}^{r_{p2}} \frac{r^2}{\sin(\alpha_p)} dr \quad (3.18)$$

However, the contact angle α_p does not remain constant since the back face of the pinion mate is spherical, described by the radius, r_s . The following expression relates the radius r , to the associated contact angle α_p .

$$r = r_s \cos(\alpha_p) \quad (3.19)$$

and taking the derivative with respect to $d\alpha_p$:

$$\frac{dr}{d\alpha_p} = -r_s \sin(\alpha_p) \quad (3.20)$$

rearranging Equation 3.20 for dr , and substituting both this and Equation 3.19 into 3.18 yields:

$$M_p = 2\pi p \int_{\alpha_{p1}}^{\alpha_{p2}} \frac{\mu_{pm} r_s^2 \cos(\alpha_p)^2}{\sin(\alpha_p)} (-r_s \sin(\alpha_p)) d\alpha_p \quad (3.21)$$

which can be simplified to:

$$M_p = -2\pi p \mu_{pm} r_s^3 \int_{\alpha_{p1}}^{\alpha_{p2}} \cos(\alpha_p)^2 d\alpha_p \quad (3.22)$$

solving the definite integral it can be shown that:

$$M_p = \pi p \mu_{pm} r_s^3 \left((\cos(\alpha_{p2}) \sin(\alpha_{p2}) + \alpha_{p2}) - (\cos(\alpha_{p1}) \sin(\alpha_{p1}) + \alpha_{p1}) \right) \quad (3.23)$$

which using geometric identities can be further simplified to:

$$M_p = \pi p \mu_{pm} r_s^3 \xi \quad (3.24)$$

$$\text{where } \xi = (\alpha_{p2} - \alpha_{p1}) + \frac{1}{2} \left(\sin(2\alpha_{p2}) - \sin(2\alpha_{p1}) \right) \quad (3.25)$$

The constant pressure term p can be expressed in terms of the axial pinion mate thrust load F_{pa} , and the contact face geometry. Classical clutch theory [82] states that for a given surface under constant pressure, at contact angle α_p , the resultant axial force can be expressed as:

$$F_{pa} = 2\pi \int_{r_{p1}}^{r_{p2}} p r dr \quad (3.26)$$

integrating between the limits and rearranging for p gives:

$$p = \frac{F_{pa}}{\pi(r_{p2}^2 - r_{p1}^2)} \quad (3.27)$$

substituting back into Equation 3.24 yields:

$$M_p = \frac{F_{pa} \mu_{pm} r_s^3 \xi}{(r_{p2}^2 - r_{p1}^2)} \quad (3.28)$$

Finally, the friction torque acting about the pinion mate axis can be resolved into the side gear rotation axis by taking account of the pinion mate - side gear ratio, d_{m2}/d_{m1} . Substituting Equation 3.14 into 3.15 and then into 3.28 gives:

$$T_p = \left(\frac{d_{m2}}{d_{m1}} \right) \frac{2 T_d \mu_{pm} r_s^3 \xi}{d_{m2} (r_{p2}^2 - r_{p1}^2)} \tan(\alpha_p) \sin(\delta_p) \quad (3.29)$$

The resulting expression is then simply a function of the input torque T_d , with the associated gradient ∇_{pp} :

$$T_p(T_d) = \frac{2 \mu_{pm} r_s^3 \xi}{d_{m1} (r_{p2}^2 - r_{p1}^2)} \tan(\alpha_p) \sin(\delta_p) T_d \quad (3.30)$$

where:

$$\frac{dT_p}{dT_d} = \nabla_{pp} = \frac{2 \mu_{pm} r_s^3 \xi}{d_{m1} (r_{p2}^2 - r_{p1}^2)} \tan(\alpha_p) \sin(\delta_p) \quad (3.31)$$

3.1.2 Ramp Locking Gradient (∇_r)

Once the differential input torque has risen above a prescribed level (defined by t_{p2} in Figure 3.2), the torque bias starts to be dominated by the ramp separating forces. Central to the prediction of the torque bias in this region, is the resolution of the applied input torque T_d , into a ramp separating force F_{ramp} . Figure 3.5 shows a free body diagram of the forces acting on one side of the ramp pair. This includes the reaction from the applied torque and the friction forces between the ramp-crosspin contact. Resolving forces about x and y axes yields the following force balance equations:

$$F_{ramp} = F_{rx} - F_{fx} \quad (3.32)$$

$$F_d = F_{ry} + F_{fy} \quad (3.33)$$

where F_d is the tangential force applied to one side of the ramp pair as a result of the applied input torque T_d :

$$F_d = \frac{T_d}{2 R_{rr}} \quad (3.34)$$

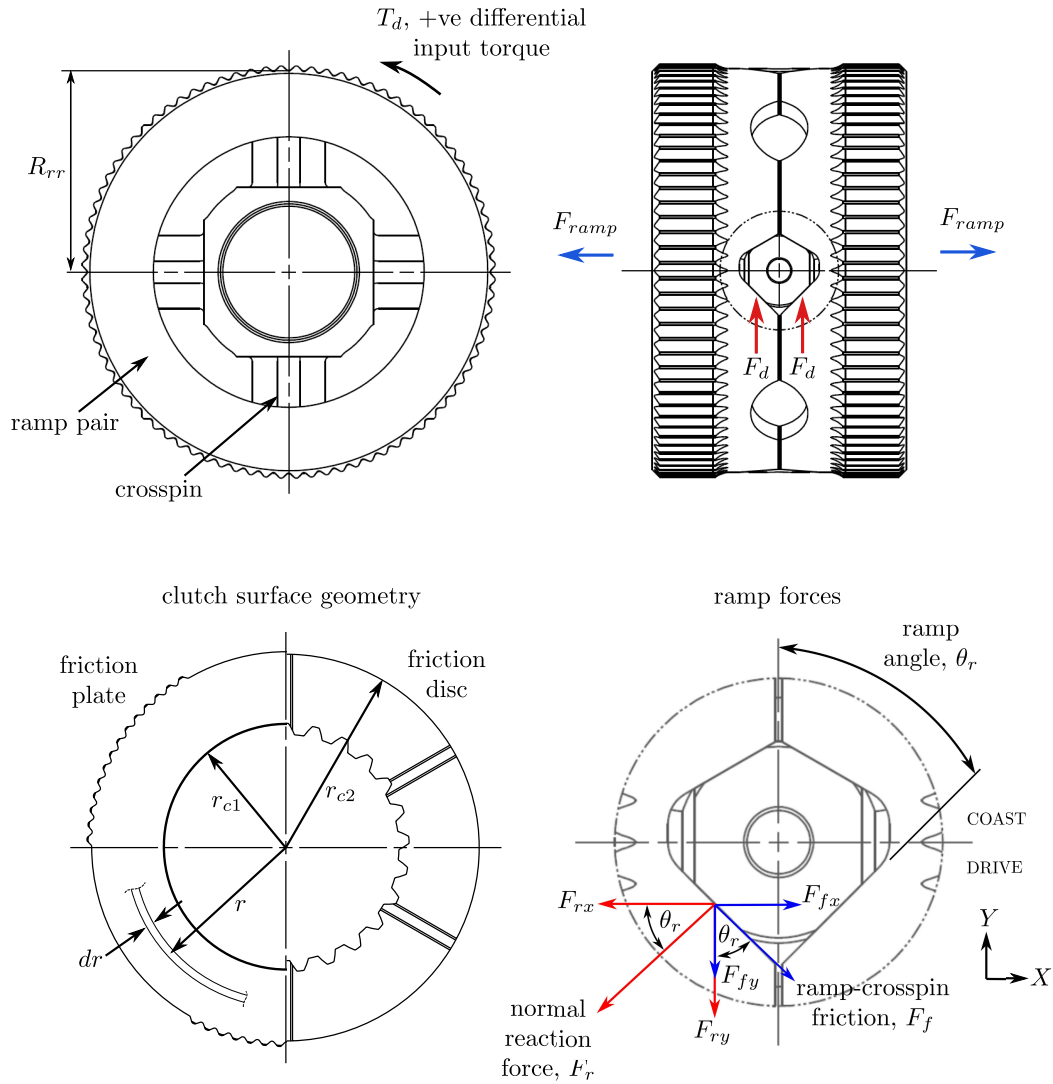


Figure 3.5: Ramp-crosspin free body diagram and clutch surface geometry

Noting that $F_{rx} = F_r \cos \theta_r$ and $F_{ry} = F_r \sin \theta_r$, and assuming that the frictional force acting on the contact is proportional to the reaction force ($F_f = \mu_r F_r$), Equations 3.32 and 3.33 become:

$$F_{ramp} = F_r \cos \theta_r - \mu_r F_r \sin \theta_r \quad (3.35)$$

$$F_d = F_r \sin \theta_r + \mu_r F_r \cos \theta_r \quad (3.36)$$

Where μ_r is the ramp-crosspin coefficient of friction and θ_r , the ramp angle. Rearranging Equation 3.36 for F_r and substituting into Equation 3.35 gives:

$$F_{ramp} = F_d \left(\frac{\cos \theta_r - \mu_r \sin \theta_r}{\sin \theta_r + \mu_r \cos \theta_r} \right) \quad (3.37)$$

Substituting Equation 3.34 for F_d gives the clamping force generated by each ramp:

$$F_{ramp} = \frac{T_d}{2 R_{rr}} \left(\frac{\cos \theta_r - \mu_r \sin \theta_r}{\sin \theta_r + \mu_r \cos \theta_r} \right) \quad (3.38)$$

where R_{rr} is the mean contact radius between the ramp and crosspin. This ramp separation force determines the clutch engagement pressure and in turn, controls the magnitude of the torque bias. Uniform pressure clutch theory [38, 82] can again be used to determine this torque transfer. By considering the torque transmitted by a single pair of clutch surfaces depicted in Figure 3.5, and integrating between the inner and outer radii, r_{c1} and r_{c2} for the elemental ring width dr , the torque bias can be described by:

$$T_{ramp} = 2 \pi \mu_p \int_{r_{c1}}^{r_{c2}} p r^2 dr \quad (3.39)$$

where μ_p is the coefficient of friction between the clutch disc and plate surfaces. As will be shown, this is crucial for model fidelity and will be discussed in more detail in Section 3.1.3. The pressure p , is assumed to be constant across the surface, defined by the expression:

$$p = \frac{F_{ramp}}{\pi (r_{c2}^2 - r_{c1}^2)} \quad (3.40)$$

substituting Equation 3.40 into 3.39 and integrating between r_{c1} and r_{c2} :

$$T_{ramp} = \frac{2}{3} F_{ramp} \mu_p \left(\frac{r_{c2}^3 - r_{c1}^3}{r_{c2}^2 - r_{c1}^2} \right) \quad (3.41)$$

Equation 3.38 can then be substituted back into 3.41, with the inclusion of the multiplication factor z_f , to describe the number of friction faces per side. The total torque bias can thus be described by:

$$T_{ramp}(T_d) = \frac{2}{3} \left[\frac{T_d}{R_{rr}} \left(\frac{\cos \theta_r - \mu_r \sin \theta_r}{\sin \theta_r + \mu_r \cos \theta_r} \right) \right] \mu_p z_f \left(\frac{r_{c2}^3 - r_{c1}^3}{r_{c2}^2 - r_{c1}^2} \right) \quad (3.42)$$

The resulting torque bias gradient ∇_r , in the ramp locking region is then simply:

$$\frac{dT_{ramp}}{dT_d} = \nabla_r = \frac{2}{3 R_{rr}} \left(\frac{\cos \theta_r - \mu_r \sin \theta_r}{\sin \theta_r + \mu_r \cos \theta_r} \right) \mu_p z_f \left(\frac{r_{c2}^3 - r_{c1}^3}{r_{c2}^2 - r_{c1}^2} \right) \quad (3.43)$$

3.1.3 Clutch Plate Friction Coefficient Calculation

Crucial to the accuracy of the above model, is the calculation of the clutch plate friction coefficient, μ_p . Previous research which has defined this for similar clutch surfaces has shown that it can vary with many factors including clamp load, oil temperature, oil additives, clutch slip speed, and friction material geometry [27, 46, 54, 57]. Early work carried out for automatic transmission clutches by Wu [120] and Ting [105], presents a three stage model which attempts to characterise how friction changes during three main stages of clutch engagement:

- i) **Full Film Lubrication** - The clutch discs are at their maximum separation distance and torque can only be transmitted through viscous shearing of the oil film. Full film hydrodynamic lubrication is in operation with separation distances in the order of tenths of millimetres (10^{-5}m). The transmitted ‘drag’ torque is proportional to the clutch slip speed and the viscosity of the oil.
- ii) **Mixed Contact** - The applied load is now large enough to squeeze the majority of the oil from between the friction plate contacts. This allows partial asperity contact in the areas of highest pressure. The torque transmitted is now a combination of viscous shearing and asperity contact friction.
- iii) **Boundary Layer Lubrication** - In the final phase of engagement, the majority of transfer torque is generated from full asperity contact and is characterised by full boundary layer lubrication. The boundary layers formed on each surface are typically two orders of magnitude smaller (10^{-7}m) than full film lubrication.

More recently, friction testing of LSD clutches by Maki [54] and Marklund [58] demonstrated that the last full asperity contact phase is dominant, since the viscous shear torque generated by the full film phase is small in comparison. Testing conducted throughout this research reinforces this claim. The duration of the first two phases was found to be less than 0.2s, before the last boundary layer phase was reached.

Clutch plate frictional properties are typically characterised by applying a constant clamp load to a single or multiple pair of clutch surfaces, whilst monitoring the transmitted torque for an increasing differential speed. A spin rig similar to the Low Velocity Friction Apparatus (LVFA) described by Frey [31] was used by James [45] to define the so called ‘ $\mu - v$ ’ curve for a single Xtrac clutch disc (see Figure 3.5) coated in a molybdenum friction material. A constant reference load F_{cref} , of 7kN was applied through a hydraulic pressure plate, whilst an oil bath surrounding the disc was maintained at 80°C. The resultant friction coefficient is then derived by rearranging Equation 3.41 for μ_p , and using the measured torque transfer and associated disc geometry. The results from one such test are shown in Figure 3.6 and demonstrates the tendency for friction to reduce as speed increases.

For the purposes of this plate LSD model, a curve fit of the test data is applied of the form [54]:

$$\mu_p(\omega_d) = c_1 \tanh(c_2\omega_d) + c_3\omega_d^{0.1} + c_4 \quad (3.44)$$

where $c_{(1..4)}$ are the curve fit parameters and ω_d , the clutch slip speed. The investigation by James [45] also included tests to evaluate the influence of clutch disc clamp load

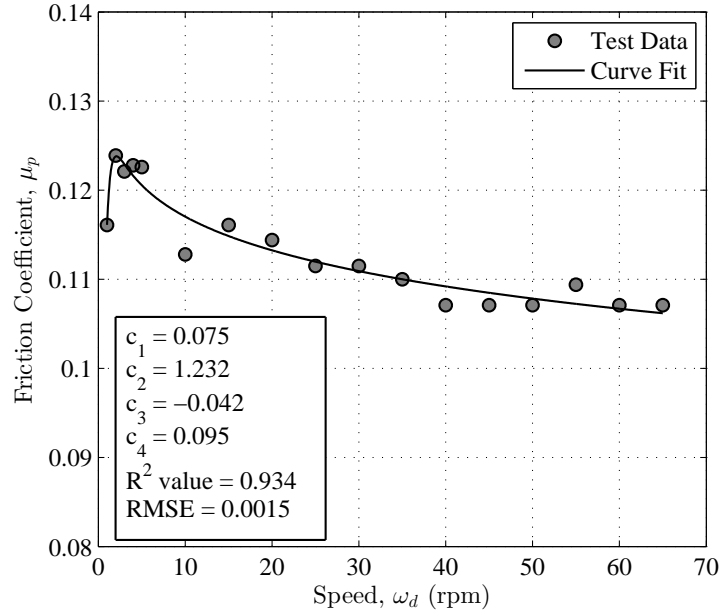


Figure 3.6: Friction characteristic of molybdenum friction disc with increasing speed, $F_{cref} = 7\text{kN}$ clamp load, bulk oil temperature 80°C , SAE 75W90 oil

F_{clamp} , and the clutch disc temperature. An example from the clamp load tests conducted is shown in Figure 3.7, and demonstrates that friction levels remain relatively constant above loads of 2kN , with a small increase below this. To reflect these characteristics, a curve fit approximation can be defined of the form:

$$\mu_p(F_{clamp}) = c_5 F_{clamp}^{c_6} + c_7 \quad (3.45)$$

where $c_{(5.7)}$ are again the respective curve fit parameters, and F_{clamp} the disc clamp force. Equation 3.45 can be normalised by a reference friction coefficient, defined at that the reference load F_{cref} , where $\mu_{ref} = c_5 F_{cref}^{c_6} + c_7$. This can then be combined with Equation 3.44 to form a final expression for the friction coefficient as a function of both load and speed:

$$\mu_p(\omega_d, F_{clamp}) = (c_1 \tanh(c_2 \omega_d) + c_3 \omega_d^{0.1} + c_4) \frac{(c_5 F_{clamp}^{c_6} + c_7)}{\mu_{ref}} \quad (3.46)$$

During the validation of the plate LSD model (see Sections 3.3 and 3.4), the load dependency was shown to have minimal influence over the resulting model error. In practice, when resolving the applied differential input torque into a resulting clamp force (see Equation 3.38), it is apparent that the LSD spends the majority of its time above 2.5kN , where the friction coefficient remains constant.

The assumption that friction is not influenced by operating temperature, is in general not valid [44, 45, 54]. Temperature changes the viscosity of the lubricating oil film and determines which of the oil additives will dominate the surface interaction at a tribological level. For the purposes of this model, an isothermal process is assumed, in

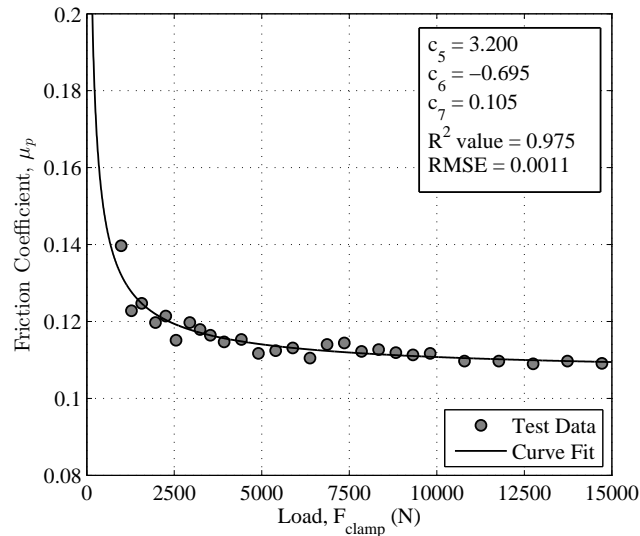


Figure 3.7: Friction characteristic of single molybdenum friction disc with increasing load, $\omega_d = 40\text{rpm}$, SAE 75W90 oil

which the surrounding lubricating oil maintains the differential at a constant operating temperature of 80°C . It is common in motorsport transmissions, to have dedicated oil feeds to the differential (instead of splash lubrication) and an appropriately sized oil cooler. Duty cycles are also well defined (since vehicles are track based) and vehicles often perform an initial warm-up lap to ensure engines, gearboxes and tyres are up to temperature. A constant temperature assumption is therefore more appropriate in this case, than perhaps a road car application, where there are bigger variations in duty cycle, and cost requirements preclude the use of such complex oil systems.

3.1.4 Example Plate LSD Performance Map

An example of how the resulting torque bias varies with input torque and differential wheel speed is shown in Figure 3.8, in the form of a 3D performance map. The differential configuration parameters and friction coefficients used in the example are defined in Tables 3.1 and 3.2.

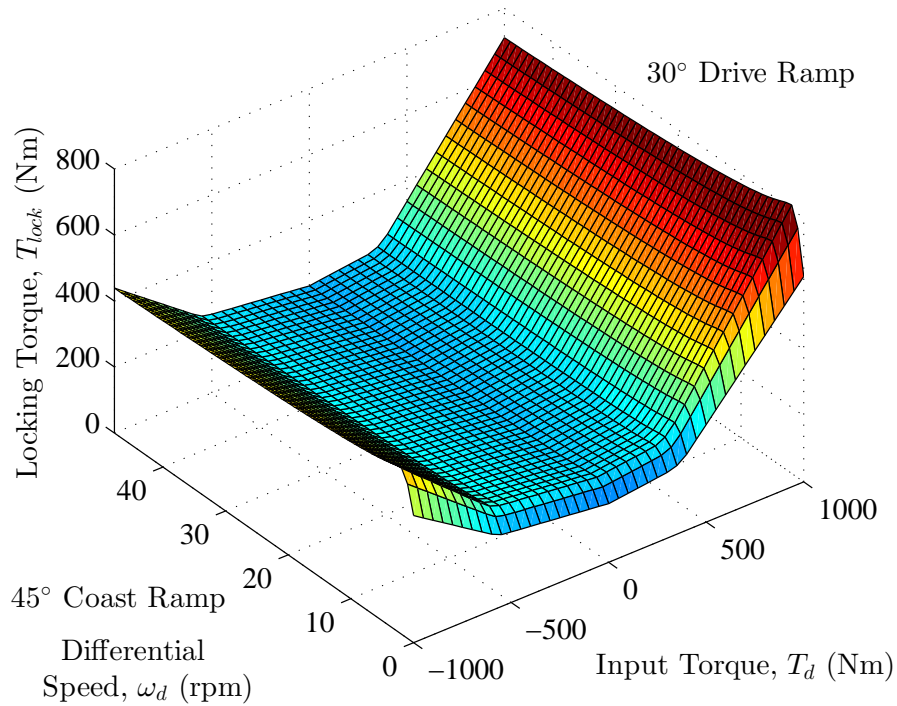


Figure 3.8: Example plate LSD torque bias performance map with input torque and differential speed

Table 3.1: Plate differential setup parameters

Parameter	Symbol	Value
Drive ramp angle	θ_{rd}	30°
Coast ramp angle	θ_{rc}	45°
Number of friction faces	z_f	12
Static positive preload	T_{pp}	150Nm
Positive preload gradient	∇_{pp}	0.05
Drive negative preload	T_{np}	50Nm
Transition preload gain	T_{pg}	1.5
Ramp friction coefficient	μ_r	0.13
Pinion mate friction coefficient	μ_p	0.10

Table 3.2: Molybdenum friction disc parameters, SAE 75W90 oil, at bulk temperature of 80°C

Parameter	Value
c_1	0.075
c_2	1.232
c_3	-0.042
c_4	0.095
c_5	3.200
c_6	-0.695
c_7	0.105

3.2 Quasi Transient Differential Test Rig (QTDTR)

A large proportion of the differential model validation process was achieved through the use of a bespoke piece of test equipment, namely the Xtrac Quasi Transient Differential Test Rig (QTDTR). Pictures of the rig installation and testing cell are shown in Figures 3.9 and 3.10. A schematic overview of the rig is detailed in Figure 3.11 which summarises the main sensor signals and method of operation.

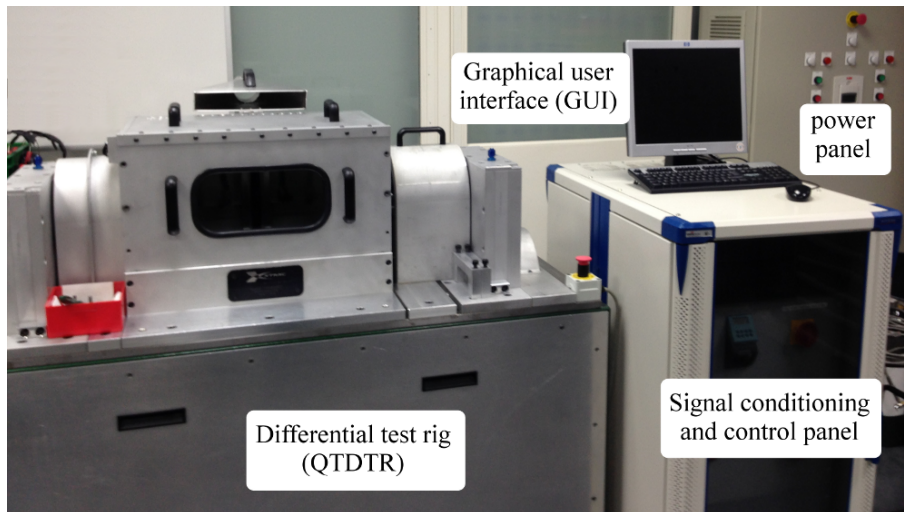


Figure 3.9: The Xtrac [121] Quasi Transient Differential Test Rig

To support the testing of multiple differential types on an industrial basis, an alternative to exact in-car conditions has been adopted. The main body of the differential cassette is held stationary, while both outputs are kinematically constrained to rotate at the same speed (ω) but in opposite directions. This is achieved with the use of left and right-hand gear train assemblies located either side of the differential cassette. Thus, referring to Figure 3.11, the resulting total differential speed is twice that of a single output. The gear trains are linked together with a transfer shaft and driven by a speed controlled 45kW three-phase motor. Consequently, only the speed difference can be controlled throughout the duration of a test (i.e. independent output speed control is not possible).

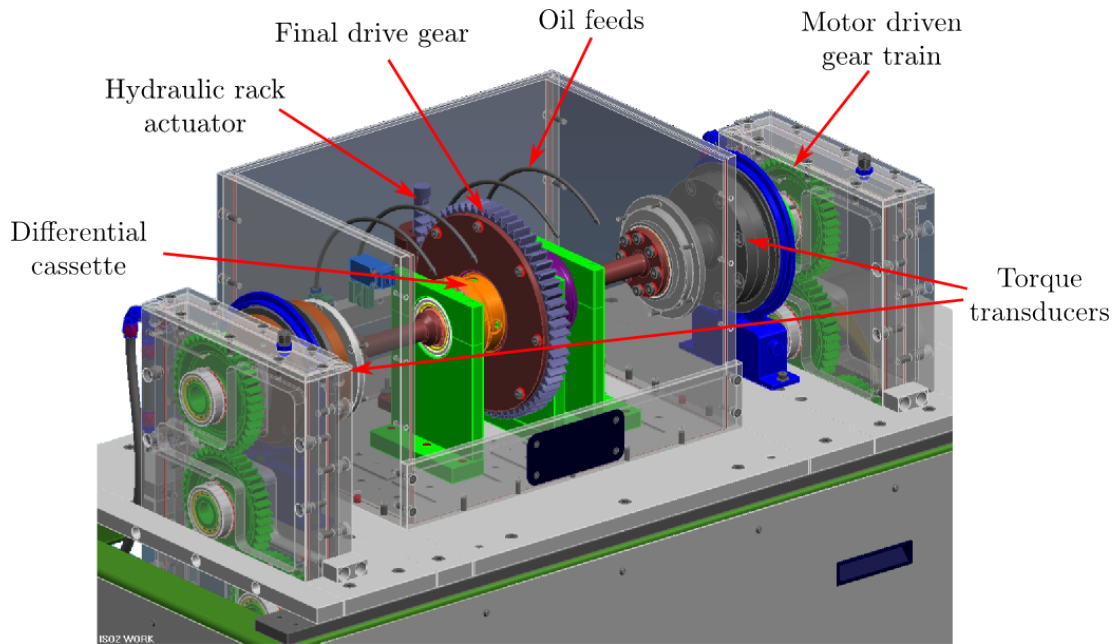


Figure 3.10: The Xtrac [121] Quasi Transient Differential Test Rig

The drive and coast torque normally applied to the differential under vehicle acceleration and braking are instead, realised through a hydraulically actuated rack and final drive gear set. An HBM U10M 25kN load cell fitted between the hydraulic actuator and rack provides an input torque feedback loop, ensuring that the applied torque can be precisely controlled for both steady state and transient test profiles. Upon actuation of the rack, the differential generates a locking torque which supports a torque difference between the two outputs ($T_1 - T_2$). This is monitored by two HBM T10F 3kNm torque sensors on each of the output shafts. One further force measuring transducer was included within the LSD clutch pack assembly to allow more direct measurement of the ramp clamping loads (see Section 3.4). The reader is referred to Appendices A and C for calibration details of all the sensors discussed above.

The rig includes a separate lubrication system which provides oil feeds directly to the differential cassette and to the associated gear meshes of the motor drive assemblies. A number of K-type thermocouples located on the cassette housing and in the oil system lines are used to monitor differential and bulk oil temperature throughout each test run.

A substantial part of this research was taken up with the design and implementation of a new hydraulic system for the rig, and in the improvement of the associated hydraulic and speed control systems. The primary aim was to better replicate the input torque and speed profiles found under representative vehicle conditions. Although this was achieved, one of the main limitations with this testing methodology is that the LSD can only be tested under ‘slipping’ conditions. In-car, the LSD will be constantly transitioning between slipping and locked states. As a result, either a fully loaded chassis dyno, or the in-car validation described in Section 4.2.3 is necessary.

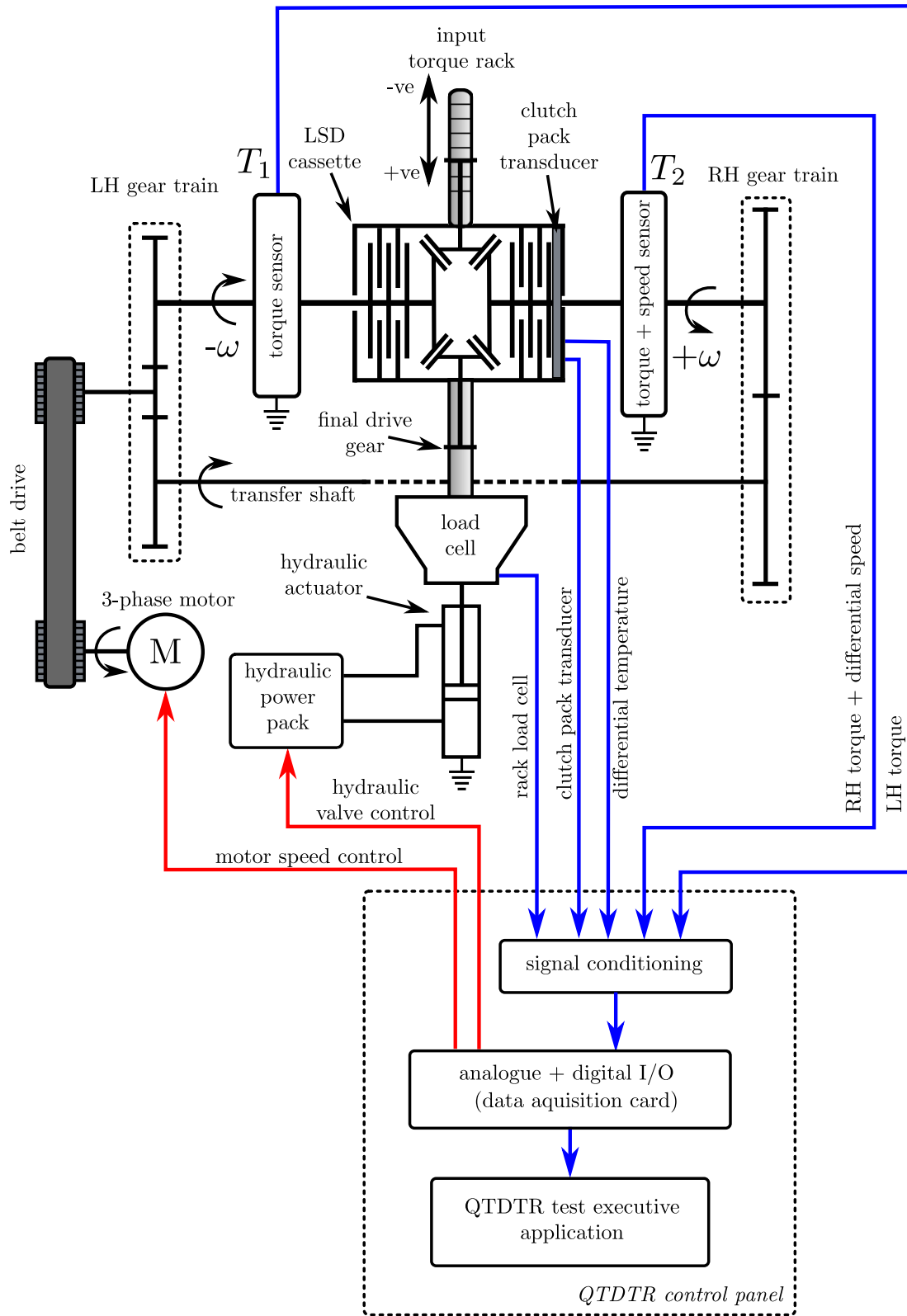


Figure 3.11: QTDTR schematic

3.2.1 Instrumentation and User-Interface

All sensors located on the QTDTR test cell are fed into a control panel which contains signal conditioning units for all torque, speed, force and temperature sensors. The conditioned signals are then read into a National Instruments PCI 6221 data acquisition card as analogue input voltages. A bespoke application termed the ‘Differential Test Rig (DTR) Test Executive’ was developed in the Visual Basic .NET programming language to view sensor output and provide motor and hydraulic actuator control. The application runs on a rack-mounted Pentium 4 PC housed within the control panel. The graphical user interface (GUI) is shown in Figure 3.12 and contains three main tabs, depending on the type of test sequence required.

- i) *Virtual Machine* mode allows the user to set a single torque and speed set point manually and log data as required. This mode is generally used to carry out a warm-up sequence or to monitor live sensor signals. The status of several safety interlocks and limit switches are also displayed on this tab.
- ii) *Steady State Sequence* mode allows the user to automate the test profile by defining a series of steady state torque and differential speed test points. Each test point maintains a constant input torque and speed difference on the LSD for a period of 2 seconds. Measurements taken over this period are then averaged to calculate an associated locking torque value. Test sequence configuration files can be saved and re-run, providing improved repeatability between tests.
- iii) *Quasi Transient Sequence* mode allows the user to input any time, input torque and speed history desired. This can take the form of simple step or ramp changes in torque and speed, or importing in-car vehicle data taken from the track. As in the Steady State Sequence case, once a configuration file is defined, the whole process can be automated.

3.3 Steady State Validation

The following section now describes how the QTDTR was used to characterise the torque bias generated from a number of plate LSD setup parameters under steady state conditions. This includes the number of friction faces, drive and coast ramp angle, and positive and negative preload. For each of the tests presented, the bulk oil and differential casing temperature were raised to 80°C using a standard warm-up procedure. This progressively cycled through increasing amounts of applied input torque, at constant positive and negative differential speeds of 40rpm.



Figure 3.12: DTR Test Executive GUI

3.3.1 Friction Faces and Ramp Angle

Figure 3.13 shows the results from a series of steady state tests which aimed to validate both the drive/coast ramp angle and the number of friction faces. The configuration detailed in Table 3.3 was used, but with the number of friction faces successively reduced from 16 to 4. To assess the fidelity of the model, two metrics were employed: the root mean squared error (RMSE) and a normalised mean squared error (NMSE) defined by [118]:

$$\text{NMSE} = \frac{100}{N \sigma^2} \sum_{i=1}^N (T_{lock_{ref},i} - T_{lock,i})^2 \quad (3.47)$$

where $T_{lock_{ref},i}$ represents the test data points, $T_{lock,i}$ the model values for $i = 1 \dots N$ points and σ , the standard deviation of the measured data. Guidelines set out by [13] are used to assess the quality of the model. An NMSE less than one percent represents an excellent model fit, whilst values below five percent represent a good model fit. These metrics are summarised in Table 3.4. The correlation of the model at 8, 12 and 16 friction faces is good with NMSE values ranging from 0.4-3.2%. However with 4 friction faces the model correlation is poor with an NMSE of 14%. A potential explanation for this is that the lubrication regime during the test does not reflect that of the idealised single friction disc test detailed in Section 3.1.3. Although oil feeds ensure that the surfaces are lubricated throughout the test, maintaining a constant temperature at the clutch plate contacts is challenging (particularly when different numbers of friction faces will generate different levels of heat). Due to the relatively small bias torque generated, the oil temperature actually started to fall (by 8°C in total) during the test. This has led to an increase in the plate friction and an associated rise in the measured locking torque. This behaviour was in-line with the findings of James [45], who tested identical clutch surfaces at a range of temperatures. What is also apparent is that there is a slight difference in the residuals between drive and coast directions. This could potentially be explained by differing levels of ramp friction (μ_r), on the drive and coast faces of the ramp - crosspin contacts. A more detailed discussion of this issue is handled in Section 3.4.1.

Table 3.3: Plate differential setup parameters, ramp and friction face validation

Parameter	Symbol	Value
Drive ramp angle	θ_{rd}	45°
Coast ramp angle	θ_{rc}	60°
Number of friction faces	z_f	4-16
Static positive preload	T_{pp}	0Nm
Drive negative preload	T_{np}	0Nm
Transition preload gain	T_{pg}	5.25
Ramp friction coefficient	μ_r	0.13
Pinion mate friction coefficient	μ_p	0.10

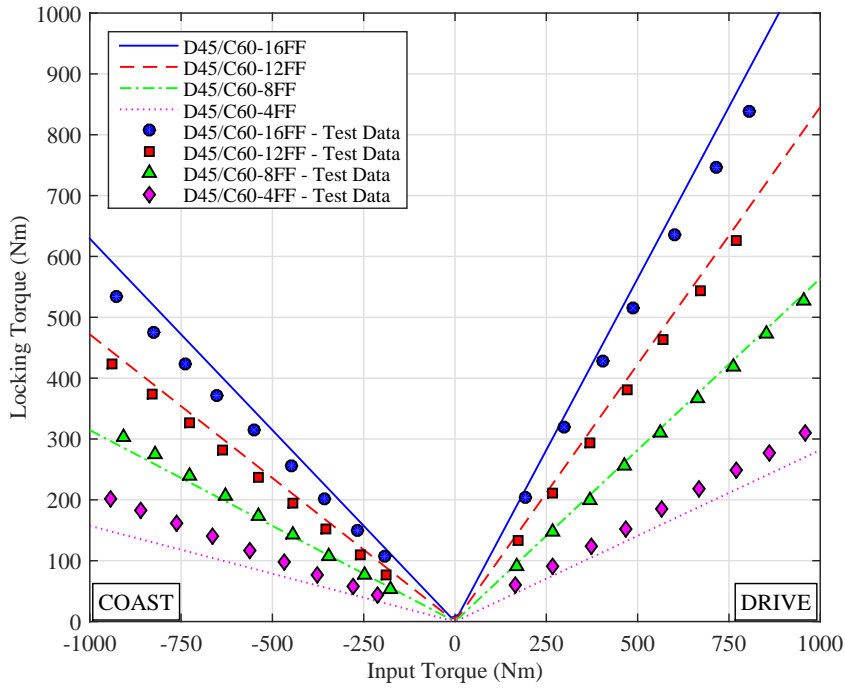


Figure 3.13: Friction face and ramp angle steady state validation, bulk oil temperature 80°C, 40rpm differential speed

Table 3.4: Ramp and friction face validation errors

Configuration (no. of friction faces)	RMSE (Nm)	NMSE (%)
16	37.5	3.2
12	17.9	1.3
8	8.6	0.4
4	35.6	14.4

3.3.2 Positive and Negative Preload

Positive and negative preload are typically achieved through the use of a belleville spring and a screw thread adjuster wheel, which allows a number of discrete settings to control spring compression (see Figure 2.1 and 2.2). In this instance, this is controlled by the relative number of detents or ‘clicks’ (n_c) against the total number on the adjuster wheel (n_{ct}). These can be related to the preload clamp force F_{pp} , where:

$$F_{pp} = \frac{n_c}{n_{ct}} t_{hp} k_b \quad (3.48)$$

where t_{hp} is the adjuster thread pitch, and k_b the belleville spring stiffness. The resulting preload torque T_{pp} , detailed in Equation 3.5, can then be found by substituting Equation

3.48 into Equation 3.41, in place of the clamp load F_{ramp} :

$$T_{pp} = \frac{2}{3} \frac{n_c}{n_{ct}} t_{hp} k_b z_f \mu_p \left(\frac{r_{c2}^3 - r_{c1}^3}{r_{c2}^2 - r_{c1}^2} \right) \tag{3.49}$$

A range of steady state tests were repeated for the LSD parameters detailed in Table 3.3, for preload values increasing from 4 to 10 clicks. The positive preload parameters are detailed in Table 3.5 and the results are shown in Figure 3.14. A summary of the associated errors in each preload configuration is given in Table 3.6.

Table 3.5: Positive preload detent adjustment, $n_{ct} = 24$, $t_{hp} = 1.25\text{mm}$, $k_b = 2.8\text{kN/mm}$, $z_f = 16$

No of clicks (n_c)	Positive Preload Torque (T_{pp})
4	40.8
6	81.7
8	122.5
10	163.3

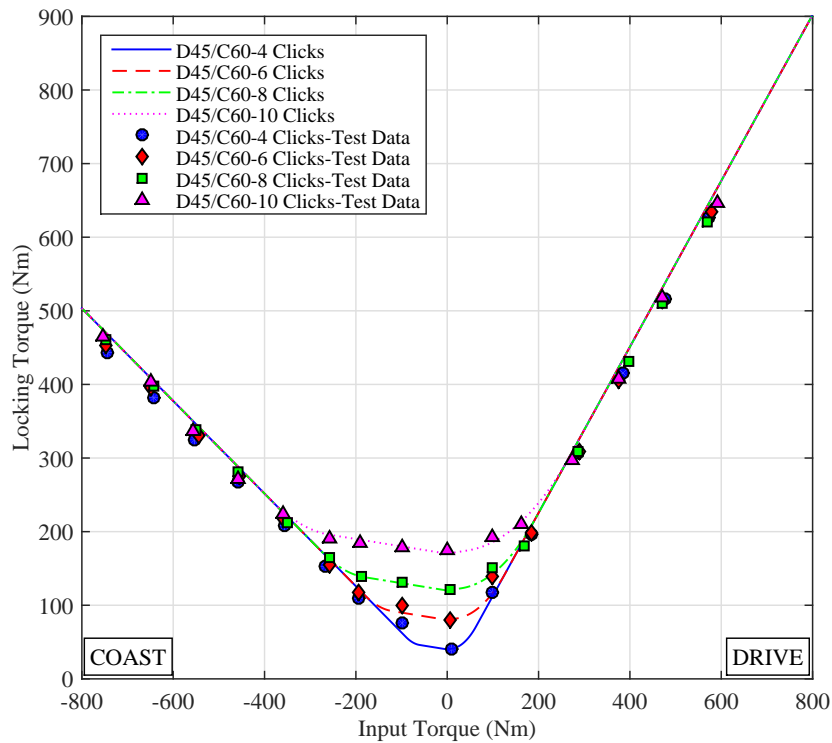


Figure 3.14: Positive preload steady state validation, bulk oil temperature 80°C, 40rpm differential speed, 16 friction faces

Table 3.6: Positive preload validation errors

Configuration (no. of clicks)	RMSE (Nm)	NMSE (%)
4	17.3	1.0
6	13.8	0.7
8	11.6	0.5
10	10.7	0.5

Again, each configuration shows a good level of agreement with the measured data points, with NMSE values ranging from 0.5-1% (see Table 3.6).

The right hand side of Equation 3.48 can also be used to evaluate the negative preload clamp force exerted by its respective belleville spring, where

$$F_{np} = \frac{n_c}{n_{ct}} t_{hp} k_b \quad (3.50)$$

Since this force acts in the opposite direction to positive preload, this can be thought of as a force which must be overcome by each ramp, before any torque bias can occur. It is more convenient therefore, to define negative preload as a threshold input torque T_{np} , (see Figure 3.2). This can be derived from Equation 3.38 by substituting the preload clamp force F_{np} for the ramp force F_{ramp} to give:

$$T_{np} = \frac{n_c}{n_{ct}} t_{hp} k_b R_{rr} \left(\frac{\cos \theta_r - \mu_r \sin \theta_r}{\sin \theta_r + \mu_r \cos \theta_r} \right)^{-1} \quad (3.51)$$

Although not substantiated in literature, it is common practice to apply negative preload to the drive side locking profile only. This is achieved by splitting the ramp pair (shown in Figure 2.2) into multiple pieces to allow the decoupling of drive and coast ramp faces. The negative preload spring is then used to preload the drive ramp (relative to the clutch pack), so that it cannot clamp the clutch plates until a threshold load has been reached. A range of steady state tests were carried out for the negative preload settings shown in Table 3.7. The specific plate LSD parameters are shown in Table 3.8 and the results are detailed in Figure 3.15. A summary of the associated model errors is also included in Table 3.9.

In this instance, a larger spread of NMSE values is seen when compared to the positive preload case, which range from 1.0-5.3%. Due to the decoupling of drive and coast ramps required for negative preload implementation, the ramps used during physical tests were different from the positive preload case. More specifically, the ramp-crosspin contact areas were different, leading to a variation in the associated friction coefficient. It is highly likely that this will have contributed to the degradation in model fidelity. Nevertheless, a maximum NMSE of 5.3% represents an acceptable model fit.

Table 3.7: Negative preload detent adjustment, $n_{ct} = 24$, $t_{hp} = 1.25\text{mm}$, $k_b = 19.6\text{kN/mm}$, $\theta_r = 55^\circ$

No of clicks (n_c)	Neg Preload Torque (T_{np})
3	260.7
6	521.4
9	782.2
12	1042.9
15	1303.6

Table 3.8: Plate differential setup parameters - negative preload validation

Parameter	Symbol	Value
Drive ramp angle	θ_{rd}	55°
Coast ramp angle	θ_{rc}	65°
Number of friction faces	z_f	16
Static positive preload	T_{pp}	0Nm
Positive preload gradient	∇_{pp}	0.05
Drive negative preload	T_{np}	(see Table 3.7)
Transition preload gain	T_{pg}	1.5
Ramp friction coefficient	μ_r	0.13
Pinion mate friction coefficient	μ_p	0.10

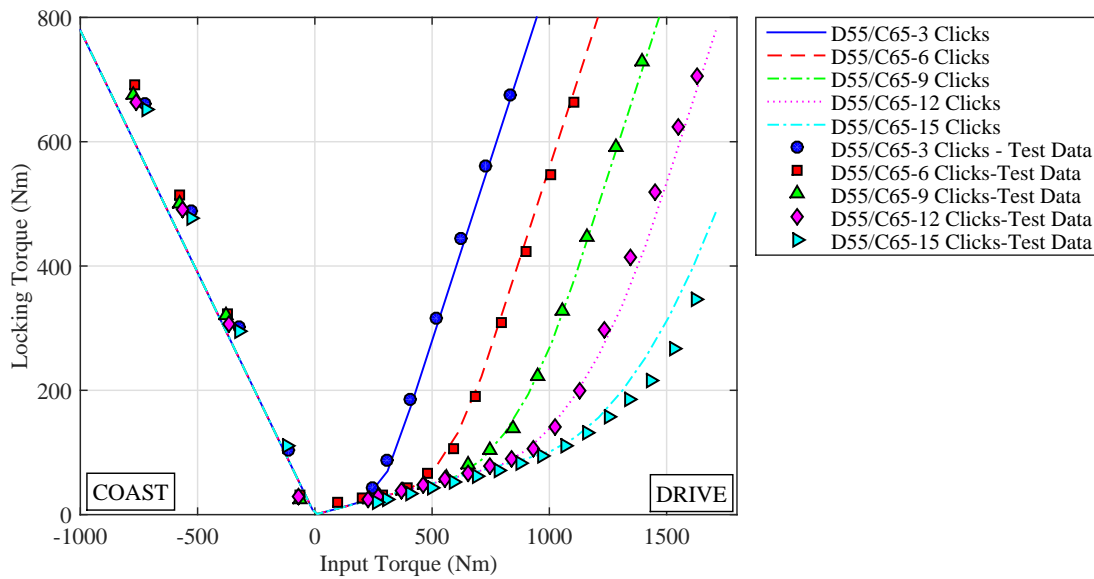


Figure 3.15: Negative preload steady state validation, bulk oil temperature 80°C , 40rpm differential speed, 16 friction faces

Table 3.9: Negative preload validation errors

Configuration (no. of clicks)	RMSE (Nm)	NMSE (%)
3	42.8	3.5
6	31.7	1.6
9	24.3	1.0
12	26.6	1.2
15	37.9	5.3

3.4 Transient Validation

Although the previous steady state characterisation gives confidence in the model fidelity, on-track and in-car use seldom reflect these idealised conditions. As will be shown in Section 4.1.7, the LSD will be subject to varying engine input torque and resistive tyre forces. Accordingly, it is important to characterise the dynamic response of the LSD, as this may influence the associated torque bias generated. This section details the results of step and ramp input torque transient tests, carried out to replicate these in-car conditions more closely.

The steady state validation showed that accurate assessment of the clutch plate and ramp friction coefficients are key to model fidelity. To supplement this process during transient testing, a bespoke transducer was developed to measure the ramp clamping loads directly. Due to its narrow profile, it could be installed within the clutch pack assembly, so that the relative magnitude of clutch and ramp contact coefficients could be evaluated more accurately. For further details on the installation and calibration of the transducer, the reader is referred to Appendix C. It should be noted that in order to house the transducer in the plate pack assembly, 2 friction plates (i.e. 2 friction faces per side) had to be removed. Thus the maximum number of friction faces allowable in this configuration was 12.

3.4.1 Step Input

The torque bias response was initially measured by applying a positive step input torque of 1000Nm, at a constant differential speed of 40rpm. Figure 3.16 shows the resulting data trace for locking torque. The input torque and differential speed histories were then used as input parameters for the steady state model described in Section 3.1. The resulting steady state locking torque is also shown in Figure 3.16.

It is clear that there is a time lag in the response, typically associated with the oil squeeze phase, where the frictional properties are transitioning between full film and boundary layer lubrication. The stiffness of the friction material is another important factor which contributes to this lag in response. To account for this behaviour, a simple first order differential equation can be defined, in which:

$$\frac{dT_{lock}}{dt} + \frac{1}{\tau} T_{lock} = T_d(t) \nabla_r \quad (3.52)$$

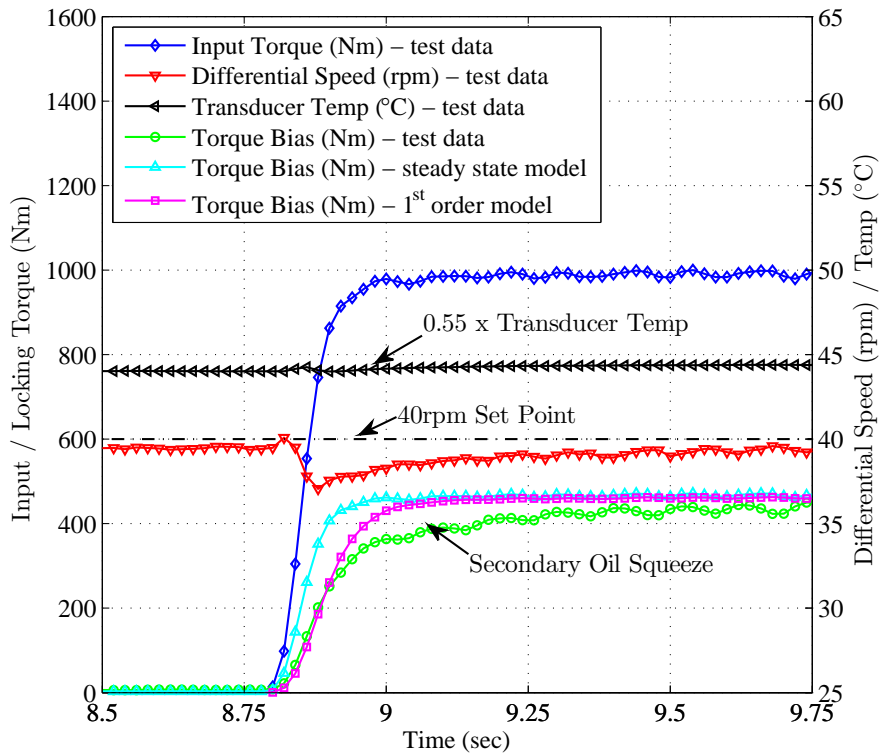


Figure 3.16: Transient step response, drive ramp $\theta_r = 60$, friction faces $z_f = 12$, 40rpm differential speed, bulk oil temperature 80°C

where τ is the system time constant and ∇_r , the steady state ramp locking gradient defined in Section 3.1.2. The resulting transfer function can be found by evaluating the differential equation in the Laplace domain, where:

$$\frac{T_{lock}(s)}{T_d(s)} = \frac{\nabla_r}{\tau s + 1} \quad (3.53)$$

The locking torque response using a time constant of $\tau = 0.05\text{s}$ is overlaid in Figure 3.16. Although the initial correlation is much better than the steady state model, there is still an appreciable error between 9.0 and 9.25s. This secondary lag before reaching steady state was investigated by conducting a number of similar tests at different rotation speeds (see Appendix B). These confirmed that the duration of the lag reduced as speed increased. It is likely that a faster rotation speed helps expel the majority of the oil during contact more quickly, thus minimising the time before steady state, boundary lubrication takes hold at 9.25s.

To evaluate the magnitude of the ramp friction coefficient μ_r , the clutch pack transducer described in Appendix C was used to measure the clamp load throughout the step input test. The theoretical clamp load was resolved from the input torque by using Equation 3.38. The results are shown in Figure 3.17 for ramp friction coefficients (μ_r) ranging from 0.11 to 0.15. Although this coefficient is likely to change with applied load, due to temperature variations between each of the ramp contact faces, a constant value of 0.13

was used throughout the modelling and validation processes presented in this thesis.

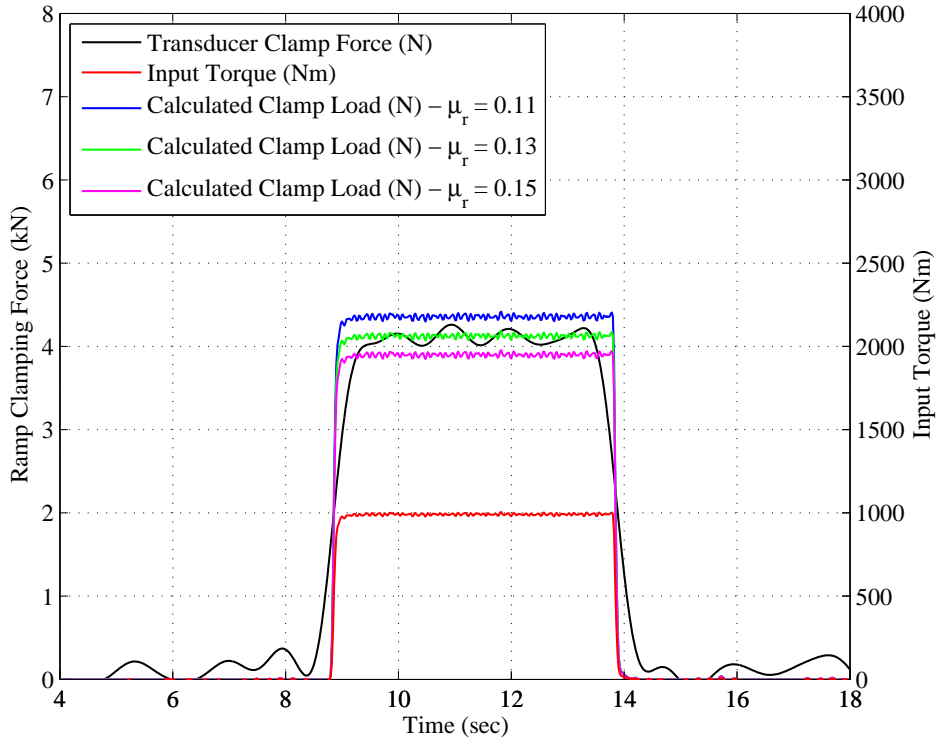


Figure 3.17: Measured and predicted ramp clamping force for $\mu_r = 0.11, 0.13, 0.15$, transient step response, drive ramp $\theta_r = 60$, friction faces $z_f = 12$, 40rpm differential speed, bulk oil temperature 80°C

3.4.2 Drive - Coast Ramp Input

In an effort to replicate more realistic test conditions, a ramp test profile was created to simulate differential input torque variations during a typical corner. This started with a 1000Nm positive torque which ramped down to a negative coast torque of the same magnitude, in less than 0.25s. This was designed to simulate the sudden on-throttle - braking transition before corner entry. This coast torque was maintained for a period of 3.0s, then ramped back up to +1000Nm in 1.0s to simulate the driver's reapplication of the throttle, post apex, during the corner exit. Since the effective steady state DC gain of the first order model changes with a variation in ramp angle, Equation 3.53 can be modified in a piecewise fashion, where ∇_r is calculated depending on the sign of the input torque. Hence:

$$\nabla_r = \nabla_{rdrive} \quad \text{for } T_d > 0 \quad (3.54)$$

$$\nabla_r = \nabla_{rcoast} \quad \text{for } T_d < 0 \quad (3.55)$$

The results are shown in Figure 3.18, and correlation is similar to that seen with the step response (see Figure 3.16). The locking torque is again over estimated according to the previous steady state results (see Figure 3.13). The reader should note that the discontinuity in the input torque profile during zero crossing was due to the backlash

in the hydraulic actuator rack (see Section 3.3 for further details on the test rig).

This test demonstrates the highly transient nature of the locking torque profile through a typical cornering simulation. While this test is carried out in idealised conditions, it does show that the smoother the differential input torque (either from the engine or brakes), the more progressive the resulting locking torque will be. Practically speaking, this means drivers who apply brake and throttle inputs more smoothly, are much less likely to induce sudden changes in locking torque, and the associated snap lock-unlock behaviour that is sometimes experienced.

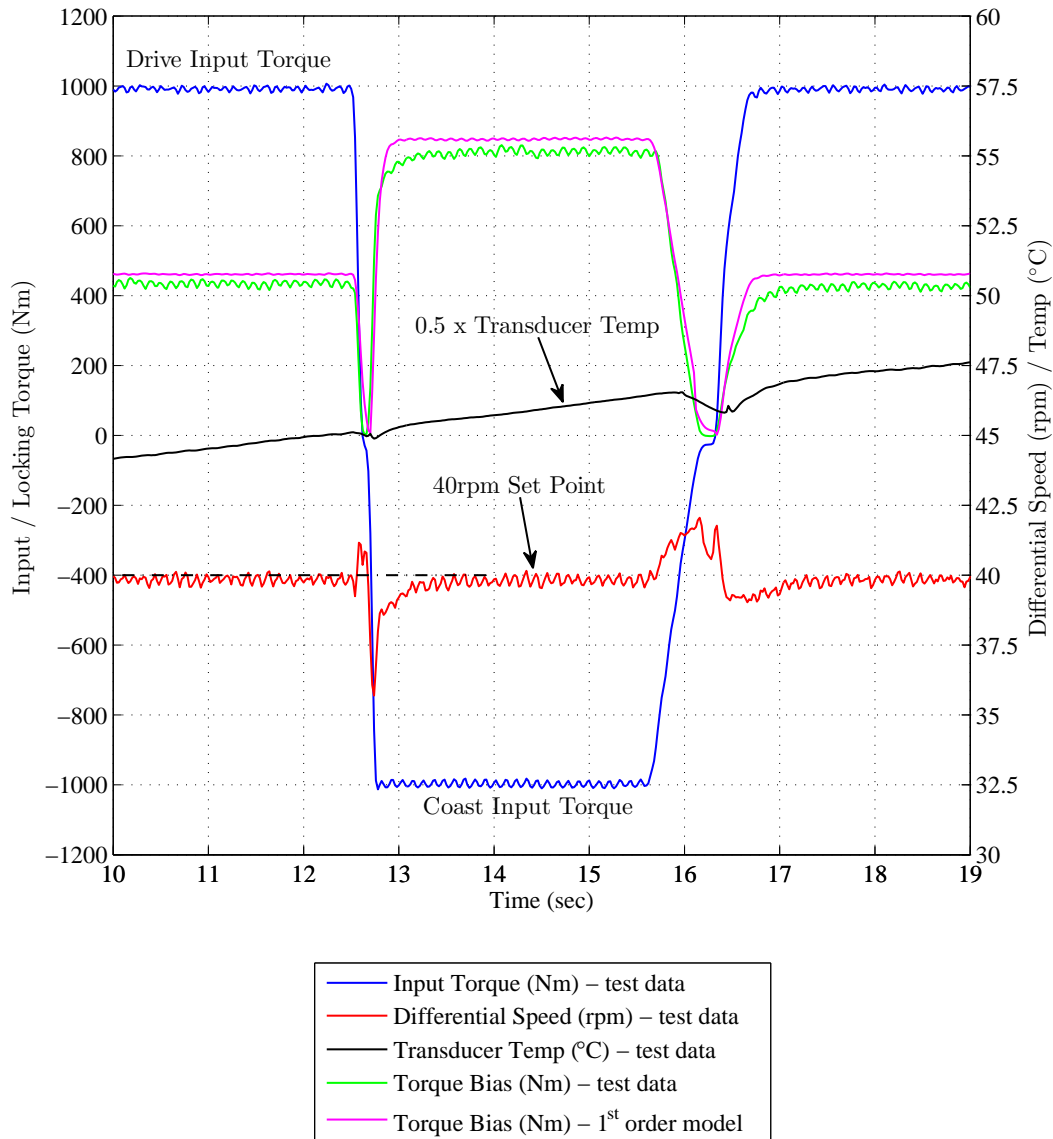


Figure 3.18: Drive and coast ramp response, drive ramp = 60° , coast ramp = 45° , friction faces = 12, 40rpm differential speed, bulk oil temperature 80°C

3.5 Viscous Coupling (VC)

In contrast to the torque sensitive LSD described in Section 3.1, speed sensing differentials are not reliant on an input torque to generate locking. Of the current types in use, VCs used in conjunction with a conventional bevel gear open differential have proved popular, since they provide a reliable and cost efficient solution, which can be easily tuned to give a range of locking characteristics [65, 74]. A model of the VC unit depicted in Figure 2.3 is presented in this section and validated against test data generated on the QTDTR. The application of this model is then extended by combining its use with that of a plate differential model in Section 3.6, to form a hybrid Viscous Combined Plate (VCP) model.

3.5.1 Fluid Viscosity Variation

The fluid viscosity relationship with temperature and shear rate has been shown to be a crucial element in the fidelity of all VC models, discussed by many researchers including Mohan [65], Takemura [99] and Taureg [100]. In this case, some of this information was available from the silicon fluid manufacturers, who typically define kinematic viscosity characteristics at a reference temperature of 25 °C. The fluid temperature (θ_s) - viscosity (ν) relationship can be described by an empirical equation of the form [65]:

$$\frac{\log(\nu)}{\log(\nu_{\theta_{s0}})} = 10^{-A_{sv} \log(\theta_s/\theta_{s0})} \quad (3.56)$$

Where θ_{s0} is the reference temperature, $\nu_{\theta_{s0}}$ a base viscosity defined at this temperature, and A_{sv} an empirical constant. For the basis of this model, a base viscosity of 300kcSt ($3.0 \times 10^5 \text{ mm}^2 \text{ s}^{-1}$) is used, but is adjusted depending on the fluid temperature to give the apparent viscosity ν . The resultant fluid viscosity variation with temperature is shown in Figure 3.19a.

Since silicon fluids are typically shear thinning (pseudoplastic), their viscosity generally reduces with shear rate ($\dot{\gamma}$). Physical testing has shown that the apparent fluid viscosity changes very little up to a critical shear rate $\dot{\gamma}_b$, after which the decrease in viscosity can be approximated to a constant gradient (m_{sf}), on a log-log plot. This relationship is described in Equation 3.57. Figure 3.19b shows this in graphical form, depicting the viscosity - shear curve at the base reference temperature of 25°C and at a standard operating temperature of 80°C. Accordingly, these have the associated critical shear rate points $\dot{\gamma}_{b25}$ and $\dot{\gamma}_{b80}$.

$$\nu = \nu_{\theta_{s0}} \left(\frac{\sqrt{\dot{\gamma}^2 + \dot{\gamma}_b^2}}{\dot{\gamma}_b} \right)^{m_{sf}} \quad (3.57)$$

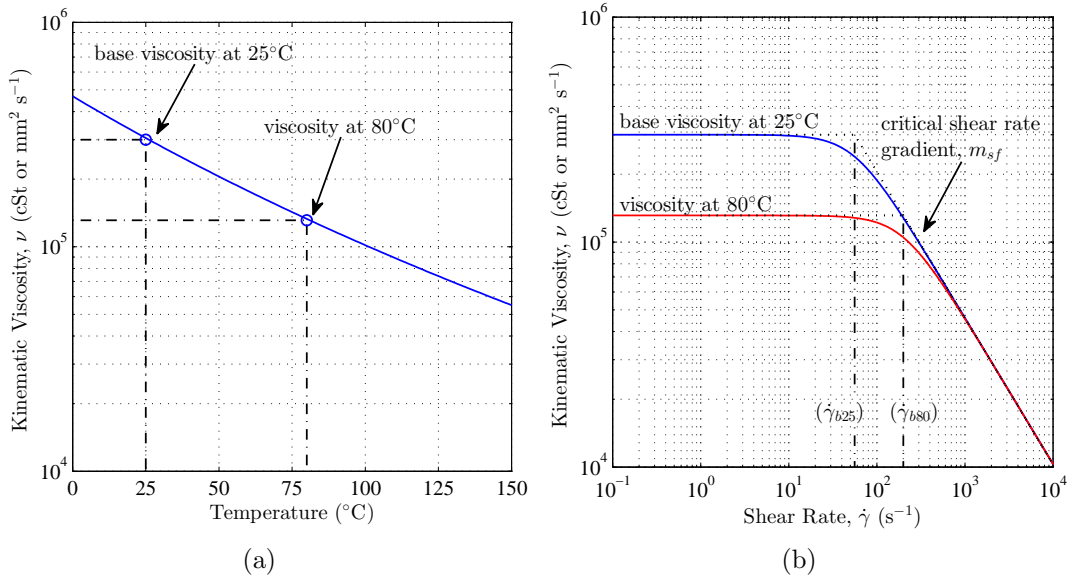


Figure 3.19: a) silicon fluid viscosity variation with temperature
 b) silicon fluid viscosity with shear rate
 ($\nu_{\theta_{s0}} = 3.0 \times 10^5 \text{ mm}^2\text{s}^{-1}$, $A_{sv} = 2.12$, $\dot{\gamma}_{b25} = 50$, $\dot{\gamma}_{b80} = 200$, $m_{sf} = -0.65$)

3.5.2 Shear Torque Calculation

The characterisation of fluid viscosity can be used to predict the associated VC torque bias by considering the shear stress of the fluid. The shear torque calculation presented below is based on the work of Mohan [65] and Takemura [99]. The shear surfaces are depicted in Figure 3.20 and are separated using a specific disc spacer. A linear fluid velocity profile was assumed, since viscous forces will dominate at Reynolds numbers $\ll 1$ [65]. For a single set of shear faces the fluid velocity gradient or shear rate $\dot{\gamma}$, is defined by:

$$\dot{\gamma} = \frac{du}{dz} = \frac{U_v}{s_v} \quad (3.58)$$

where U_v is the relative tangential velocity of the shear surface and s_v , their separation distance. The force acting on an elemental area dA can be described by:

$$dF = \tau_s dA \quad (3.59)$$

where τ_s is the shear stress of the fluid, which can also be described in terms of the fluid properties and velocity gradient as:

$$\tau_s = \nu \rho_v \frac{\omega_d r}{s_v} \quad (3.60)$$

where ω_d is the rotational speed difference, r the radius of the elemental area, and ρ_v the density of the silicon fluid. Substituting Equation 3.60 into 3.59 and noting that

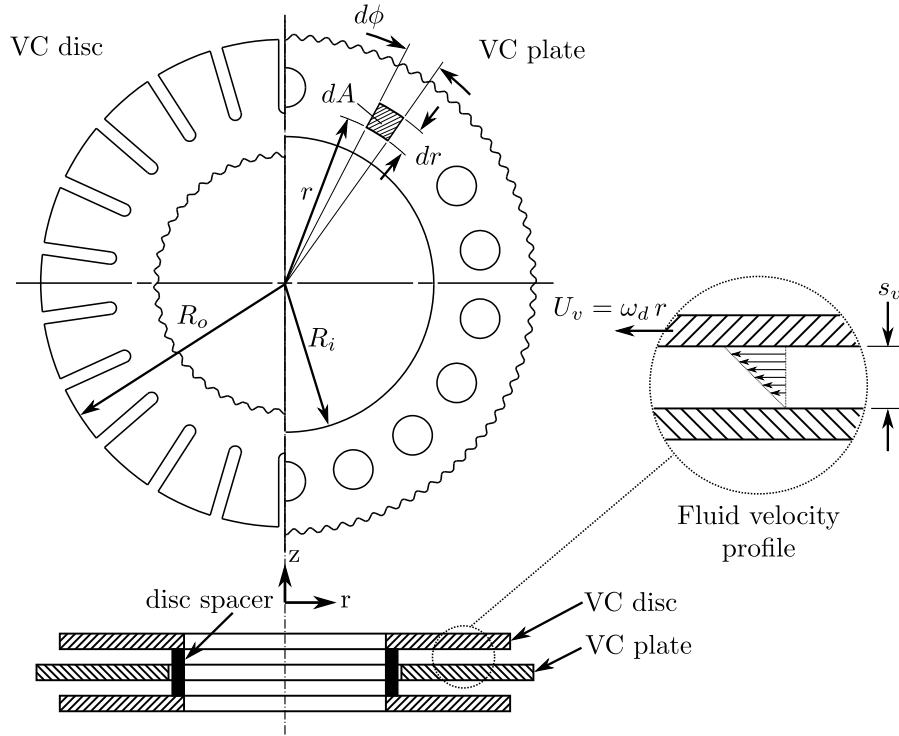


Figure 3.20: VC disc and plate geometry

$dA = r dr d\phi$, the resulting tangential force can be described by:

$$dF = \nu \rho_v \frac{\omega_d}{s_v} r^2 dr d\phi \quad (3.61)$$

and similarly, the resultant torque due to the elemental force is:

$$dT = r dF = \nu \rho_v \frac{\omega_d}{s_v} r^3 dr d\phi \quad (3.62)$$

By integrating over the total area of the shear surface, for z_s shear surfaces, a total viscous torque can then be defined as:

$$T_{vc} = z_s \int_{R_i}^{R_o} \int_0^{2\pi} \nu \rho_v \frac{\omega_d}{s_v} r^3 d\phi dr \quad (3.63)$$

taking the definite integral between 0 and 2π with respect to $d\phi$:

$$T_{vc} = z_s \int_{R_i}^{R_o} 2\pi \nu \rho_v \frac{\omega_d}{s_v} r^3 dr \quad (3.64)$$

and between R_i and R_o with respect to dr :

$$T_{vc} = z_s \frac{\pi \nu \rho_v \omega_d}{2 s_v} (R_o^4 - R_i^4) \quad (3.65)$$

Finally the factor K_a can be defined to represent the proportion of the shear surface area taken up with holes, slots or perforations. It is common to machine slots into the external diameter of the shear discs and holes into the surface of the shear plates (see Figure 3.20). This is to both stabilise the torque bias characteristics and increase the service life of the unit [65]. The final expression for the viscous shear torque can thus be described as:

$$T_{vc} = K_a z_s \frac{\pi \nu \rho_v \omega_d}{2 s_v} (R_o^4 - R_i^4) \quad (3.66)$$

During the operation of the VC, the shearing action of the plates against the fluid will also provide an additional temperature rise which is related to the amount of shear work done on the silicon fluid. The rate of heat generation can be expressed by:

$$\frac{dQ}{dt} = \omega_d T_{vc} \quad (3.67)$$

where Q is the heat generated as a result of fluid shear. For the purposes of this model, the heat transfer within the VC is assumed to be adiabatic i.e. all the energy generated from shearing of the fluid is responsible for its temperature rise. No heat conduction to the VC housing is assumed. Physical testing on the QTDTR showed that for test durations below 15s, the housing temperature rise was minimal ($< 1^\circ\text{C}$), which provided the basis for this assumption. Test durations longer than this threshold however, were shown to prove the adiabatic assumption invalid. All VC models presented in this thesis will be assumed to operate under this time threshold.

The rate of shear energy can be related to the associated temperature rise by:

$$\frac{dQ}{dt} = \omega_d T_{vc} = m_s c_s \frac{d\theta_s}{dt} \quad (3.68)$$

where m_s and c_s are the fluid mass and specific heat capacity. For transient models, Equation 3.68 was used to recalculate the fluid temperature at each simulation step. The revised temperature was then used to re-evaluate the apparent viscosity and shear rate relationship defined in Equations 3.56 and 3.57. For steady state models, the temperature of the fluid was assumed to remain at a constant operating temperature of 80°C .

3.5.3 Transient VC Validation

The VC model was validated against test data generated on the QTDTR, by carrying out a ramped speed input test. The VC was first warmed up until the outer casing reached a temperature of 80°C , then the differential speed was increased to 70rpm over a period of 7s, whilst locking torque was monitored. It should be noted that although some of the fluid parameters were available from the silicon fluid manufacture, the temperature constant A_{sv} , shear-viscosity slope m_{sf} , and details of how the critical shear rate $\dot{\gamma}_b$ varied with temperature were unavailable for the specific fluid used. Consequently, these parameters were fitted to a series of experimental locking torque curves, generated at several starting temperatures ranging from 50 to 100°C . The model parameters from the VC unit shown in Figure 2.3 and the resulting fluid parameter

properties are detailed in Table 3.10. The calculated locking torque is then compared to the experimental data in Figure 3.21.

Table 3.10: VC setup and fluid parameters

Parameter	Symbol	Value
No. of shear faces	Z_s	28
Base fluid viscosity	$\nu_{\theta 0}$	300 kSt
Plate separation	s_v	0.13mm
Plate geometry factor	K_a	0.86
Temperature-viscosity constant	A_{sv}	0.18
Critical shear rate	$\dot{\gamma}_b$	55 - 200s ⁻¹
Shear rate-viscosity slope	m_{sf}	-0.565
Silicon fluid density	ρ_v	970 kg m ⁻³
Silicon fluid mass	m_s	43g
Silicon specific heat capacity	c_s	1500 J kg ⁻¹ K ⁻¹

The results demonstrate the relatively high viscosity of the fluid at low rpm, with a steep increase in locking torque at values below 20rpm. As the rpm and resultant shear rate increases, so the apparent viscosity starts to reduce, until the steady state speed is reached after 9s. At this point, the locking torque levels off, but still decreases, albeit at a much slower rate, due to the internal heating of the fluid. The external temperature of the casing remains almost constant throughout the test (temperature increase is <1°C). Although the associated NMSE is below 1%, this will not be the case for longer duration tests, where heat transfer past the fluid-casing boundary will start to influence fluid viscosity much more significantly.

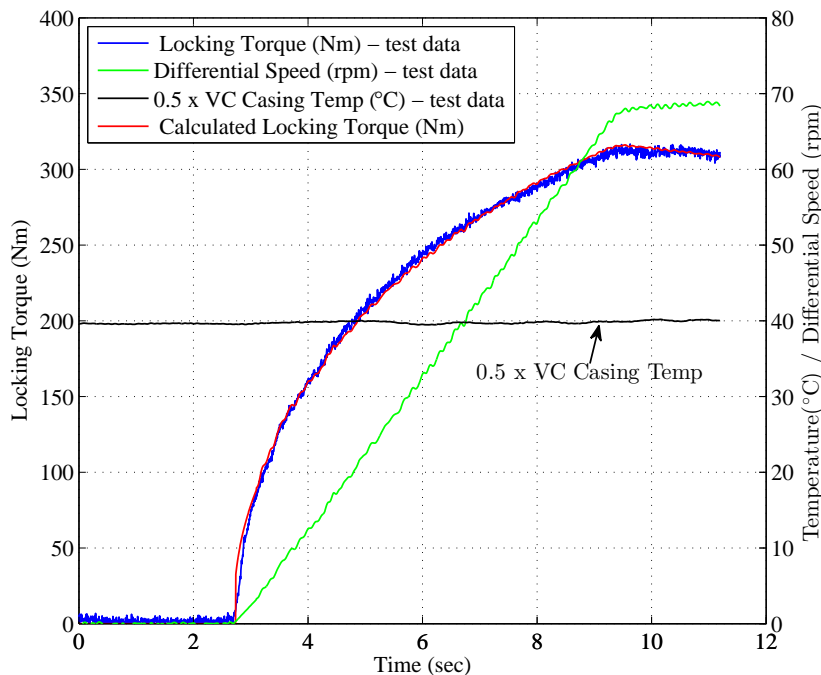


Figure 3.21: VC unit ramp speed validation, 80°C casing temperature

3.6 Viscous Combined Plate (VCP)

It is common in motorsport to combine the use of a torque sensitive plate LSD and a speed sensitive VC to form a Viscous Combined Plate (VCP) differential. This is thought to combine the quick response of a plate LSD with the speed sensing VC element used to dampen any spikes in transfer torque. The specific VCP which forms the basis of the subsequent model is described in Section 2.1.3, and depicted in Figure 2.4.

The total transfer torque due to the respective torque and speed sensing elements, simply combines Equations 3.13 and 3.66 to form a VCP locking torque:

$$\text{under drive} \quad T_{vcp} = T_{lock-drive} + T_{vc} \quad (3.69)$$

$$\text{under coast} \quad T_{vcp} = T_{lock-coast} + T_{vc} \quad (3.70)$$

An example VCP map is shown in Figure 3.22, which uses the plate LSD parameters detailed in Table 3.1, the plate friction characteristics in Table 3.2, and the VC parameters listed in Table 3.10. At low rpm, the torque bias behaves in a very similar fashion to the plate LSD model, but as the speed difference increases the locking increases more significantly. Overall, at a 50rpm differential speed, the VC has added over 250Nm of additional locking torque to that generated by the plate LSD alone. This is likely to have the greatest influence on handling when wheel speed differences are highest, typically at the apex of a corner (the reader is referred to Section 6.2.3 for a more detailed discussion).

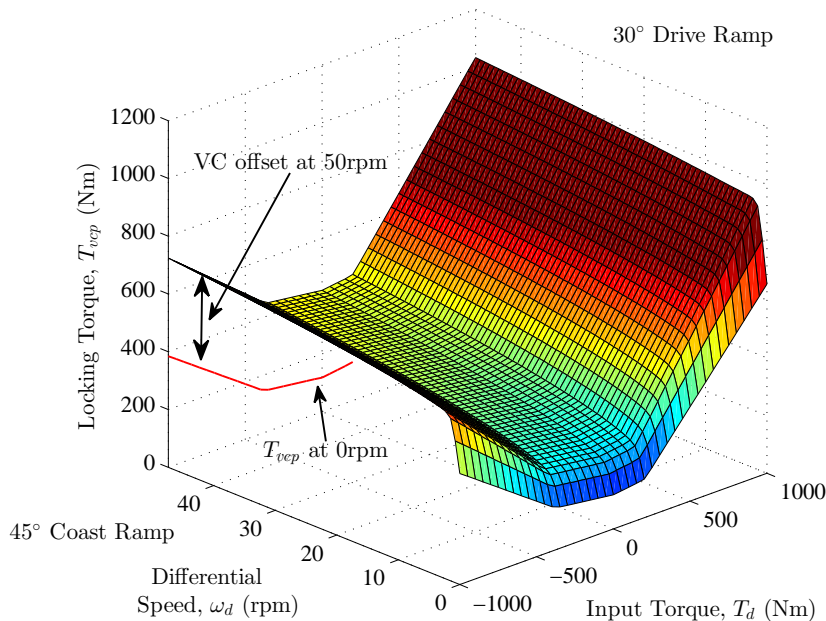


Figure 3.22: Example VCP torque bias map with input torque and differential speed

3.6.1 VCP Validation

A steady state validation of the VCP model was conducted in a similar manner to those described in Section 3.3, but split into two stages. First, the plate LSD was tested in isolation with the VC link shaft removed (see Figure 2.4). This would provide confirmation of the relative contribution of torque and speed sensing elements. The VC link shaft was then reinstated to measure the combined bias torque. Each data point was generated from an averaged reading over a period of 2s. Before each point was recorded, both the bulk oil temperature and the VC casing temperature were warmed to 80°C. The plate LSD parameters of the VCP used during the validation are defined in Table 3.11 and the results are shown in Figure 3.23. It should be noted that the physical VCP used during tests had different ramp geometry to that presented in earlier plate LSD sections. As a result of a larger ramp-crosspin contact radius (R_{rr}) the ramp clamp force and resulting locking torque levels are reduced. A summary of the associated model errors are given in Table 3.12.

Table 3.11: Plate differential setup parameters, VCP validation

Parameter	Symbol	Value
Drive ramp angle	θ_{rd}	60°
Coast ramp angle	θ_{rc}	30°
Number of friction faces	z_f	12
Static positive preload	T_{pp}	0Nm
Drive negative preload	T_{np}	0Nm
Ramp friction coefficient	μ_r	0.13
Pinion mate friction coefficient	μ_p	0.10

Table 3.12: VCP validation errors

Configuration	RMSE (Nm)	NMSE (%)
VC inactive	36.8	3.9
VC active	37.7	3.4

The model correlation is shown to be acceptable, with both associated NMSE values below 4%. What is more apparent however, is the discrepancy between drive and coast regions. The coast side shows a much greater error under both configurations. One of the main challenges faced during physical testing was temperature control of the LSD assembly and the lubricating oil. During a typical steady state test profile, the bulk temperature rise was less than 5°C. However, at the clutch plate interface, the local contact temperature can be higher, depending on the effectiveness of the external oil feeds. The rise in contact temperatures will influence the associated friction coefficient, such that by the end of the steady state test profile (where coast test points are typically taken), the resulting locking torque can start to reduce [45].

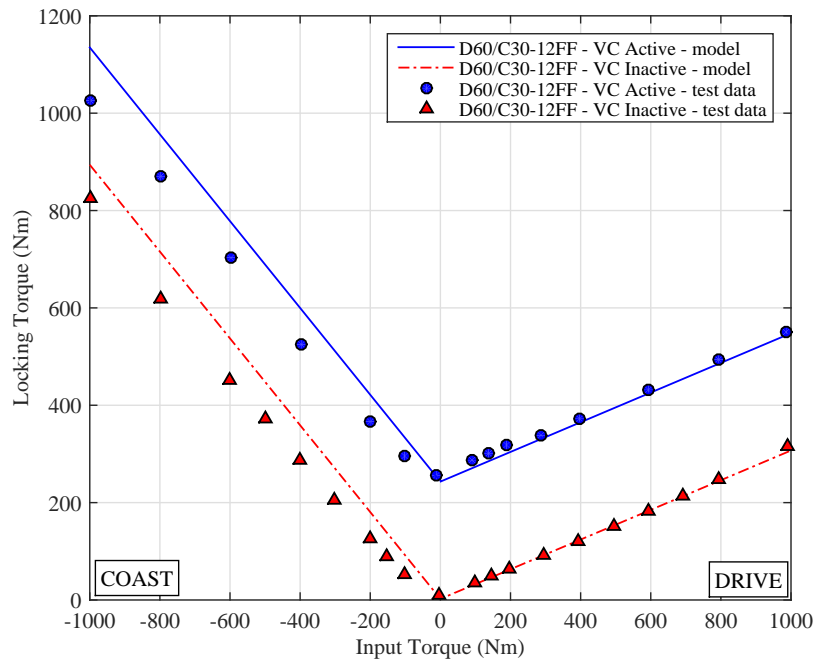


Figure 3.23: VCP steady state validation, bulk oil and VC casing temperature 80°C, 40rpm differential speed

3.7 Conclusions

Three comprehensive LSD models were presented, which included a torque sensing plate type (Salisbury), a speed sensing VC and a hybrid VCP which combined both speed and torque sensing elements. The plate LSD torque bias characteristics were evaluated from a semi-empirical model which defined three torque bias regions: a linear positive preload at low input torque levels (0-250Nm) and a much more aggressive ramp locking region at higher input torque levels (250Nm+). These were separated by a nonlinear transition, which was proportional to the magnitude of applied positive and negative preload. The resulting model allowed the evaluation of changes in drive and coast ramp angle, the number of friction faces and the positive/negative preload offset. A bespoke differential test rig was developed for validation purposes, which allowed both steady state and transient tests to be conducted. The steady state validations for each configuration parameter reduced the associated model error originally presented by Dickason [24] from over 40% in the ramp locking region, to less than 15% in preload, nonlinear transition and ramp torque bias regions.

The key to model fidelity was shown to be the friction coefficients associated with the ramp-crosspin, pinion mate-ramp and clutch plate inter-facial contacts. These all vary significantly with a number of factors including temperature, sliding speed, lubrication conditions and material wear. To augment the estimation of these friction coefficients, an attempt was made to isolate individual friction elements. The testing of a single pair of friction faces permitted the sliding speed and applied load influences to be included in the friction plate model. A bespoke transducer was also developed to measure the ramp clamping loads directly within the differential housing. This

provided a much more accurate assessment of the ramp-crosspin friction than would otherwise be the case. This methodology has been justified by the resulting correlation with experimental test data.

The steady state model was shown to provide a good approximation of transient behaviour in step response rig tests. Correlation was improved through the use of a first order lag function with a time constant of 0.05s. The resulting model was able to replicate the dynamic torque biasing behaviour of a typical off/on throttle input torque event.

The modelling of a speed sensitive VC LSD proved to be more challenging due to the highly influential thermal characteristics of the shear fluid. An adiabatic thermal model was used, with the critical relationships between shear rate, temperature and ultimate fluid viscosity established from empirical test data. The resulting model correlation gave an associated NMSE below 1%. It must be noted however, that test durations above 10s are likely to yield more inaccurate results.

Overall, a range of adjustable motorsport LSD models have been created and validated to within acceptable limits. These models will now form the basis of nonlinear vehicle simulations and time optimal parameter sensitivity studies.

Chapter 4

Vehicle Modelling and Validation

This chapter describes the creation of a 7DOF vehicle model developed in the MATLAB/Simulink environment. This is one of the primary tools used to evaluate LSD influence on ultimate vehicle performance in subsequent chapters. For validation purposes, the model is parameterised around a front wheel drive (FWD) saloon racing vehicle. Track testing data generated with two opposing LSD configurations then forms the basis of a validation of both vehicle and differential models.

4.1 Vehicle Model Structure

The 7DOF model employed is based on a previously published and validated RWD vehicle model produced by Casanova [15] and Brayshaw [10]. It has been modified to represent a FWD Touring Car application fitted with the more comprehensive differential models described in Chapter 3. The model includes 3 planar degrees of freedom as longitudinal, lateral and yaw motions, in addition to 4 wheel rotations. The main modelling assumptions made were:

- Lateral and longitudinal load transfer effects are included with a quasi steady state approximation. Roll and pitch angles relative to a rigid body-fixed coordinate system are assumed to be small, which is the case for a racing vehicle of this type.
- The track surface is assumed to be perfectly flat, with no camber or gradients. The unsprung mass and vehicle ride behaviour is neglected.
- Suspension and steering systems are considered rigid bodies, so that steering wheel inputs result in a directly proportional road wheel movement (i.e. no compliance steer effects).
- A steady state Magic Formula tyre model is used which allows longitudinal and lateral tyre forces to be calculated as a function of the combined slip conditions, a static camber angle and normal load. Rotational tyre dynamics and gyroscopic effects have been neglected.

The structure of the model is outlined in Figure 4.1 and is used in two main ways throughout this thesis. The first, is in an open loop manner where steering and throttle inputs are defined for the course of the manoeuvre. The second, allows aspects of driver control to be investigated by using closed loop vehicle control. Both the vehicle trajectory and speed can be pre-defined, with the required steer and throttle inputs

giving some indication of driveability. Additional realism is included through the use of saturation functions derived from the longitudinal slip condition of each tyre. If excessive slip is seen, the associated velocity error fed into the throttle controller will be reduced. This allows the driver model to ‘back off’ under extreme circumstances. Further details on the driver model can be found in Section 4.1.11.

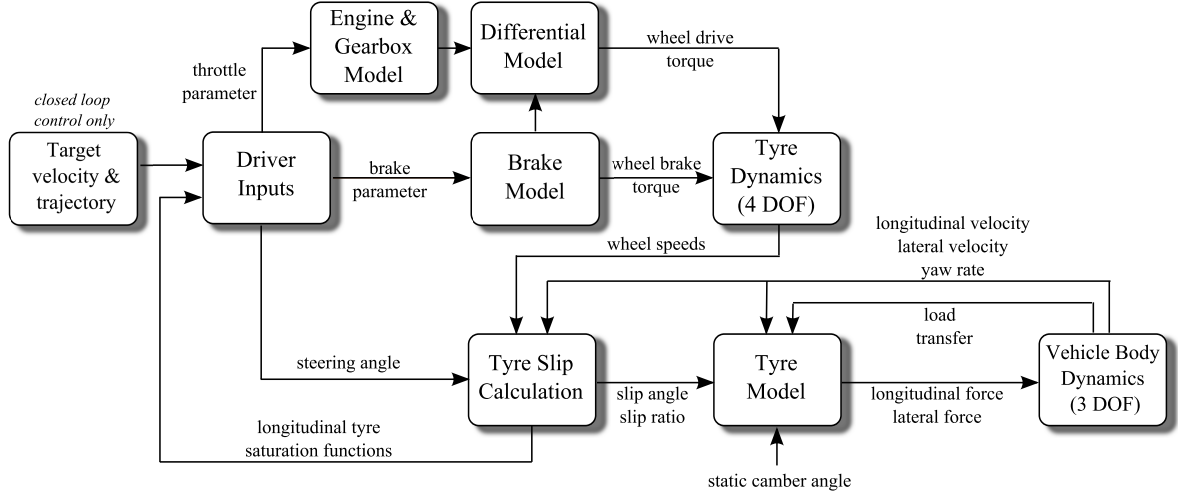


Figure 4.1: 7DOF vehicle model structure

4.1.1 Chassis Equations of Motion

The planar vehicle model is shown in Figure 4.2 and adopts the standard SAE axis sign convention. For convenience, parameters are defined at each wheel with the subscript n , where $n = 1..4$, and represents the front left, front right, rear left and rear right wheels respectively. The four wheel rotations, as well as an idealised roll axis for the weight transfer model are illustrated in Figure 4.3.

The longitudinal (U), lateral (V) and yaw (r) motions in an inertial ground fixed reference frame (XYZ) are defined by the equations:

$$m(\dot{U} - Vr) = \cos \delta_{rw}(F_{x1} + F_{x2}) - \sin \delta_{rw}(F_{y1} + F_{y2}) + F_{x3} + F_{x4} - F_{drag} \quad (4.1)$$

$$m(\dot{V} + Ur) = \sin \delta_{rw}(F_{x1} + F_{x2}) + \cos \delta_{rw}(F_{y1} + F_{y2}) + F_{y3} + F_{y4} \quad (4.2)$$

$$I_{zz}\dot{r} = (\cos \delta_{rw}(F_{x1} - F_{x2}) - \sin \delta_{rw}(F_{y1} + F_{y2}))\frac{t_f}{2} + (F_{x3} - F_{x4})\frac{t_r}{2} \quad (4.3)$$

$$+ a(\sin \delta_{rw}(F_{x1} + F_{x2}) + \cos \delta_{rw}(F_{y1} + F_{y2})) - b(F_{y3} + F_{y4})$$

Where m is the lumped vehicle mass and I_{zz} the vehicle yaw inertia.

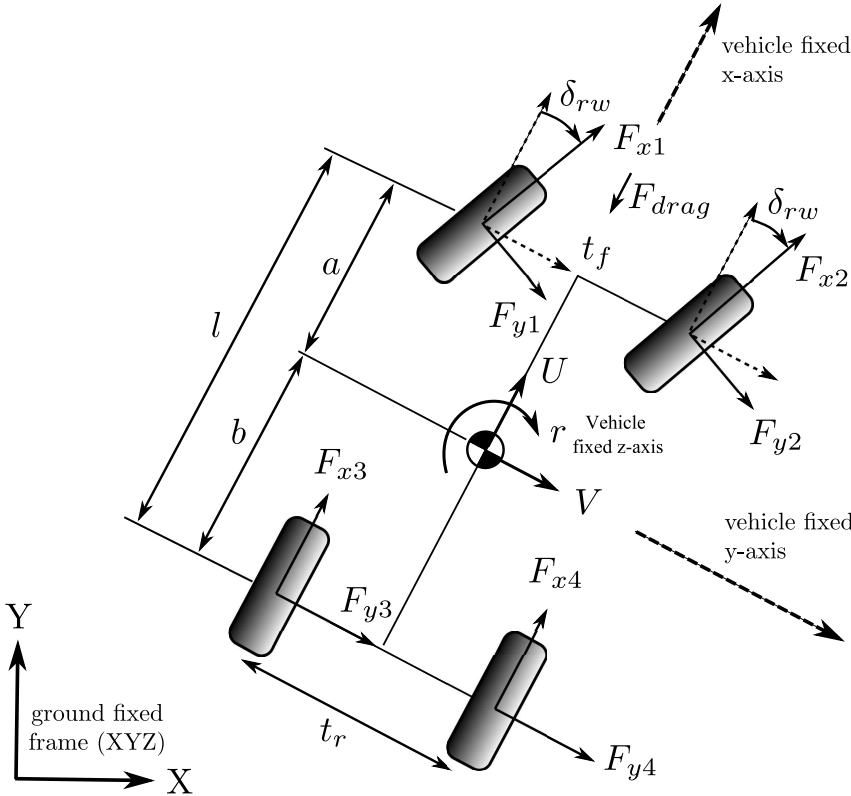


Figure 4.2: 3DOF planar model

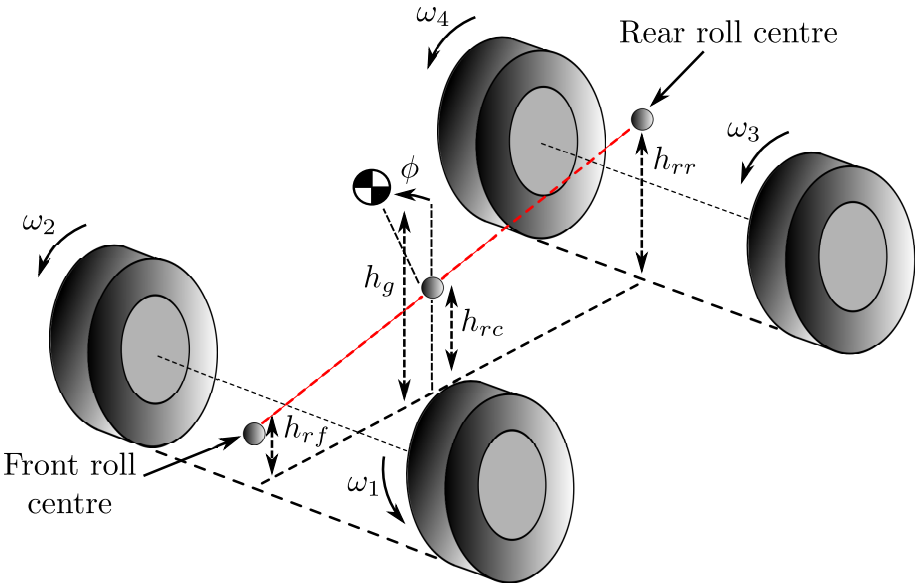


Figure 4.3: Load transfer roll model

4.1.2 Load Transfer

The vertical load on each tyre F_{zn} , is an important factor, since this is one of the parameters which determines ultimate force generation capability. The instantaneous load on each tyre is calculated from the initial static load distribution (F_{z0n}), in addition to load transfer from longitudinal (F_{zaxn}) and lateral accelerations (F_{zayn}), where:

$$F_{zn} = F_{z0n} + F_{zaxn} + F_{zayn} \quad (4.4)$$

For the longitudinal acceleration case, it is assumed that body pitch will be minimal in a stiffly sprung racing suspension, and that the vehicle can be treated as a lumped mass m , located at its CG. By taking moments about the tyre contact patches, the longitudinal load transfer at each wheel is given by:

$$F_{zaxn} = \frac{h_g m \dot{U}}{2l} \quad (4.5)$$

In the lateral case, load transfer is generated through the lateral acceleration of the vehicle body, and through migration of the CG through roll angle ϕ . This roll angle can be defined in terms of other vehicle parameters under steady state conditions [15], and thus is not included as an extra degree of freedom. The sprung and unsprung masses are lumped together in the analysis, in the form of the total vehicle mass m . The use of relative roll stiffness factors R_{sf} and R_{sr} , allow the load transfer to be apportioned between front and rear accordingly. The resultant front and rear lateral load transfer can then be expressed as:

$$F_{zayf} = \frac{U r m}{t_f} \left(\frac{b h_{rf}}{l} + R_{sf}(h_g - h_{rc}) \right) \quad (4.6)$$

$$F_{zayr} = \frac{U r m}{t_r} \left(\frac{a h_{rr}}{l} + R_{sr}(h_g - h_{rc}) \right) \quad (4.7)$$

where h_{rf} , h_{rr} are the front and rear roll centre heights, h_g the centre of gravity height and h_{rc} the roll centre height at the CG. The total resultant normal load on each tyre is calculated by summing Equations 4.5 - 4.7 in addition to the static wheel load:

$$F_{z1} = \frac{mgb}{2l} - \frac{h_g m \dot{U}}{2l} + \frac{U r m}{t_f} \left(\frac{b h_{rf}}{l} + R_{sf}(h_g - h_{rc}) \right) \quad (4.8)$$

$$F_{z2} = \frac{mgb}{2l} - \frac{h_g m \dot{U}}{2l} - \frac{U r m}{t_f} \left(\frac{b h_{rf}}{l} + R_{sf}(h_g - h_{rc}) \right) \quad (4.9)$$

$$F_{z3} = \frac{mga}{2l} + \frac{h_g m \dot{U}}{2l} + \frac{U r m}{t_r} \left(\frac{a h_{rr}}{l} + R_{sr}(h_g - h_{rc}) \right) \quad (4.10)$$

$$F_{z4} = \frac{mga}{2l} + \frac{h_g m \dot{U}}{2l} - \frac{U r m}{t_r} \left(\frac{a h_{rr}}{l} + R_{sr}(h_g - h_{rc}) \right) \quad (4.11)$$

For instances when high lateral and longitudinal load transfer causes an inside wheel to lift, the resulting tyre normal load defaults to ϵ where $\epsilon = 10^{-3}\text{N}$.

4.1.3 Engine

The torque supplied by the engine is generated from a two dimensional lookup table using both the engine speed ω_e , and a longitudinal control parameter u_{tb} , as its inputs. The torque curve characteristics are taken from a 2.0 litre turbo Touring Car engine. Since the influence of engine inertia on differential and driven wheel behaviour is significant in the lower gears, the equation of motion of the engine rotation is included in the analysis:

$$J_e \dot{\omega}_e = T_e - \frac{T_d}{G_r} \quad (4.12)$$

where J_e is the rotational inertia of the engine, T_e the torque generated at the engine crank, T_d the torque delivered to the differential and G_r the combined gearbox and final drive ratio. The engine rpm is calculated from the driven wheel speeds due to the kinematic constraint imposed by the differential. The engine speed can therefore be defined as:

$$\omega_e = G_r \frac{(\omega_1 + \omega_2)}{2} \quad (4.13)$$

Where ω_1 and ω_2 represent the driven (front) wheel speeds. As will be shown in Section 4.1.8, this constraint will be used to simplify the associated equations of motion for the driven wheels, thus removing the need for a dedicated engine DOF.

4.1.4 Gearbox

The total gear ratio is determined by a smoothed step function which changes gear based on vehicle speed. This allows the transition between gears to be modelled more efficiently and avoids the added model complexity from discrete changes in gear states. The total gear ratio is defined in Equation 4.14 by:

$$\begin{aligned} G_r = & G_{r1} + \\ & 1/2(G_{r2} - G_{r1})(1.0 + \sin(\tan^{-1}(10.0(U - U_{g1})))) + \\ & 1/2(G_{r3} - G_{r2})(1.0 + \sin(\tan^{-1}(10.0(U - U_{g2})))) + \dots \end{aligned} \quad (4.14)$$

where G_{rm} represents the total gear ratio in the m^{th} gear. Similarly U_{gm} , is the threshold vehicle speed to shift from the $(m-1)^{\text{th}}$ gear to the m^{th} gear. An example of the resulting function is shown in Figure 4.4.

4.1.5 Brakes

When the longitudinal control parameter, u_{tb} (which ranges from a maximum of 1 for acceleration, to -1 for maximum deceleration) turns negative, braking torques to front T_{bf} , and rear T_{br} axles are distributed with a constant brake balance B_f . These brake torques are split equally between left and right wheels. The total maximum brake

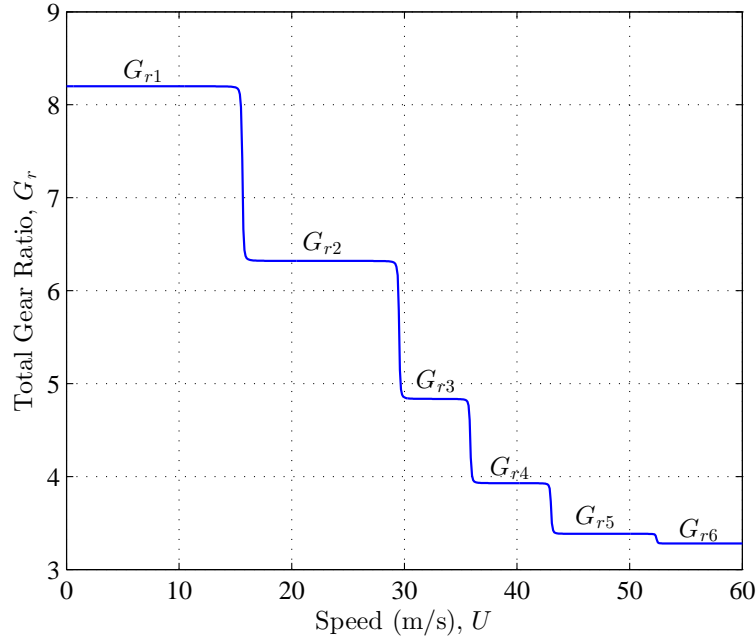


Figure 4.4: Total gear ratio function - example only

torque available is given by T_{bmax} such that:

$$\text{while } u_{tb} < 0 \quad T_{brake} = -u_{tb} T_{bmax} \quad (4.15)$$

$$T_{bf} = B_f T_{brake} \quad (4.16)$$

$$T_{br} = (1 - B_f) T_{brake} \quad (4.17)$$

4.1.6 Differential Operating States

The differential allows the distribution of engine torque to both the driven wheels and can be categorised into three states of operation: open, limited slip and locked. A schematic of a FWD transmission layout for a plate type limited slip differential is shown in Figure 4.5.

As described in Section 4.1.3, the effective rotational inertia of the engine when realised through the gearbox is significant in the lower gears. The resulting differential input torque T_d , can be expressed by the nominal engine torque T_e , less the torque associated with accelerating the engine inertia J_e . Rearranging Equation 4.12 for T_d yields:

$$T_d = T_e G_r - J_e \dot{\omega}_e G_r \quad (4.18)$$

and taking the first derivative of ω_e with respect to time in Equation 4.13 gives:

$$\dot{\omega}_e = G_r \frac{(\dot{\omega}_1 + \dot{\omega}_2)}{2} \quad (4.19)$$

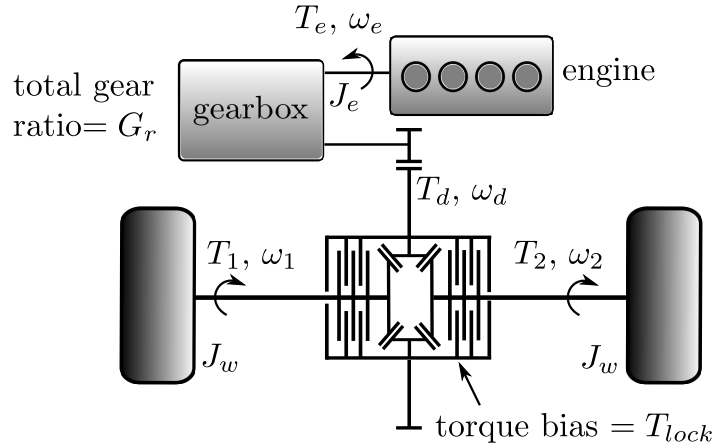


Figure 4.5: FWD gearbox layout schematic (plate type LSD case)

substituting into Equation 4.18 allows the removal of all $\dot{\omega}_e$ terms and yields the final expression for the differential input torque under acceleration:

$$T_d = T_e G_r - J_e G_r^2 \frac{(\dot{\omega}_1 + \dot{\omega}_2)}{2} \quad (4.20)$$

4.1.6.1 Open State

The fundamental limitation of the open differential is that engine torque must always be equally apportioned between each driven wheel and no torque biasing ability is present. The torque delivered to front left T_1 , and front right T_2 , wheels is therefore:

$$T_1 = T_2 = \frac{T_d}{2} \quad (4.21)$$

4.1.6.2 Limited Slip State

In the limited slip case, a torque bias is supported between the faster and slower rotating wheels. The torque delivered to each wheel can therefore be modified to:

$$T_1 = \frac{T_d}{2} - \Delta T \quad (4.22)$$

$$T_2 = \frac{T_d}{2} + \Delta T \quad (4.23)$$

Where ΔT is made up of an LSD bias torque T_{lock} , which can be generated by any of the torque or speed sensing LSD models described in Chapter 3. The direction of the torque transfer is controlled through the relative speed difference of the driven wheels such that:

$$\Delta T = \frac{1}{2} T_{lock} \text{sgn}(\omega_1 - \omega_2) \quad (4.24)$$

4.1.6.3 Locked State

When the differential is locked, both driven wheels are constrained to rotate together with input torque T_d . This is reflected in the equations of motion for a locked front axle (see Equation 4.31).

4.1.7 Plate/VCP Limited Slip and Locked Operation

Section 4.1.6 has defined three operating states for differentials - open, limited slip and locked. LSDs typically operate within limited slip and locked states for the majority of the time. The plate LSD model described in Section 3.1 is able to transition between these two states depending on a number of vehicle and environmental factors. If the bias torque which the LSD clutch can support is smaller than the torque generated by the difference in the two longitudinal tyre forces, the clutch will slip. If however, the bias torque is larger and the relative wheel speed difference is low (e.g. below a threshold of 0.1 rad/s or 0.95 rpm), then the differential will lock. This control logic is summarised more formally in Figure 4.6.

It should be noted that the speed sensing VC model presented in Section 3.5 cannot lock in the same way as a plate LSD. Visco-lok [33] devices which achieve this are available, but the locking method is less predictable than their plate LSD counterparts. The VC model presented here can only operate in limited slip mode, unless used as part of a VCP.

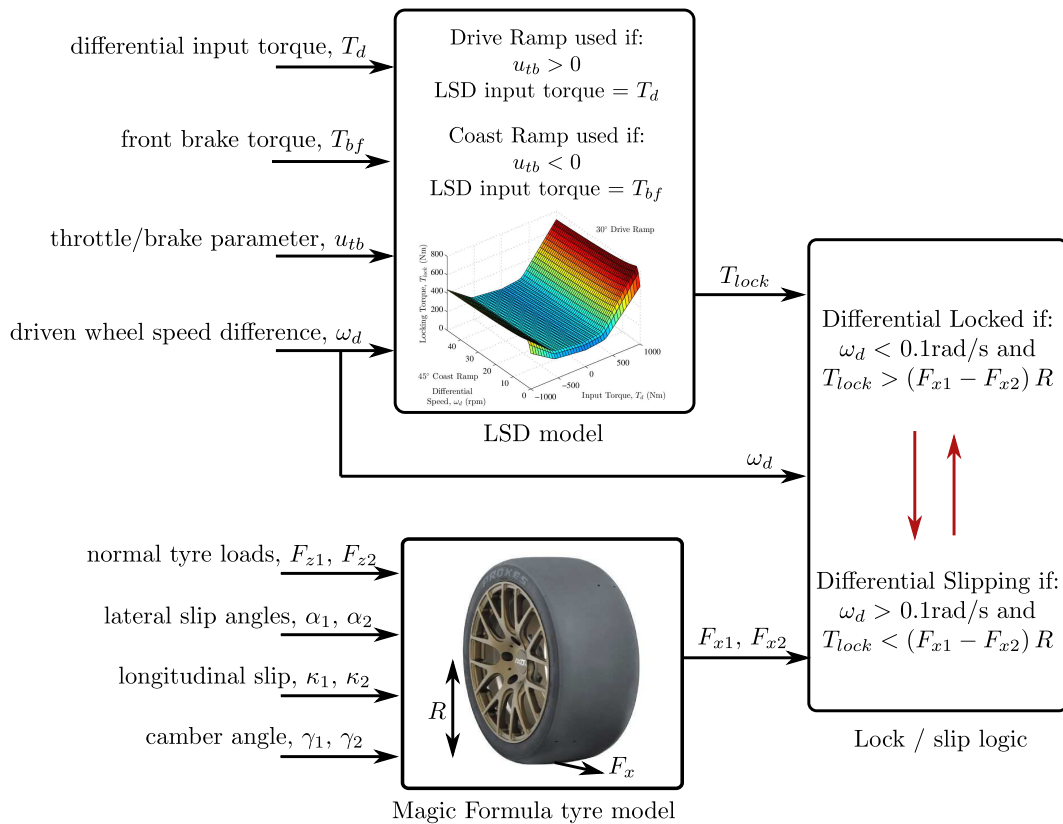


Figure 4.6: Schematic showing limited slip and locked states of plate LSD

4.1.8 Equations of Wheel Motion

Figure 4.7 shows the drive and braking forces acting on each wheel. The wheels are assumed to be a rigid disc with pure rotation and no lateral movement relative to the vehicle body.

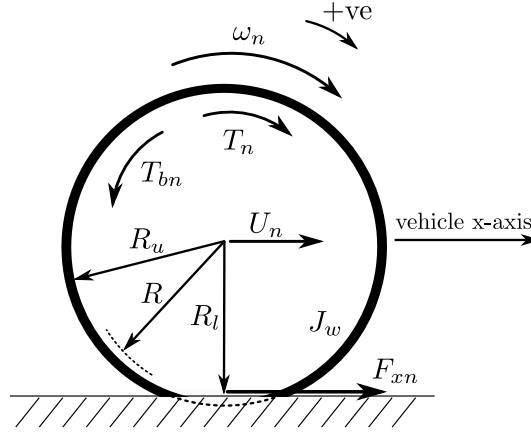


Figure 4.7: Wheel free body diagram

R represents the effective rolling wheel radius such that $R_l < R < R_u$, where R_l is the loaded radius and R_u the unloaded radius. Front and rear effective radii are defined as R_f and R_r , respectively. Evaluating moments acting on wheel inertia J_w , for open and limited slip states, the driven wheel equations of motion can be defined as:

$$J_w \dot{\omega}_1 = T_1 - F_{x1} R_f - T_{b1} \quad (4.25)$$

$$J_w \dot{\omega}_2 = T_2 - F_{x2} R_f - T_{b2} \quad (4.26)$$

where T_n is the drive torque from the engine, including any differential torque bias, T_{bn} the brake torque, and F_{xn} the longitudinal tyre force at each wheel. Substituting Equation 4.20 into 4.22 and 4.23 and then into Equations 4.25 and 4.26 yields:

$$J_w \dot{\omega}_1 = \frac{1}{2} T_e G_r - \Delta T - \frac{1}{4} J_e G_r^2 (\dot{\omega}_1 + \dot{\omega}_2) - F_{x1} R_f - T_{b1} \quad (4.27)$$

$$J_w \dot{\omega}_2 = \frac{1}{2} T_e G_r + \Delta T - \frac{1}{4} J_e G_r^2 (\dot{\omega}_1 + \dot{\omega}_2) - F_{x2} R_f - T_{b2} \quad (4.28)$$

Where in the case of an open differential, ΔT is equal to zero. On inspection, these equations are coupled since both contain $\dot{\omega}_1$ and $\dot{\omega}_2$ terms. Rearranging and solving for $\dot{\omega}_1$ and $\dot{\omega}_2$ gives:

$$\dot{\omega}_1 = \frac{(\frac{1}{2} T_e G_r - \Delta T - F_{x1} R_f - T_{b1})(J_w + \frac{1}{4} J_e G_r^2) - (\frac{1}{4} J_e G_r^2)(\frac{1}{2} T_e G_r + \Delta T - F_{x2} R_f - T_{b2})}{J_w^2 + \frac{1}{2} J_w J_e G_r^2} \quad (4.29)$$

$$\dot{\omega}_2 = \frac{(\frac{1}{2} T_e G_r + \Delta T - F_{x2} R_f - T_{b2})(J_w + \frac{1}{4} J_e G_r^2) - (\frac{1}{4} J_e G_r^2)(\frac{1}{2} T_e G_r - \Delta T - F_{x1} R_f - T_{b1})}{J_w^2 + \frac{1}{2} J_w J_e G_r^2} \quad (4.30)$$

In the locked differential state, these equations can be simplified using combined wheel inertias to give an equivalent equation of motion for the driven axle:

$$\dot{\omega}_a = \dot{\omega}_1 = \dot{\omega}_2 = \frac{(T_e G_r - F_{x2} R_f - F_{x1} R_f - T_{bf})}{2J_w + J_e G_r^2} \quad (4.31)$$

For the undriven rear wheels, where the driving torques T_3 and T_4 are equal to zero, Equations 4.25 and 4.26 can be reduced to take the form:

$$J_w \dot{\omega}_3 = -F_{x3} R_r - T_{b3} \quad (4.32)$$

$$J_w \dot{\omega}_4 = -F_{x4} R_r - T_{b4} \quad (4.33)$$

4.1.9 Tyre Model

Tyre forces are calculated with the Pacejka 1997 variant Magic Formula model [70]. This uses normal tyre load, slip angle, slip ratio and a static camber angle to generate the longitudinal and lateral tyre forces of a representative 235/610R17 Touring Car racing slick. The model relies on semi-empirical curve fitting coefficients, taken from a series of tests measuring tyres forces at various conditions of slip. Only an overview of the tyre force calculation will be given in this section. The interested reader is referred to Pacejka's full work [70]. Pure longitudinal F_{x0} and lateral F_{y0} forces are found using the traditional Magic Formula expressions:

$$F_{x0} = D_x \sin(C_x \arctan(B_x \kappa - E_x (B_x \kappa - \arctan(B_x \kappa)))) \quad (4.34)$$

$$F_{y0} = D_y \sin(C_y \arctan(B_y \alpha - E_y (B_y \alpha - \arctan(B_y \alpha)))) \quad (4.35)$$

where κ represents the longitudinal wheel slip and α the lateral slip angle (see Section 4.1.9.1). The associated B , C , D and E coefficients relate to the characteristics of the tyre force curve. These include the tyre's sensitivity to normal load, the initial slip stiffness and the shape of the curve after its peak. Example longitudinal and lateral tyre force curves at $F_z = 3, 4, 5,$ and 6kN are shown in Figures 4.8a-b.

Crucially, the model also calculates these tyre forces under combined slip conditions, due to the strong coupling between longitudinal and lateral tyre forces. The final components of tyre force F_x and F_y are defined by:

$$F_x = F_{x0} \cos(C_{x\alpha} \arctan(B_{x\alpha} \alpha)) \quad (4.36)$$

$$F_y = F_{y0} \cos(C_{y\kappa} \arctan(B_{y\kappa} \kappa)) \quad (4.37)$$

where the associated $C_{x\alpha}$, $C_{y\kappa}$, $B_{x\alpha}$, $B_{y\kappa}$ constants are calculated with a further set of Pacejka coefficients found experimentally. The coupling between longitudinal and lateral components is illustrated in Figures 4.9a-b. These use the modulus of F_x and F_y components ($|F_x + F_y|$) to demonstrate how the total tyre force varies as a function of slip ratio and slip angle.

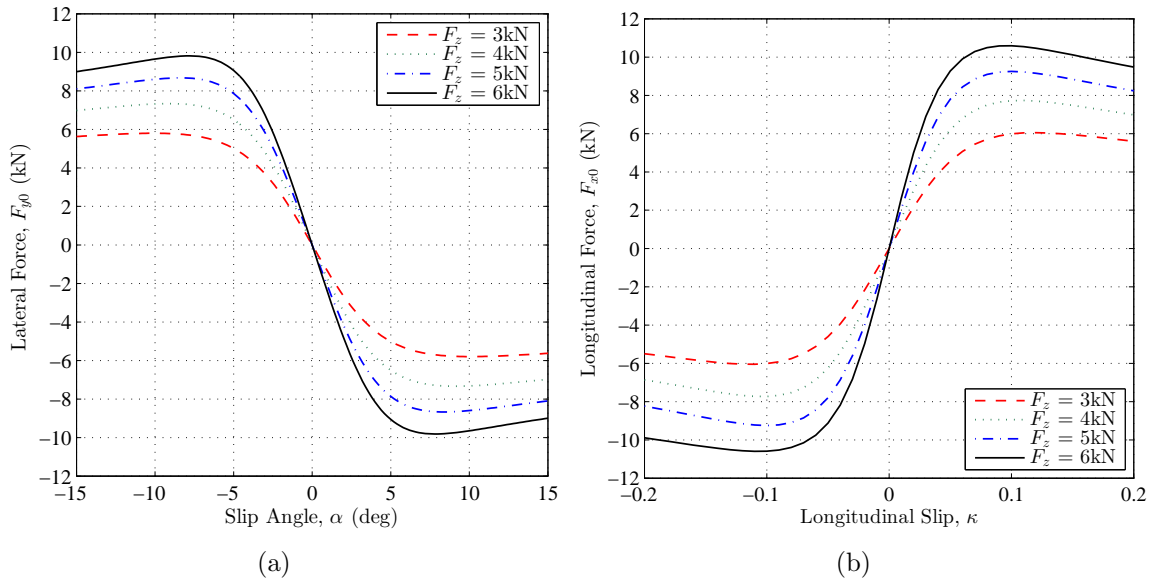


Figure 4.8: a) Pure lateral tyre force with slip angle at $F_z = 3, 4, 5$ and 6 kN
 b) pure longitudinal tyre force with longitudinal slip (235/610R17 racing slick)

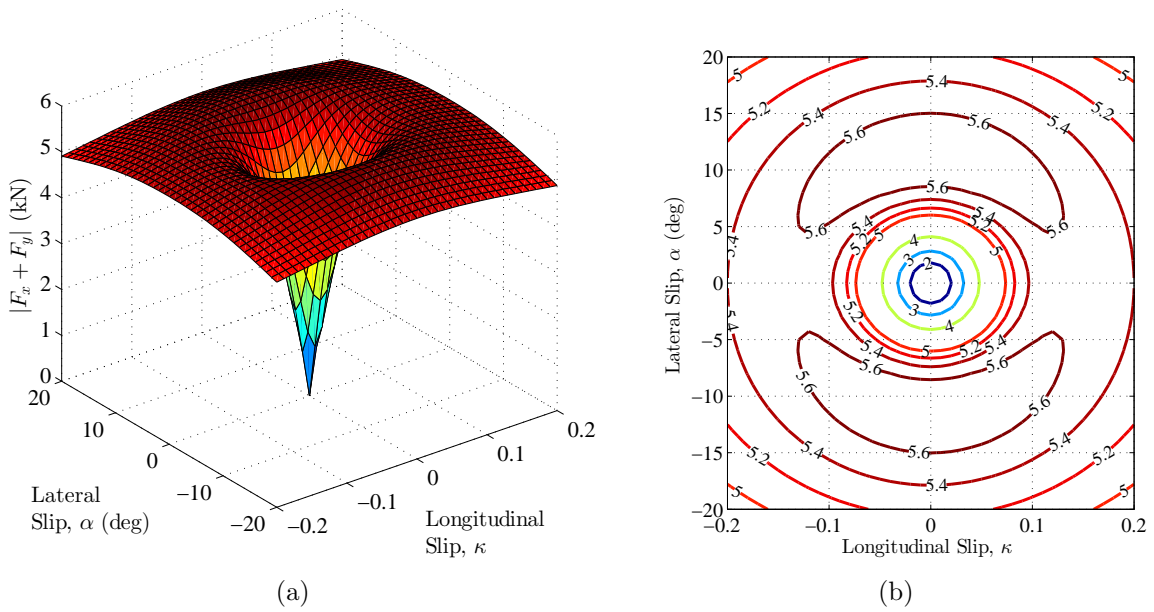


Figure 4.9: a) Modulus of total tyre force as function of slip angle and slip ratio
 b) contour plot showing lines of constant tyre force (235/610R17 racing slick)

4.1.9.1 Slip Angle and Slip Ratio Calculation

To evaluate slip quantities at each tyre, the longitudinal and lateral velocities at each respective wheel centre position are required. Longitudinal velocity is calculated by combining the velocity at the vehicle CG with the additional component due to yaw:

$$U_1 = U + r \left(\frac{t_f}{2} \right), \quad U_2 = U - r \left(\frac{t_f}{2} \right) \quad (4.38)$$

$$U_3 = U + r \left(\frac{t_r}{2} \right), \quad U_4 = U - r \left(\frac{t_r}{2} \right) \quad (4.39)$$

Similarly, the lateral velocity at the front and rear axles centres can be calculated using:

$$V_1 = V_2 = V + ar \quad (4.40)$$

$$V_3 = V_4 = V - br \quad (4.41)$$

Referring back to Figure 4.7, wheel centre longitudinal velocities U_n , can be used to calculate the slip ratio at each wheel:

$$\kappa_1 = \frac{U_1 - \omega_1 R_f}{U_1}, \quad \kappa_2 = \frac{U_2 - \omega_2 R_f}{U_2} \quad (4.42)$$

$$\kappa_3 = \frac{U_3 - \omega_3 R_r}{U_3}, \quad \kappa_4 = \frac{U_4 - \omega_4 R_r}{U_4} \quad (4.43)$$

And similarly, slip angles can be calculated by evaluating the proportion of longitudinal and lateral velocities, accounting for the front steer angle, δ_{rw} :

$$\alpha_1 = \arctan \frac{V_1}{U_1} - \delta_{rw}, \quad \alpha_2 = \arctan \frac{V_2}{U_2} - \delta_{rw} \quad (4.44)$$

$$\alpha_3 = \arctan \frac{V_3}{U_3}, \quad \alpha_4 = \arctan \frac{V_4}{U_4} \quad (4.45)$$

4.1.10 Aerodynamic Loads

A simple aerodynamic drag model is used, which gives the resistive force applied to counter the vehicle's longitudinal acceleration. No vertical downforce is considered since the magnitude of these forces are relatively small for a saloon racing vehicle of this type. The longitudinal drag force is therefore:

$$F_{drag} = \frac{1}{2} C_d \rho_a A_f U^2 \quad (4.46)$$

where C_d is the drag coefficient, ρ_a the air density and A_f the frontal vehicle area.

4.1.11 Driver Model

The steering and longitudinal control parameters can be controlled in a number of ways depending on the user requirements. The first, allows the user to describe a time history of both steering and throttle/brake inputs to evaluate the vehicle's open loop response. Perhaps of more use for the racing application, is the ability to compare control inputs when the vehicle is following a specified trajectory. In these instances, an optical lever preview steer model [15] was employed (see Figure 4.10), which uses a pre-defined path to generate proportional steering corrections based on errors in vehicle position e_i , and attitude angle e_ψ . These errors are summed and limited with saturation functions, to ensure the resulting steering gain is within realistic limits. Using the proportional attitude gain K_ψ , and positional gain K_i , the final road wheel angle can be described by:

$$\delta_{rw} = K_\psi e_\psi + \sum_{i=1}^p K_i e_i \quad (4.47)$$

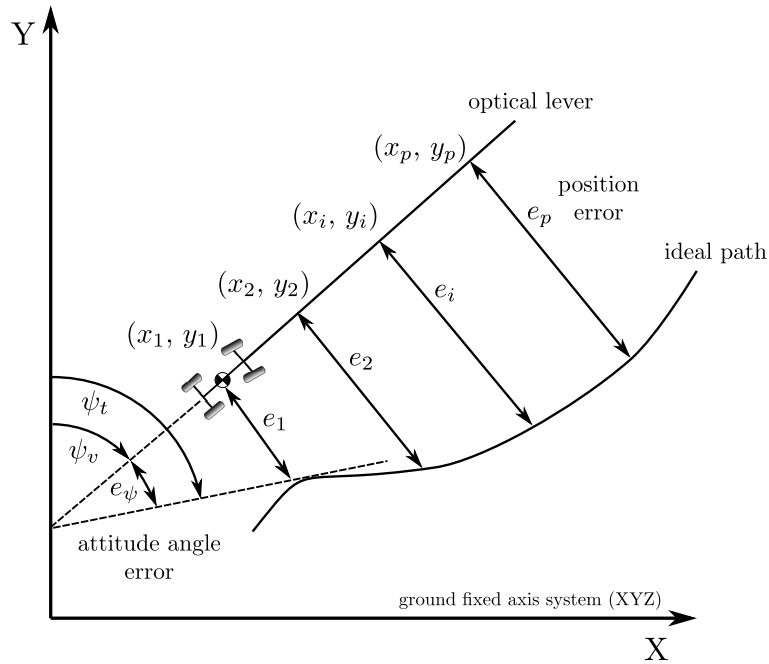


Figure 4.10: Preview steer driver model [92]

For further details, the model is described in full by Sharp [92]. The longitudinal throttle/brake parameter u_{tb} , is PI (Proportional Integral) controlled, used in conjunction with saturation functions generated from the longitudinal slip condition of each tyre. This effectively limits the control input under conditions in which the tyres have exceeded their optimum longitudinal slip ratio (i.e. slip at which peak longitudinal force is generated). This adds an additional degree of driver realism, allowing throttle and brake control inputs to 'back off' under extreme circumstances. The throttle/brake control parameter can therefore be described by:

$$u_{tb} = K_{vp} e_v + K_{vi} \int e_v dt \quad (4.48)$$

where K_{vp} and K_{vi} are the associated proportional and integral gains. e_v describes the error between the actual and target velocity multiplied by saturation functions generated from each tyre. The function $S_{n\kappa}$ can be defined for each wheel such that:

$$S_{n\kappa} = 0.5(\sin(\arctan(10(\kappa_n - \kappa_{nl})))) + 0.5 \quad (4.49)$$

where κ_{nl} is the maximum longitudinal slip that each tyre can support. The resulting velocity error can then be expressed in terms of its raw value e_{vr} , and Equation 4.49:

$$e_v = e_{vr} \prod_{n=1..4} S_{n\kappa} \quad (4.50)$$

4.2 Vehicle Model Verification

In order to verify that the vehicle model was functioning without error and replicated realistic behaviour, lap data from a FWD BTCC (British Touring Car Championship) vehicle was used as a basis. The following sections detail the reconstruction of the racing line and a simulated lap replay. Two very different plate LSD configurations are then validated in the parent vehicle system.

4.2.1 Racing Line Reconstruction

Since GPS path data was unavailable, the racing line was reconstructed from lateral acceleration and speed data. This method, previously described by Casanova [15], considers the vehicle a point mass at its CG and ignores the effect of any vehicle side slip. This is a reasonable assumption when side slip angles are typically below 5-6°, which is generally the case for non-rally type racing vehicles [19]. The resulting track curvature k_t , and path radius r_t , can be described by the expression:

$$k_t = \frac{1}{r_t} \approx \frac{a_y}{U^2} \quad (4.51)$$

where a_y is the vehicle lateral acceleration and U , the longitudinal velocity component. The vehicle speed history is taken from on-board hall-effect speed sensors measuring the rotation of each of the wheels. The speed sensor trigger wheel generated 50 pulses per revolution and was logged at rate of 40Hz for each wheel. As a more robust means of measurement, only the highest undriven wheel speed is used, to avoid the effects of wheelspin under heavy acceleration and lock-up under heavy braking. The resulting profile is then filtered using a Chebyshev type II low pass filter. This particular filter was chosen since the transition to its stopband is more marked than other filter types (e.g. Butterworth). This was found to be better suited at eliminating noise, but maintaining signal accuracy when there were sharp changes in speed (e.g. under heavy braking at speed). The speed profile of a qualifying lap around the Snetterton 300 circuit is shown in Figure 4.11, and the resulting path trajectory in Figure 4.12. The calculated lap distance (4.8km) is within 5% of official figures, measured around the centreline of the circuit. This error is obviously open to variations in the racing line, but gives some indication as to the accuracy of the racing line reconstruction process. The generated

racing line is overlaid with the track boundaries between turns 1-7 and 9-10 in Figures 4.13 and 4.14.

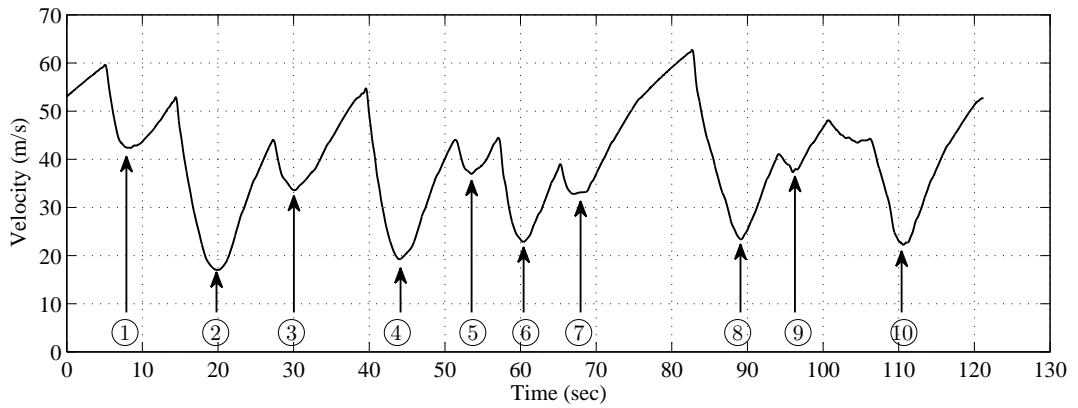


Figure 4.11: Snetterton 300 longitudinal velocity profile

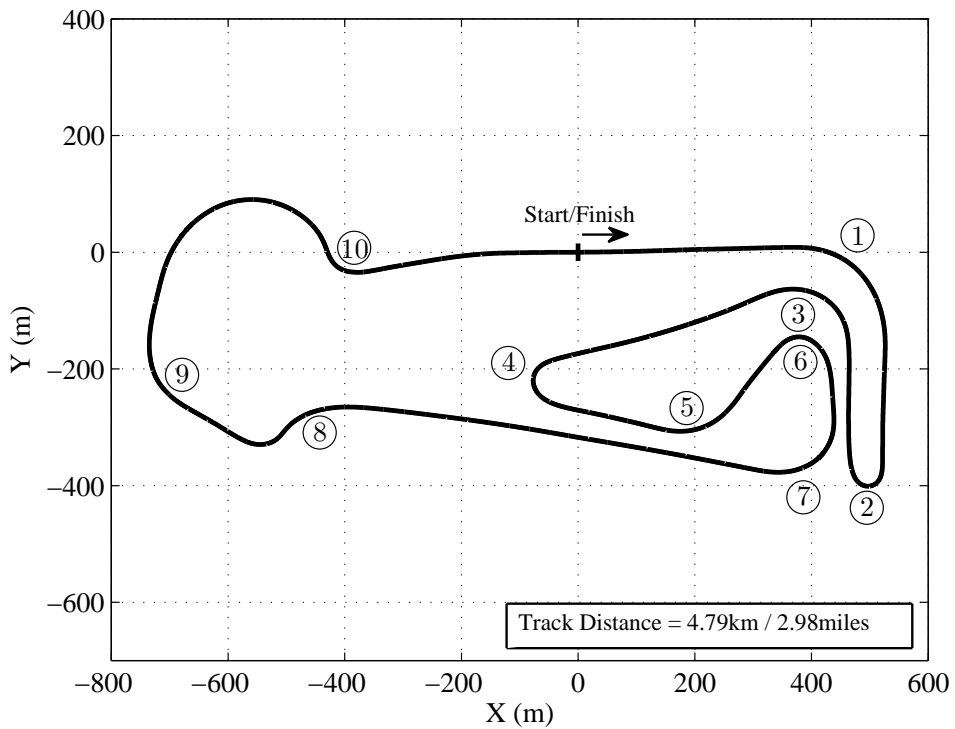


Figure 4.12: Snetterton 300 racing line reconstruction

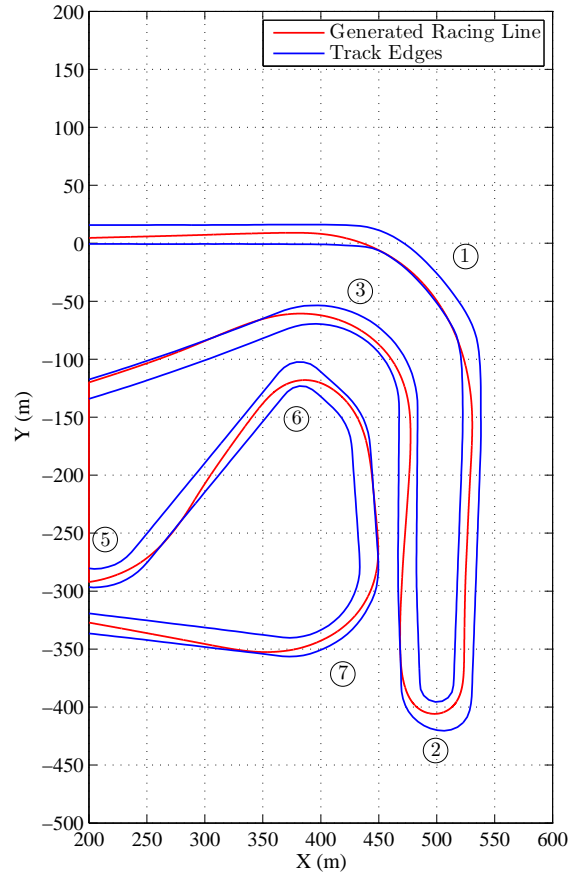


Figure 4.13: Snetterton 300 racing line reconstruction - turns 1-3, 5-7

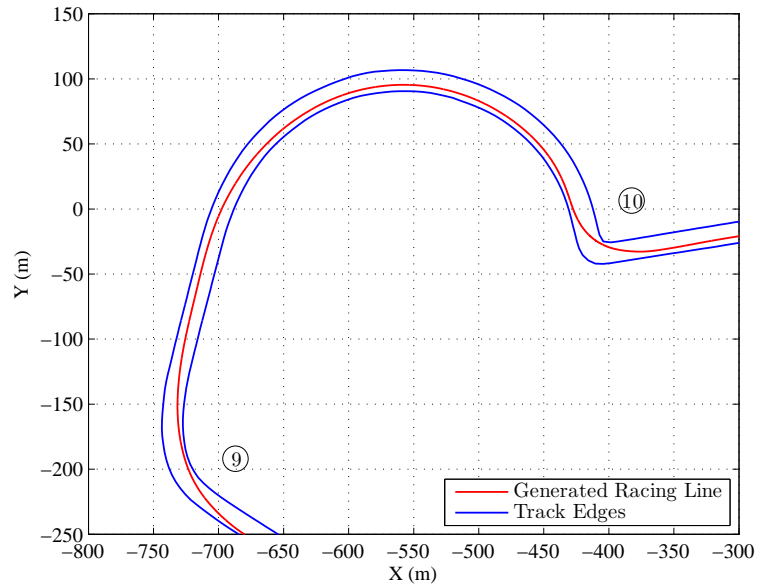


Figure 4.14: Snetterton 300 racing line reconstruction - turns 9-10

4.2.2 Lap Replay

Both the speed history and racing line reconstruction were used in combination with the driver model described in Section 4.1.11. These acted as targets for the model to follow with its respective throttle/brake and steering controllers. In effect, a simulated lap replay was conducted to determine whether the model was capable of replicating differences in differential behaviour and if the performance window of the vehicle was representative. Figures 4.15 and 4.16 show the vehicle accelerations and speed throughout the lap distance. The difference between the target and simulated vehicle speed is small (see Figure 4.16), equating to a total root mean square (RMS) error of 1.08m/s over the duration of the lap. The RMS path error (see e_1 in Figure 4.10) was 0.16m. The reader should note that small errors between simulated and actual vehicle speed and acceleration are to be expected since these are effectively modelling inputs.

Figure 4.17 depicts the time histories of steering wheel angle, throttle and brake variables. In this case, throttle data has been normalised between 0 and 1 and similarly, an average of the front and rear brake line pressures have been normalised between 0 and -1. In general, they again show a good level of agreement. The differences between traces can be accounted for by a number of the simplifying modelling assumptions. The track is assumed to be flat, with no camber, and with a constant coefficient of friction at all points along the racing line. Perhaps most significantly, local grip variations between corners will exist, which starts to push the limits of these assumptions. The grip that the tyres can support also varies with tyre carcass temperature and the number of heat cycles the tyres have previously seen [47]. In practice, this makes accurate assessment of tyre forces extremely difficult, without costly tyre slip sensors [10]. This is likely to contribute to the variation in steering trace error, which is shown to change throughout the lap distance.

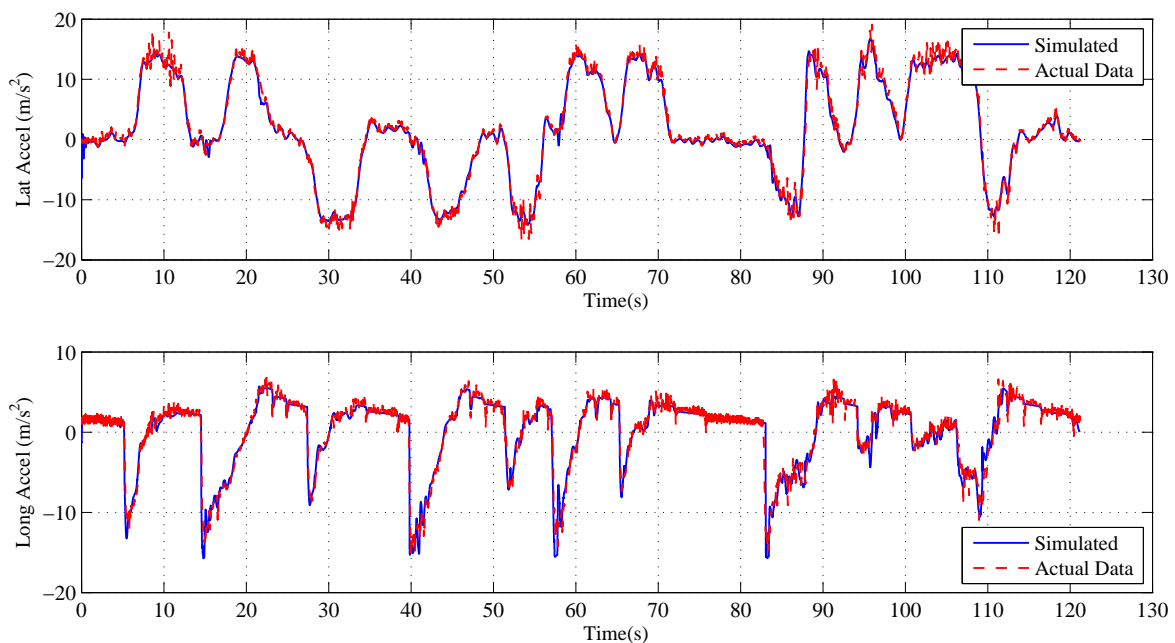


Figure 4.15: Comparison of simulated and actual lateral (top) and longitudinal (bottom) acceleration data

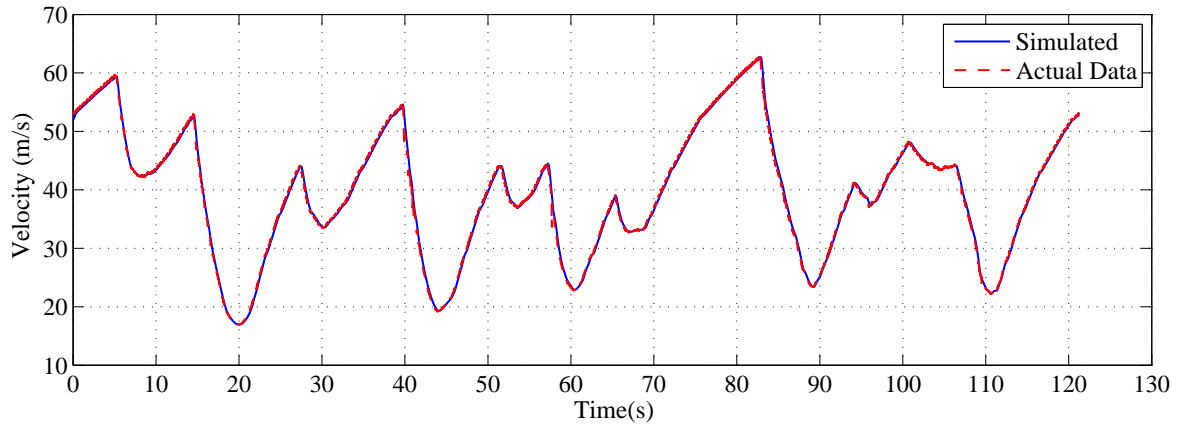


Figure 4.16: Actual and simulated longitudinal velocity profiles, RMS error = 1.08m/s

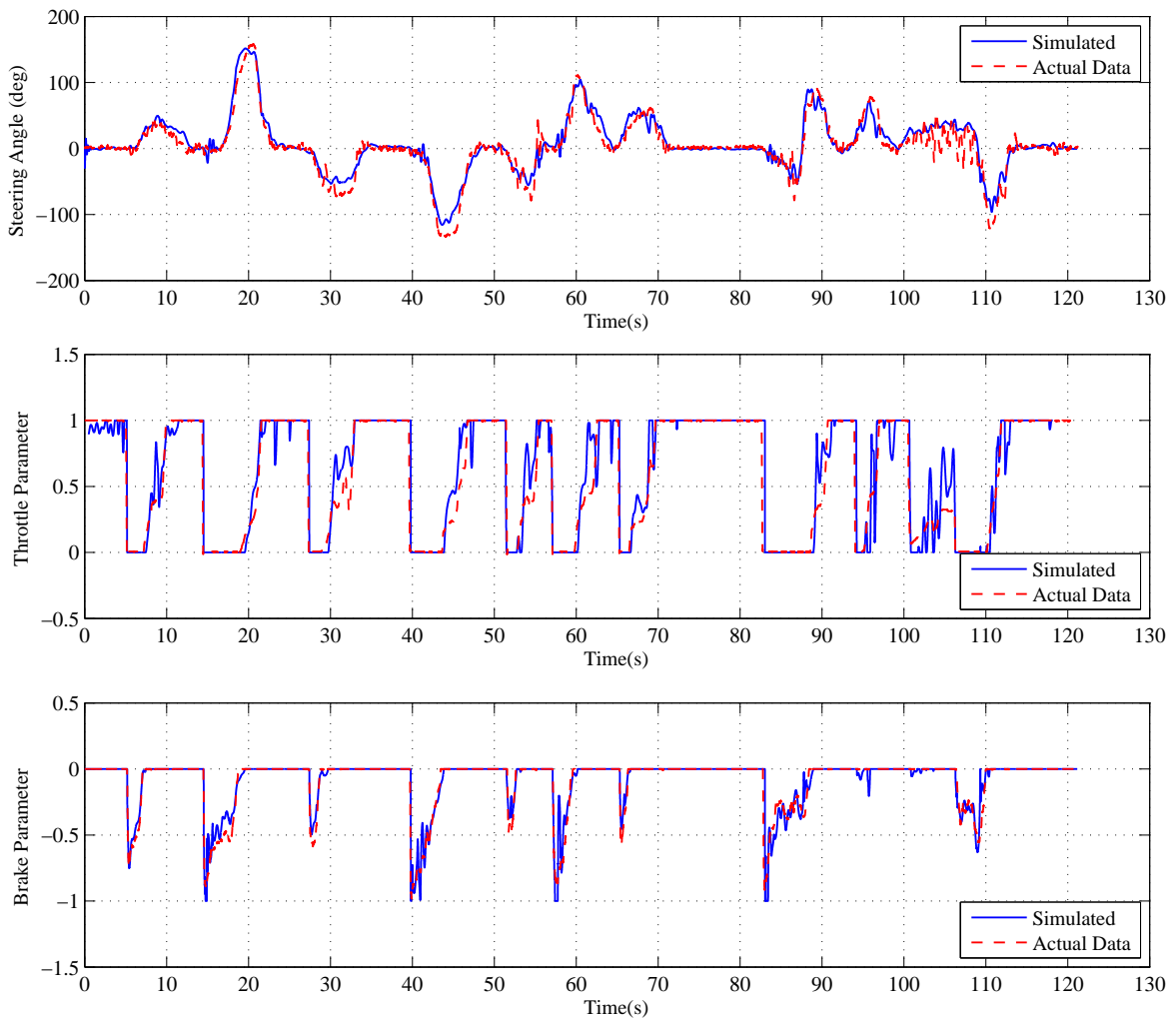


Figure 4.17: Steering wheel angle - road wheel angle \times 15:1 rack ratio (top), throttle (middle) and brake (bottom) histories

4.2.3 Differential Validation

The vehicle model was shown to replicate the performance window of the real vehicle over a lap distance. Of crucial importance however, is the ability of the model to detect changes in differential behaviour. As a result, two further laps of data were used to validate two opposing differential strategies. The two plate LSD configurations considered are described in Table 4.1.

Table 4.1: Plate differential parameters - Setup 1

Parameter	Symbol	Setup 1	Setup 2
Drive ramp angle	θ_{rd}	60°	30°
Coast ramp angle	θ_{rc}	45°	75°
Number of friction faces	z_f	12	12
Static positive preload	T_{pp}	165Nm	165Nm
Drive negative preload	T_{np}	0Nm	0Nm

The intent was to represent the two extremes of LSD operation. Setup 1 is a more benign configuration on drive, governed by the higher 60° ramp angle developing a relatively small torque bias. Setup 2 is more aggressive under acceleration, with a lower 30° drive ramp developing much higher levels of locking and encouraging the LSD to lock more readily. In general, Setup 1 should act more like an open differential and Setup 2, more like a locked differential.

The ideal metric for differential validation is measurement of the torque transmitted to each of the driven wheels. This gives a direct evaluation of the torque bias generated by the differential. While measurement systems that achieve this are available, they are costly to implement and were not available during the track tests conducted. The methodology adopted here, was to use the driven wheel speed traces, and more specifically, the driven wheel speed difference. While this cannot give any information as to the differential torque bias itself, it is a more practical marker of the differential's mode of operation (locked or slipping). The point at which the differential locks or starts to slip is a function of the differential locking torque and the instantaneous longitudinal tyre forces that the driven wheels can transmit. If the locking history of the differential is within acceptable levels, this must mean tyre grip levels and differential torque bias are accurate enough to replicate realistic LSD behaviour.

Figures 4.18 and 4.19 show the resulting driven wheel speed difference for the two setups considered. Figure 4.18 demonstrates the more open nature of Setup 1, as the vehicle spends more time with a non-zero wheel speed difference. This manifests itself as corner exit wheelspin, as the more open LSD limits the vehicle longitudinal acceleration. This is also illustrated in Figures 4.20 and 4.21, which categorise the percentage of lap time spent at a particular wheel speed difference. The more open behaviour of Setup 1 has resulted in 63% of the lap spent between -0.5 and +0.5 rad/s. Contrast this with Setup 2, which spends over 75% of the lap in this region, and it is clear that Setup 2 has encouraged the LSD to lock much more readily. The reader should note that the discrepancy at 40s in Figure 4.19 was due

to the vehicle running over a kerb and locking up the inside driven wheel under braking.

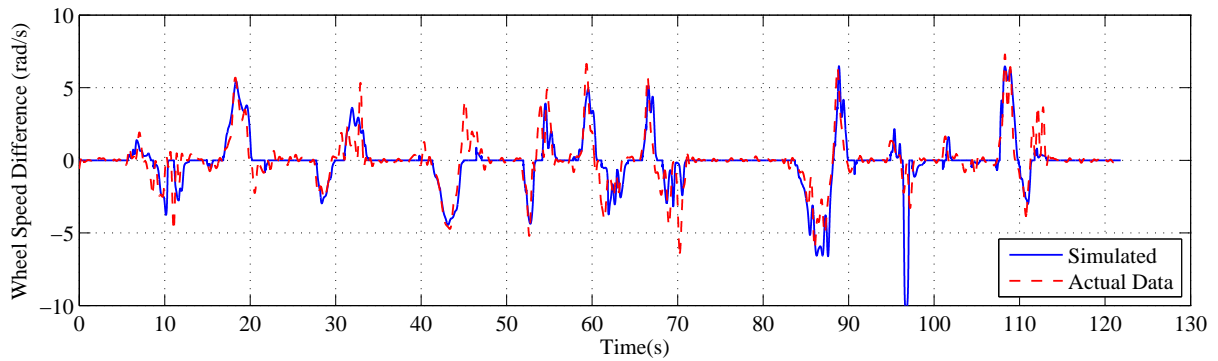


Figure 4.18: Differential Setup 1 - driven wheel speed difference

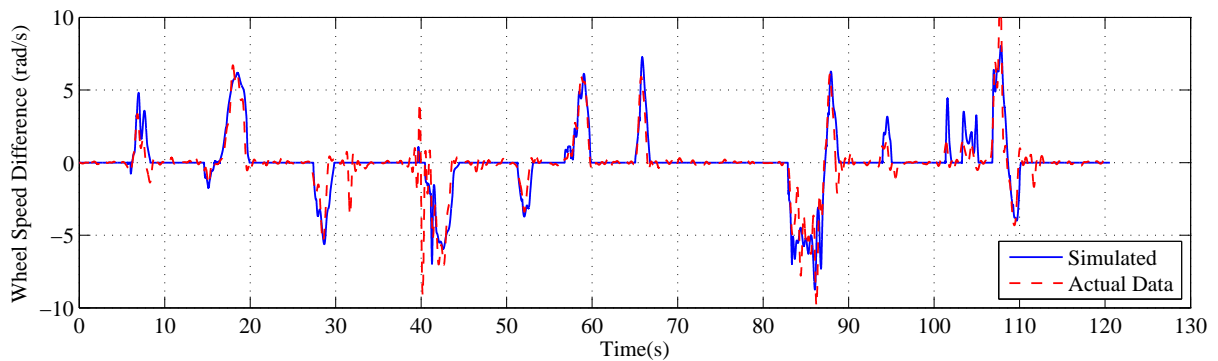


Figure 4.19: Differential Setup 2 - driven wheel speed difference

To analyse the torque bias throughout the lap, it is convenient to plot the (simulated) transmitted torque to the left and right hand driven wheels. The results are shown in Figures 4.22 and 4.23. Any point that lies away from the ‘open differential line’ represents a torque bias in either the drive or coast region. Again, it is clear that Setup 2 is able to support more torque bias under acceleration, since a larger proportion of the drive region is covered (see Figure 4.23). Conversely, under coast conditions where one would expect more torque bias from Setup 1 (due to the larger 45° ramps angle), very little difference is seen between configurations. A potential explanation for this is that the majority of braking is carried out in a straight line, with the LSD in a locked state. With equal brake torques applied to each wheel, the force capability of each tyre is likely to be very similar and thus the resultant torque ratio between both, very close to unity.

In summary, the model correlated well with driven wheel speed difference data, with the simulation replicating locking characteristics over a number of high and low speed corners. As in the vehicle model case, there are differences at particular corners due to localised changes in track friction and the resultant error in tyre force calculation. Overall, validation against the two datasets has shown that the differential model is capable of demonstrating realistic differences in LSD behaviour and is suitable for comparative analysis of LSD configuration changes.

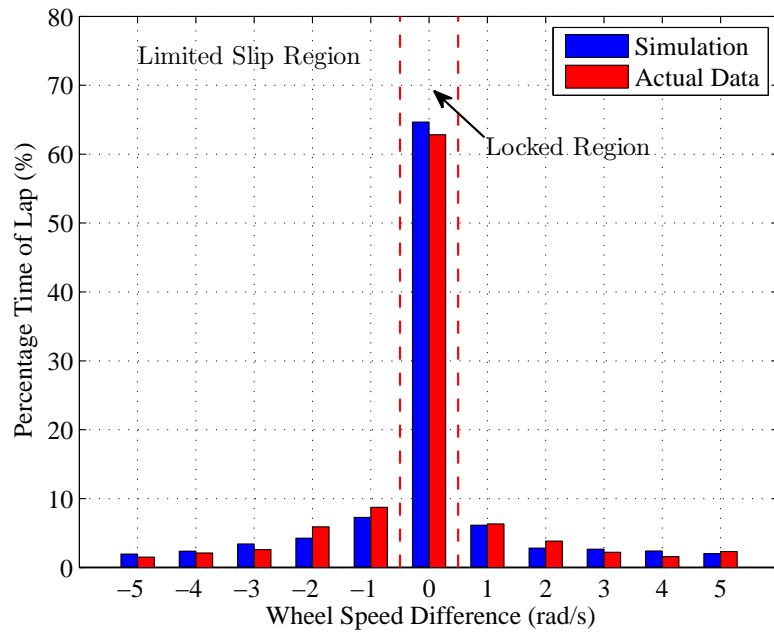


Figure 4.20: Differential Setup 1 - percentage lap time vs driven wheel speed difference

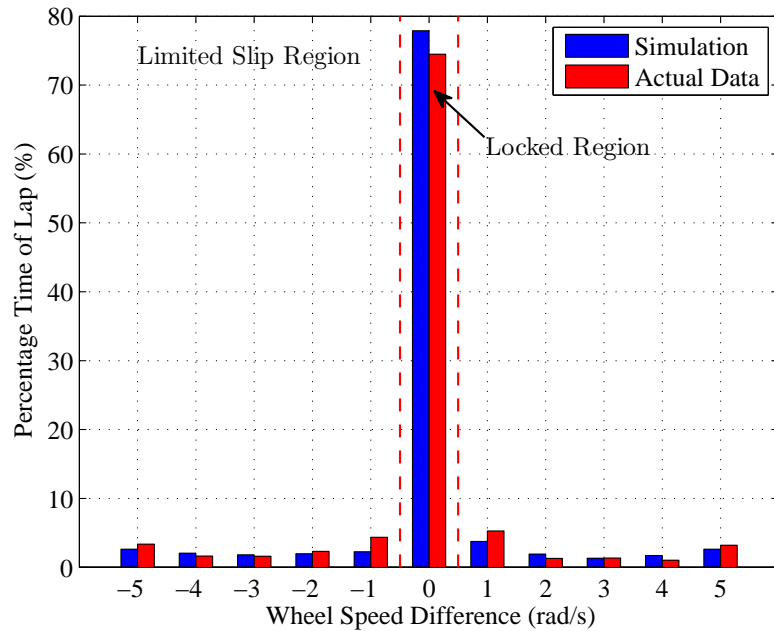


Figure 4.21: Differential Setup 2 - percentage lap time vs driven wheel speed difference

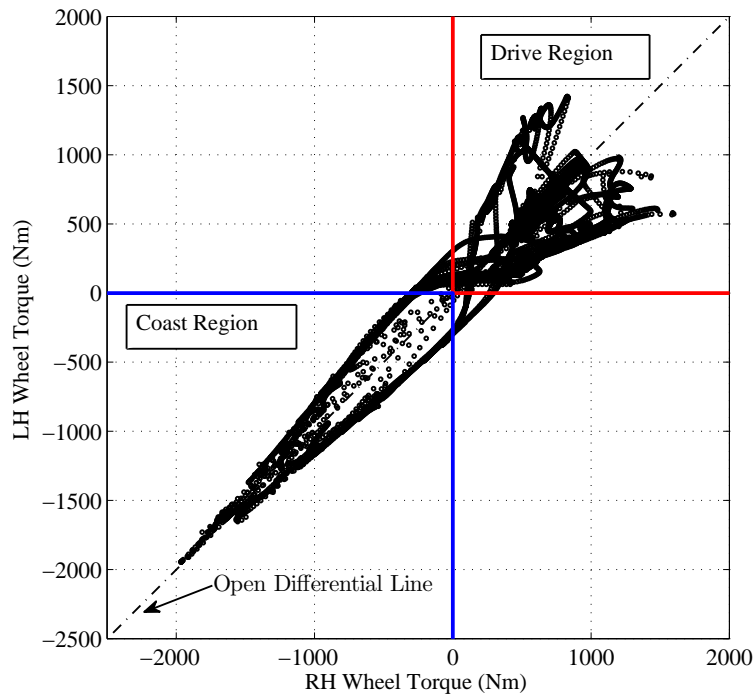


Figure 4.22: Differential Setup 1 - transmitted wheel torque (simulation only)

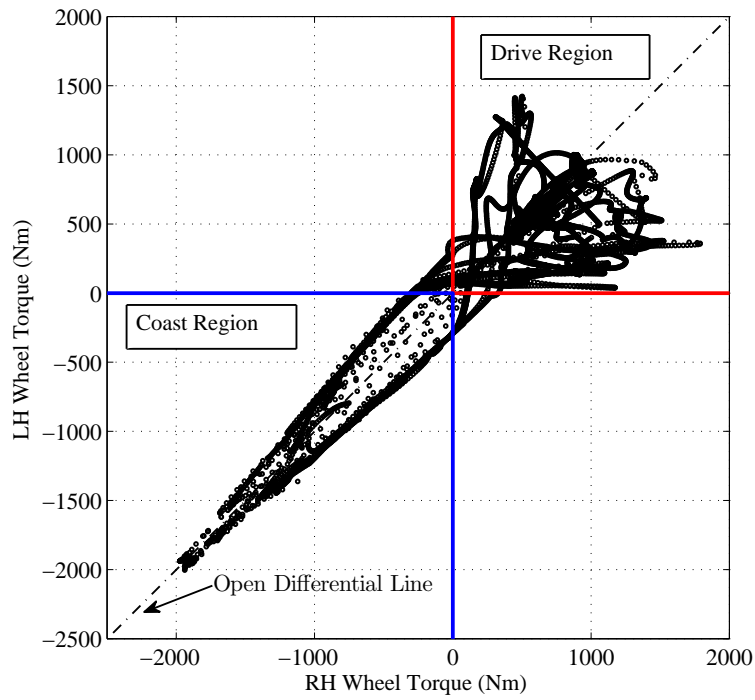


Figure 4.23: Differential Setup 2 - transmitted wheel torque (simulation only)

4.3 Conclusions

In this chapter, a 7DOF nonlinear vehicle model constructed in the Matlab/Simulink environment has been presented. Qualifying lap data around the Snetterton 300 circuit allowed a representative racing line for a FWD saloon racing vehicle to be generated. This was used in combination with velocity and steering controllers to validate both vehicle and LSD models. This validation process demonstrated that the resulting control histories and vehicle accelerations correlated well with measured track data. Furthermore, the highly transient lock/unlock behaviour of a plate type LSD was also validated against differential wheel speed throughout the duration of the lap. Two very different plate LSD parameter sets both gave good correlation with the measured wheel speed difference. This illustrated that the interaction of environmental factors (e.g longitudinal tyres forces) which influence differential behaviour have been captured. Overall, the validation process has shown that vehicle and differential models are capable of predicting differences in LSD behaviour and shall be used as the basis of further comparative analysis in subsequent chapters.

Chapter 5

QSS Time Optimal Solutions

In this chapter, the influence of LSD setup parameters are investigated with the use of a time optimal QSS GG diagram method. This is used to carry out a number of parametric investigations, to give insight into those configurations which yield the quickest lap time around a typical racing circuit. The LSD torque bias is then included in the optimisation process itself, to provide a more efficient way of finding optimal torque bias profiles. This is developed into a robust method for finding the optimal setup parameters of a typical torque sensing clutch plate LSD. Finally, a novel passive LSD device is proposed, which is more able to replicate optimal torque bias characteristics than existing hardware. Due to increased availability of experimental vehicle data for validation purposes, previous chapters have considered a FWD vehicle. For the remainder of this thesis however, investigations are confined to the RWD case, since this is more applicable to the vast majority of racing vehicles.

5.1 Generating the GG Diagram

The GG diagram is an established tool for demonstrating the vehicle performance limits [8, 10, 62] and provides an intuitive framework to quantify the influence of any vehicle setup changes. It characterises the maximum longitudinal and lateral acceleration capability of the vehicle and can be reproduced at a range of vehicle speeds. An increase in the GG envelope indicates that there is potential to reduce an associated lap time, the magnitude of which, will depend on the track configuration and its specific combination of low to high speed corners.

The GG envelope has traditionally been generated under quasi steady state conditions, in which yaw and side slip accelerations (\dot{r} , \dot{V}) are neglected, and a constant longitudinal acceleration (\dot{U}) is assumed. It is important to note that all current methods aim to predict purely the open loop performance limits of the vehicle, not the driver's ability to use them. In the context of this work, the method proposed by Blasco-Figueroa and Brayshaw [8, 10] is used as a basis, with the addition of revised constraints for increased robustness and more comprehensive LSD models. The generation and maximisation of the GG envelope can be transformed into a nonlinear constrained optimisation problem,

which for the general case, can be described by [68]:

$$\text{maximise } y = f(\mathbf{x}) \quad \text{for } \mathbf{x} \in \mathbb{R}^n \quad (5.1)$$

$$\text{subject to } c_i(\mathbf{x}) = 0, \quad i = 1, \dots, p_e \quad (5.2)$$

$$c_i(\mathbf{x}) \leq 0, \quad i = p_e + 1, \dots, p_i \quad (5.3)$$

where $f(\mathbf{x})$ is the objective function, $c_i(\mathbf{x}) = 0$, $i = 1, \dots, p_e$, the equality constraints and $c_i(\mathbf{x}) \leq 0$, $i = p_e + 1, \dots, p_i$, the inequality constraints. In this GG diagram approach, the objective function takes multiple forms depending on which region of the GG envelope is being generated. Figure 5.1 depicts a typical GG contour and the points where the objective function switches between maximising longitudinal acceleration (\dot{U}) in the straight-ahead case (points A and B), and maximising lateral acceleration (U_r), in the combined longitudinal and lateral acceleration case (point C).

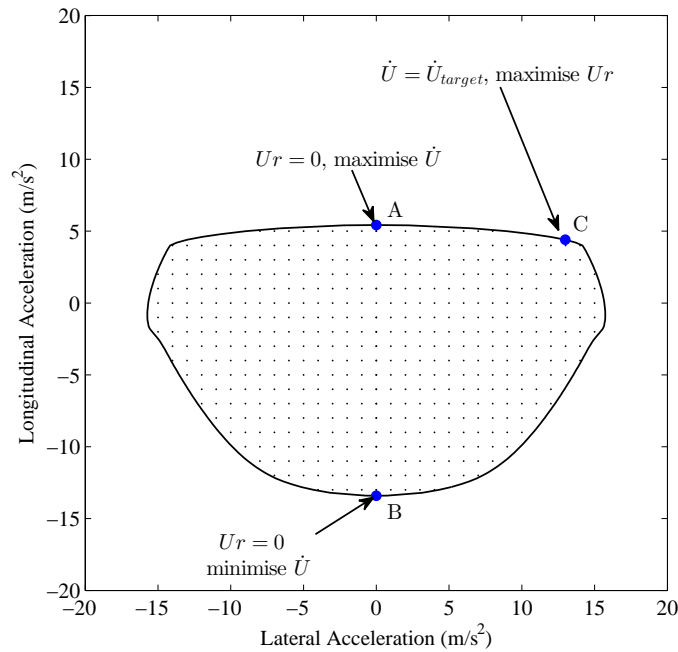


Figure 5.1: GG acceleration envelope example

In the pure longitudinal case (points A & B), the state vector can be represented by those parameters which influence only longitudinal tyre forces, namely front and rear axle speeds (ω_f , ω_r), and a throttle/brake parameter, u_{tb} .

$$\text{state vector } \mathbf{x} = [\omega_f, \omega_r, u_{tb}]^T \quad (5.4)$$

The objective function is simply to maximise the longitudinal acceleration under both driving and braking conditions:

$$\text{maximise } f(\mathbf{x}) = \dot{U} \quad (\text{driving conditions}) \quad (5.5)$$

$$\text{minimise } f(\mathbf{x}) = \dot{U} \quad (\text{braking conditions}) \quad (5.6)$$

The resultant pure longitudinal acceleration points can be found at a range of target speeds (U_{target}) throughout the vehicle operating range. This then allows an array of acceleration points (\dot{U}_{target}), ranging from the longitudinal extremes, to be used in evaluating the maximum lateral acceleration possible at each of these points. In this combined lateral case (point C), the state vector is extended to include those terms which also influence lateral tyre forces. Steer angle (δ_{rw}), side slip velocity (V), yaw rate (r) and individual wheel speeds ($\omega_{1..4}$) are therefore added to the state vector:

$$\text{state vector } \mathbf{x} = [\delta_{rw}, \omega_1, \omega_2, \omega_3, \omega_4, u_{tb}, V, r]^T \quad (5.7)$$

The objective function is now to maximise lateral acceleration, which in the QSS case, where $\dot{V} = 0$ is simply:

$$\text{maximise } f(\mathbf{x}) = Ur \quad (5.8)$$

The state vector variables used in the longitudinal and combined acceleration cases of the optimisation are summarised in Table 5.1. Those terms which can be changed by the optimiser are checked, whilst those that are known are defined with the appropriate constants.

Table 5.1: GG optimisation state vector variables

Parameter	Unit	Symbol	Point A,B	Point C
Steer Angle	rad	δ_{rw}	0	✓
FL Wheel Speed	rad/s	ω_1	✓	✓
FR Wheel Speed	rad/s	ω_2	$= \omega_1 = \omega_f$	✓
RL Wheel Speed	rad/s	ω_3	✓	✓
RR Wheel Speed	rad/s	ω_4	$= \omega_3 = \omega_r$	✓
Throttle/Brake	-	u_{tb}	✓	✓
Side Slip Velocity	m/s	V	0	✓
Side Slip Acceleration	m/s ²	\dot{V}	0	0
Yaw Rate	rad/s	r	0	✓
Yaw Acceleration	rad/s ²	\dot{r}	0	0
Long Velocity	m/s	U	U_{target}	U_{target}
Long Acceleration	m/s ²	\dot{U}	✓	\dot{U}_{target}

At each stage of the optimisation the objective function is subject to the equality and inequality constraints defined by:

$$c_{eq}(\mathbf{x}) = \begin{bmatrix} \dot{V} \\ \dot{r} \\ \dot{U} - \dot{U}_{target} \\ \dot{\omega}_1 U_1 - \omega_1 \dot{U} \\ \dot{\omega}_2 U_2 - \omega_2 \dot{U} \\ \dot{\omega}_3 U_3 - \omega_3 \dot{U} \\ \dot{\omega}_4 U_4 - \omega_4 \dot{U} \end{bmatrix} = 0, \quad c_{ineq}(\mathbf{x}) = \begin{bmatrix} \omega_e - \omega_{emax} \\ \alpha_1 - \alpha_{1max} \\ \alpha_3 - \alpha_{2max} \\ \beta - \beta_{max} \\ F_{zmin} - F_{z2} \\ F_{zmin} - F_{z4} \end{bmatrix} \leq 0 \quad (5.9)$$

The first three elements of the equality constraint c_{eq} , enforce QSS conditions. Practically speaking, this means manipulating the state variables until the vehicle equations of motion balance (see Equations 4.1 - 4.3). In a similar manner, the last four constraints impose equilibrium conditions on each of the wheels (see Equations 4.25, 4.26, 4.32, 4.33). These are derived by considering the longitudinal slip ratio κ_n of each wheel, where:

$$\kappa_n = \frac{R_{f,r}\omega_n - U_n}{U_n} \quad (5.10)$$

and assuming that under QSS conditions, the rate of change of longitudinal wheel slip will be small:

$$\frac{d}{dt}\kappa_n \approx 0 \text{ for } n = 1...4 \quad (5.11)$$

U_n represents the longitudinal velocity component at each corner of the vehicle (see Equations 4.38 - 4.39). Differentiating with respect to time, Equations 5.10 and 5.11 can be simplified to give each wheel equilibrium constraint:

$$\dot{\omega}_n U_n - \omega_n \dot{U} = 0 \quad (5.12)$$

The inequality constraint c_{ineq} , imposes limits on the maximum engine rpm ω_{emax} , and the peak slip angle α_{nmax} , that the more dominant outside tyres can reach. The Magic Formula [69] tyre model allowed this maximum slip angle to be recalculated at each optimisation point, to account for combined slip and vertical tyre load influences. A limit on the maximum side slip angle β_{max} , was also used to prevent the optimiser from considering solutions which were highly unstable. Lastly, the inside tyres were constrained to have a minimum vertical load F_{zmin} , to prevent unwanted tyre lifting.

In practice, the highly nonlinear objective and constraint functions must be solved iteratively, to establish a search direction at each major iteration. Modern state-of-the-art computer methods have focused on solution of the KKT conditions (see Section 1.3.2.2) to provide an efficient way of achieving this. If the problem is convex, the KKT conditions are both necessary and sufficient for a global minimum to be found. In this case however, the problem is not convex and as a result, second order derivatives of the Lagrangian function (called the Hessian) are required. For a minima to occur, the

Hessian matrix must be positive definite at the solution point.

For this research, a Sequential Quadratic Programming (SQP)[68] algorithm was implemented using the nonlinear constrained optimisation solver *fmincon*, in Matlab [60]. An overview of the algorithm is included below, but the interested reader is referred to Chapter 18 of Wright [68] for a more detailed description.

- i) *Stage 1* - supply a feasible state vector \mathbf{x}_k , at iteration $k = 0$.
- ii) *Stage 2* - calculate/update the Hessian matrix \mathbf{H}_k of the Lagrangian function

$$\mathbf{H}_k = \nabla^2 \mathcal{L}(\mathbf{x}_k, \lambda_k) \quad (5.13)$$

- iii) *Stage 3* - form a quadratic approximation of the objective function:

$$q_k(\mathbf{d}) = \frac{1}{2} \mathbf{d}^T \mathbf{H}_k \mathbf{d} + \mathbf{d}^T \nabla f(\mathbf{x}_k) \quad (5.14)$$

subject to the linearised constraints:

$$\nabla c_i(\mathbf{x}_k)^T \mathbf{d} + c_i(\mathbf{x}_k) = 0, \quad i = 1, \dots, p_e \quad (5.15)$$

$$\nabla c_i(\mathbf{x}_k)^T \mathbf{d} + c_i(\mathbf{x}_k) \leq 0, \quad i = p_e + 1, \dots, p_i \quad (5.16)$$

- iv) *Stage 4* - solve the quadratic sub-problem for the search direction \mathbf{d} .
- v) *Stage 5* - perform a line search to find the scalar step length parameter α_k , such that:

$$f(\mathbf{x}_k + \alpha_k \mathbf{d}) < f(\mathbf{x}_k) \quad (5.17)$$

- vi) *Stage 6* - check to see if KKT conditions have been met. If not, update the value of $k \rightarrow k + 1$ and repeat from Stage 2 until converged.

In the Matlab optimisation toolbox, the gradients of the objective and constraint functions are typically evaluated using finite difference approximations [60]. Due to the truncation errors associated with omitting the higher order Taylor series terms [79], errors will be introduced into the optimisation process. Combined with the round-off errors relating to floating point number machine precision, this combined error is significant enough to influence solution accuracy, or in some cases, prevent convergence altogether. To limit these errors, an Algorithmic Differentiation (AD) toolbox [29] was used to compute derivatives. This relies on successive application of the chain rule, to break down complex expressions into simpler arithmetic operations, which can be differentiated symbolically. This process allows the truncation errors to be avoided, with accuracy reliant only on the machine precision.

5.2 Initial Results

The plate LSD configuration in Table 3.1 and vehicle parameters from a RWD Touring Car (see Appendix D) were used to generate the example GG map shown in Figure 5.2. With minimal downforce effects from a saloon vehicle of this type, positive acceleration capability is seen to reduce with speed. This is due to the increase in drag as the vehicle becomes power limited. This also explains the small increase in braking ability with speed, and why peak lateral accelerations lie below the zero longitudinal acceleration line. As one might expect, peak lateral acceleration diminishes with speed, since longitudinal tyre forces are greater at higher speeds, thus reducing maximum lateral force capability.

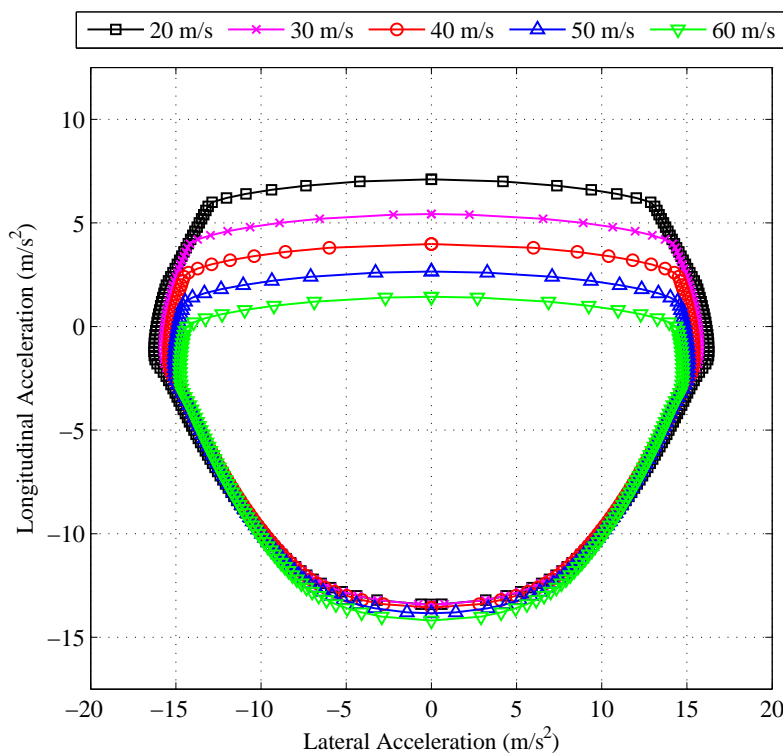


Figure 5.2: GG diagram for RWD Touring Car

To assess the impact of LSDs on ultimate performance, the two extremes of operation are considered first. Figure 5.3 shows a comparison between the GG maps of the same RWD vehicle fitted with open and fully locked differentials. The comparison clearly demonstrates the advantage that the locked differential gives. At lower speeds (Figures 5.3a-b), the envelope is larger in all areas. Under positive accelerations, where the vehicle is traction limited (excess engine torque is able to overcome available tyre grip), the locked device improves the overall tractive effort of the driven axle. In doing so, this prevents the inner unloaded wheel from spinning up and becoming super saturated. This also gives a small increase in the lateral force capability of the axle, increasing peak lateral acceleration from 14.45 to 14.5m/s^2 . The envelope is larger under negative, braking accelerations for a similar reason. Under these conditions, the locked axle has prevented the inner wheel from locking under braking. This has increased the associated lateral force capability of the axle and the resulting GG area.

The pattern at higher speeds is similar, but with a marked difference. This is most apparent at 60m/s (see Figures 5.3e-f), where again the GG envelope is larger in most regions apart from those nearing peak lateral acceleration. Here, the locked differential is shown to have a lower lateral acceleration peak (13.4m/s² compared to 13.67 m/s² for the open differential). This is also the case at 40 and 50m/s (see Figures 5.3c-d), although to a lesser extent. Since the driven wheels are constrained to rotate at the same speed (as in the locked case), the magnitude of longitudinal slip ratios of inner and outer tyres are higher than the equivalent open differential. This can be related more practically to the additional tyre ‘scrub’ that is known to occur with any locked device [62]. Although greatly improving traction, a small amount of lateral force capability has been sacrificed at higher speeds.

The difference in GG contours has been treated more formally in Table 5.2 which summarises the GG map area of each configuration. This reinforces the findings and shows the performance gain of the locked device is less significant at higher speeds.

Table 5.2: Area of constant velocity GG contours (open-locked comparison)

Speed (m/s)	Open (baseline) area (m/s ²) ²	Locked area (m/s ²) ²	Difference (%)
20	372.43	485.99	+23.36
30	340.69	433.79	+21.46
40	314.11	394.76	+20.43
50	292.20	366.21	+20.21
60	272.60	342.99	+20.52

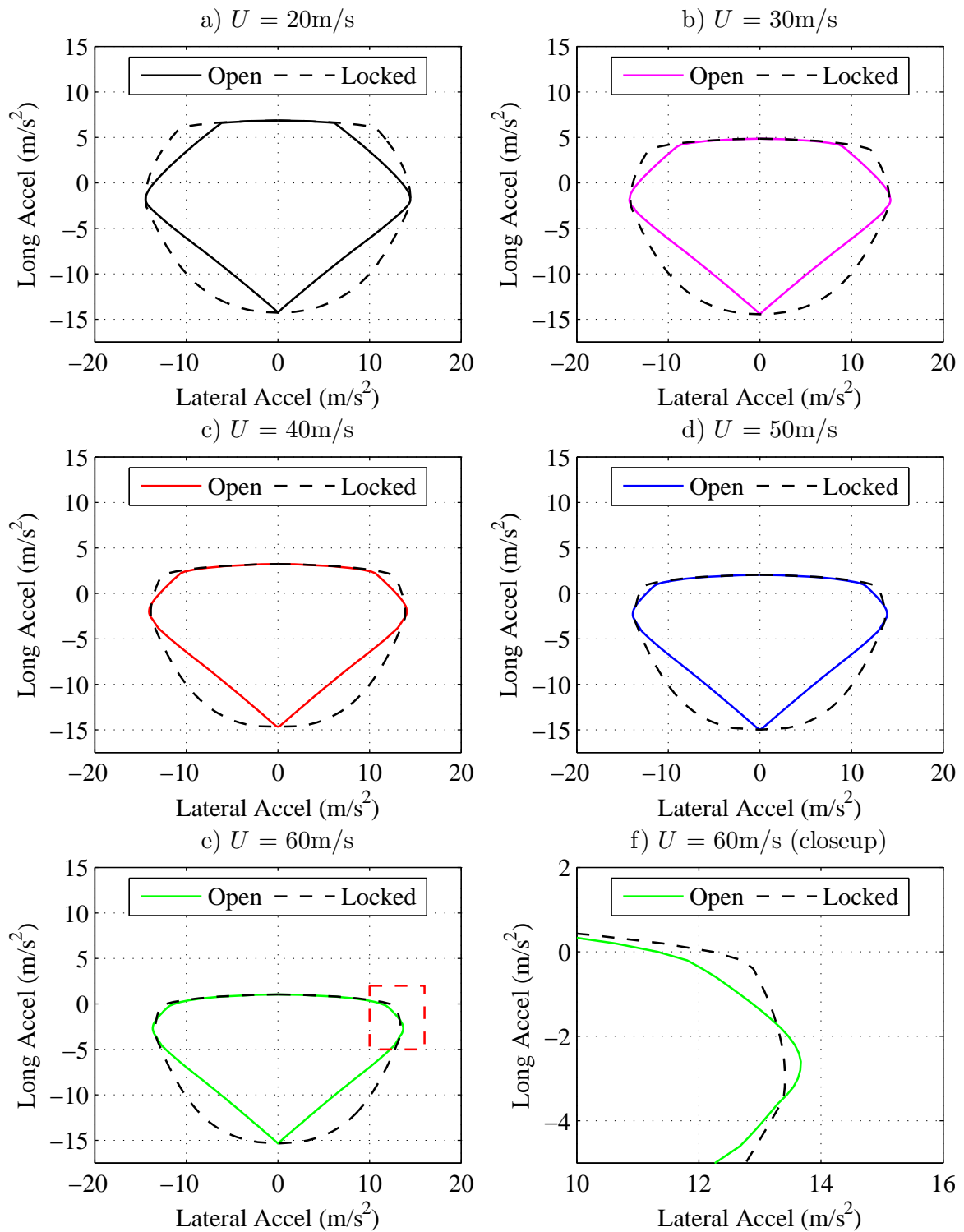


Figure 5.3: GG envelope for open and locked differentials

5.3 Generating the Time Optimal Solution

Blasco-Figueroa [8] describes a method in which these GG profiles can be used as the basis of a lap simulation program, to predict minimum lap time and vehicle parameter time histories. The method relies on interpolating between GG profiles at discrete path curvature points around the lap. A more detailed description of the method is included in Section 1.3.1 and in the work of Brayshaw [10] and Kelly [47]. Using Equation 4.51 the curvature profile of the Snetterton 300 circuit has been generated using lateral acceleration and speed data from a RWD saloon racing vehicle (see Section 4.2.1 and Appendix D for vehicle parameters). This racing line is obviously open to variation due to driving style, but it is assumed that driver-to-driver differences are small. In this work, the apex points of the circuit are derived from the corresponding velocity profile of the vehicle track data. The specific distance at which the minimum speed points occur are overlaid with the calculated curvature in Figure 5.4. The predicted

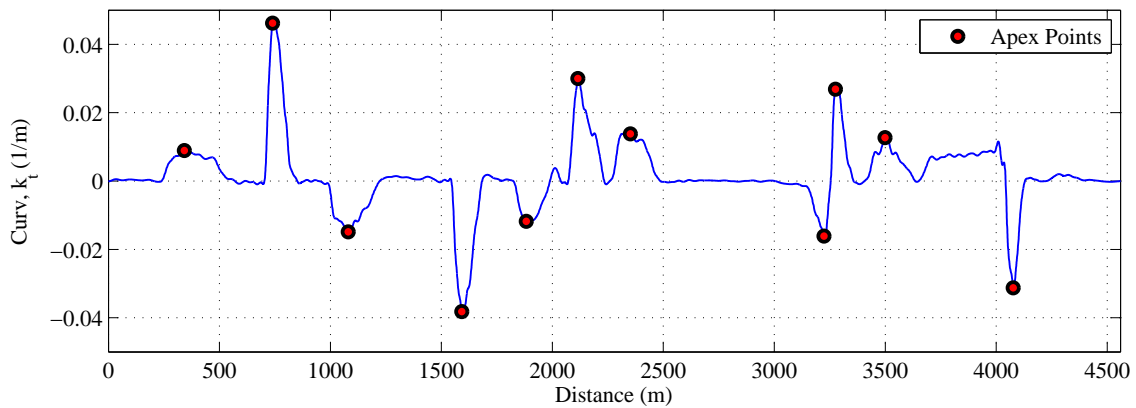


Figure 5.4: Snetterton 300 apex points

speed of the vehicle at each of these apex points is found by assuming that the vehicle has reached its peak lateral acceleration (i.e. no longitudinal acceleration component) at this point. By interpolating between GG profiles, the time histories for speed, longitudinal and lateral acceleration can be generated and used to determine the associated lap time. This has been carried out for the RWD saloon racing vehicle considered here and overlaid with the measured vehicle data in Figure 5.5. The plate LSD parameters detailed in Table 3.1 were used in this analysis, but with 80Nm positive preload, 0Nm negative preload and 16 friction faces. It should also be noted that although every effort was made to use representative tyre data (see Section 4.1.9), both longitudinal and lateral tyre forces were scaled by -5% to replicate on-track friction levels more closely.

In general the correlation is good, but the QSS simulation is shown to over estimate the braking phases of the lap. This may be attributable to one of the inherent assumptions of the QSS method, which allows the vehicle to brake right up to the apex of the corner. In reality, a driver may want to carry out the majority of braking before turning into the corner to avoid instability. This is reflected in the QSS lap time (see Table 5.3) which is some 1.3s quicker than the recorded lap time.

Table 5.3: QSS lap time comparison

	Actual	QSS Simulation	Difference (s)
Lap Time (s)	119.900	118.596	-1.304 (1.09%)

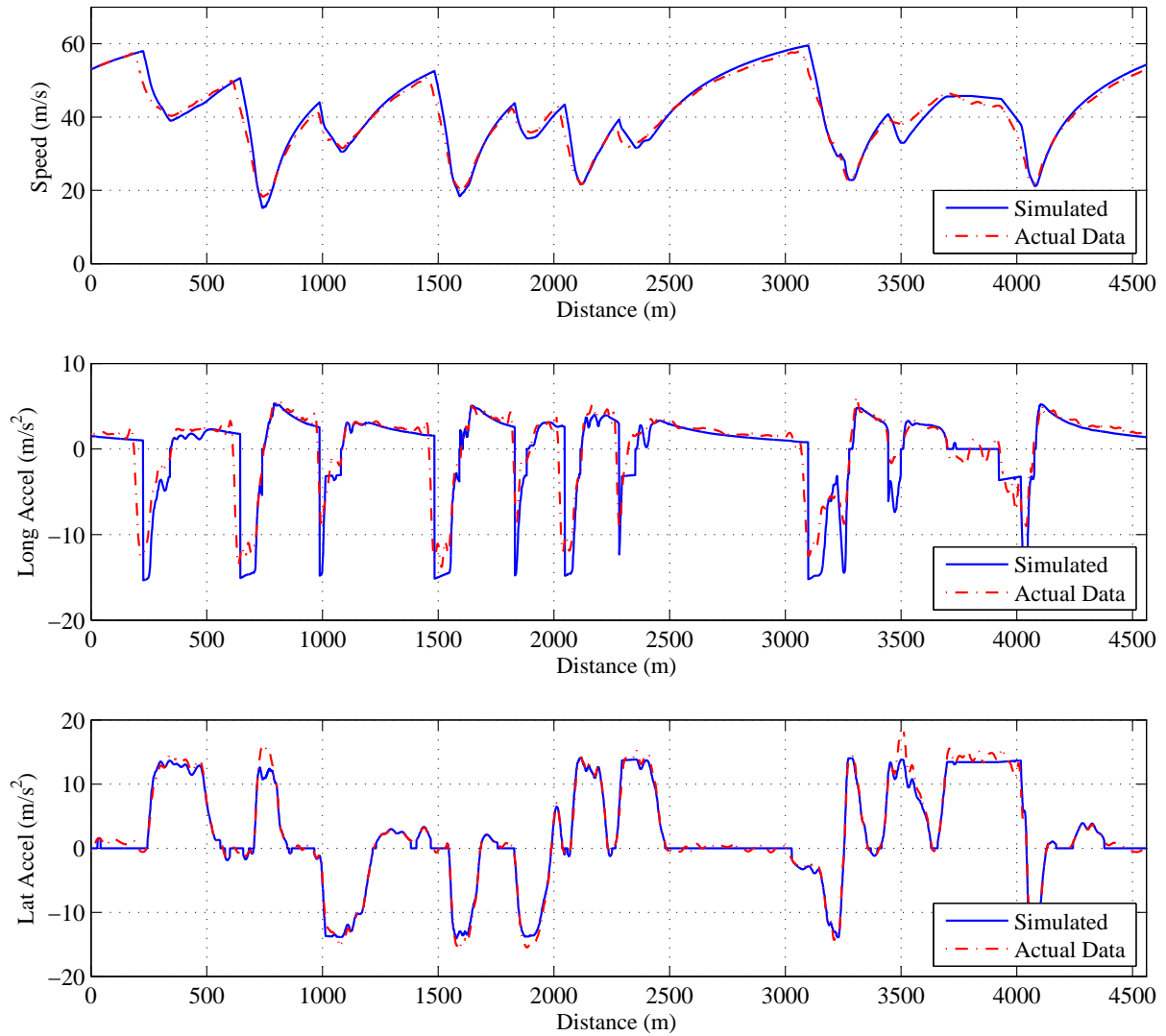


Figure 5.5: QSS speed (top), longitudinal acceleration (middle) and lateral acceleration (bottom) time histories

5.4 Parameter Sensitivity - Plate LSD

In order to assess the influence of torque sensing, plate differential setup parameters on minimum lap time, a number of parametric studies were conducted. The following sections detail the impact of i) drive and coast ramp angle, ii) the no. of friction faces and iii) positive and negative preload.

5.4.1 Ramp Angles

The QSS lap simulation method described in Section 5.3 has been used to investigate the influence of ramp angle on lap time. The same RWD vehicle is considered, with all other vehicle and LSD parameters (e.g. friction faces and preload) remaining constant throughout the investigation. Drive and coast angles have been varied from 30-70° in 5° increments. Figure 5.6 demonstrates the impact of the coast ramp for multiple drive ramp settings. Similarly, Figure 5.7 illustrates the influence of the drive ramp for multiple coast ramp settings. The ‘open’ and ‘locked’ labels are designed to show the relative extremes of operation, not the discrete states.

Under coast conditions in Figure 5.6, a decreasing ramp angle essentially shifts behaviour under braking from open to that of a locked differential. Increased amounts of torque bias are shown to reduce the associated lap time in all cases. Evaluation of the changes in the GG contour (see Figure 5.9) demonstrates how the envelope increases in the braking regions, as the coast ramp angle reduces. The lap time sensitivity in Figure 5.6 shows identical behaviour for all drive ramp settings, which equates to a 0.6s lap time reduction, when moving from the most benign ramp angle of 70°, to the most aggressive angle of 30°.

Under positive acceleration conditions in Figure 5.7, decreasing the drive ramp angle is again seen to reduce lap times, but only until saturation occurs at drive angles below 40°. The lap time sensitivity is much greater than in the coast angle case, with lap times reducing by approximately 1.5s between 70° and 40°. Below this, the lap time increases, but only in the order of thousandths of seconds, until the LSD is essentially locked. This is highlighted more clearly in Figure 5.8, where the optimum angle of 36° gives the minimum lap time of 118.544s. Referring back to Figure 5.3e, this can be explained by the excessive torque bias compromising the ultimate cornering capacity of the tyres at higher speeds. Assessment of the GG envelope itself (see Figure 5.10) confirms the increase in the positive acceleration region, and the saturation that occurs at lower ramp angles.

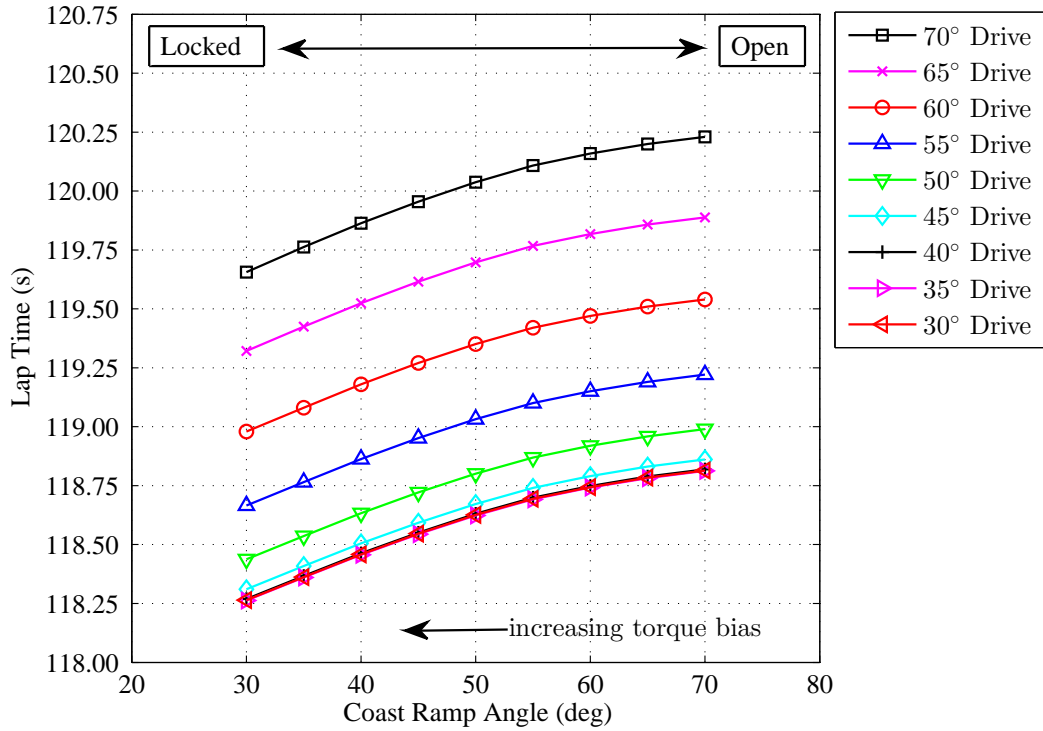


Figure 5.6: Coast ramp lap time sensitivity, 16 friction faces, 80Nm positive preload, 0Nm negative preload

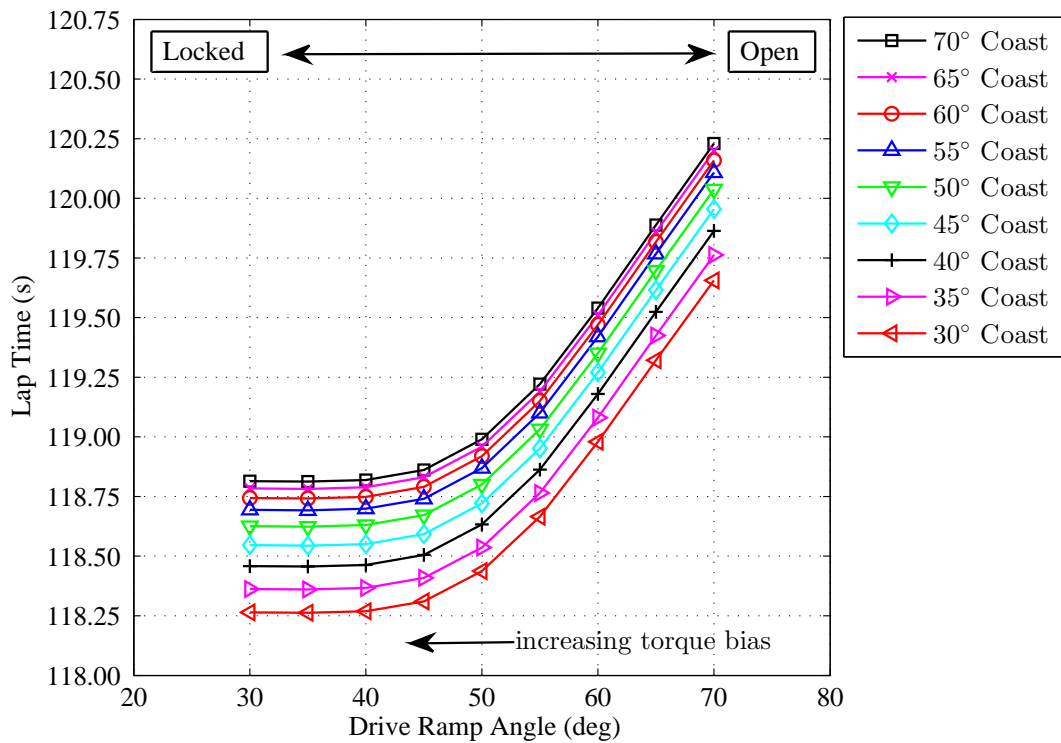


Figure 5.7: Drive ramp lap time sensitivity, 16 friction faces, 80Nm positive preload, 0Nm negative preload

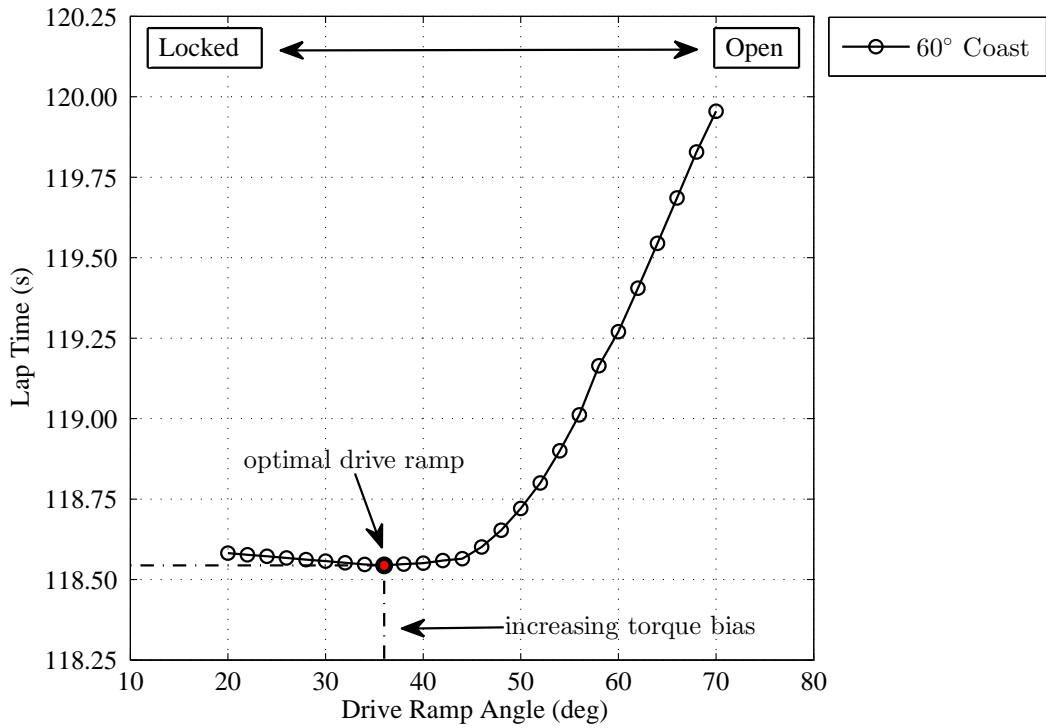


Figure 5.8: Drive ramp lap time sensitivity, 16 friction faces, 80Nm positive preload, 0Nm negative preload (optimal solution)

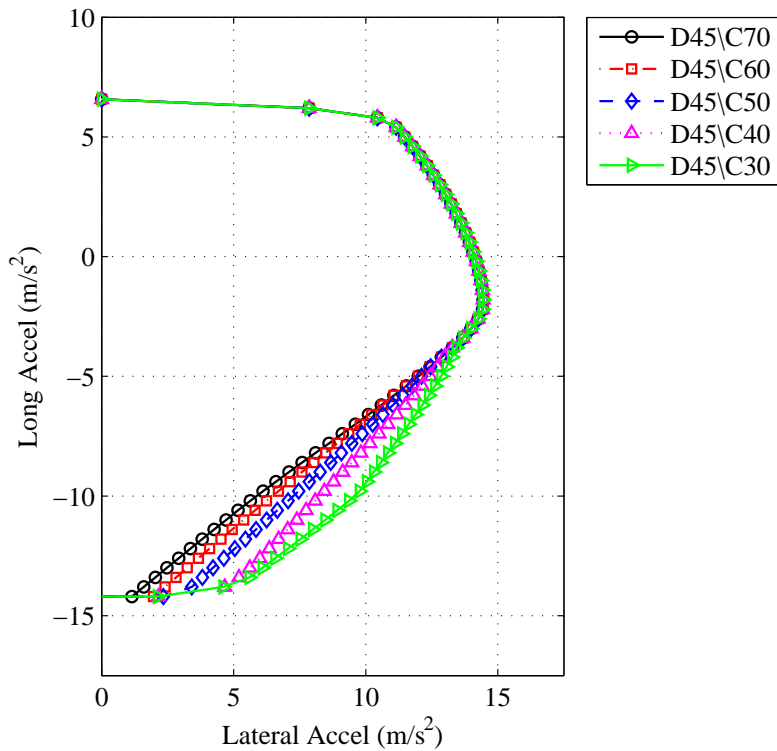


Figure 5.9: GG envelope variation with coast ramp angle (20m/s)

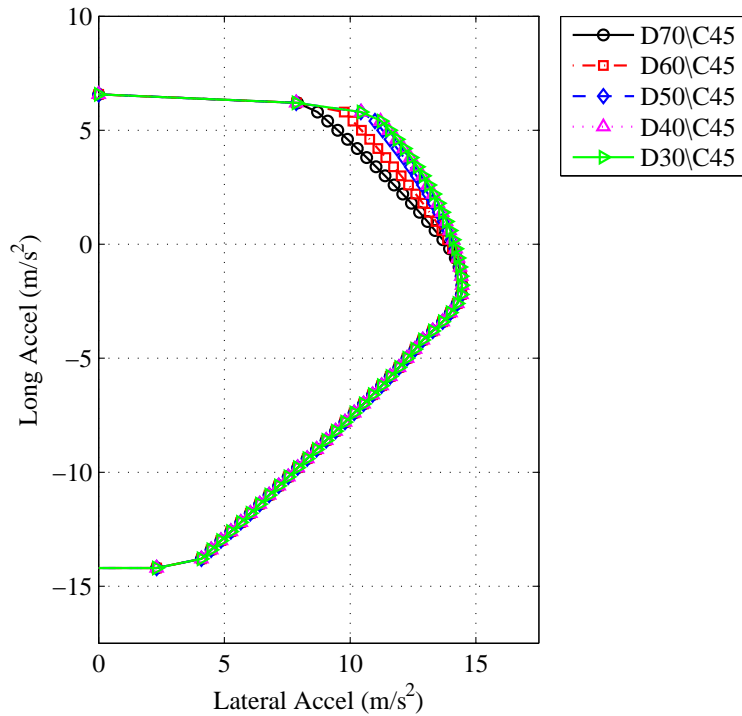


Figure 5.10: GG envelope variation with drive ramp angle (20m/s)

5.4.2 Friction Faces

In this section, the influence of the number of friction faces on lap time is investigated. In contrast to the previous ramp study, a change in the number of active friction faces will affect both the drive and coast locking regions. In this study, friction faces are increased from 4-16, for a number of varying ramp combinations. In Figure 5.11 the coast ramp angle is held constant at 45° , whilst the drive angle is varied from 30° - 70° . Similarly in Figure 5.12, the drive ramp is held constant at 30° whilst the coast angle was varied from 30° - 70° .

Under decreasing drive ramp conditions (Figure 5.11), the lap time is seen to reduce universally as friction faces increase. This influence is most pronounced at lower drive ramp angles, where ramp locking gradients are highest. The minimum time solution is again seen to saturate at lower drive angles and friction face numbers above 12. This is highlighting the dominance of the ramp angle in determining the effective ‘gain’ of friction face changes. With the 70° drive ramp, the lap time difference is 0.5s between 4 and 16 friction faces. With the 30° drive ramp, this time difference has increased to almost 1.5s. Under the decreasing coast ramp conditions in Figure 5.12, all configurations are again shown to reduce the lap time significantly between 4-8 friction faces. Above this however, the lap times start to diverge. At a coast angle of 70° , there is very little difference in lap time between the 12-16 friction face configurations. Here, the shallow ramp locking gradient has meant the relative change in torque bias (as friction faces increase) are small, resulting in minimal lap time difference. At the most aggressive ramp angle of 30° however, the steeper locking gradient has meant there are still significant reductions in lap time (0.3s) between 10 and 16 friction faces.

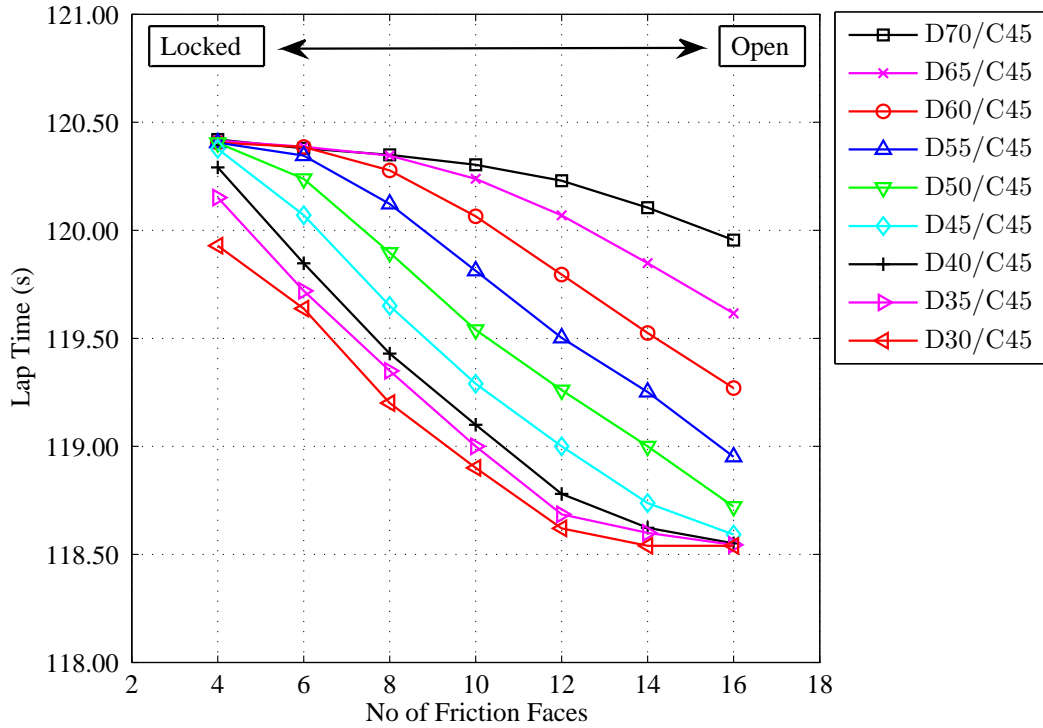


Figure 5.11: Friction face lap time sensitivity with varying drive ramp angle, 16 friction faces, 0Nm negative preload, 80Nm positive preload

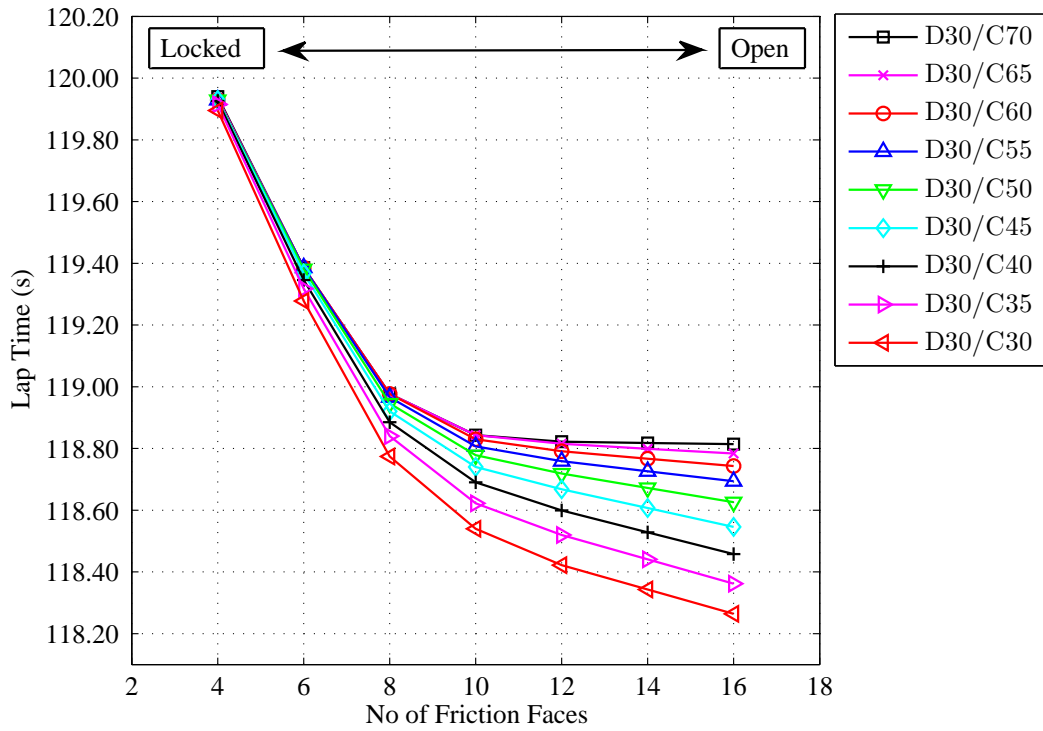


Figure 5.12: Friction face lap time sensitivity with varying coast ramp angle, 16 friction faces, 0Nm negative preload, 80Nm positive preload

5.4.3 Positive and Negative Preload

Both the ramp angle and the number of friction faces have been shown to significantly influence lap time, since these both alter the fundamental ramp locking gradient ∇_r (see Section 3.1.2). Positive preload however, only adjusts the torque bias at very low input torque levels, so one would expect a much smaller influence. Figure 5.13 shows that this is indeed the case. Two configurations have been shown, the first D45/C45 ramp angle setup, reflecting a more aggressive locking strategy, and the second D60/C75 a more benign, open strategy. Positive preload is increased from zero to 200Nm in 25Nm increments.

It is apparent that the more open setup increases the effectiveness of preload changes. A total lap time reduction of 0.6s is seen at a preload of 200Nm. Contrastingly, a reduction of only 0.2s is seen with the more aggressive D45/C45 ramp strategy. Of course, due to the larger levels of overall torque bias, this configuration still yields a lap time of 118.4s which is over 0.8s quicker (at 200Nm preload) than the D60/C75 setup, with a lap time of 119.2s.

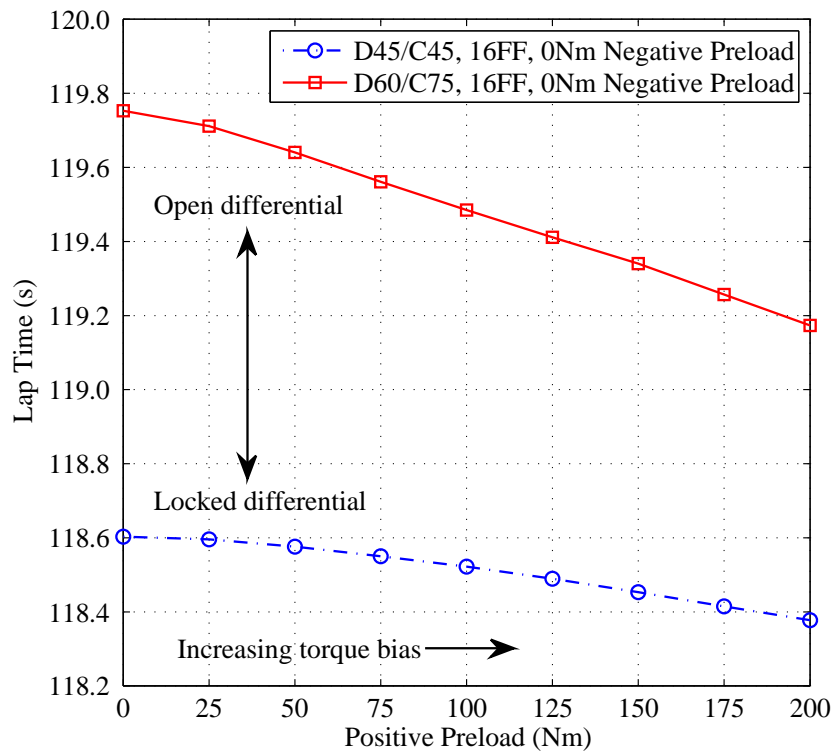


Figure 5.13: Positive preload lap time sensitivity, 16 friction faces, 0Nm negative preload

In contrast to positive preload, the addition of negative preload actually reduces the torque bias magnitude when differential input torque is low. Although unsubstantiated in literature, it is common practice to apply negative preload only to the drive side ramp. Preliminary investigations conducted as part of this work, confirmed that coast negative preload produced universally slower lap times. As a result, this analysis focuses solely on drive side negative preload. Three different drive angles are considered (30° , 45° and 60°) with negative preload increasing from zero to 300Nm in 20Nm increments. The

results from the study are shown in Figure 5.14. Initially, for the D60/C45 configuration, negative preload is detrimental to lap time, with over a 0.4s increase at 300Nm. The preload has made the LSD more open at relatively low input torques, and as a result, is less able to support a torque bias. As the drive angle reduces (promoting a steeper ramp gradient), lap time changes become far less pronounced and in the D30/C45 case, remain seemingly constant. Figure 5.15 depicts a closeup of this last case, which indicates there is actually an optimum, at 140Nm. The lap time advantage however is minimal, and is in the order of thousandths of seconds (0.006s). Although this time gain is negligible, it will be shown that if negative preload can be varied with vehicle speed, a much bigger performance advantage can be realised (see Section 5.7.1).

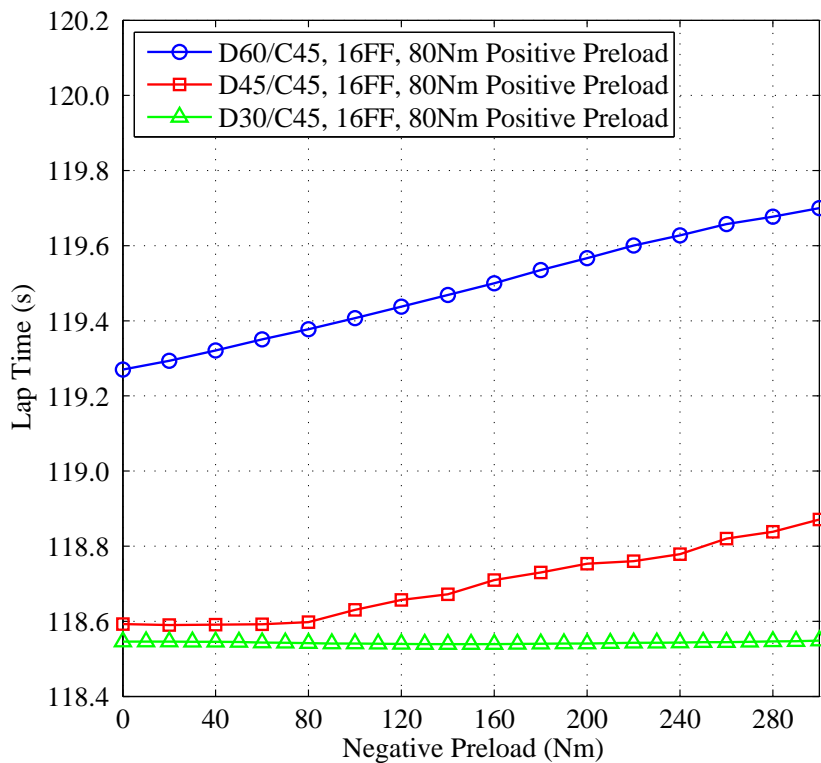


Figure 5.14: Negative preload lap time sensitivity, 16 friction faces, 80Nm positive preload

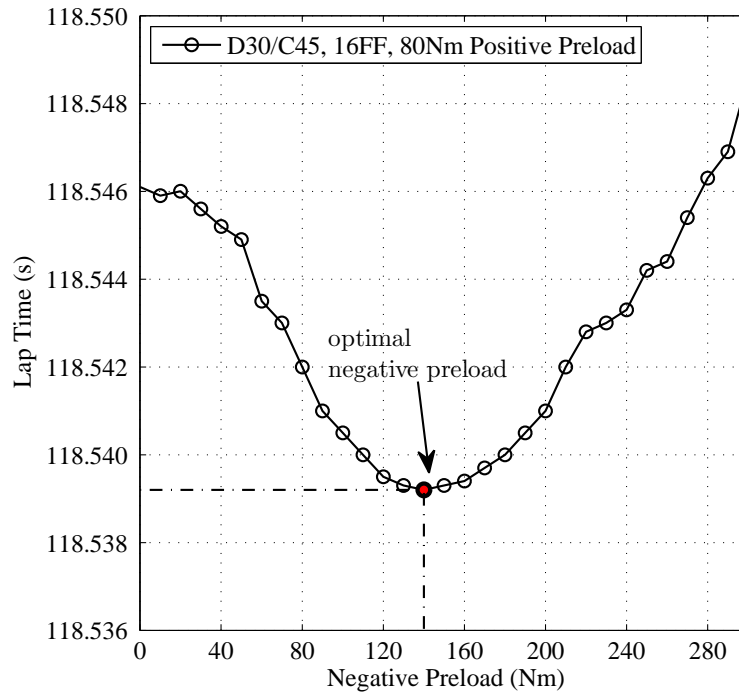


Figure 5.15: Negative preload lap time sensitivity, 16 friction faces, 80Nm negative preload (closeup)

5.5 Parameter Sensitivity - VC

The previous section has shown that the setup parameters of a torque sensing plate LSD have a significant influence on ultimate vehicle performance. In this section, a similar parametric investigation is conducted, with the purely speed sensing VC model presented in Section 3.5. The VC parameters in Table 3.7 are used, but with the number of shear faces increased from 0-80. Example torque bias profiles for a range of shear faces are shown in Figure 5.16.

The results of the lap time sensitivity study are presented in Figure 5.17. As the number of shear faces increases, so too does the torque bias as the VC LSD transitions between open and locked states. As in the plate LSD case, as the torque bias increases, so the lap time reduces in a nonlinear fashion. The lap time improvement is shown to be over 3.5s at 80 shear faces. At this point, the lap time starts to saturate at 118.25s. The changes to the GG envelope give some insight into why this occurs, and demonstrates how its shape differs from the previous torque sensing device. Figures 5.18 and 5.19 illustrate the GG maps at 20 and 60m/s, for 0, 40, 60 and 80 shear faces. Similar to friction face changes in a plate LSD, shear face changes are global and increase the GG area under both positive acceleration and braking regions. One of the most significant differences, is the more circular form of the contour. This can be explained by the speed sensing element having a greater influence at high cornering accelerations, where the driven wheel speed difference is greatest. It is clear that as the VC approaches a locked axle, the associated GG contour changes start to become much smaller (between 60 and 80 shear faces for example). The consequence of this is that lap time improvements will also start to saturate.

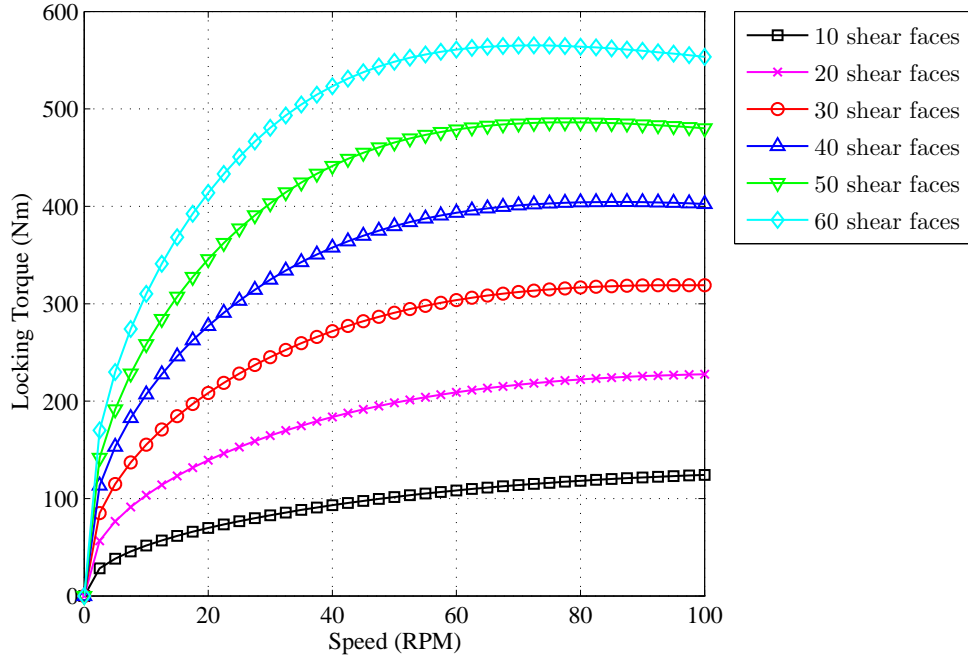


Figure 5.16: VC torque bias characteristics

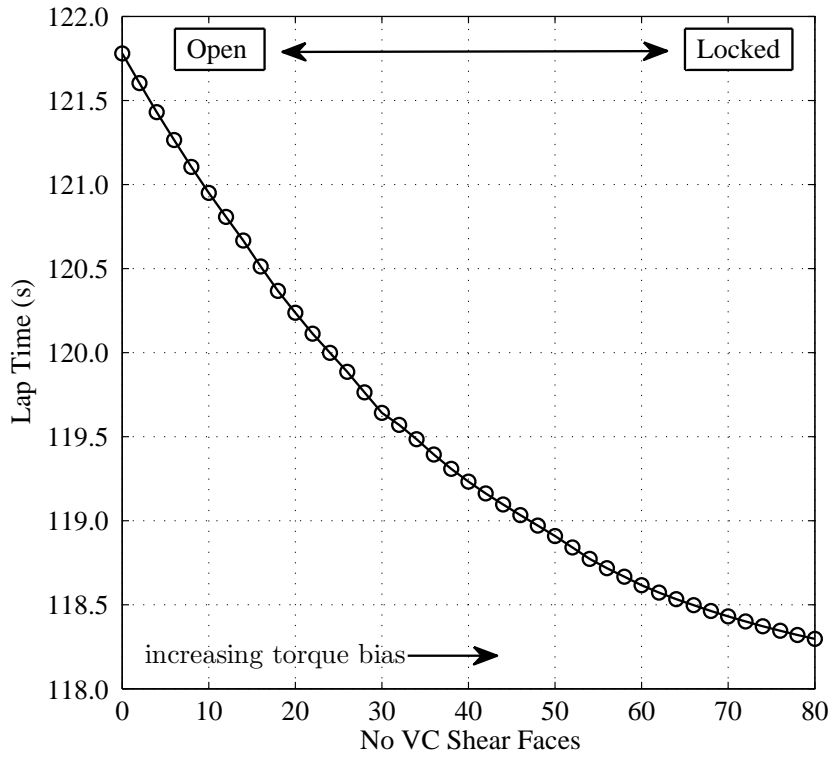


Figure 5.17: VC lap time sensitivity

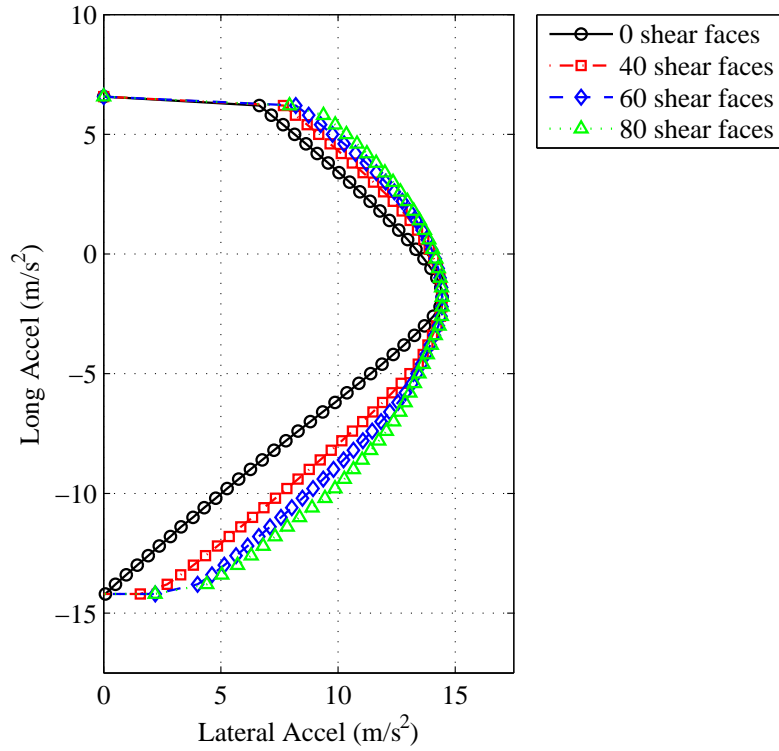


Figure 5.18: GG envelope variation with VC shear faces (20m/s)

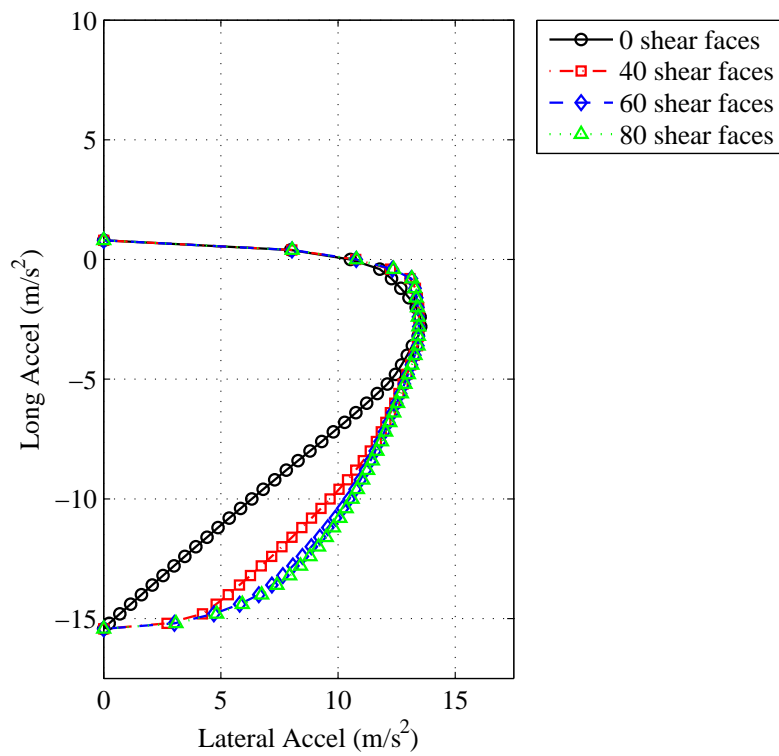


Figure 5.19: GG envelope variation with VC shear faces (60m/s)

5.6 Parameter Sensitivity - VCP

A final parametric study was carried out to investigate the influence of the relative contribution of torque and speed sensing elements in a VCP differential. The parameters defined in Table 3.11 were used, with two combinations of ramp angle, D30/C45 and D65/C30. The results are detailed in Figure 5.20. Similar to the VC study, the lap time

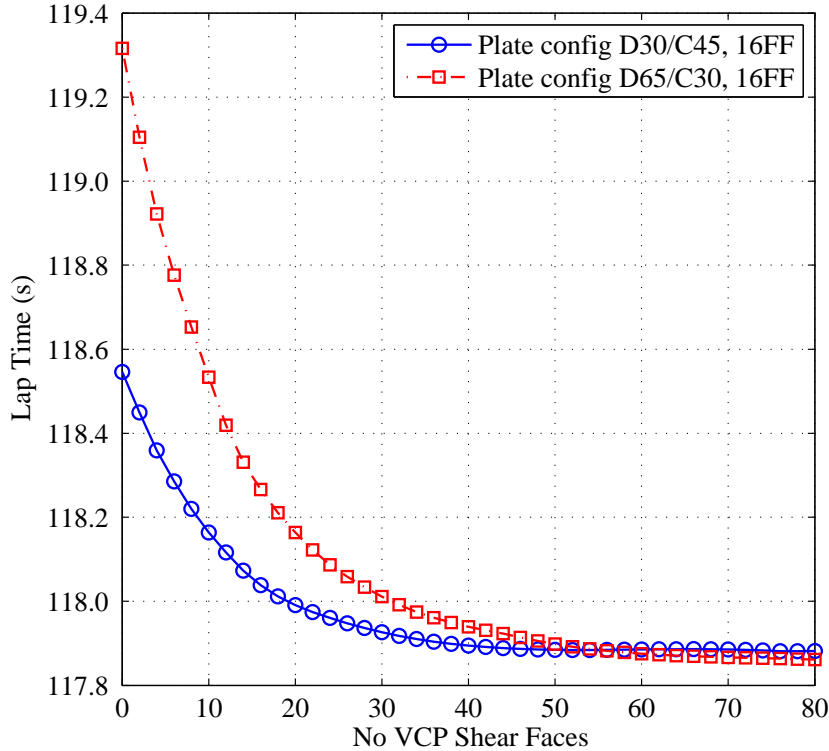


Figure 5.20: VCP lap time sensitivity

is seen to saturate, but this time at a much lower value of 50 shear faces in the D30/C45 case, and 60 shear faces in the D65/C30 case. The additional torque bias provided by the plate LSD has allowed the transition between open and locked states to occur more quickly. Interestingly, the saturated lap time of the D65/C30 configuration (117.86s) is 0.018s quicker than the D30/C45 setup, which yielded a lap time of 117.88s with a VC fitted with 80 shear faces. Referring back to the discussion in Section 5.2 it was shown that too much locking can reduce the peak lateral acceleration at higher speeds. In this case, the more aggressive D30/C45 strategy has yielded a locked axle at 80 shear faces. The more benign D65/C30 configuration has allowed a small increase in peak lateral acceleration since it is more ‘open’ in this region. The associated increase in the GG area has given the 0.018s of lap time improvement.

5.7 LSD Optimisation

Although the parametric studies presented in previous sections provide insight into how to optimise the LSD torque bias profile, it is time consuming to carry out such studies for multiple differential and vehicle configurations.

To make this process more efficient, the torque bias can be included as a parameter in the optimisation itself. This is achieved by using an active clutch plate LSD, similar to that described in Section 2.2. Equation 3.41 can be modified to reflect a hydraulic pressure H_p , applied to the clutch pack, to generate the resulting locking torque:

$$T_{lock} = \frac{2}{3} \frac{H_p}{H_a} \mu_p \left(\frac{r_{c2}^3 - r_{c1}^3}{r_{c2}^2 - r_{c1}^2} \right) \quad (5.18)$$

where H_a is the corresponding hydraulic piston area. The state vector in Equation 5.7 is extended to include this additional parameter:

$$\text{state vector } \mathbf{x} = [\delta_{rw}, \omega_1, \omega_2, \omega_3, \omega_4, u_{tb}, V, r, H_p]^T \quad (5.19)$$

To reflect practical limits on hydraulic system pressure, the inequality constraints are also modified to include the maximum pressure value, H_{pmax} . In this case, the pressure has been limited to 200bar.

$$c_{ineq}(\mathbf{x}) = \begin{bmatrix} \omega_e - \omega_{emax} \\ \alpha_1 - \alpha_{1max} \\ \alpha_3 - \alpha_{2max} \\ \beta - \beta_{max} \\ F_{zmin} - F_{z2} \\ F_{zmin} - F_{z4} \\ H_p - H_{pmax} \end{bmatrix} \leq 0 \quad (5.20)$$

The resulting GG envelope from the parameter optimisation is shown in Figure 5.21. The associated lap time compared to open and locked configurations is also detailed in Table 5.4.

Table 5.4: Active LSD lap time comparison

	Open	Locked	Active LSD
Lap Time (s)	121.780	118.053	117.961

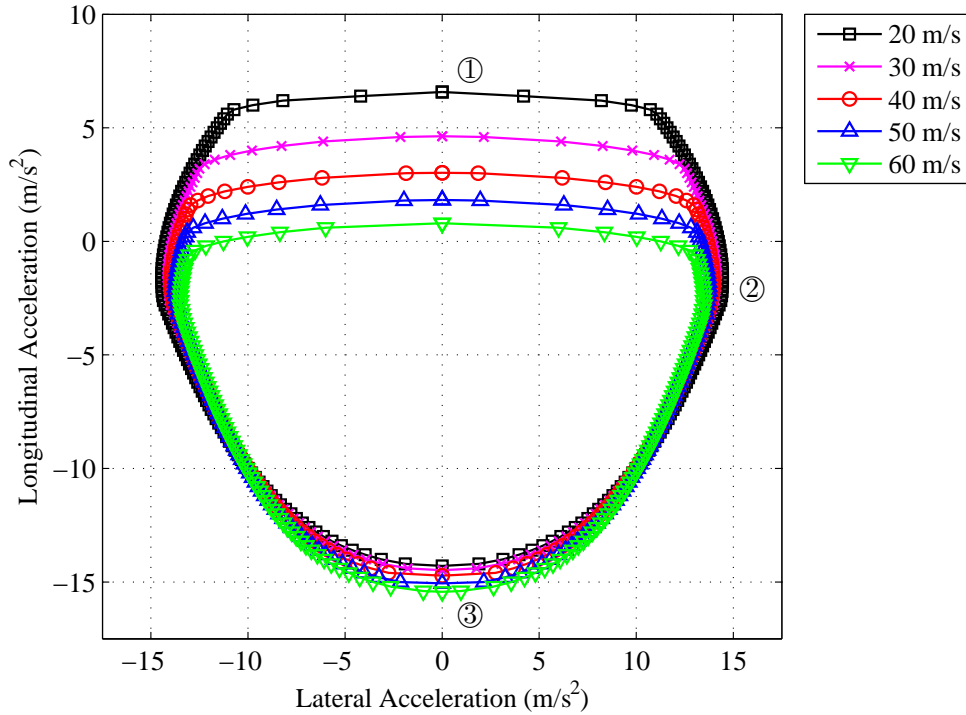


Figure 5.21: Active differential GG envelope

It is clear that the active LSD has provided the quickest lap time and is 0.092s quicker than the locked axle configuration. By analysing the associated GG area at each speed (see Table 5.5) it is apparent that most of this performance gain has come at higher speeds (40-60m/s), where the GG area increase is greatest.

Table 5.5: Area of constant velocity GG contours (locked-active comparison)

Speed (m/s)	Locked area (m/s ²) ²	Active area (m/s ²) ²	Difference (%)
20	479.66	479.70	+0.008
30	428.75	429.58	+0.194
40	389.67	390.67	+0.256
50	361.02	362.02	+0.277
60	336.62	337.53	+0.268

The hydraulic pressure traces depicted in Figure 5.22 demonstrate why this is the case. At the lowest speed of 20m/s the pressure remains at its maximum 200bar during straight line acceleration (point 1) and straight line braking (point 3). Only for a brief period during the very highest lateral accelerations does the pressure reduce slightly to 180bar at point 2. Practically speaking, the LSD is effectively locked at such high pressures, which is highlighted in the minimal difference (0.008%) between locked and active GG areas at this speed (See Table 5.5). At higher speeds, the active LSD still locks the axle in straight line acceleration and braking, but reduces the pressure much more significantly during cornering (point 2). This is why a much bigger difference

(relatively speaking) in GG areas is seen at higher speeds, where the increase is between 0.25-0.27%. This has equated to a 0.092s lap time advantage. Although this may not sound significant, in the motorsport environment, this is a performance gain that many racing teams would pursue.

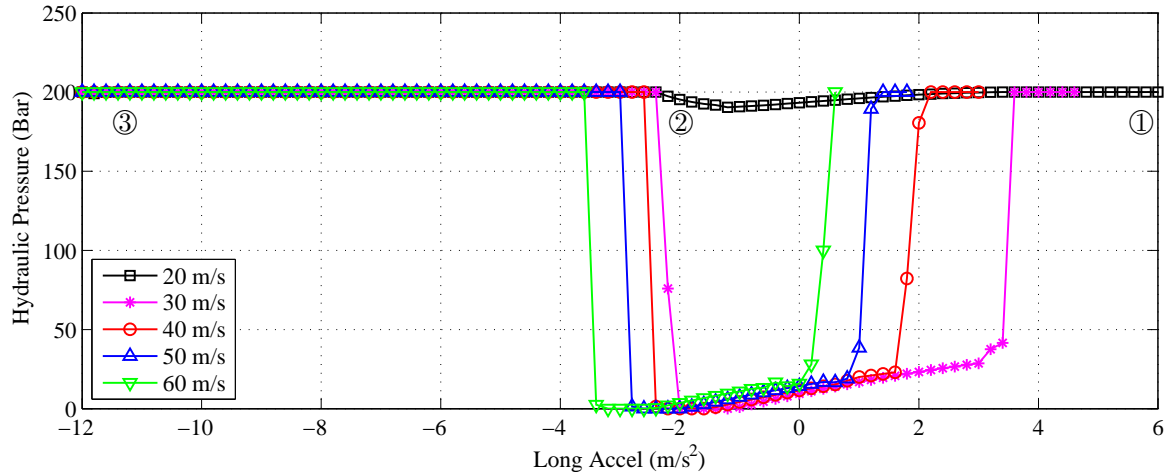


Figure 5.22: Active differential hydraulic pressure (20-60m/s)

The implications of the hydraulic pressure traces in Figure 5.22 can be more easily understood by plotting the associated torque bias around the GG edge. Figures 5.23a-b depict the GG profiles at 20 and 60m/s with the optimal torque bias profiles overlaid. In the low speed case (Figure 5.23a), the peak lateral acceleration occurs when a negative torque bias of 170Nm is applied (see point 2). In the high speed case however (Figure 5.23b), the torque bias falls to zero in this region (see point 2, between $A_x = -2.2$ and -3.4 m/s²). What is also apparent, is that the longitudinal acceleration at which the peak lateral acceleration occurs shifts back as drag increases at higher speeds. At 20m/s peak lateral acceleration occurs at $A_x = -1.8$ m/s², compared to $A_x = -2.8$ m/s² at 60m/s. This has important consequences for the application of these results to passive LSD devices. These are discussed in the following section.

5.7.1 Optimal Passive LSD characteristics

The torque bias parameter optimisation method in Section 5.7 can be used to generate an LSD control algorithm based on longitudinal acceleration or any other chosen vehicle parameter [10]. In this section however, its use is extended to investigate optimal passive LSD characteristics, since these are more applicable to the vast majority of other racing formulae in which active devices are banned. Once forced by regulation to utilise a passive LSD device, the question then arises as to whether a speed or torque sensing strategy is best. Experience has shown that the vast majority of LSDs in motorsport are torque sensing. The evidence presented in Figure 5.22 suggests that this may be because the torque flowing through the transmission more closely correlates to the optimal torque bias profile (i.e. high torque bias under braking and acceleration and a smaller torque bias at the corner apex). Conversely, speed sensing devices tend to support higher torque bias levels at the corner apex, and much lower levels at the corner entry and exit, where wheel speed differences are small. For

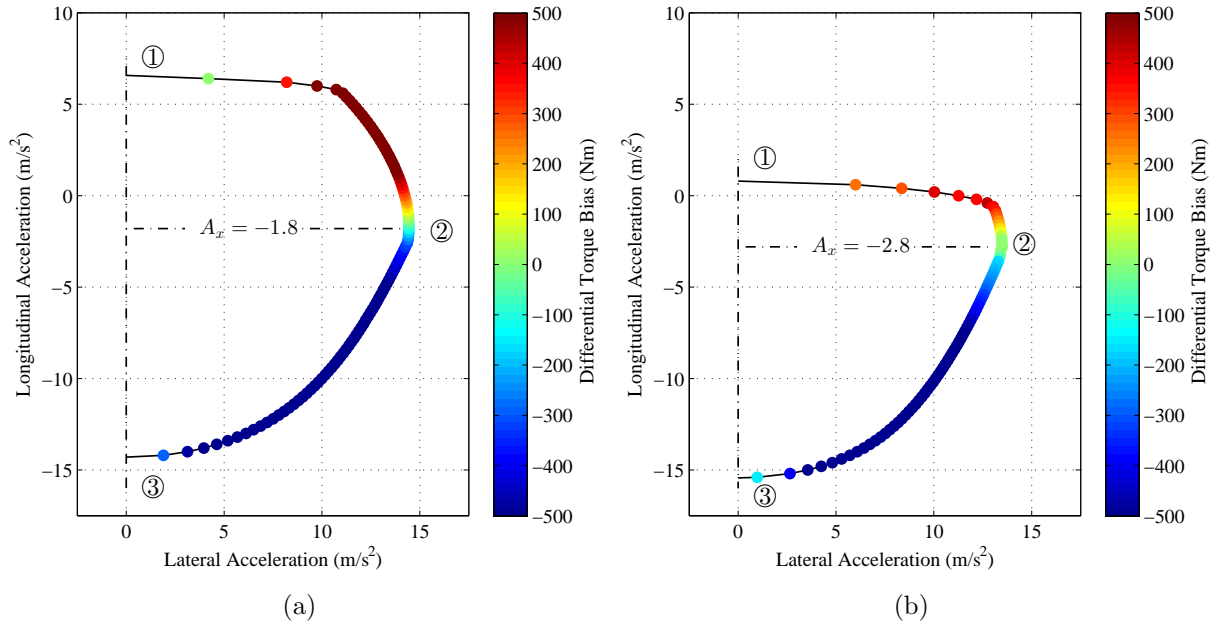


Figure 5.23: a) QSS optimal torque bias profile at 20m/s
 b) QSS optimal torque bias profile at 60m/s

the purposes of this work therefore, the use of the parameter optimisation method is confined to torque sensing devices only.

The hydraulic pressure traces shown in Figure 5.22 and Equation 5.18 can be used to derive the associated torque bias at each acceleration point. To gain insight into the optimal torque sensing ramp gradients, the resultant torque bias can be plotted against the LSD input torque. In Figure 5.24, these points have been plotted against engine torque (multiplied by the gear ratio) under drive conditions, and the total rear axle brake torque under coast conditions. The reader should note that the locking torque values are half the magnitude of those presented in earlier Figures (3.13 - 3.15), due to the way in which locking torque is measured experimentally. The torque bias at both 20 and 60m/s has been included to demonstrate the difference between optimal low and high speed configurations. The characteristics have been fitted to the plate differential model described in Section 3.1 and the resulting setup parameters are summarised in Table 5.6.

Table 5.6: Fitted plate differential setup parameters

Parameter	20m/s	60m/s
Drive ramp angle (°)	36	36
Coast ramp angle (°)	30	29
Number of friction faces	16	16
Static positive preload (Nm)	25	0
Drive negative preload (Nm)	245	260
Coast negative preload (Nm)	-250	-45

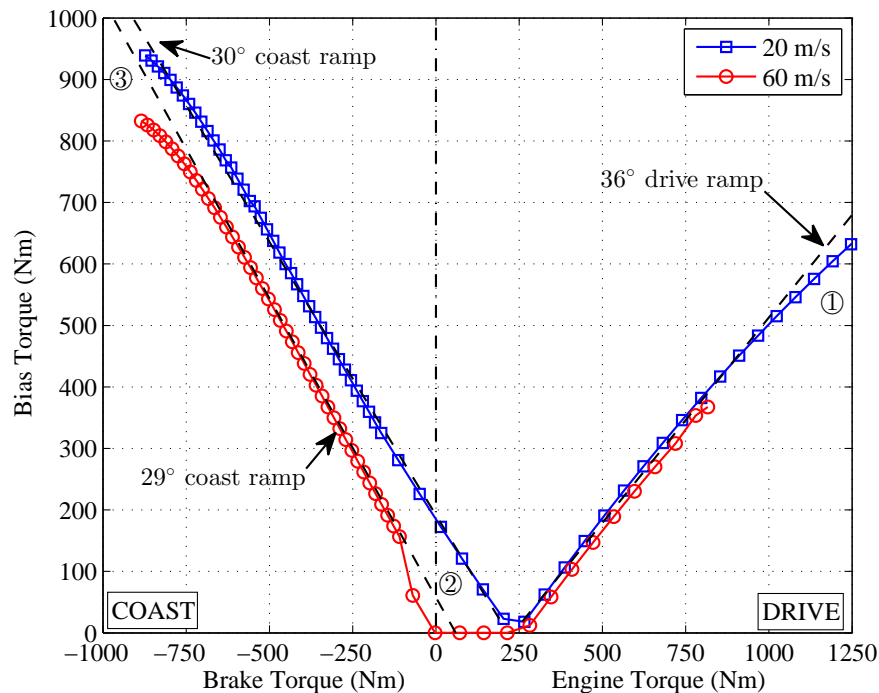


Figure 5.24: Optimal passive torque sensing characteristics

Under drive conditions, the ramp locking gradient is similar at both low and high speeds, equivalent to a 36° ramp angle. It is reassuring to note that this is identical to the quickest configuration seen in the lap time sensitivity study (see Figure 5.8). At 20m/s, 245Nm of negative preload is used, with a small amount of positive preload (25Nm). At 60m/s however, the negative preload is maintained, but the positive preload drops to zero. Interestingly, under coast conditions, the ramp locking gradients are again very similar. These are equivalent to 29° and 30° coast ramp angles.

More significantly, the point at which the coast side torque bias starts is quite different. In the high speed case, the length of the zero torque bias (i.e. open) region is much longer than at low speeds. As was shown in Section 5.7 this can be explained by the effects of longitudinal drag which increase with speed. This shifts back the longitudinal acceleration at which the peak lateral acceleration occurs, since the resultant driving torque is zero at this point. As has already been shown in Section 5.2, the peak lateral capability of the tyres can be extracted by limiting the torque bias at very high cornering accelerations. In terms of the associated torque bias characteristics, this means elongating the open region of the LSD at higher speeds.

Figure 5.25 combines these main findings in a locking torque schematic, which forms the basis of a future torque sensitive LSD design. It features a drive side negative preload which stays constant throughout the speed range, but with a locking gradient still tunable through the standard ramp and friction faces parameters. The positive preload reduces with speed, as negative preload increases. Because the nature of the GG envelope is coupled so heavily with tyre, engine and aerodynamic characteristics, differences in any of these areas are likely to have a significant impact on the resultant

optimal passive LSD characteristics. The methodology outlined above is therefore crucial in allowing LSD setup to be optimised effectively.

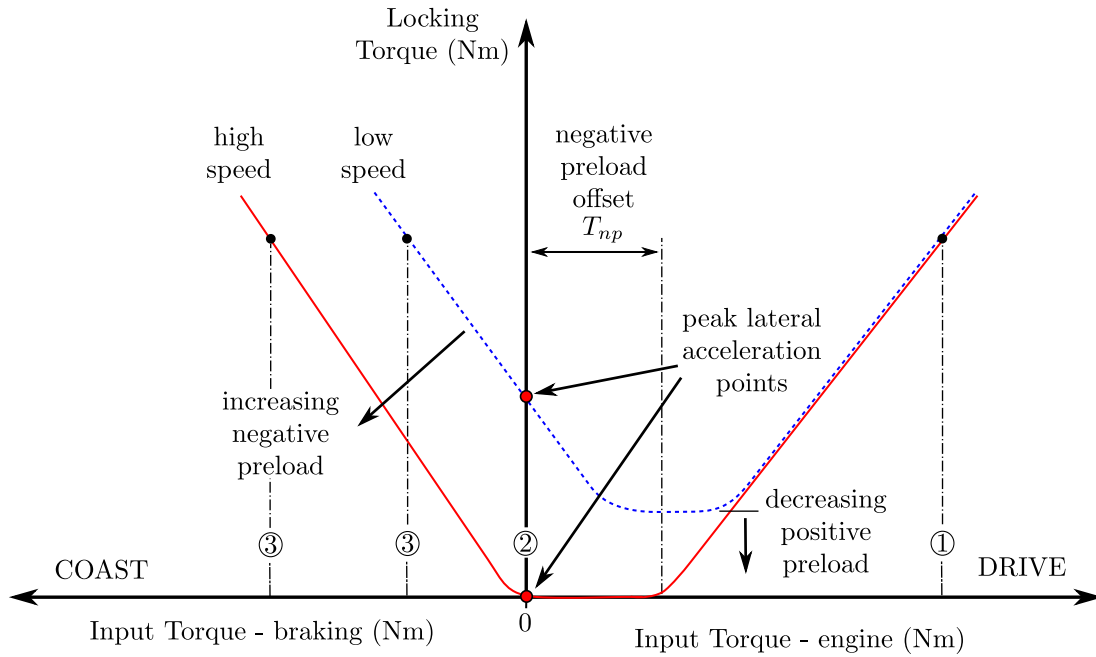


Figure 5.25: Optimal torque sensitive bias profile schematic

5.8 Conclusions

This chapter has described a quasi steady state optimisation method, which allows the acceleration envelope of a race vehicle to be found with any number of LSD configurations. This method was validated against track data to predict the lap time of a RWD saloon racing vehicle around the Snetterton 300 circuit, to within 1.3%.

Parametric studies showed that drive and coast ramp angles were the most dominant setup parameters of a torque sensing plate type LSD. Higher amounts of torque bias under coast conditions led to reduced lap times universally. In the positive acceleration case however, the lap time improvement was shown to saturate. A drive ramp angle of 36° was shown to give the quickest lap time for the RWD saloon racing vehicle considered. Ramp angles were also shown to influence the effectiveness of other parameter changes including the number of friction faces and positive/negative preload.

Although positive preload reduced lap times in all cases, negative preload was detrimental at lower speeds and where the ramp angle configuration gave more benign, open characteristics. In the case of a more locked D30/C45 ramp setup, negative preload provided a marginal improvement of 0.007s at an optimum negative preload of 140Nm.

The speed sensitive VC and VCP types were shown to have a more significant influence at higher lateral accelerations, where the driven wheel speed difference is greatest. Lap time improvements again saturated once a threshold amount of bias torque had been reached.

An active, hydraulic LSD model was used in a more efficient parameter optimisation process, to provide further insight into the ideal torque bias profile. At low speeds, this was shown to be very similar to that of a locked differential. As the vehicle speed increased however, the torque bias was progressively reduced at peak lateral accelerations. Under heavy braking and acceleration the LSD was shown to remain locked at all speeds. These type of characteristics are more akin to passive torque sensing devices, than their speed sensitive counterparts. The lap time improvement of the active LSD over a spool axle was 0.092s.

The results from the active LSD evaluation were fitted against traditional ramp locking gradients for a plate type LSD. An optimum drive angle of 36° correlated well with the optimal angle found in previous parametric studies. This suggests that the method is a robust way to find optimal passive LSD setup parameters. The results from the study were used to propose a novel torque biasing device, able to vary both positive and negative preload with vehicle speed.

Chapter 6

Extensions to the QSS Method

In this chapter, the QSS GG diagram method is extended, to allow the behaviour of a RWD vehicle below the acceleration limit to be studied in more detail. By defining a feasibility region bounded by the GG envelope, yaw moment contours for multiple LSD types are generated. These are used to demonstrate differences between speed and torque sensing devices and how they apply yaw moments at different phases of a typical cornering manoeuvre. The same framework is used to illustrate differences in vehicle stability and agility through linearisation of the vehicle model. Eigenvalue and yaw rate bandwidth metrics are presented as a more practical way to understand the driveability of a particular setup, and as a method of tailoring vehicle characteristics to suit varying driver preferences. This is used to demonstrate how an active LSD would keep the vehicle agile at low lateral accelerations, but maximise stability at higher lateral accelerations.

6.1 The Feasibility Region

The methods presented in Chapter 5 considered the limit case, where longitudinal and lateral acceleration were maximised to optimise ultimate vehicle performance. A key factor in determining how close a driver can get to this limit, is the perceived balance between vehicle stability and agility. A vehicle which has been setup to achieve the right handling balance in the driver's view, will allow the driver to attack the circuit, more able to exploit the vehicle's performance envelope. It is not sufficient therefore, to focus simply on lap time, or even the balance of the vehicle at the limit. An understanding of how the vehicle balance changes up to the limit is required to help determine whether a driver might be able to extract the most from a particular setup.

The well known Milliken Moment Method [62] achieves this by characterising a normalised yaw moment against lateral acceleration, for lines of constant side slip and steering angle. Multiple diagrams can be used to demonstrate additional effects including longitudinal acceleration and path radius. What follows however, is the description of an alternative method, which the author believes is easier for race engineers to relate practically to the manoeuvre on track and provides a more intuitive framework to optimise open loop vehicle characteristics.

Referring back to Section 5.1, the GG diagram method can be extended by considering multiple feasibility points within the GG boundary. An example of this is illustrated

as point ‘D’ in Figure 6.1. More formally, a grid of acceleration points $a_{j,i}$, with longitudinal components a_{xj} , and lateral components a_{yi} can be defined. Since lateral acceleration is now defined (and therefore the yaw rate r , under QSS conditions), the optimisation can be transformed into a simpler feasibility problem. For each acceleration point therefore:

$$\dot{U} = a_{xj}, \quad j = 1 \dots p \quad (6.1)$$

$$Ur = a_{yi}, \quad i = 1 \dots m \quad (6.2)$$

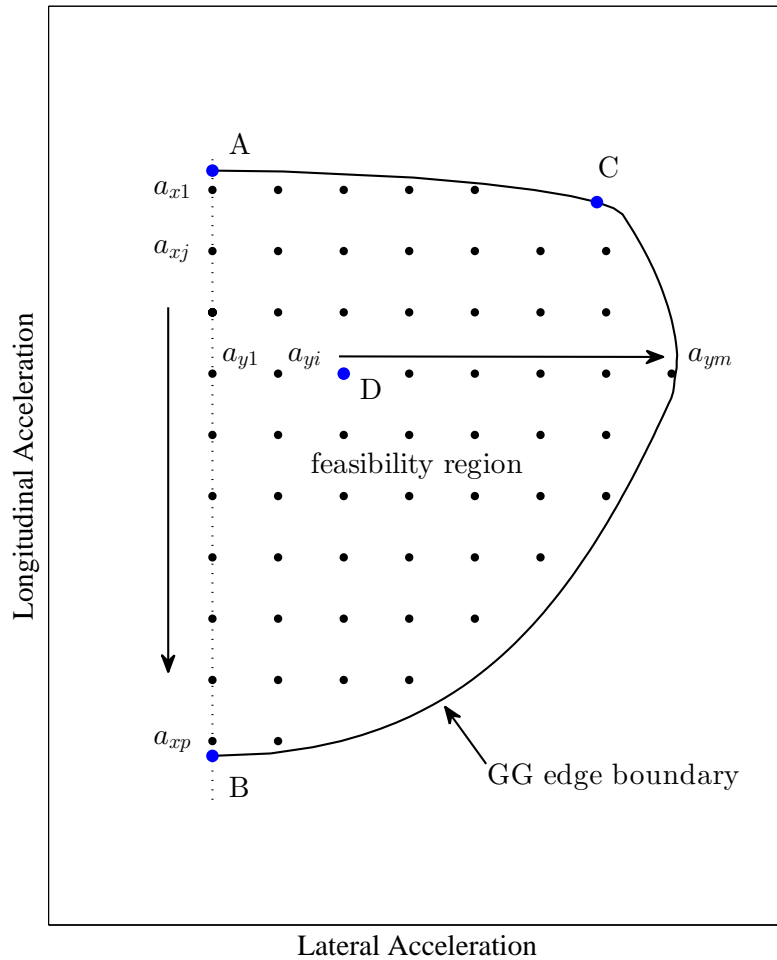


Figure 6.1: GG feasibility point grid example

The original state vector (see Equation 5.7) can be simplified by the removal of yaw rate such that:

$$\text{state vector } \mathbf{x} = [\delta_{rw}, \omega_1, \omega_2, \omega_3, \omega_4, u_{tb}, V]^T \quad (6.3)$$

and similarly, the original equality constraints (see Equation 5.9) can be modified to reflect the constant lateral acceleration term:

$$c_{eq}(\mathbf{x}) = \begin{bmatrix} \dot{V} \\ \dot{r} \\ \dot{U} - \dot{U}_{target} \\ Ur - a_{yi} \\ \dot{\omega}_1 U_1 - \omega_1 \dot{U} \\ \dot{\omega}_2 U_2 - \omega_2 \dot{U} \\ \dot{\omega}_3 U_3 - \omega_3 \dot{U} \\ \dot{\omega}_4 U_4 - \omega_4 \dot{U} \end{bmatrix} = 0 \quad (6.4)$$

Table 5.1 has been updated to reflect those variables which are used during feasibility calculations and are summarised in Table 6.1.

Table 6.1: GG optimisation state vector variables

Parameter	Unit	Symbol	Point A,B	Point C	Point D
Steer Angle	rad	δ_{rw}	0	✓	✓
FL Wheel Speed	rad/s	ω_1	✓	✓	✓
FR Wheel Speed	rad/s	ω_2	$= \omega_1 = \omega_f$	✓	✓
RL Wheel Speed	rad/s	ω_3	✓	✓	✓
RR Wheel Speed	rad/s	ω_4	$= \omega_3 = \omega_r$	✓	✓
Throttle/Brake	-	u_{tb}	✓	✓	✓
Side Slip Velocity	m/s	V	0	✓	✓
Side Slip Acceleration	m/s ²	\dot{V}	0	0	0
Yaw Rate	rad/s	r	0	✓	a_{yi}/U_{target}
Yaw Acceleration	rad/s ²	\dot{r}	0	0	0
Long Velocity	m/s	U	U_{target}	U_{target}	U_{target}
Long Acceleration	m/s ²	\dot{U}	✓	\dot{U}_{target}	a_{xj}

The objective function in this feasibility region can take multiple forms. This could describe the relative importance of stability and agility metrics (see Section 6.5) to meet specific driver preferences. However, the aim in this initial section, is to present the method and use it to gain insights into differential behaviour and its impact on the vehicle. As a result, the optimisation scheme is used merely to find a feasible combination of states for each acceleration point. The objective therefore is solely to satisfy the associated inequality and equality constraints:

$$c_{eq}(\mathbf{x}) = 0 \quad (6.5)$$

$$c_{ineq}(\mathbf{x}) \leq 0 \quad (6.6)$$

6.2 Feasibility Results - LSD Yaw Moment

To help understand the influence of the LSD torque bias on handling balance, the yaw moment that they create must be evaluated. This moment is generated whenever there is a difference in torque delivered to the driven wheels and as will be shown, can take the form of both understeer and oversteer moments. The differential yaw moment N_{diff} , can be calculated by using the formula:

$$N_{diff} = \frac{T_{lock}t_r}{2R_r} \quad (6.7)$$

where t_r is the vehicle rear track, R_r the rear wheel radius and T_{lock} the differential bias torque. In the sections that follow, yaw moment contours for a clutch plate type, VC and VCP differentials are presented and discussed. Particular attention is given to how the yaw moment varies through the GG envelope and how these relate to specific cornering phases of a typical race vehicle cornering manoeuvre.

6.2.1 Torque Sensing Plate LSD

The yaw moment contour generated by a torque sensing plate LSD is shown both at 20m/s in Figure 6.2 and at 60m/s in Figure 6.3. The LSD parameters used in the analysis are detailed in Table 6.2. For clarity, only the positive lateral acceleration region of the GG envelope is shown. Negative differential yaw moments give rise to stabilising understeer moments, and positive, de-stabilising oversteer moments.

Table 6.2: Plate differential parameters

Parameter	Symbol	Value
Drive ramp angle	θ_{rd}	30°
Coast ramp angle	θ_{rc}	45°
Number of friction faces	z_f	16
Static positive preload	T_{pp}	80Nm
Drive negative preload	T_{np}	0Nm

In Figure 6.2 at 20m/s, the yaw moment magnitude is shown to increase with both positive and negative longitudinal accelerations. In the positive acceleration case, this is due to the relatively high engine torque being transmitted to the differential from a high gear ratio and minimal drag maximising the vehicle's acceleration capability. Under steady state cornering conditions ($a_x = 0$), at a lateral acceleration of 9m/s², the direction of the yaw moment starts out negative (see region 1). As longitudinal and lateral acceleration increases however, lateral load transfer effects start to dominate, and the inside driven wheel starts to spin faster than the outer. This switches the torque transfer direction and the resulting yaw moment to oversteer (see region 2), as the GG boundary is reached. Conversely, under braking, the direction of the yaw moment is negative throughout (see region 3). This can again be explained by load transfer effects, which encourage the more lightly loaded inner rear wheel to rotate

slower under braking, and maintain an outer to inner wheel (understeer) torque bias. This is as a result of the inner wheel being very close to locking up under heavy braking.

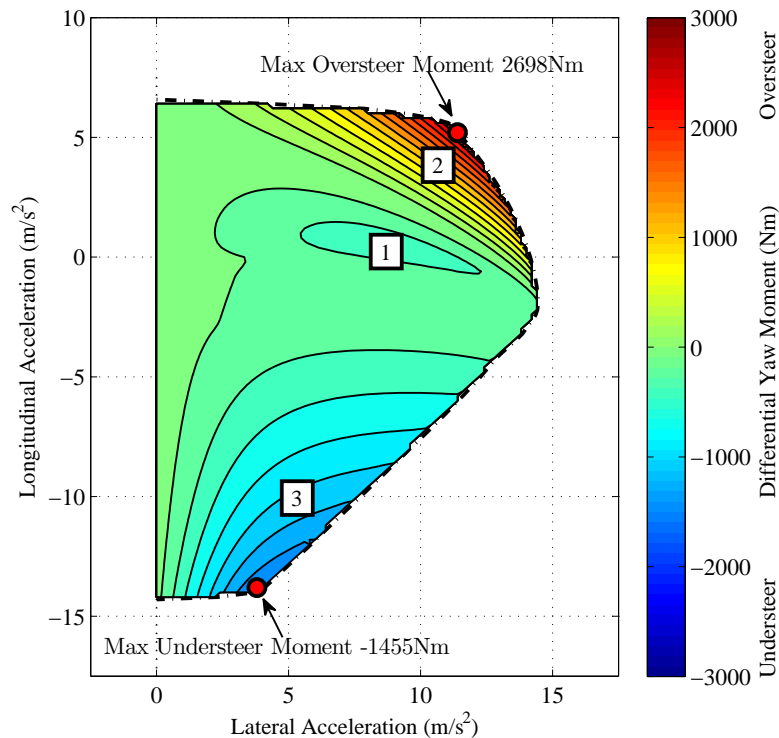


Figure 6.2: Differential yaw moment contours - plate LSD (20m/s)

The relative magnitude of the peak yaw moment under positive acceleration (2698Nm) is seen to be significantly larger than under negative accelerations (-1455Nm), on account of the more aggressive drive side ramp angle. This is shown to occur at a lateral acceleration level of 11m/s^2 , which relates to the middle of the corner exit phase of a typical 90° bend (see Section 6.4.1). Conversely, the maximum understeer moment under braking occurs at an early phase of the corner entry, when the vehicle is almost braking in a straight line. This is indicated by the lateral acceleration at this point which is approximately 4m/s^2 .

In the high speed case, at 60m/s (see Figure 6.3), the driven rear wheels are having to operate at higher longitudinal slip ratios, to overcome the increased levels of drag at this speed. As a result, the total lateral force capability of the rear axle is reduced. A consequence of this is that the switch in torque transfer direction occurs more quickly between braking and positive acceleration regions (when compared to the 20m/s case). This is evident in the closer contours surrounding this transition area (see region 1). The magnitude of the peak yaw moment under braking (-1509Nm) is very similar to that seen at lower speeds, since braking forces are relatively independent of vehicle speed. Since the vehicle is close to its terminal velocity, the peak oversteer moment occurs at a small negative longitudinal acceleration of -1m/s^2 . Furthermore, as the selected gear ratio is low, the engine is operating at a lower torque level. This results in a smaller differential input torque, and a smaller LSD torque bias. The associated yaw moment has reduced by over 40% to 1518Nm.

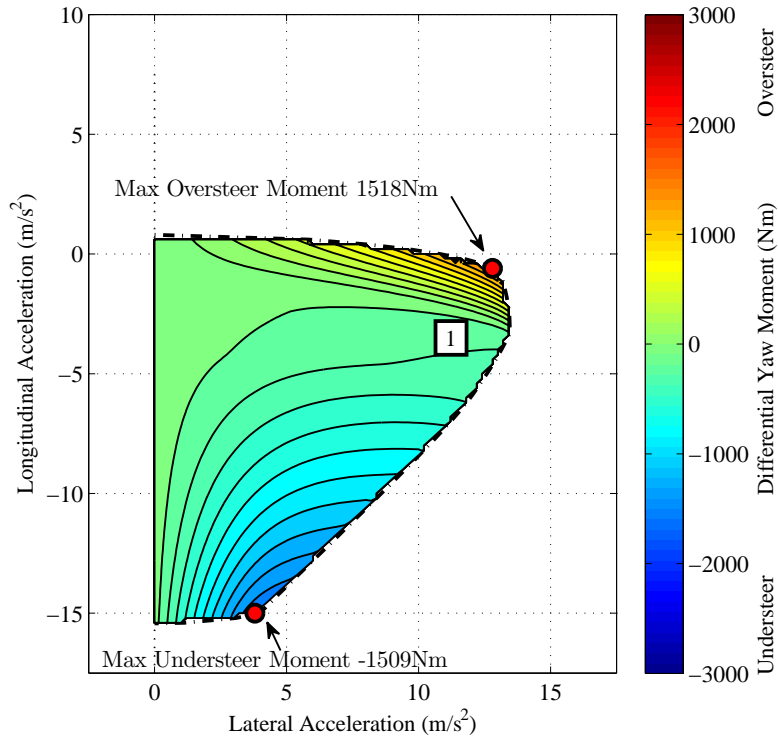


Figure 6.3: Differential yaw moment contours - plate LSD (60m/s)

These findings suggest that the ability of torque sensing devices to stabilise the vehicle under braking do not change with speed. Under acceleration however, the LSD oversteer moment decreases significantly with vehicle speed.

6.2.2 Speed Sensing VC

The yaw moment contour generated by a speed sensing VC LSD is shown both at 20m/s in Figure 6.4 and at 60m/s in Figure 6.5. The VC parameters used in the analysis are detailed in Table 6.3.

Table 6.3: VC setup and fluid parameters

Parameter	Symbol	Value
No. of shear faces	Z_s	60
Base fluid viscosity	$\nu_{\theta 0}$	300 kSt
Plate separation	s_v	0.13mm
Plate geometry factor	K_a	0.86
Temperature-viscosity constant	A_{sv}	0.18
Critical shear rate	$\dot{\gamma}_b$	55 - 200s ⁻¹
Shear rate-viscosity slope	m_{sf}	-0.565
Silicon fluid density	ρ_v	970 kg m ⁻³
Silicon fluid mass	m_s	43g
Silicon specific heat capacity	c_s	1500 J kg ⁻¹ K ⁻¹

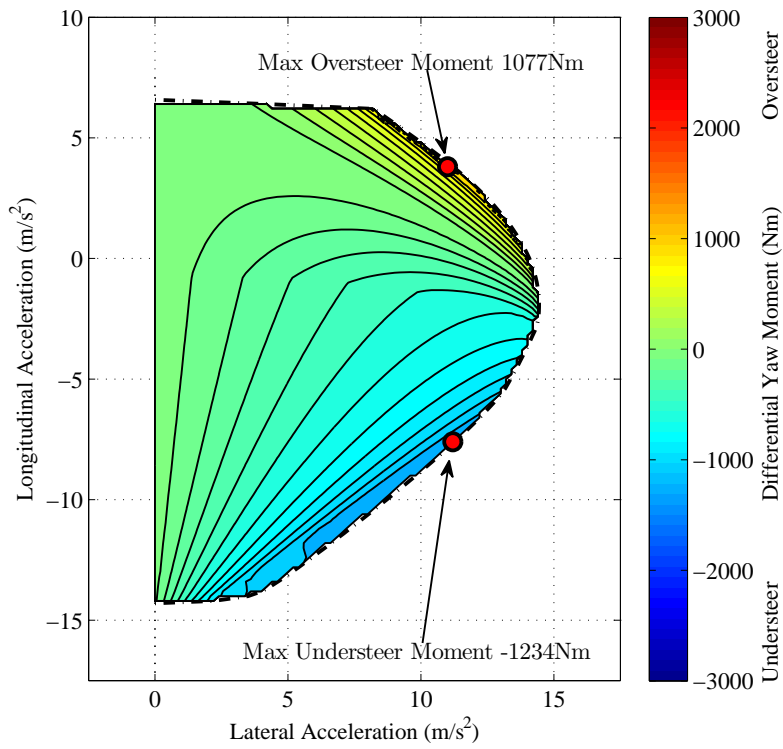


Figure 6.4: Differential yaw moment contours - VC LSD (20m/s)

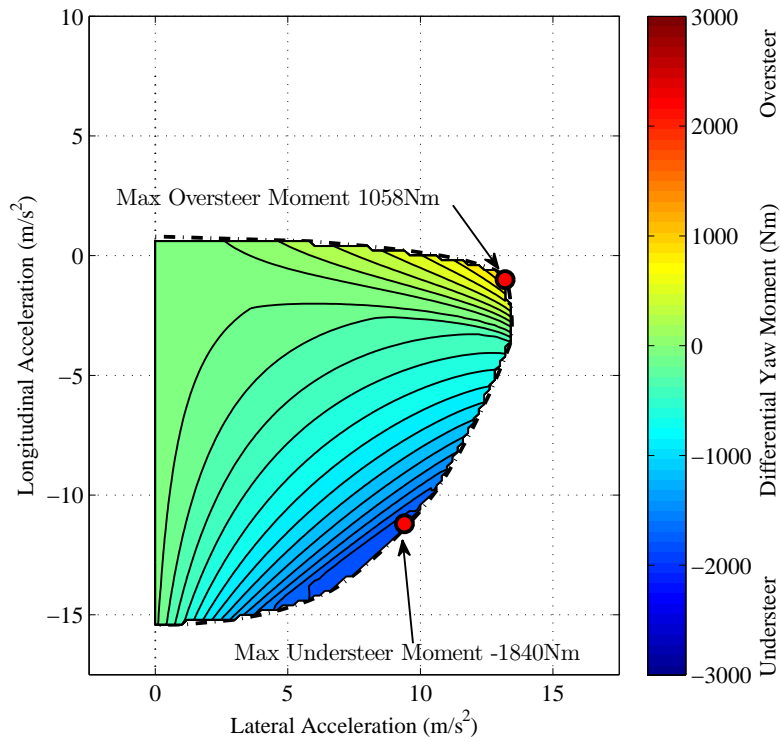


Figure 6.5: Differential yaw moment contours - VC LSD (60m/s)

What is immediately apparent is the change in shape of the contours. In the torque sensing case (Figures 6.2 and 6.3), the contours were strongly dependent on longitudinal acceleration, since this is coupled to the resultant torque flowing through the transmission. In the speed sensing case, yaw moments are shown to be more dependent on lateral acceleration levels. Evidently, this is coupled to the fact that the torque bias now relies on wheel speed difference. Higher lateral accelerations (for a given speed) mean a tighter cornering radius and a larger difference between inner and outer wheel speeds.

In the low speed case at 20m/s (see Figure 6.4), there is also a shift in the location of the peak understeer moment under braking. This has migrated from a lateral acceleration level of 4m/s^2 in the plate LSD case (Figure 6.2), to over 11m/s^2 with the VC. One can infer therefore, that the VC is likely to provide its largest stabilising understeer moment, much closer to the corner apex (where peak lateral acceleration occurs), than the torque sensing equivalent. Another noticeable trend is an increase in the yaw moment magnitude from -1234Nm at 20m/s, to -1840Nm at 60m/s. At first this appears counter-intuitive, as one would expect lower wheel speed differences at higher speeds, since the inner and outer path radii that the wheels follow should be smaller for an equivalent acceleration point. However, in this region of heavy braking and cornering, the inside rear wheel is close to locking up in both the low and high speed case. The wheel speed difference is therefore dictated by the outside wheel, which of course, will produce a greater wheel speed difference and resultant torque bias at higher speeds. This is also highlighted by the increase in the GG area in this braking region, between 20 and 60m/s.

6.2.3 Speed and Torque Sensing VCP

To demonstrate the influence of the speed and torque sensing VCP, a plate differential with the parameters defined in Table 6.2, is paired with a VC with 40 shear faces. The remaining VC parameters are identical to those defined in Table 6.3. The low and high speed yaw moment contours are presented in Figures 6.6 and 6.7.

As one might expect, the resulting contour shapes are a combination of the speed and torque sensing contours presented in earlier sections. Interestingly, little difference in the contour shape, or maximum oversteer moment is seen at both speeds, when compared to the pure torque sensing case (Figures 6.2 and 6.3). At 20m/s, the oversteer moment has increased by 0.3% and only increases by 4.48% at 60m/s. In this instance, the high ramp locking gradient (generated by the 30° drive ramp angle) has almost entirely locked the axle and hence the wheel speed difference is very low. The additional torque bias that the VC can support in this region is therefore very small.

Under braking conditions, the difference is far more substantial. The maximum understeer moment has increased by over 64% at both speeds, with appreciably larger GG boundaries under combined braking and cornering. This can be explained by the more conservative 45° coast ramps providing more open baseline characteristics. In this instance, the VC can make a much bigger contribution to the total torque bias since the axle is further away from locking (i.e. wheels are not as close to synchronising).

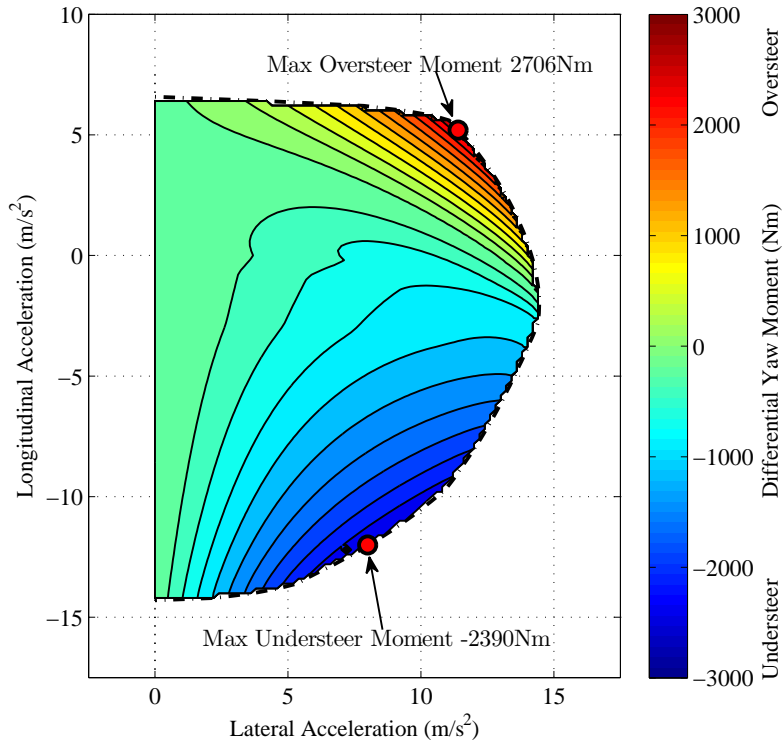


Figure 6.6: Differential yaw moment contours - VCP LSD (20m/s)

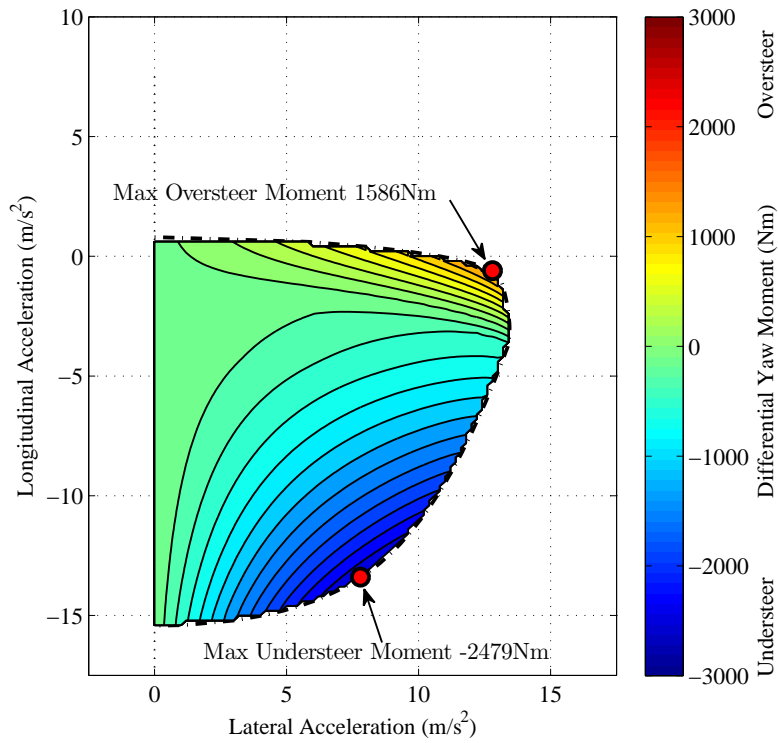


Figure 6.7: Differential yaw moment contours - VCP LSD (60m/s)

6.3 The Stability vs Agility Balance

The QSS lap simulation described in Chapter 5 was used to generate a theoretical optimum setup which yielded the quickest lap time. Experience has shown however, that this does not always result in a quicker vehicle on track, if the balance between stability and agility does not let the driver fully explore the limits of the vehicle. In qualitative terms, this normally means preventing the unwanted instability brought on by excessive oversteer during the braking phase of corner, without detrimentally affecting the agility of the vehicle (with excessive understeer), during the corner exit phase. It is therefore key to evaluate the impact of setup changes on both ultimate lap time and the stability-agility balance.

In the method which follows, stability and agility contours bounded by the GG envelope are found using multiple linearisations of the vehicle model at different operating points. This linearised system is then used to generate eigenvalues to show system stability and extract a yaw rate response transfer function for vehicle agility. By unifying both the limit condition and the vehicle stability-agility contours into one framework, a more practical method of relating vehicle handling to the specific manoeuvre type on track is presented. It also provides a more intuitive basis on which to optimise vehicle handling characteristics for specific vehicle conditions or to suit varying driver preferences.

6.3.1 Vehicle Model Linearisation

In this analysis, Lyapunov's indirect or linearisation method [96] is used to generate a localised, linear description of the entire GG envelope. The lateral and yaw chassis degrees of freedom, and the four wheel motions described in Equations 4.2 - 4.3, 4.25 - 4.26 and 4.32 - 4.33, can be expressed as a system of equations with the state variables:

$$\frac{dV}{dt} = f_1(U, V, r, \omega_1, \omega_2, \omega_3, \omega_4, \delta_{rw}, T_3, T_4, T_{bf}, T_{br}) \quad (6.8)$$

$$\frac{dr}{dt} = f_2(U, V, r, \omega_1, \omega_2, \omega_3, \omega_4, \delta_{rw}, T_3, T_4, T_{bf}, T_{br}) \quad (6.9)$$

$$\frac{d\omega_n}{dt} = f_{2+n}(U, V, r, \omega_1, \omega_2, \omega_3, \omega_4, \delta_{rw}, T_3, T_4, T_{bf}, T_{br}), \quad n = 1..4 \quad (6.10)$$

where the system inputs are the steering angle δ_{rw} , rear wheel torques T_3, T_4 and the front and rear axle brake torques T_{bf}, T_{br} . Each QSS acceleration point within the GG envelope represents a trimmed operating point such that:

$$f_{1..2}(U_0, V_0, r_0, \omega_{1,0}, \omega_{2,0}, \omega_{3,0}, \omega_{4,0}) = 0 \quad (6.11)$$

where V_0 and r_0 are the trimmed state variable values of side slip velocity and yaw rate at the QSS acceleration point, and $\omega_{1..4,0}$ the wheel speeds. The rates of change of the wheel speeds are not zero since the vehicle is considered in the quasi steady state. Referring back to the wheel constraint Equation 5.12, rearranging for $\dot{\omega}_n$ and substituting a_{xj} for

\dot{U} and r_0 for r , the resulting wheel accelerations can then be described as:

$$f_3(U_0, V_0, r_0, \omega_{1,0}, \omega_{2,0}, \omega_{3,0}, \omega_{4,0}) = \frac{\omega_{1,0} a_{xj}}{U_0 + r_0 \frac{t_f}{2}} \quad (6.12)$$

$$f_4(U_0, V_0, r_0, \omega_{1,0}, \omega_{2,0}, \omega_{3,0}, \omega_{4,0}) = \frac{\omega_{2,0} a_{xj}}{U_0 - r_0 \frac{t_f}{2}} \quad (6.13)$$

$$f_5(U_0, V_0, r_0, \omega_{1,0}, \omega_{2,0}, \omega_{3,0}, \omega_{4,0}) = \frac{\omega_{3,0} a_{xj}}{U_0 + r_0 \frac{t_r}{2}} \quad (6.14)$$

$$f_6(U_0, V_0, r_0, \omega_{1,0}, \omega_{2,0}, \omega_{3,0}, \omega_{4,0}) = \frac{\omega_{4,0} a_{xj}}{U_0 - r_0 \frac{t_r}{2}} \quad (6.15)$$

Although the Magic Formula tyre model [69] describes steady state tyre forces, it is highly nonlinear in form. As a result, tyre forces are also linearised about the operating slip conditions and normal tyre load. An example of the lateral tyre force linearisation is shown diagrammatically in Figure 6.8. Using a Taylor series expansion, the linearised

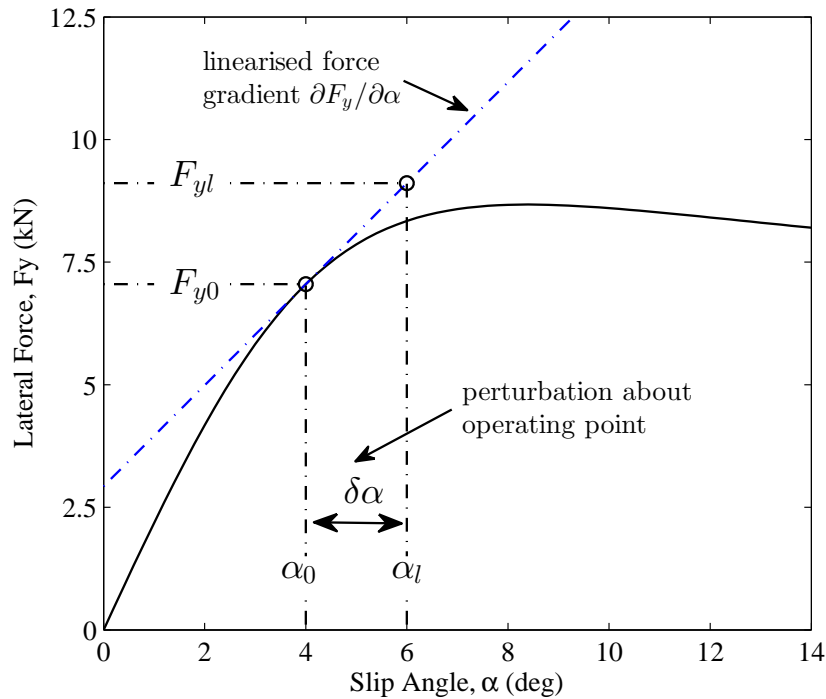


Figure 6.8: Linearised lateral tyre force

force resulting from a small perturbation can be defined as:

$$F_{yl} = F_{y0} + \delta\alpha \left. \frac{\partial F_y}{\partial \alpha} \right|_{\alpha=\alpha_0} \quad (6.16)$$

where the slip angle perturbation $\delta\alpha$, and linearised coefficient $C_{\alpha 0}$ are described by:

$$\delta\alpha = \alpha_0 - \alpha_l \quad (6.17)$$

$$C_{\alpha 0} = \left. \frac{\partial F_y}{\partial \alpha} \right|_{\alpha=\alpha_0} \quad (6.18)$$

Similarly, this process is repeated for longitudinal tyre forces such that:

$$F_{xl} = F_{x0} + \delta\kappa \left. \frac{\partial F_x}{\partial \kappa} \right|_{\kappa=\kappa_0} \quad (6.19)$$

where the slip ratio perturbation $\delta\kappa$, and longitudinal coefficient $C_{\kappa 0}$ are defined by:

$$\delta\kappa = \kappa_0 - \kappa_l \quad (6.20)$$

$$C_{\kappa 0} = \left. \frac{\partial F_x}{\partial \kappa} \right|_{\kappa=\kappa_0} \quad (6.21)$$

The linearised tyre forces can be expressed in terms of the state variables and the linearised tyre force gradients $C_{\alpha 0}$, $C_{\kappa 0}$. These can be substituted back into Equations 6.8 - 6.10 to give a complete linear system model. These are put into standard state space form, so that the rates of change of the vehicle states with regard to a small perturbation can be defined by:

$$\delta\dot{\mathbf{X}} = \mathbf{A}_j \delta\mathbf{X} + \mathbf{B}_j \delta\mathbf{U} \quad (6.22)$$

$$\delta\mathbf{Y} = \mathbf{C} \delta\mathbf{X} \quad (6.23)$$

Where $\delta\mathbf{X}$ and $\delta\mathbf{U}$ are state and input vectors and \mathbf{C} the output matrix of the system.

$$\delta\mathbf{X} = \begin{bmatrix} V - V_0 \\ r - r_0 \\ \omega_1 - \omega_{10} \\ \omega_2 - \omega_{20} \\ \omega_3 - \omega_{30} \\ \omega_4 - \omega_{40} \end{bmatrix}, \quad \delta\mathbf{U} = \begin{bmatrix} \delta_{rw} - \delta_{rw_0} \\ T_3 - T_{30} \\ T_4 - T_{40} \\ T_{bf} - T_{bf_0} \\ T_{br} - T_{br_0} \end{bmatrix}, \quad \mathbf{C} = \mathbf{I}^{6 \times 6}$$

\mathbf{A}_j and \mathbf{B}_j are the Jacobian of the \mathbf{A} and \mathbf{B} state and input matrices. For the interested reader, a more complete description of their formulation is included in Appendix E.

6.3.2 Eigenvalue Analysis

Section 1.4.1 outlined the use of eigenvalues for representing system stability. For QSS systems however, inferences drawn from eigenvalue analysis should only be used with caution. This has been shown to be especially relevant when eigenvalues are near or cross the imaginary axis [26, 95]. Although eigenvalues cannot represent a true nonlinear description of stability in all situations, they are strongly linked to inherent system stability. They are presented here as a qualitative measure, providing a more practical and intuitive basis to compare setup changes which are likely to influence the driver’s perception of stability. The eigenvalues, λ_e of the linearised \mathbf{A}_j matrix can be found at each longitudinal a_{xi} , and lateral a_{yi} , acceleration point, by solving the associated characteristic equation:

$$\det(\mathbf{A}_j - \lambda_e \mathbf{I}) = 0 \tag{6.24}$$

In Figures 6.9 and 6.10, the dominant (most positive) real part of the system eigenvalues have been plotted throughout the GG envelope at 20 and 60m/s. The contours are created for the same RWD vehicle considered in previous sections (see Appendix D), fitted with the plate LSD parameters in Table 6.2. The chosen grid spacing between acceleration points was 0.2m/s^2 .

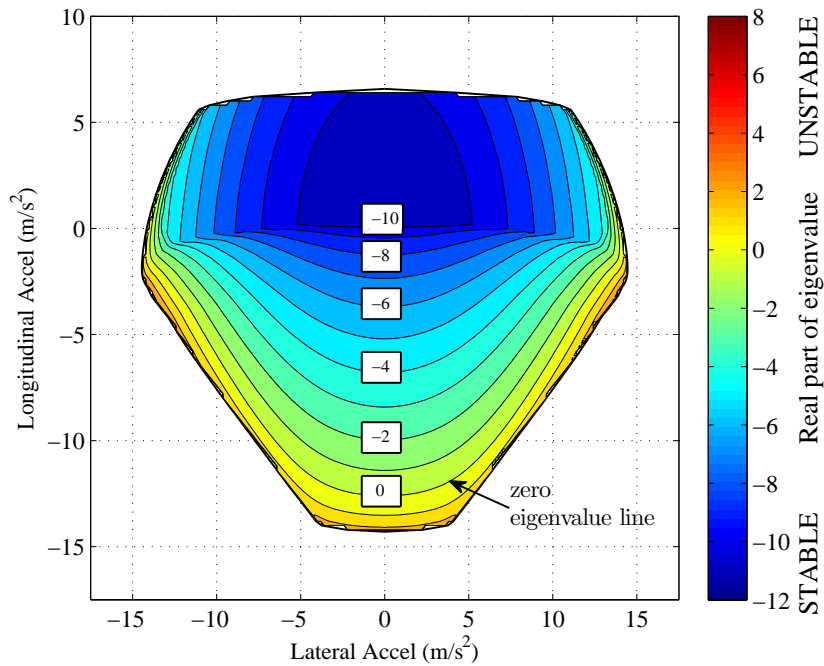


Figure 6.9: Eigenvalue contour throughout GG envelope at 20m/s (plate LSD)

At 20m/s, it is apparent that the system is mostly stable, exhibiting negative eigenvalues, except under very hard braking conditions. This indeed follows subjective driver observations, in which the vehicle feels most unstable and more likely to adopt oversteer behaviour during combined heavy braking and cornering. There is also a marked difference in the stability contour between driving and braking conditions. Under positive acceleration, there are relatively small changes in stability as longitudinal acceleration increases. Conversely, under braking, the system shows a

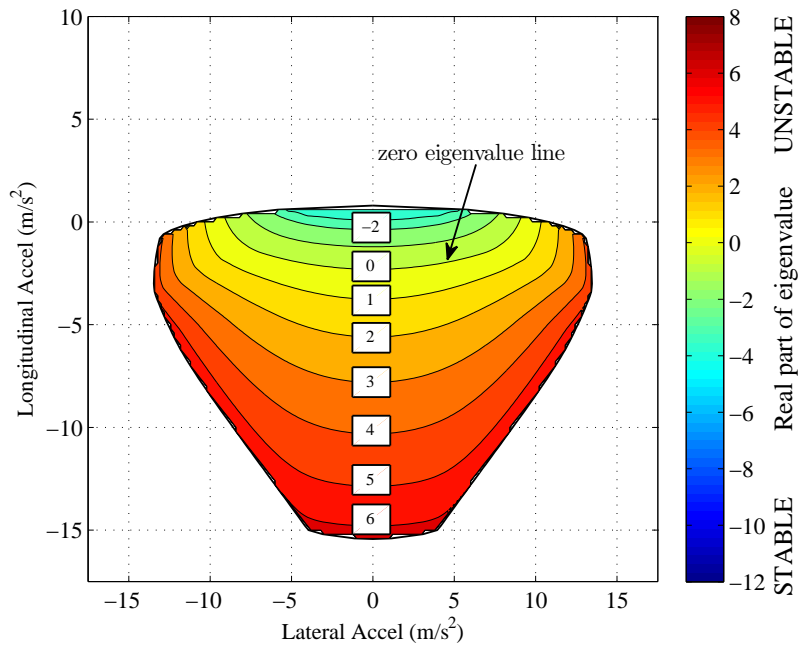


Figure 6.10: Eigenvalue contour throughout GG envelope at 60m/s (plate LSD)

much greater sensitivity, since longitudinal load transfer has ensured the rear wheels cannot support the same lateral force as the front.

In Figure 6.10 at 60m/s, a large proportion of the GG envelope is dominated by positive eigenvalues, indicating that the system is largely open loop unstable at this speed. Of course, open loop instability under braking conditions is known to occur [122, 47] and underlines the importance of the driver in vehicle stability considerations. This raises an important question as to the level of open loop instability that skilled racing drivers can tolerate. Nevertheless, the characterisation of open loop stability gives useful insights into the impact of setup changes. Addressing this question, for the time being at least, remains outside the scope of this work.

In order to qualitatively validate eigenvalues generated from the QSS method, they have been compared to equivalent eigenvalues found from the linearisation of the full nonlinear simulation model outlined in Chapter 4. The model was used in closed loop form, with preview steering and PI controllers determining the vehicle trajectory and speed. These were used to carry out a 150m radius skid pan manoeuvre, whilst maintaining the velocity profile detailed in Figure 6.11a. This provided a 3m/s^2 constant acceleration to a steady state speed of 40m/s, followed by a 3m/s^2 deceleration back down to 20m/s. Five time points ($t_1 - t_5$) are highlighted and correspond to equivalent acceleration points on the QSS eigenvalue contours. The simulation model has been linearised at 0.1s time intervals and the dominant eigenvalues shown in Figure 6.11b. The equivalent QSS points are overlaid and also summarised in Table 6.4.

As in the QSS contour case, Figure 6.11b shows that the dominant eigenvalues move closer to zero as speed increases. The largest changes occur at 7.2s, as the vehicle transitions from constant acceleration to the steady state, and again at 12.6s, where the

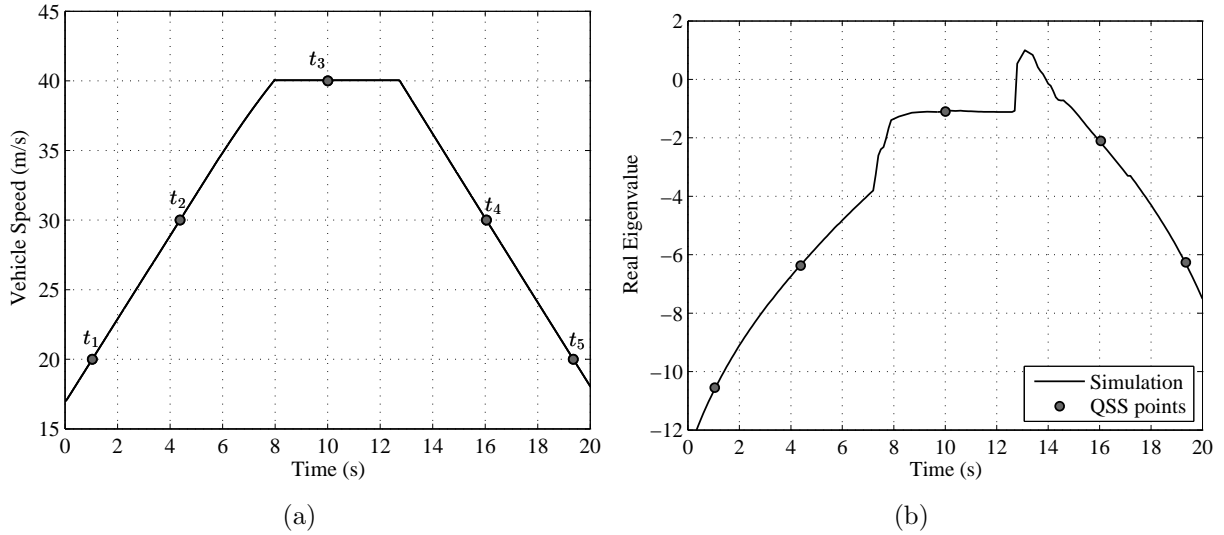


Figure 6.11: a) Velocity profile for 150m radius skid pan nonlinear simulation
 b) eigenvalues of linearised simulation model generated at 0.1s intervals, overlaid with equivalent QSS points at $t_1 - t_5$

Table 6.4: QSS and simulation model eigenvalue summary

Time Point (s)	Speed (m/s)	Long Accel (m/s ²)	Lat Accel (m/s ²)	λ - QSS	λ - Simulation	Difference (%)
$t_1 = 1.0$	20	3	2.7	-10.67	-10.55	1.17
$t_2 = 4.4$	30	3	6.0	-6.34	-6.37	0.55
$t_3 = 10.0$	40	0	10.7	-1.05	-1.08	3.02
$t_4 = 16.0$	30	-3	6.0	-2.20	-2.10	4.80
$t_5 = 19.4$	20	-3	2.7	-6.38	-6.26	1.85

vehicle starts to decelerate. This actually forces the eigenvalue into the positive region for a brief period. There are small errors (below 5% - see Table 6.4) between QSS and simulation eigenvalues due to the interpolation scheme used to find eigenvalues over the QSS contour (these errors can be further reduced by using a smaller interval between feasibility grid points). Nevertheless, the small error demonstrates that the QSS optimisation routine is able to find realistic operating points, which generate eigenvalue contours that vary progressively and demonstrate behaviour typically experienced by race drivers (namely a destabilisation of the vehicle under braking and near the lateral acceleration limit).

6.3.3 Yaw Rate Analysis

Although not the only metric used for directional authority, the yaw rate response [43] has proved a successful indicator of transient behaviour and in many cases, correlated well with subjective driver evaluations [116, 1]. In this analysis, it is used to get a sense of how the open loop control potential of the vehicle changes throughout the performance envelope.

The steering - yaw rate transfer function can be extracted from the linearised system by taking the Laplace transform of Equations 6.22 and 6.23:

$$s\delta\mathbf{X}(s) = \mathbf{A}_j\delta\mathbf{X}(s) + \mathbf{B}_j\delta\mathbf{U}(s) \quad (6.25)$$

$$\delta\mathbf{Y}(s) = \mathbf{C}\delta\mathbf{X}(s) \quad (6.26)$$

By rearranging Equation 6.25 for $\delta\mathbf{X}(s)$ and substituting into Equation 6.26 yields:

$$\delta\mathbf{Y}(s) = \mathbf{C}_{tf}((s\mathbf{I} - \mathbf{A}_j)^{-1}\mathbf{B}_{tf}\mathbf{U}(s)) \quad (6.27)$$

where

$$\mathbf{B}_{tf} = [1 \ 0 \ 0 \ 0 \ 0 \ 0]^T \quad (6.28)$$

$$\mathbf{C}_{tf} = [0 \ 1 \ 0 \ 0 \ 0 \ 0] \quad (6.29)$$

which defines a single input, single output (SISO) system. The transfer function describing the response between steering input δ_{rw} , and the resultant yaw rate r , can be described by:

$$\delta\mathbf{H}(s)_{\delta_{rw}}^r = \delta\mathbf{Y}(s)/\delta\mathbf{U}(s) \quad (6.30)$$

substituting Equation 6.27 into 6.30 gives:

$$\delta\mathbf{H}(s)_{\delta_{rw}}^r = \mathbf{C}_{tf}((s\mathbf{I} - \mathbf{A}_j)^{-1}\mathbf{B}_{tf}) \quad (6.31)$$

It should be noted that when analysing the yaw rate response, it is typical to evaluate both the absolute yaw rate gain and the associated bandwidth, both of which are inter-related. In an effort to define a metric that more practically relates to the agility of the vehicle, a bespoke yaw rate bandwidth metric is defined. This is expressed as the bandwidth $f_{\delta_{rw}}^r$, in Hz, when the yaw rate gain (in rad/s/rad) reaches an absolute value of $1/\sqrt{2}$. This can be thought of as the range of frequencies for which a reference yaw rate response is achievable. Due to the large variation in vehicle responses throughout the GG region, the bandwidth has been normalised by its value at the acceleration point $a_x = 0$ and $a_y = 0$. The bandwidth is again found for multiple linearisation points, and has been generated for the plate differential parameter set in Table 6.2. The resulting contours at 20 and 60m/s are shown in Figures 6.12 and 6.13.

At 20m/s (Figure 6.12), the peak normalised yaw bandwidth contour of 1.1 occurs during heavy straight-line braking. This is due to the reduced vertical load on the rear tyres generating increased levels of oversteer. Note that the system eigenvalues are

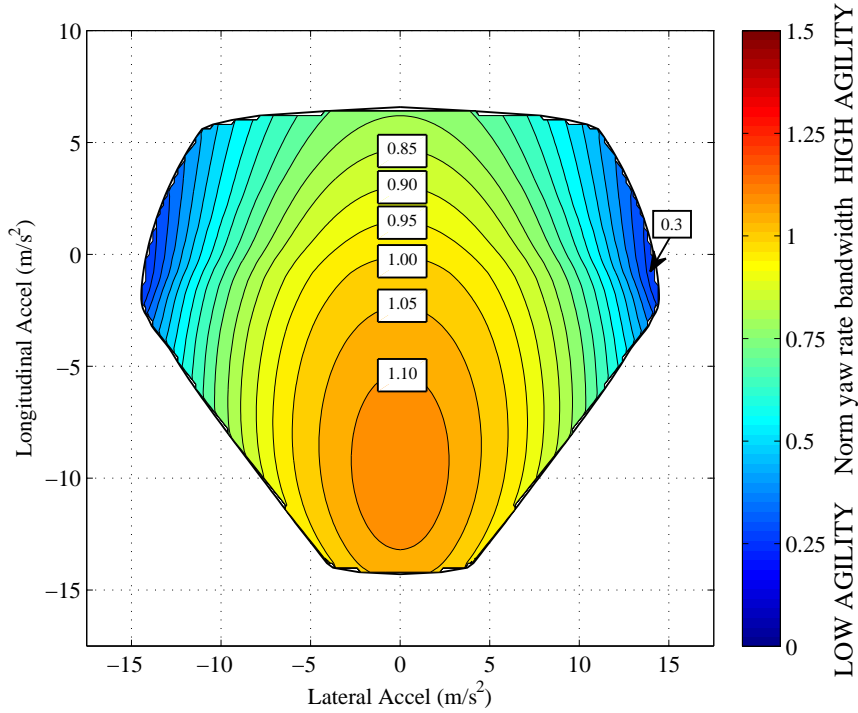


Figure 6.12: Normalised yaw rate bandwidth at 20m/s (plate LSD)

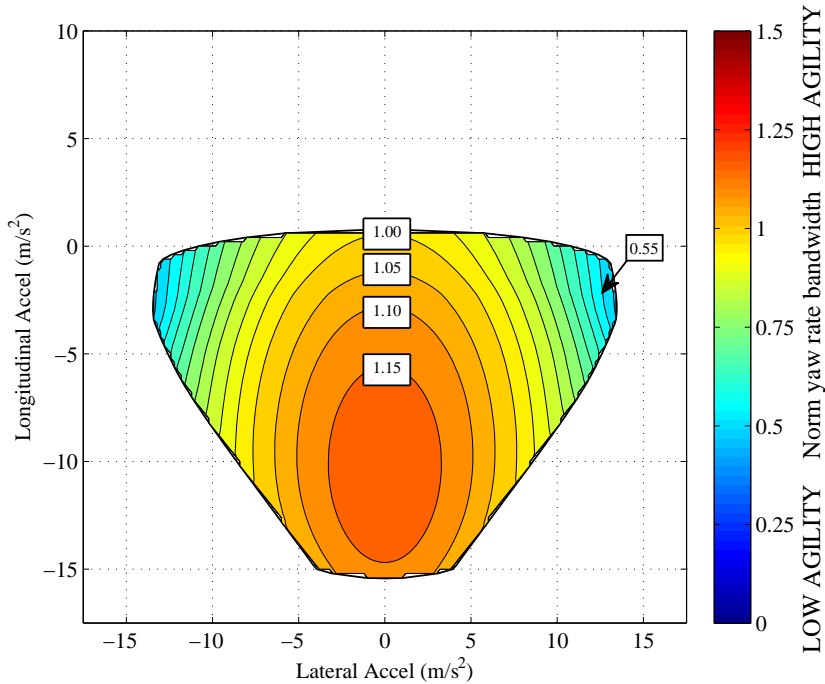


Figure 6.13: Normalised yaw rate bandwidth at 60m/s (plate LSD)

bordering on unstable at this stage (see Figure 6.9). Indeed, a skilled race driver will be able to use this increase in yaw response to help turn in the vehicle faster [67]. However, this is a delicate balance, as increases in lateral acceleration during this braking region rapidly decreases yaw bandwidth as the vehicle moves to more unstable oversteer. Under positive longitudinal acceleration, the yaw response reduces, since vertical loads

on the front tyres have decreased and mild understeer behaviour dominates. As the lateral acceleration limit of the vehicle approaches, the yaw bandwidth diminishes to approximately 0.3. A yaw response bode plot for a constant longitudinal acceleration of 0.4m/s^2 is shown in Figure 6.14. This confirms that the drop in yaw rate bandwidth at higher lateral accelerations (13m/s^2), is due to a reduced yaw response and a decrease in yaw damping, more typical of understeer behaviour [1]. This is due to the base vehicle configuration having a slight forward weight bias, and the understeer yaw moment generated from the differential in this region (see region 1, Figure 6.2).

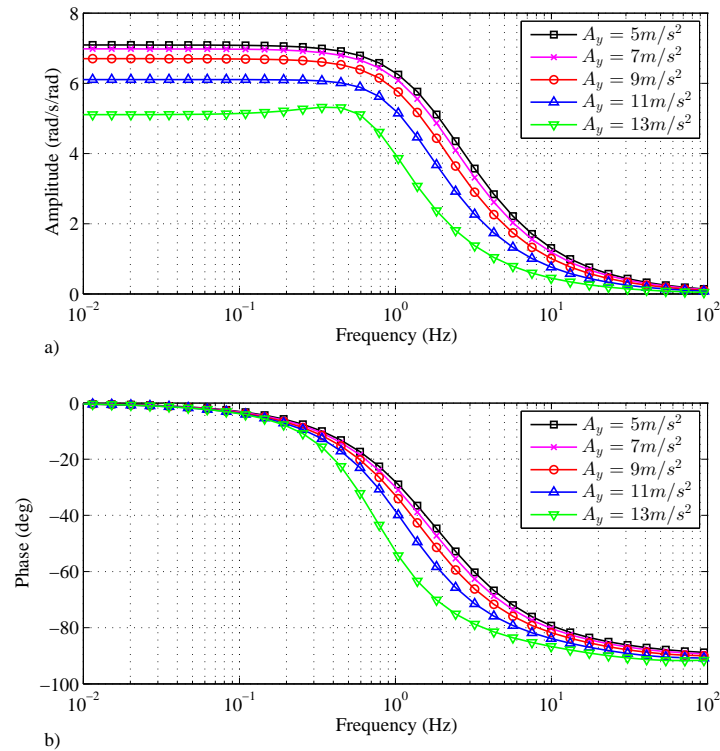


Figure 6.14: a) Yaw rate response amplitude plot at 20m/s , $a_x = 0.4\text{m/s}^2$
 b) yaw rate response phase plot at 20m/s , $a_x = 0.4\text{m/s}^2$

At 60m/s (Figure 6.13), the yaw bandwidth contours look similar, with the heavy braking regions giving the peak bandwidth contour of 1.15. One of the marked differences however, is the bandwidth at the peak lateral acceleration, which is shown to increase to approximately 0.55. A potential explanation for this is that the car is more balanced at high speed, since some of the rear axle lateral capacity has been lost with the increased longitudinal slip needed to overcome increased drag forces. The resulting loss in lateral grip has balanced out the inherent understeer at low speed, providing a more agile yaw response.

The eigenvalue analysis (Figure 6.10) has confirmed that the system is largely open loop unstable in the braking regions, and at the lateral acceleration limit during mild positive accelerations. The yaw response bode plot at a longitudinal acceleration of 0.4m/s^2 is shown in Figure 6.15 and illustrates how the yaw response increases as the lateral limit of 8m/s^2 is approached. At this stage, the rear axle is starting to saturate to the point of instability. For all but a small positive longitudinal acceleration, low lateral

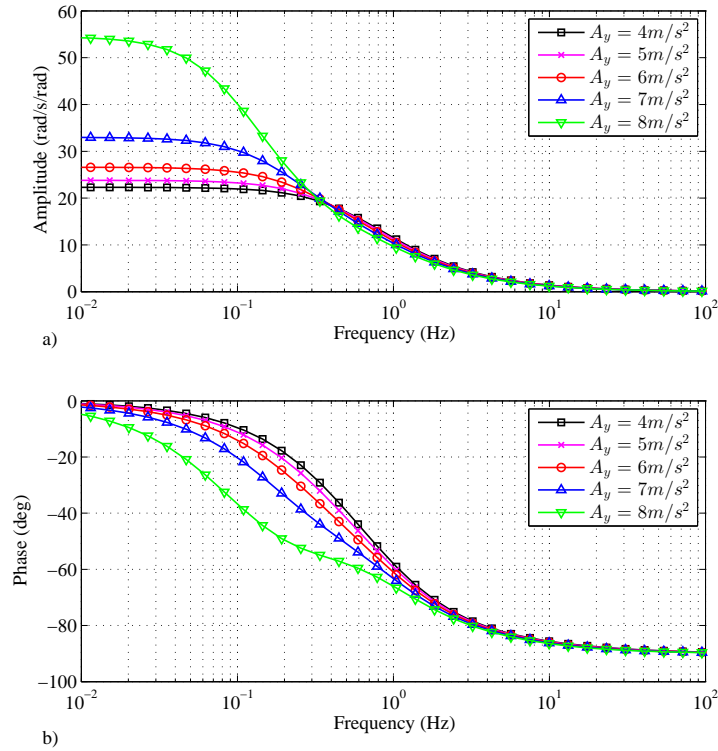


Figure 6.15: a) Yaw rate response amplitude plot at 60m/s, $a_x = 0.4\text{m/s}^2$
 b) yaw rate response phase plot at 60m/s, $a_x = 0.4\text{m/s}^2$

acceleration region, the system is critically damped, indicative of oversteer behaviour [1]. It is important to note that for the stable, negative eigenvalue case, the bandwidth measurement is valid indefinitely since all transient parts of the yaw response fall to zero. However, in the unstable, positive eigenvalue case, the bandwidth value only applies at the instant where the frozen time value is taken and where all transient parts of the response are assumed to be zero. The use of yaw rate bandwidth in the unstable case has provided insight, but must be used with caution.

6.3.4 Understeer Angle

To qualitatively confirm these findings with a more practical measure of handling, an additional metric, in the form of an understeer angle can also be defined within the feasibility region. This is a simplistic, but useful comparison between the vehicle's steer angle and the theoretical (low speed) kinematic steer angle required to negotiate a turn. Several authors [10, 15, 47] have used this to give an indication of the handling balance under limit conditions. The kinematic steer angle δ_k , can be defined as:

$$\delta_k = \frac{l r}{U} \quad (6.32)$$

and the resulting understeer angle is then simply:

$$\delta_{ua} = \delta_{rw} - \delta_k \quad (6.33)$$

Positive understeer angles indicate understeer behaviour, while negative values, oversteer. The understeer angle contours (in degrees) have been plotted at 20 and 60m/s in Figures 6.16 and 6.17.

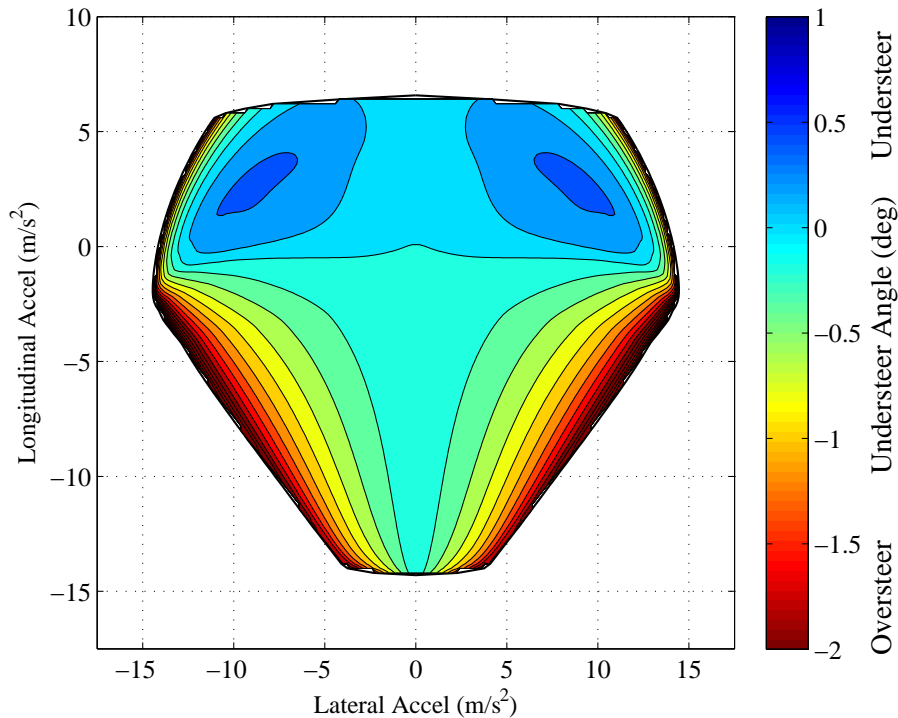


Figure 6.16: Understeer angle contour (20m/s)

These plots demonstrate the behaviour witnessed in the earlier frequency analysis (see Figures 6.14 and 6.15) is consistent with what one would expect from a RWD vehicle with a slight forwards weight bias and identical front and rear tyres. At 20m/s and 0.4m/s^2 longitudinal acceleration, the vehicle starts to understeer as lateral acceleration approaches 13m/s^2 . This correlates with the decrease in system damping illustrated in Figure 6.14a. As lateral acceleration increases further to its limit of 14m/s^2 , the understeer angle turns negative very quickly, indicating that the rear tyres have saturated and the vehicle has started to become unstable. Closer inspection of the eigenvalue contours in this region (see Figure 6.9) reinforce these findings, in that they turn positive and the contour spacing (hence rate of change) has become much smaller.

In the high speed case, at 60m/s (see Figure 6.17), at the same longitudinal acceleration of 0.4m/s^2 , negative understeer angles dominate. Here, no understeer is seen at lower lateral accelerations, and the vehicle progressively increases its level of oversteer as the lateral limit is reached at 13.5m/s^2 . This is consistent with the critically damped yaw response shown in Figure 6.15, which decreases its bandwidth as the lateral limit is approached.

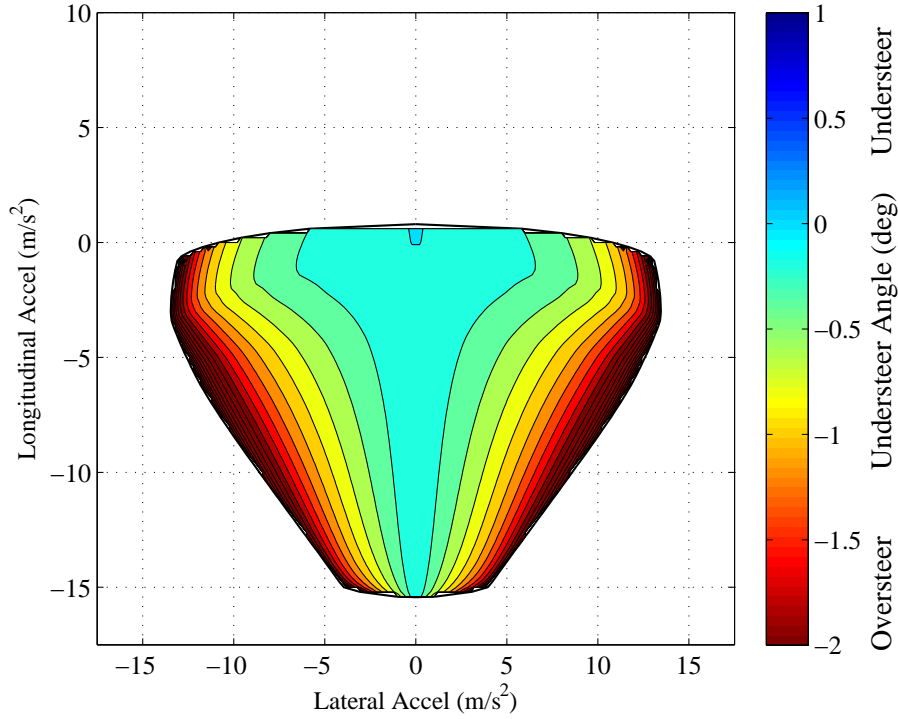


Figure 6.17: Understeer angle contour (60m/s)

6.4 Setup Change Example

In order to show how the methods described can be used to demonstrate changes in the driveability of the vehicle, three different plate differential parameter sets are defined in Table 6.5. Setup A is a more benign configuration, with higher 60° drive and coast ramp angles promoting a lower torque bias. Setup B is a more aggressive configuration, with lower 30° drive and 40° coast ramp angles, giving much higher levels of bias torque. Setup C is identical to Setup B, apart from the addition of 225Nm drive-side negative preload.

Table 6.5: Plate differential setup parameters

Parameter	Symbol	Setup A	Setup B	Setup C
Drive ramp angle	θ_{rd}	60°	30°	30°
Coast ramp angle	θ_{rc}	60°	40°	40°
Number of friction faces	z_f	16	16	16
Positive preload	T_{pp}	20	20	20
Drive negative preload	T_{np}	0Nm	0Nm	225Nm

6.4.1 Stability and Agility

To illustrate how quick and practical comparisons can be made between differential setups, four key acceleration points ($a_{y1..4}$, $a_{x1..4}$), can be defined close to the GG envelope edge (see Figure 6.18a). These are designed to relate to generalised braking (1), corner entry (2), apex (3) and corner exit (4) phases. It is acknowledged that the relation between these acceleration points and typical cornering phases is open to considerable variation due to driving style. These points are chosen for illustrative purposes only. A suggestion as to how these points relate to positions during a typical 90° corner manoeuvre is shown in Figure 6.18b.

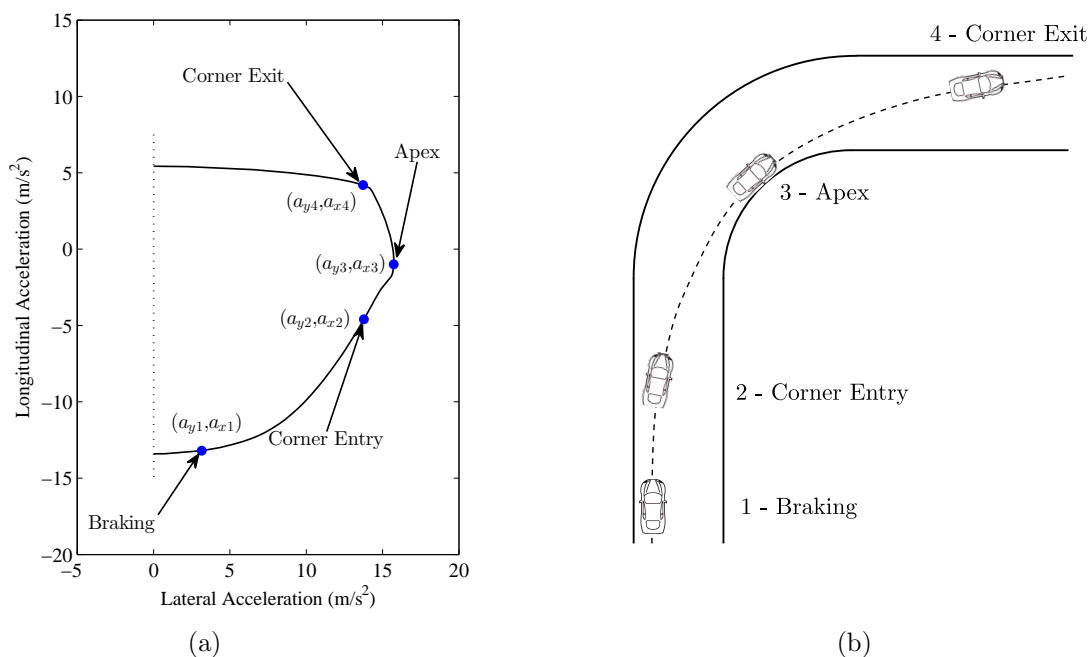


Figure 6.18: a) GG edge contour with cornering phases
b) cornering phases on 90° bend

The dominant eigenvalues and normalised yaw rate bandwidth for each of these acceleration points are shown at 20m/s in Table 6.6 and at 60m/s in Table 6.7. At 20m/s, setup B is shown to reduce eigenvalues at all phases of the corner (compared to setup A), indicating a widespread increase in relative stability. As one might expect, setup C shows no difference in the braking and corner entry phases, but does indicate a decrease in stability at the corner apex, since the eigenvalue becomes more positive. In terms of vehicle agility, the increases in stability during the entry phases have been met with an associated decrease in bandwidth, mainly due to the greater differential understeer moment generated under braking. Vehicle agility during the apex phase is similar between all setups, although during the corner exit, the higher torque bias levels of setup B and C increases bandwidth. This can be explained by the generation of a larger oversteer moment in this corner phase, helping to turn the vehicle and make it more agile.

Table 6.6: Eigenvalue and yaw rate bandwidth setup comparison (20m/s)

	Braking	Corner Entry	Apex	Corner Exit
Long Accel Point (m/s ²)	$a_{x1} = -11.0$	$a_{x2} = -5.8$	$a_{x3} = -1.0$	$a_{x4} = 4.4$
Lat Accel Point (m/s ²)	$a_{y1} = 5.2$	$a_{y2} = 11$	$a_{y3} = 14.0$	$a_{y4} = 11$
Setup A - $\text{Re}(\lambda_A)$	1.67	3.16	-0.22	-4.92
Setup B - $\text{Re}(\lambda_B)$	0.91	2.19	-0.43	-5.23
Setup C - $\text{Re}(\lambda_C)$	0.91	2.19	-0.12	-5.22
Setup A - $f_{A,\delta_{rw}}^r$	1.18	0.81	0.25	0.40
Setup B - $f_{B,\delta_{rw}}^r$	1.16	0.78	0.24	0.43
Setup C - $f_{C,\delta_{rw}}^r$	1.16	0.78	0.25	0.43

Table 6.7: Eigenvalue and yaw rate bandwidth setup comparison (60m/s)

	Braking	Corner Entry	Apex	Corner Exit
Long Accel Point (m/s ²)	$a_{x1} = -12.0$	$a_{x2} = -7.4$	$a_{x3} = -1.4$	$a_{x4} = 0.4$
Lat Accel Point (m/s ²)	$a_{y1} = 5.2$	$a_{y2} = 10$	$a_{y3} = 12.8$	$a_{y4} = 10$
Setup A - $\text{Re}(\lambda_A)$	6.61	6.67	3.60	0.15
Setup B - $\text{Re}(\lambda_B)$	6.18	6.13	4.08	0.90
Setup C - $\text{Re}(\lambda_C)$	6.18	6.13	3.78	0.78
Setup A - $f_{A,\delta_{rw}}^r$	1.29	1.04	0.53	0.70
Setup B - $f_{B,\delta_{rw}}^r$	1.26	1.01	0.56	0.73
Setup C - $f_{C,\delta_{rw}}^r$	1.26	1.01	0.54	0.73

At 60m/s (see Table 6.7) stability is again seen to increase in the braking and corner entry phases. However, during the apex and corner exit, the higher torque bias of setup B increases eigenvalues, indicating an associated decrease in relative stability. This behaviour has been alleviated to some extent by the use of negative preload in setup C, which is shown to improve stability in both apex and corner exit phases. Changes to the yaw bandwidth in the entry phases are again similar to trends seen at 20m/s. However, the more aggressive torque bias characteristics of setup B and C are shown to improve agility both at apex and corner exit phases. This can be explained by the nature of the torque bias at high speed. Since the switch to an oversteer differential yaw moment happens much earlier in the cornering phase (see Figure 6.3), the vehicle is more unstable, but agile as a result.

6.5 Handling Optimal Methods

Throughout this chapter, the feasibility region within the GG envelope has been used to extract information about the LSD yaw moment imparted to the vehicle, and how this influences stability and agility under different acceleration conditions. This provides a useful framework on which to make predictions about vehicle handling in different cornering phases, both at low and high speed. The real benefit of this methodology however, is the ability to incorporate stability and agility metrics in the optimisation process itself. In this way, the LSD torque bias can be tailored to suit a whole range of varying driver styles. Referring back to Section 1.4, it is worth reiterating that while optimising the magnitude of the GG envelope will maximise the performance potential of the vehicle, optimising the stability and agility contours should allow the driver to extract the most from it.

The challenge of course, is in deciding what level of stability or agility will give the driver confidence, and ultimately allow one particular setup to be more ‘driveable’ than another. The quantitative correlation of these objective metrics with subjective driver assessments is therefore a key part of this process. This area of research is vast, with several authors having attempted to quantify driveability more rigorously [1, 62, 116]. This task however, is outside the scope of this research. Instead, to demonstrate the method, some assumptions are made as to the type of contours a race driver may prefer; namely a highly agile vehicle below the limit, but one which feels more stable as the limit is reached [67].

To achieve this within the current GG framework, the original feasibility conditions given in Equations 6.5 and 6.6 can be modified to include both the dominant system eigenvalue ($\lambda_{e_{max}}$) and the yaw rate bandwidth $f_{\delta_{rw}}^r$. Weighting factors placed on both metrics can then be used to define their relative importance.

A grid of acceleration points are illustrated in Figure 6.19, with the weighting on stability and agility linearly scaled from high agility at low lateral accelerations, to high stability at peak lateral accelerations. For each longitudinal acceleration point, a maximum lateral limit is defined such that for:

$$\dot{U} = a_{xj}, \quad j = 1 \dots p \quad (6.34)$$

$$Ur = a_{yi}, \quad i = 1 \dots m \quad (6.35)$$

Within the grid of acceleration points, the maximum lateral acceleration at the edge of the GG envelope can be expressed as:

$$a_{ymax,j} = \max(a_{yi}) \quad (6.36)$$

The objective function uses the weighting factors Ws and Wa which are linearly scaled between zero and one. For each grid point therefore, the resulting objective function is to minimise:

$$J = Ws_{j,i} \lambda_{e_{max}} - Wa_{j,i} f_{\delta_{rw}}^r \quad (6.37)$$

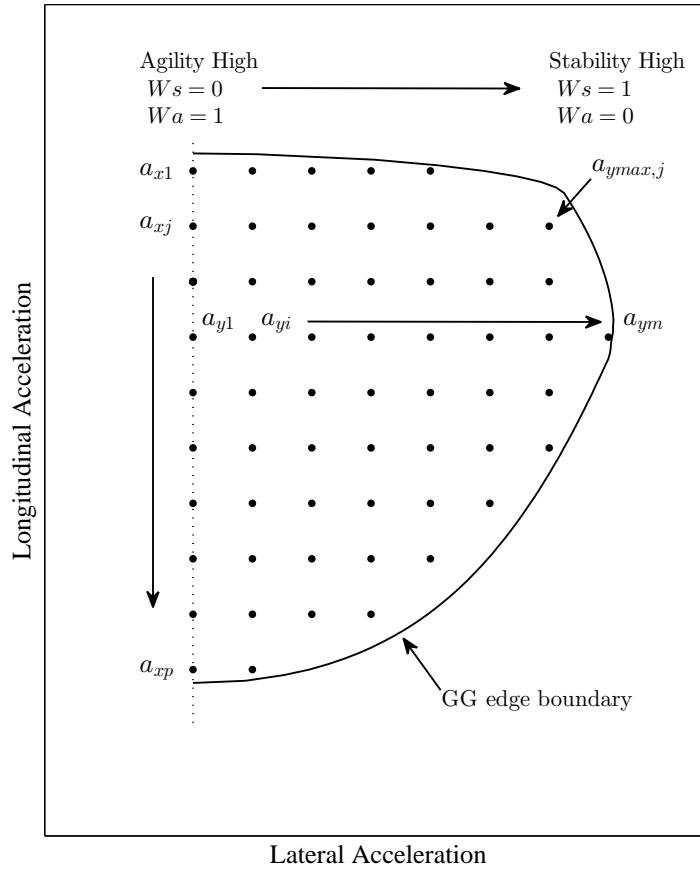


Figure 6.19: GG acceleration point grid

where W_s represents the weighting factor applied to the dominant eigenvalue:

$$W_{s_{j,i}} = \frac{a_{yi} - a_{ymax,j}}{a_{ymax,j}} + 1, \quad i = 1 \dots m \quad j = 1 \dots p \quad (6.38)$$

Similarly, the weighting factor applied to the yaw rate bandwidth is:

$$W_{a_{j,i}} = 1 - W_{s_{j,i}} \quad (6.39)$$

The active LSD model described in Section 5.7 is used to demonstrate the method for the RWD saloon racing vehicle previously described (see Appendix D). The resulting LSD yaw moment and hydraulic pressure contours at 20m/s are illustrated in Figures 6.20 and 6.21.

The hydraulic pressure across the vast majority of the GG envelope remains at zero indicating that an open differential gives the quickest yaw response at lower lateral accelerations. Under combined braking and cornering conditions however, the pressure progressively increases to its maximum (200bar), which is where the peak understeer moment of -2690Nm is generated. In this region, close to the lateral acceleration limit, this understeer moment is helping to stabilise the vehicle. Conversely, under combined positive acceleration and cornering conditions, the hydraulic pressure also increases, to give a peak oversteer moment of 2456Nm. On the face of it, this seems

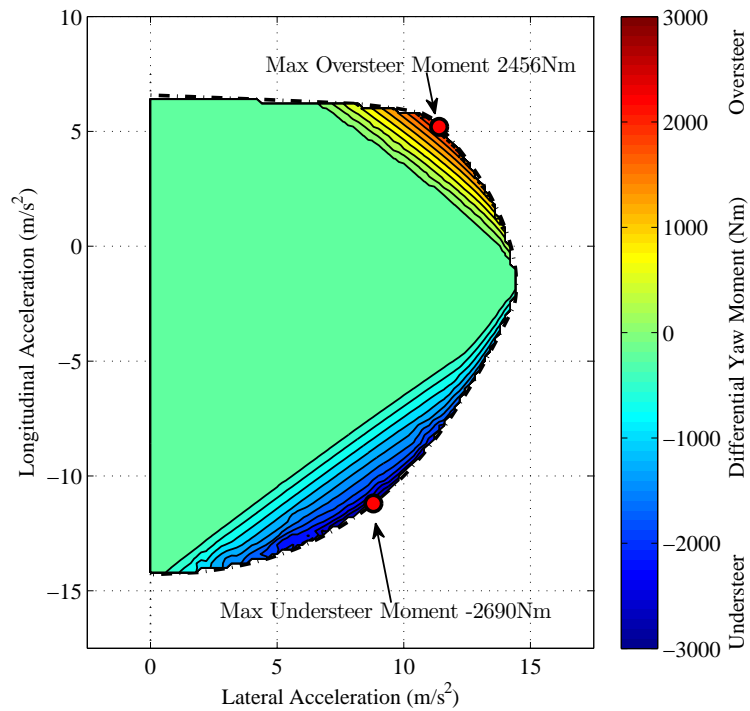


Figure 6.20: Active LSD yaw moment contours (20m/s)

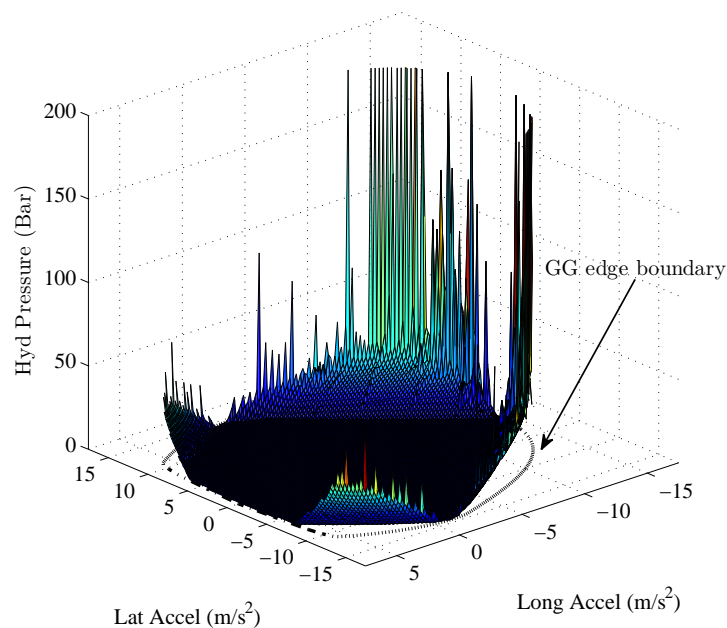


Figure 6.21: Active LSD pressure contour (20m/s)

counter-intuitive, since the optimiser should be promoting more stabilising understeer moments as the GG boundary is reached. Even in the active LSD case however, only the magnitude, not the direction of the torque transfer can be controlled (this is as a result of the driven wheel speed difference). Even so, this raises a secondary question as to why the optimiser has not limited the oversteer moment to zero. This can be

explained by the influence of lateral load transfer. In reality, the acceleration points in this region would not even be feasible without some kind of oversteer moment. A torque bias to the outer, more loaded outside wheel is required, to give an overall level of traction capable of maintaining these acceleration points. All that the optimiser can do in this instance (to maximise stability at peak lateral acceleration), is to limit the magnitude of the oversteer moment. When comparing to the passive plate LSD characteristics detailed in Figure 6.2, it is apparent that the peak oversteer moment has reduced from 2698Nm (in the passive case), to 2456Nm in the active case (-9.8%). Overall, the minimisation of the objective function has forced the optimiser to delay the onset of the torque bias to improve agility, but limit the maximum torque bias magnitude to improve stability at the lateral acceleration limit.

The results from the high speed case at 60m/s are shown in Figures 6.22 and 6.23. The most pronounced difference is in the reduction of the peak oversteer moment. This has reduced to only 748Nm and occurs in a very limited region of the GG envelope. The remainder of the area leading up to this, demonstrates essentially open differential behaviour. At this higher speed, the optimiser was able to find feasible acceleration points, by limiting the magnitude of the oversteer moment to maintain vehicle stability at the limit. Interestingly, if a comparison is again made to the passive plate LSD case (Figure 6.3) the yaw moment is under half that of the passive LSD (1518Nm). This reinforces the earlier findings (see Section 5.7), that the torque bias must be reduced at higher speeds due to the higher operational slip ratio of the rear tyres.

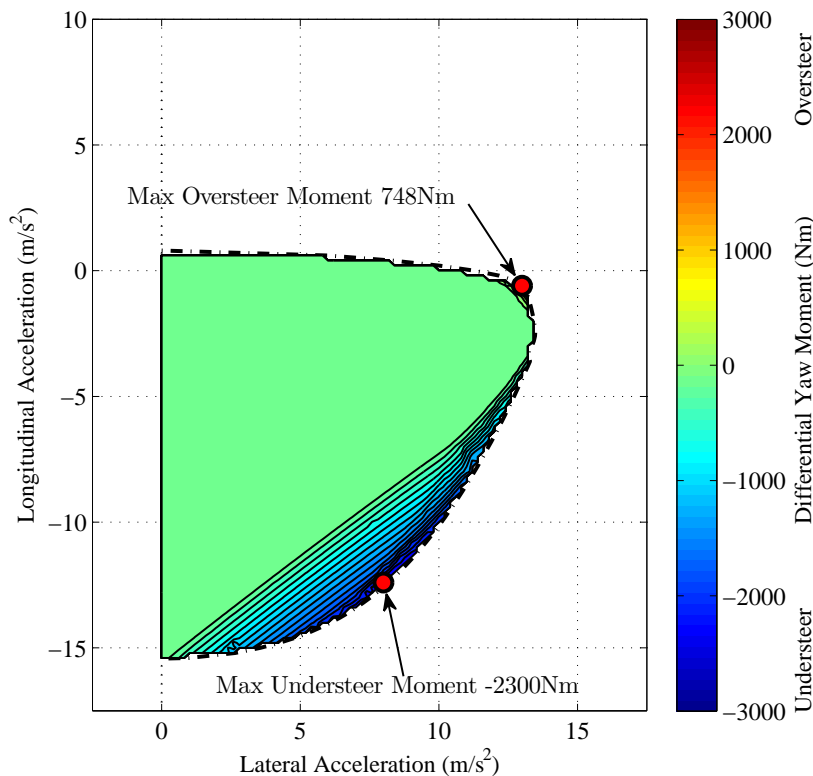


Figure 6.22: Active LSD yaw moment contours (60m/s)

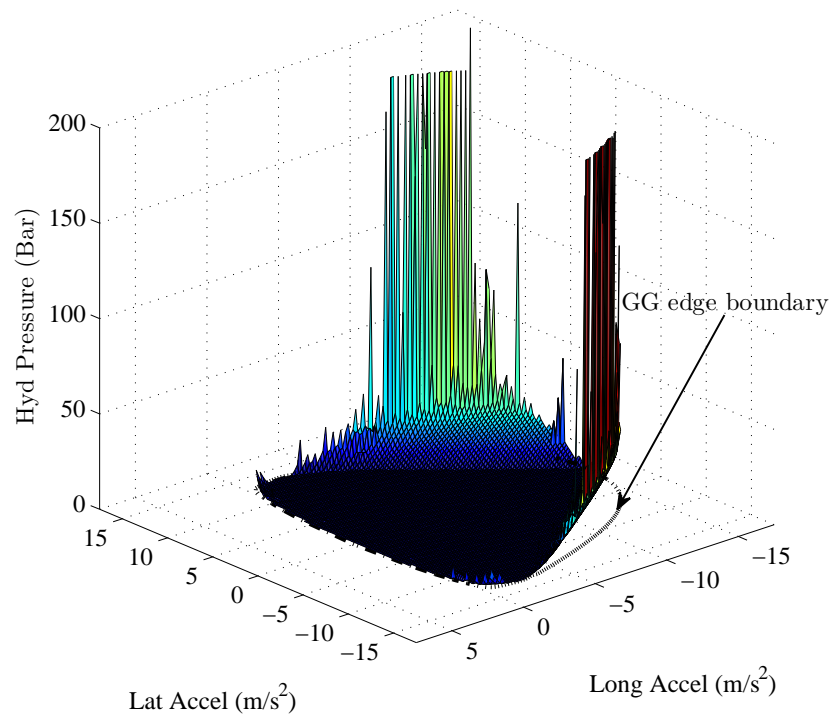


Figure 6.23: Active LSD pressure contour (60m/s)

6.6 Conclusions

In this chapter, an exploration into how the vehicle states are changing up to the GG limit is presented. The QSS optimisation routine described in Chapter 5 has been extended, to allow a number of vehicle parameters to be defined within a so-called feasibility region, bounded by the GG edge. This framework was used to demonstrate the behaviour of a number of torque and speed sensing LSD devices throughout the envelope.

The yaw moment generated by a torque sensing, plate LSD was shown to be highly dependant on longitudinal acceleration. This device generated its peak yaw moments in regions of the GG map which correspond to typical entry and exit phases of a corner. Due to the strong coupling between the induced yaw moment and the gearbox torque, moments generated under acceleration reduced with vehicle speed. Conversely, moments generated under braking remained more constant throughout the vehicle speed range.

The yaw moment contours from a VC LSD illustrated that speed sensing devices provide their greatest yaw moments much closer to the peak lateral acceleration region. This corresponds to a point much closer to the apex of a typical corner. Under positive longitudinal acceleration, yaw moments remain constant between low and high speed regimes. Under braking however, these increase significantly with vehicle speed, due to the inevitable speed difference seen between the outer wheel, and an inner wheel which is close to locking up.

The same feasibility region method was also used to investigate vehicle driveability. The vehicle model was linearised at multiple operating points, to allow stability and agility metrics to be extracted. The resulting GG contour of dominant eigenvalues were shown to qualitatively represent typical behaviour seen by racing drivers; namely an unstable vehicle under heavy braking and at the lateral acceleration limit. Vehicle agility was represented by a bespoke yaw rate bandwidth metric. The resulting contours again demonstrated behaviour similar to that experienced by skilled drivers.

The driveability metrics were evaluated at four key points in the GG contour, designed to replicate the braking, corner entry, apex and corner exit conditions of a typical 90° bend manoeuvre. For the plate LSD setups considered, higher levels of torque bias increased stability at low speeds, but reduced the associated vehicle agility. At higher speeds, increased locking under positive acceleration actually made the car more unstable. These detrimental effects were shown to be alleviated to some extent, with the use of negative preload.

Finally, these concepts are developed into a methodology to tailor the torque bias across the GG region, to suit a particular driveability metric contour. In the future, it is intended that this should allow LSD torque bias characteristics to be better suited to individual driver requirements.

Chapter 7

Dynamic Time Optimal Solutions

This chapter builds on the QSS time optimal solutions presented in Chapter 5 by presenting an alternative, dynamic time optimal method. Nonlinear optimal control theory is used to allow both the vehicle control history and the racing line to be optimised for minimum manoeuvre time. The differential torque bias is included in the optimisation process, allowing the optimal LSD torque bias throughout 90° bend and lane change manoeuvres to be found. Aspects of tyre wear are also addressed, in a qualitative comparison between open, locked and optimal LSD strategies. The chapter concludes with an assessment of how the optimal torque bias profile varies with road friction, and how these bias histories can be used to determine optimal passive plate LSD setup parameters.

7.1 Optimal Control Method

A review of optimal control methods was included in Section 1.3.2, but in general, its goal is to predict the inputs (in this case the steering, throttle and torque bias) required to minimise a specific performance index (i.e. manoeuvre time). Crucially, it also allows the full system dynamics to be included. This is important, as it means the influence of transient properties, like the yaw rate response or a lag in torque bias transfer, can be quantified in real terms. The provision for the racing line to be found from the process is also a significant advantage. From practical experience, it is known that the optimal vehicle setup, control history and racing line, are all elements which are strongly coupled to each other [15]. As a result, QSS methods can only ever give a partial view of the true optimal solution.

In the sections that follow, an indirect optimal control formulation is presented (see Section 1.3.2) which is based on application of Pontryagin's minimum principle [78]. This gives an analytical form of the necessary conditions for optimality, and uses Lagrange multipliers and penalty functions to transform the constrained problem into an unconstrained one. Although more complex to formulate, it is generally acknowledged that indirect solutions are more accurate and robust [3, 48]. To achieve this, some revisions to the original vehicle model described in Chapter 5 were necessary. Additional constraints have also been imposed, to replicate more realistic driver responses, system dynamics, as well as the track boundary itself.

7.1.1 Model Revisions

To better account for the influence of suspension dynamics on longitudinal and lateral load transfers, each normal tyre load is now described by the first order differential equation:

$$\tau_z \dot{F}_{zn} + F_{zn} = F_{zns}, \quad n = 1..4 \quad (7.1)$$

where F_{zn} is the resulting dynamic normal load, F_{zns} the steady state normal load calculated from Equations 4.8 - 4.11, and τ_z is the suspension time constant.

The engine torque delivery to the rear wheels has also been simplified, to allow a more compact description of the equations of motion of the wheels. The throttle control parameter u_{tb} , has been replaced with γ_t , which describes the maximum available torque to all four wheels under both driving and braking conditions. The revised expressions for the propulsive and brake torques delivered to the wheels is defined by:

$$T_1 = \frac{(1 - k_p)\gamma_t}{2}, \quad T_2 = \frac{(1 - k_p)\gamma_t}{2} \quad (7.2)$$

$$T_3 = \frac{k_p\gamma_t}{2} + T_{lock}, \quad T_4 = \frac{k_p\gamma_t}{2} - T_{lock} \quad (7.3)$$

where k_p describes the proportion of torque distribution between the front and rear wheels. In the driving case, $k_p = 1$ (for the RWD vehicle considered), and under braking conditions $k_p = 1 - B_f$. It should also be noted that the total difference between the torque at the left and right hand driven wheels is $T_3 - T_4 = 2T_{lock}$.

Due to the complexity of the original Pacejka tyre model [69] and the requirement of the vehicle equations of motion to be derived analytically, a simplified tyre model was employed. This captured the three dominant properties of the original model. Both the peak and location of the coefficient of friction vary with load, in both longitudinal and lateral tyre axes. Also, the slip stiffness relationship with load is retained in each of the tyre axes. A more detailed description of the model is given in Appendix F.

Another key difference between the proposed dynamic method and previous QSS methodologies, is that the racing line no longer needs to be predefined. In this case, the track is simply defined as a centreline with equidistant left and right hand track boundaries. The position and orientation of the vehicle on the road is tracked using a curvilinear coordinate system (s_t, s_v, ψ_d) , which is detailed in Figure 7.1. s_t is the position of the vehicle along the road centreline, s_v the lateral offset and ψ_d , the angle of the vehicle with respect to a tangent line at s_t . The differential equations relating the vehicle velocity to the track coordinates are:

$$\dot{s}_t = \frac{U \cos \psi_d - V \sin \psi_d}{1 - s_v k_t} \quad (7.4)$$

$$\dot{s}_v = U \sin \psi_d + V \cos \psi_d \quad (7.5)$$

$$\dot{\psi}_d = r - k_t \frac{U \cos \psi_d - V \sin \psi_d}{1 - s_v k_t} \quad (7.6)$$

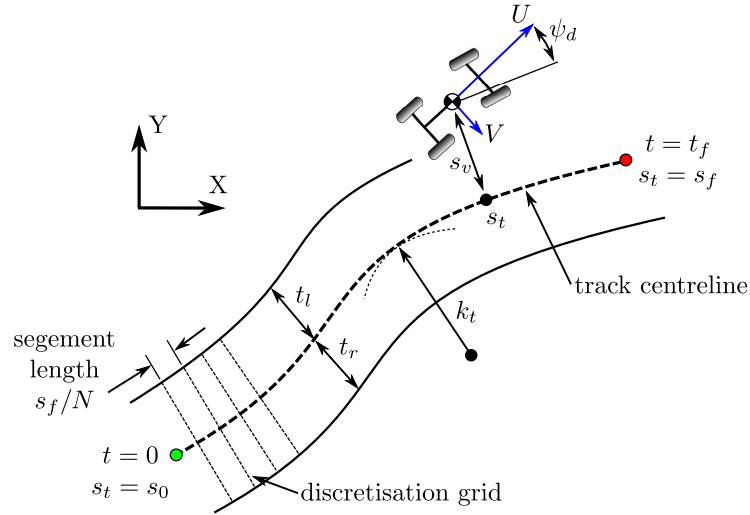


Figure 7.1: Curvilinear track coordinates

where k_t is the local curvature of the road.

The resulting vehicle model can then be described by a system of 14 first order nonlinear differential equations defined in Equations 4.1 - 4.3, 4.25 - 4.26 , 4.32 - 4.33, 7.1 and 7.4 - 7.6 and as many state variables:

$$\mathbf{x} = [U, V, r, \omega_1, \omega_2, \omega_3, \omega_4, F_{z1}, F_{z2}, F_{z3}, F_{z4}, s_t, s_v, \psi_d]^T \quad (7.7)$$

The control vector consists of the steering angle δ_{rw} , propulsive/brake torque γ_t and the LSD locking torque T_{lock} :

$$\mathbf{u} = [\delta_{rw}, \gamma_t, T_{lock}]^T \quad (7.8)$$

7.1.2 Inequality Constraints

In order to replicate physical limitations of the vehicle, track and the driver, a number of inequality constraints are included in the problem definition. These are used in combination with penalty functions (see Section 7.1.3) designed to penalise the performance index when these constraints are violated.

To reflect the maximum vehicle steering angle, this is limited to δ_{\max} , with the corresponding inequality constraint defined as:

$$|\delta_{rw}| \leq \delta_{\max} \quad (7.9)$$

Similarly, the rate of steering is limited to reflect the bandwidth of a human driver. This varies according to driver skill level, but normally ranges from 1-5 Hz [1, 61]:

$$\left| \dot{\delta}_{rw} \right| \leq \dot{\delta}_{\max} \quad (7.10)$$

Again, due to driver limitations and a lag in the engine and brake dynamics, a limit is imposed on the braking and throttling action γ_t :

$$|\dot{\gamma}_t| \leq \dot{\gamma}_{t_{\max}} \quad (7.11)$$

The engine is considered an idealised torque provider, always operating at its peak power P_{\max} . Due to the RWD configuration considered, the total power delivered to the rear wheels is therefore limited to:

$$\frac{\gamma_t}{2} (\omega_3 + \omega_4) \leq P_{\max} \quad (7.12)$$

As demonstrated in Section 3.4, the torque bias of a typical speed or torque sensing differential also exhibits a lag in its system response. To reflect this, a maximum torque bias rate is imposed:

$$\left| \dot{T}_{lock} \right| \leq \dot{T}_{lock_{\max}} \quad (7.13)$$

In addition, the torque bias direction is constrained to reflect the sign of the speed difference between driven wheels:

$$\text{sgn}(T_{lock}) = \text{sgn}(\omega_4 - \omega_3) \quad (7.14)$$

Finally, in order to keep the vehicle trajectory within the specified road geometry, the front and rear vehicle extremities are constrained to fall within the left and right track edges:

$$-t_l \leq s_v - b \sin \psi_d \leq t_r \quad (7.15)$$

$$-t_l \leq s_v + a \sin \psi_d \leq t_r \quad (7.16)$$

where t_l and t_r are the left and right hand road width boundaries respectively (see Figure 7.1). A summary of the inequality constraint values used in subsequent simulations are detailed in Table 7.1.

Table 7.1: Vehicle and track inequality constraint values

Parameter	Symbol	Value	Unit
Suspension time-lag	τ_z	0.2	s
Engine power	P_{\max}	215	kW
Braking torque distribution	k_p	0.48	-
Propulsive torque distribution	k_p	1.00	-
Max torque rate	$\dot{\gamma}_{t_{\max}}$	10	kNm/s
Max torque bias rate	$\dot{T}_{lock_{\max}}$	10	kNm/s
Max wheel steer angle	δ_{\max}	20	deg
Max wheel steer rate	$\dot{\delta}_{\max}$	100	deg/s
Left hand track boundary	t_l	5	m
Right hand track boundary	t_r	5	m

7.1.3 Solution of Equations

In this section, a summary of how the vehicle and track equations are formulated into the necessary conditions for optimality is described. The derivation is taken directly from Chapter 2 of Bryson [11], with some of the more complex steps generalised for conciseness. The vehicle model and track related variables describe a set of first-order nonlinear differential equations, representing the rate of change of the 14 state variables (see Equation 7.7) with respect to time:

$$\dot{\mathbf{x}} = \mathbf{f}(\mathbf{x}(t), \mathbf{u}(t)) \quad (7.17)$$

where:
$$\mathbf{x}(t_0) = \mathbf{x}_0, \quad t \in [t_0, t_f] \quad (7.18)$$

Since the goal of the optimisation is to minimise time, the independent variable must be transformed from time t , to the distance based track parameter, s_t . This is achieved with the use of the scaling factor $S_f(s)$:

$$\frac{d\mathbf{x}}{ds} = \frac{d\mathbf{x}}{dt} \cdot \left(\frac{ds}{dt}\right)^{-1} = \mathbf{f}(\mathbf{x}(t), \mathbf{u}(t)) S_f(s) = \mathbf{f}(\mathbf{x}(s), \mathbf{u}(s)) \quad (7.19)$$

where $s = s_t$ and:

$$S_f(s) = \left(\frac{ds}{dt}\right)^{-1} = \frac{1 - s_v k_t}{U \cos \psi_d - V \sin \psi_d} \quad (7.20)$$

The general form of the performance index originally presented in Equation 1.3 can therefore be modified to:

$$J = \phi[\mathbf{x}(s_f)] + \int_{s_0}^{s_f} L[\mathbf{x}(s), \mathbf{u}(s)] ds \quad (7.21)$$

where $s_0 = 0$ and s_f is the final manoeuvre distance. Since the intention is simply to maximise the vehicle velocity over the entire distance of the manoeuvre, the cost on the final states values $\phi[\mathbf{x}(s_f)]$ are not required and are set to zero. Thus, the resulting performance index only uses the second Lagrange term of Equation 7.21:

$$J = \int_{s_0}^{s_f} S_f(s) ds \quad (7.22)$$

where:

$$\mathbf{x}(s_0) = \mathbf{x}_0, \quad s \in [s_0, s_f] \quad (7.23)$$

The system equations describing the vehicle and track dynamics are considered as an equality constraint and are adjoined to Equation 7.22 with the vector of Lagrange multipliers $\boldsymbol{\lambda}$, to describe the augmented performance index \bar{J} :

$$\bar{J} = \int_{s_0}^{s_f} [H(s) - \boldsymbol{\lambda}^T(s) \dot{\mathbf{x}}] ds \quad (7.24)$$

where the Hamiltonian $H(s)$ is defined by:

$$H(s) = L[\mathbf{x}(s), \mathbf{u}(s)] + \boldsymbol{\lambda}^T(s)\mathbf{f}[\mathbf{x}(s), \mathbf{u}(s)] \quad (7.25)$$

The integral term in Equation 7.24 can be separated out:

$$\bar{J} = \int_{s_o}^{s_f} H(s) ds - \int_{s_o}^{s_f} \boldsymbol{\lambda}^T(s)\dot{\mathbf{x}} ds \quad (7.26)$$

and the second term of Equation 7.26 can be integrated by parts to give:

$$\bar{J} = \int_{s_o}^{s_f} H(s) ds - \left\{ [\boldsymbol{\lambda}^T(s)\mathbf{x}(s)]_{s_o}^{s_f} - \int_{s_o}^{s_f} \dot{\boldsymbol{\lambda}}^T(s)\mathbf{x}(s) ds \right\} \quad (7.27)$$

which can be simplified to:

$$\bar{J} = -\boldsymbol{\lambda}^T(s_f)\mathbf{x}(s_f) + \int_{s_o}^{s_f} [H(s) + \dot{\boldsymbol{\lambda}}^T(s)\mathbf{x}(s)] ds + \boldsymbol{\lambda}^T(s_o)\mathbf{x}(s_o) \quad (7.28)$$

For the performance index to reach an extremum, the gradient at the stationary point must be zero. By taking partial derivatives with respect to $\mathbf{x}(t)$ and $\mathbf{u}(t)$, and considering the change from a small change $\delta\mathbf{u}(t)$ in the input, the change in the performance index $\delta\bar{J}$, can then be defined as:

$$\delta\bar{J} = [-\boldsymbol{\lambda}^T\delta\mathbf{x}]_{s=s_f} + [\boldsymbol{\lambda}^T\delta\mathbf{x}]_{s=s_o} + \int_{s_o}^{s_f} \left[(\mathbf{H}_x + \dot{\boldsymbol{\lambda}}^T)\delta\mathbf{x} + \mathbf{H}_u\delta\mathbf{u} \right] ds \quad (7.29)$$

where \mathbf{H}_x and \mathbf{H}_u are the derivatives of the Hamiltonian H with respect to \mathbf{x} and \mathbf{u} . In practice, solution of Equation 7.29 involves solving the following set of equations:

$$-\boldsymbol{\lambda}^T(s_f) = 0 \quad (7.30)$$

$$\boldsymbol{\lambda}^T(s_o) = 0 \quad (7.31)$$

$$\mathbf{H}_x + \dot{\boldsymbol{\lambda}}^T = 0 \quad (7.32)$$

$$\mathbf{H}_u = 0 \quad (7.33)$$

Equations 7.30, 7.32 and 7.33 constitute the Euler-Lagrange equations in the calculus of variations [11]. Equation 7.32 is also known as the co-state equation and is a measure of the sensitivity of the performance index to changes in the state variables. Constraints on the end values of the states are included by modifying Equation 7.28 to include the additional term of the form:

$$\boldsymbol{\psi}[\mathbf{x}(s_f)] = 0 \quad (7.34)$$

where $\boldsymbol{\psi}$ is simply a vector of functions of the final states at $s = s_f$. The derivation of $\delta\bar{J}$ in Equation 7.29 therefore includes an additional $\boldsymbol{\nu}^T\boldsymbol{\psi}_x$ term on the right hand side,

where $\boldsymbol{\nu}$ is the associated Lagrange multiplier and $\boldsymbol{\psi}_x$ the gradient of $\boldsymbol{\psi}$ with respect to \mathbf{x} . It follows that the modified version of Equation 7.30 is therefore defined as:

$$\boldsymbol{\nu}^T \boldsymbol{\psi}_x - \boldsymbol{\lambda}^T(s_f) = 0 \quad (7.35)$$

So far, equality constraints have been included in the performance index through the use of Lagrange multipliers. The inequality constraints defined in Section 7.1.2 however, are included through the summation of a number (equal to q) of penalty functions. For example, when the track boundaries or maximum steering angle is exceeded, the penalty function magnitude increases significantly, preventing non-feasible solutions being pursued. Equation 7.24 can be modified to include these extra penalty terms:

$$\bar{J} = \int_{s_o}^{s_f} [H(s) + \sum_{i=1}^q p_i [d_i(\mathbf{x}(s), \mathbf{u}(s))] - \boldsymbol{\lambda}^T(s) \dot{\mathbf{x}}] ds \quad (7.36)$$

where p_i represents a penalty function of the form [3]:

$$p_i = \left(1 + \frac{d_i}{h_i}\right)^{n_i} \quad (7.37)$$

h_i is employed to define the length of the region for which the resulting penalty function value will be zero (or very close to it) and dictates the point at which the inequality constraint becomes active. n_i is used to control the sharpness of the function when the limiting value has been exceeded and d_i , is the associated constrained parameter (see Equations 7.9 - 7.16).

Following the steps presented through Equations 7.26 - 7.29, revised Euler-Lagrange equations can be derived for the modified performance index which include the additional penalty functions terms. In practice, due to the complexity of these operations, this process is carried out symbolically with the use of a bespoke Maple [56] library called XOptima [3]. This was developed by the University of Padua specifically for optimal control problems of this type and allows the differential equations generated from the performance index to be solved as a two point boundary value problem. The initial conditions at $s = s_0$ are defined by Equation 7.23, with the final boundary conditions at $s = s_f$ described by Equation 7.35. The set of differential expressions including the vehicle and track model (Eq. 7.19), the free initial states (Eq. 7.31), the co-state equations (Eq. 7.32) and the optimality equation (Eq. 7.33) are all solved using a finite difference discretisation scheme, to yield a large set of algebraic equations. The manoeuvre length s_f , is split into N segments, the value of which is chosen to give a segment length of 0.5m along the centreline of the track (see Figure 7.1). The generation of multiple algebraic equations has essentially translated the optimal control task into a simpler root-finding problem. Nevertheless, the total number of equations generated for a typical manoeuvre is still substantial. These are in the order of 15-20,000, for the simulations presented in Section 7.2. The numerical solver employed solves these equations simultaneously, but uses a number of routines to reduce the total number of equations. Full details of the algebraic solver are given by Bertolazzi [3].

7.1.4 Tyre Wear

Although not well documented in literature, it is well known in the motorsport industry that in certain instances, a locked differential typically brings with it increased levels of tyre wear. This has particular significance when considering vehicle lap times over a race distance, as peak tyre forces gradually degrade with extended use. These factors must be borne in mind when considering any potential LSD configuration.

The creation of quantitative tyre wear models is a complex task and is currently a highly active area of research [47, 49, 21]. Many racing teams are attempting to predict tyre wear characteristics over a typical race distance, to help with race-strategy type decisions. In this analysis, the qualitative approach proposed by Da Silva [21] is used to demonstrate the potential of LSD configuration to influence tyre wear. The rate of tyre wear W_r , can be described as the amount of rubber lost from a unit surface per tyre revolution. A common assumption is that this is proportional to the amount of frictional work W_f , performed by the tyre [49, 21]. The wear rate can be described by the expression:

$$W_r = A_b W_f \quad (7.38)$$

where A_b is an abrasability factor, defined as the amount of rubber lost per unit area, per unit frictional work. This depends on many factors, including the rubber compound and carcass construction, as well as the road surface smoothness, tyre temperature and any interfacial contaminants (water for example) between the tyre-road contact [21, 113]. For this comparative, qualitative analysis, its value is held constant, to allow the influence of LSD configuration to be isolated and understood more easily. Both lateral and longitudinal slip generate significant frictional work at the tyre contact patch. However, since one of the primary goals of an LSD is to limit excessive longitudinal slip, the analysis presented below focuses on the frictional work developed by longitudinal slip of the driven wheels only. It is acknowledged that results should be treated with due caution, as the strong coupling with lateral slip will influence the relative slip velocity at the contact patch. The longitudinal friction energy developed at one tyre can be defined as [21]:

$$W_f = \int_{s_o}^{s_f} |F_x \kappa| \frac{F_z}{F_{zref}} ds \quad (7.39)$$

where F_{zref} is a reference normal load. Thus, the total frictional energy developed at the rear (driven) axle is:

$$W_{frear} = \int_{s_o}^{s_f} |F_{x3} \kappa_3| \frac{F_{z3}}{F_{zref}} ds + \int_{s_o}^{s_f} |F_{x4} \kappa_4| \frac{F_{z4}}{F_{zref}} ds \quad (7.40)$$

This expression can be thought of as the longitudinal frictional wear energy (units in kJ) generated when developing longitudinal tyre forces. The inclusion of the normalised tyre load also allows load transfer effects, known to influence wear rate, to be included in the analysis.

7.2 Simulation Results

The following sections demonstrate how the optimal control method has been used to find the torque bias profile which yields the minimum time solution. A 90° bend and lane change manoeuvre were considered in the analysis, which compares the optimal LSD to traditional open and locked differential solutions.

7.2.1 90° bend

The manoeuvre times from a 100m straight - 30m radius -100m straight combination, in addition to the total longitudinal rear tyre wear energy are summarised in Table 7.2. The resulting vehicle trajectories are also shown in Figure 7.2.

Table 7.2: Manoeuvre time summary - 90° bend

	Open	Locked	Optimal LSD
Time (s)	7.486	7.370	7.369
Wear Energy (kJ)	13.1	18.6	18.1

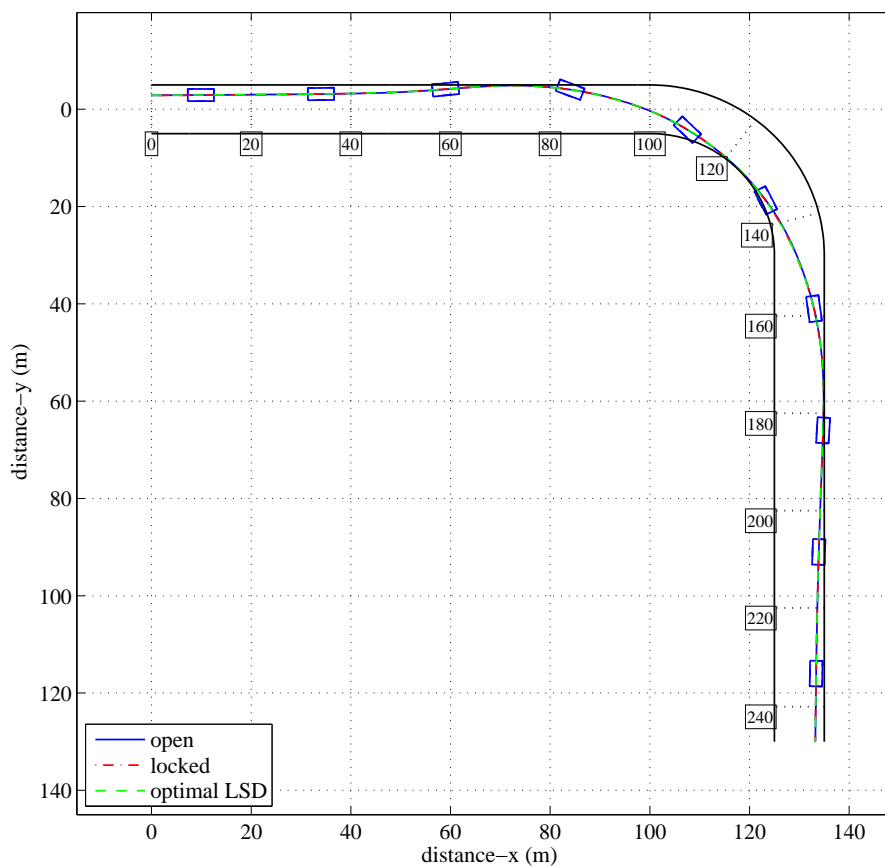


Figure 7.2: Vehicle trajectory - 90° bend

As in the QSS case, the time difference between open and locked differentials is substantial. For the 90° bend, this is 0.116s, which extrapolated over a lap distance, will be in the order of seconds faster. The optimal LSD configuration however, is shown to be virtually identical to the locked solution, although the total longitudinal tyre wear has reduced by 2.4% to 18.1kJ. Figure 7.3 shows the longitudinal slip energy over the duration of the run and confirms that this advantage is held from start to finish. As one might expect, the big increases in slip energy occur under braking before the corner entry and during the corner exit phase. At the apex, where longitudinal acceleration is at its lowest, wear energy remains fairly constant.

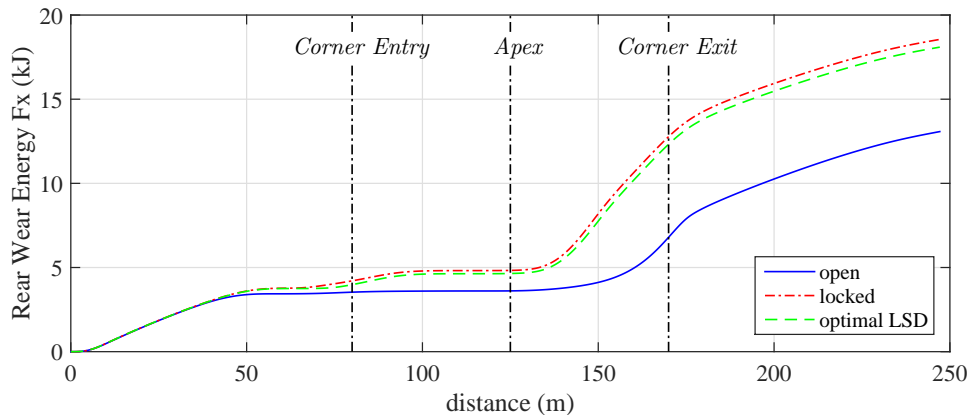


Figure 7.3: Total driven wheel tyre wear energy - longitudinal slip only (corner entry, apex and corner exit points labelled at 80m, 125m and 170m)

The vehicle speed histories are shown in Figure 7.4a, which demonstrate that both the locked and optimal LSD can brake later into the corner and accelerate much more quickly after the apex. It is interesting to note that although the vehicle trajectory is similar in all cases (Figure 7.2), the point at which minimum speed is reached is over 10m later (at 145m) in the open case. In fact, the open differential can support a slightly higher apex speed (+0.5m/s), but loses this advantage since it cannot support the same level of longitudinal acceleration. This confirms the earlier findings discussed in Section 5.2, that open differentials actually allow a higher peak lateral acceleration, and therefore a higher associated apex speed.

The direction of the torque bias under braking (see Figure 7.4d) is shown to be negative, hence inducing a stabilising understeer moment. This has helped the vehicle to generate a higher peak braking torque at 82m, which is illustrated in Figure 7.4c (-1122Nm compared to -921Nm for the open differential), and a less oscillatory steering input (Figure 7.4b) during the corner entry. In this instance, the yaw moment has prevented the counter-steering input required by the open configuration. The magnitude of the torque bias in this phase is large enough to synchronise (or lock) the rear wheels. This is demonstrated in the rear wheel speed traces in Figure 7.5a. The slipping/locked status of the differential is also overlaid with the racing line in Figure 7.6, and it is evident that the LSD remains locked up until the apex at 125m (the locked state is defined as the condition when $|\omega_3 - \omega_4| < 0.1\text{rad/s}$). After this, the LSD is shown to open up, and promote an inner to outer (positive) torque bias and hence an oversteer moment. The differential remains open until 150m, whereupon the differential re-locks during the

corner exit. These results suggest that from a driver point of view, the LSD plays its most crucial roll under braking, where the vehicle has been shown to be highly unstable.

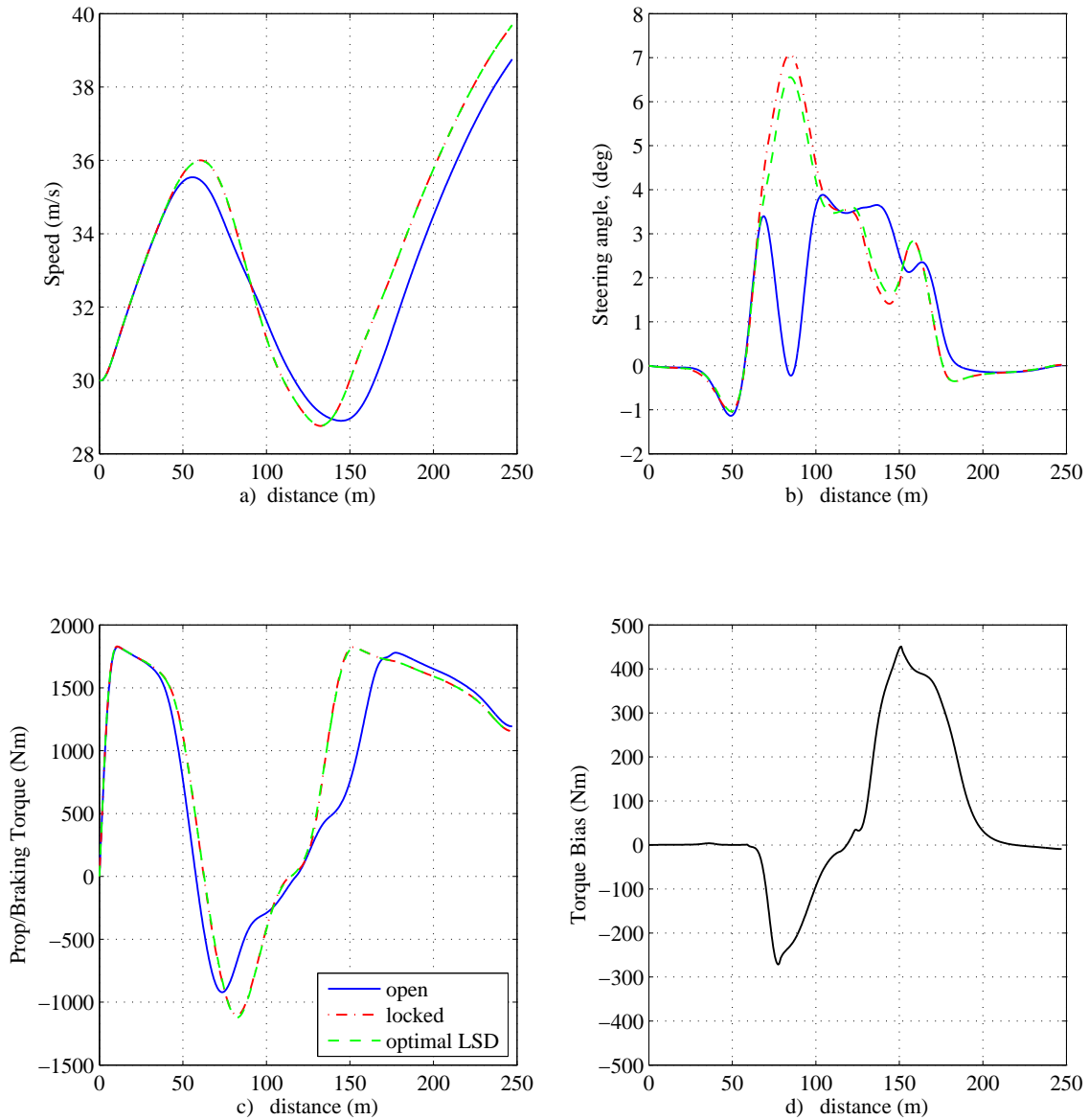


Figure 7.4: a) absolute speed ($\sqrt{U^2 + V^2}$) b) road wheel steering angle (δ_{rw}),
 c) total propulsive ($\gamma_t > 0$) and braking ($\gamma_t < 0$) torque,
 d) optimal torque bias $T_{lock} = \frac{1}{2}(T_3 - T_4)$ (LSD only)

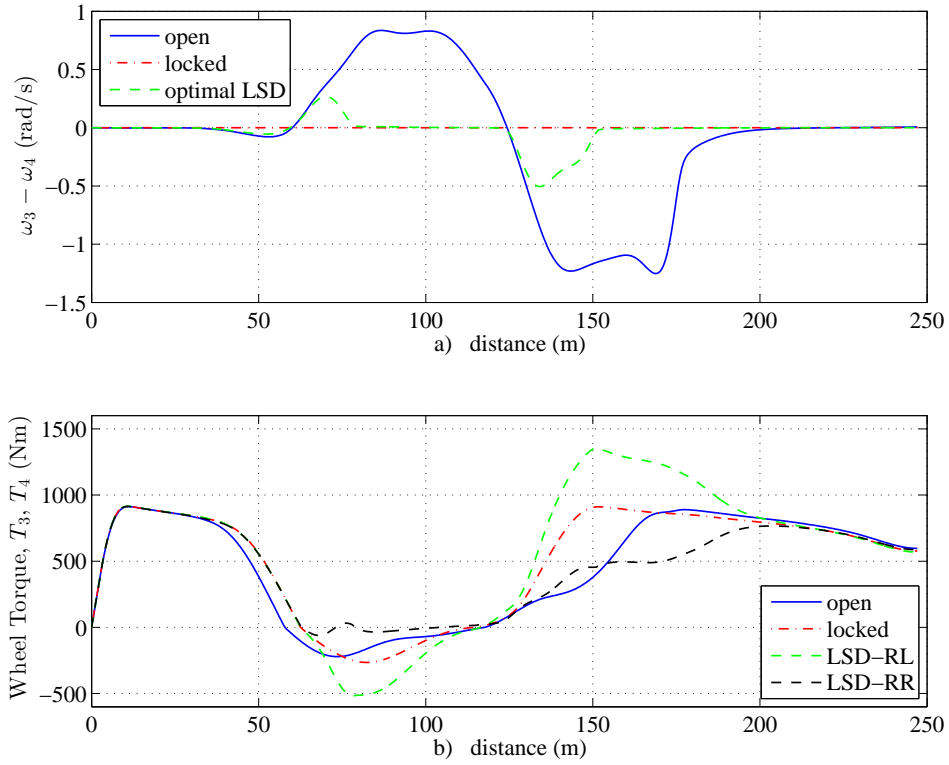


Figure 7.5: a) driven wheel speed difference ($\omega_3 - \omega_4$) b) rear wheel torque T_3, T_4

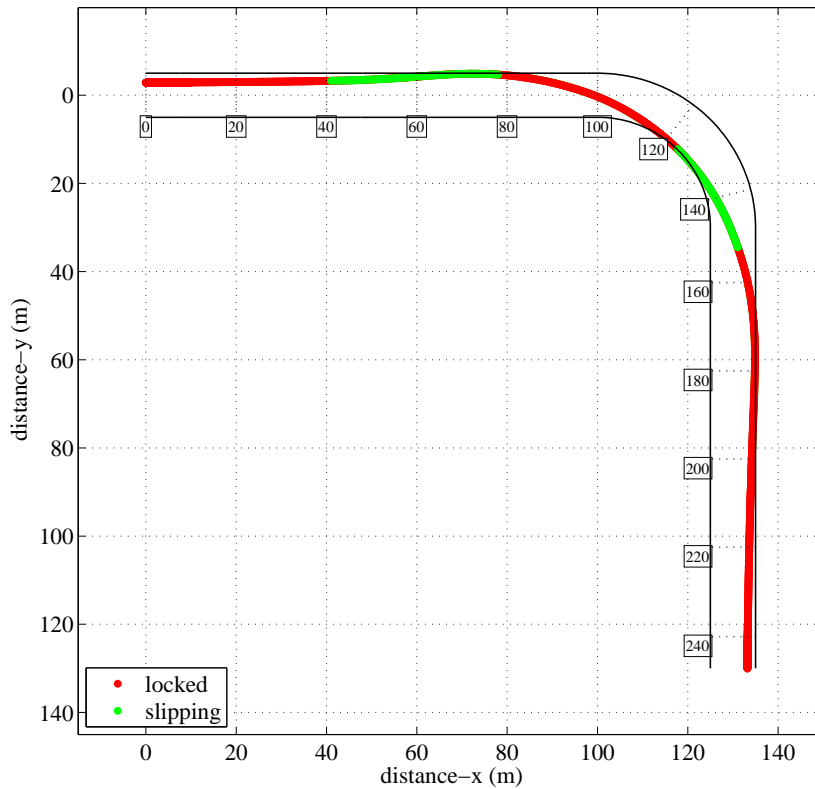


Figure 7.6: 90° bend - slipping/locked status

7.2.2 Lane Change

To demonstrate the influence of differential configuration on a more demanding set of corners, a lane change manoeuvre was also considered. This consisted of a 100m straight and 25m radius turns, separated by a smaller 25m straight. The resulting manoeuvre times and vehicle trajectory curvatures are shown in Table 7.3 and Figure 7.8a.

Table 7.3: Manoeuvre time summary - lane change

	Open	Locked	Optimal LSD
Time (s)	12.069	11.848	11.839
Wear energy (kJ)	30.7	31.6	33.7

The difference in time between locked and open solutions is still significant at 0.22s. However, there is a more noticeable difference between the optimal LSD and locked devices, with the difference increasing to 0.01s. Through a series of similar corners over a lap distance, this time difference could be in the order of tenths of seconds, which is a performance advantage that many racing teams would pursue. The time difference between these configurations is shown in Figure 7.7 and illustrates that the gain is generated at two key points in the manoeuvre, at 160m and 260m.

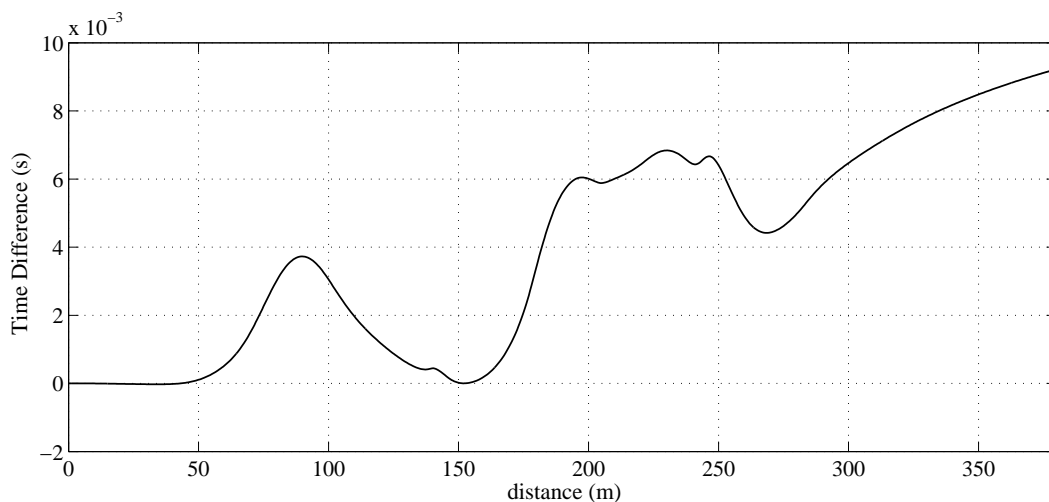


Figure 7.7: Locked - optimal LSD time difference

On track, this corresponds to the points where the vehicle is changing directions (from right to left and vice versa). Assessment of the total propulsive torque in Figures 7.9c-d confirms that the optimal LSD is able to maintain a higher torque in these regions. It is interesting to note that in general, oval based race vehicles (which only turn in one direction) are usually fitted with spool differentials. The results presented here (tyre wear considerations apart) demonstrate that the optimal LSD provides its greatest performance gains for twisty manoeuvres, where the start and end of many corners roll into each other. In the case of an oval therefore, the performance of a locked differential, in raw manoeuvre time terms, will be very similar to that of an optimal LSD.

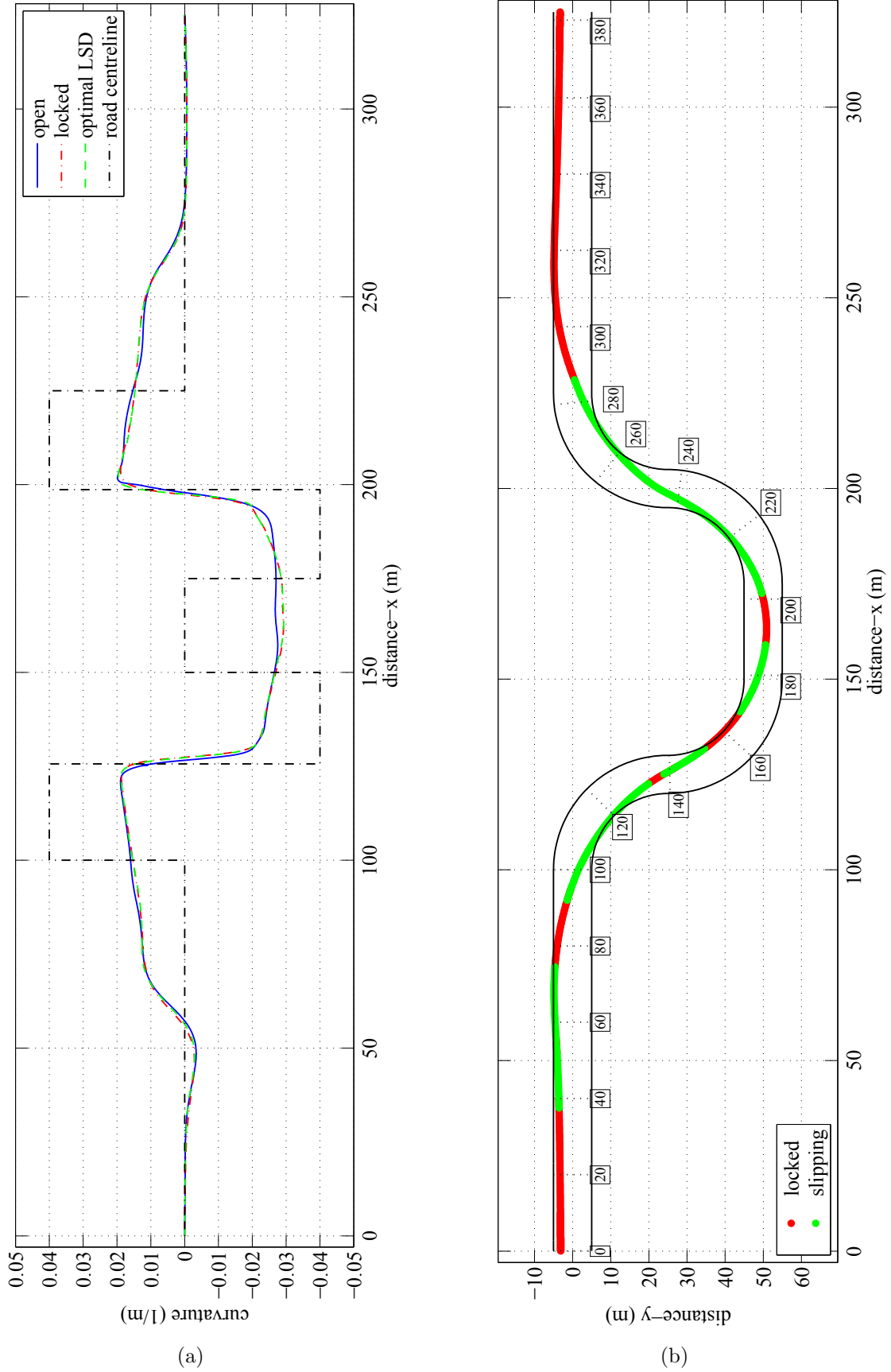


Figure 7.8: a) lane change vehicle trajectory curvature b) slipping/locked status

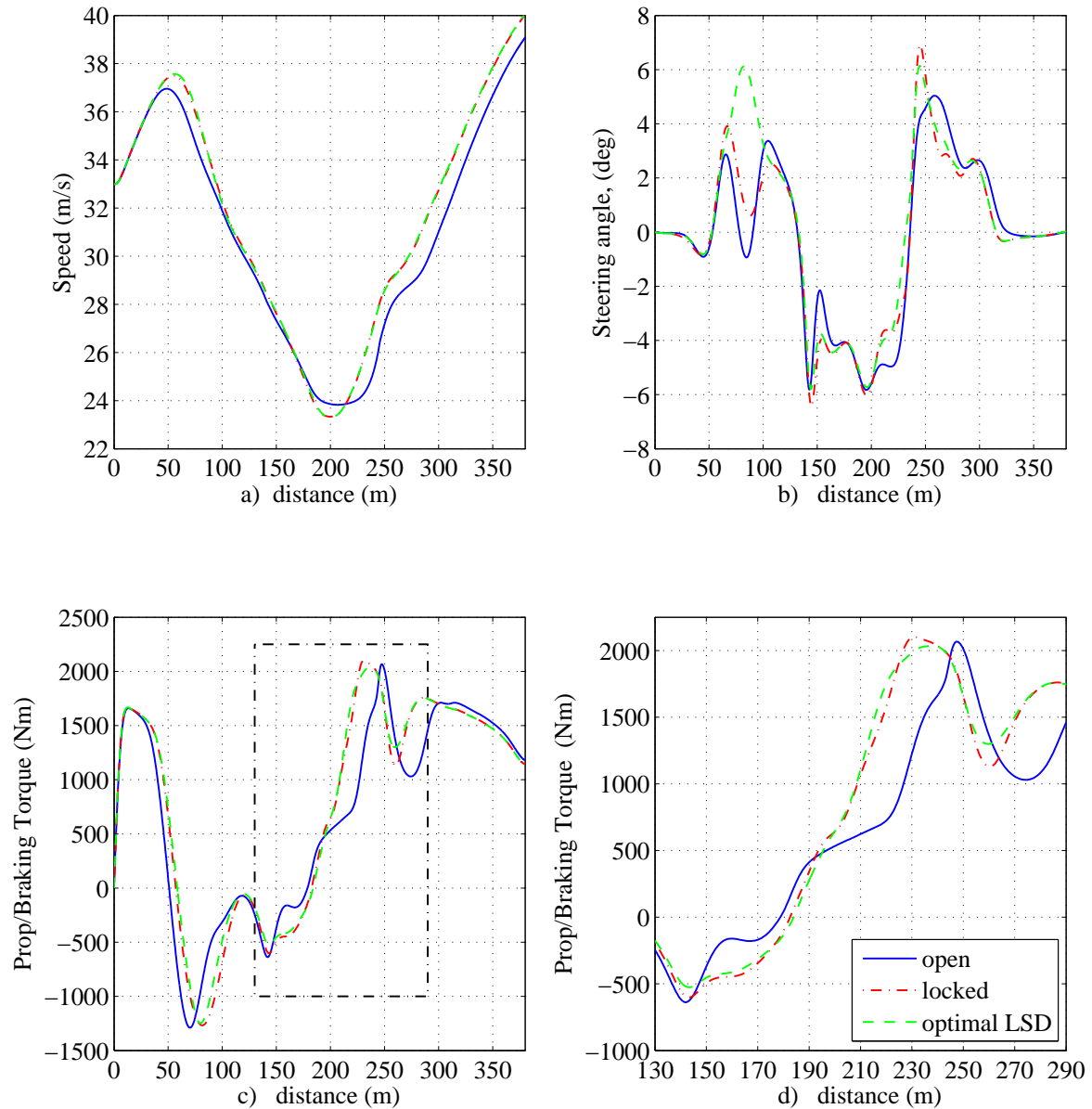


Figure 7.9: a) absolute speed ($\sqrt{U^2 + V^2}$) b) road wheel steering angle (δ_{rw}),
 c) total propulsive ($\gamma_t > 0$) and braking ($\gamma_t < 0$) torque,
 d) total propulsive/braking torque - closeup

The optimal and locked differential vehicle trajectory curvatures shown in Figure 7.8a are virtually identical. There is a more marked difference in the open differential curvature however. The open configuration is shown to encourage a slightly earlier entry to the first corner at 120m, so that a larger radius (i.e. smaller curvature) can be maintained at the subsequent corner at 175m. This has allowed a slightly higher apex speed of 23.7m/s to be achieved which is +0.6m/s when compared to locked and LSD configurations (see Figure 7.9a).

The driven wheel speed difference and wheel torques are detailed in Figures 7.10a-c. These are related to the track in Figure 7.8b, which shows the slipping/locked status throughout the manoeuvre. If the locked phase at 80m is compared to the steering trace in Figure 7.9b, it is noticeable that the steering is less oscillatory in this region. Here,

the induced understeer moment has again helped to stabilise the vehicle. Conversely, the oversteer moment generated just before 215m has helped to turn the vehicle, with an associated decrease in the required steering angle. As the vehicle changes from left to right hand bends at 245m, the understeering moment is seen to increase the input required to negotiate this last section.

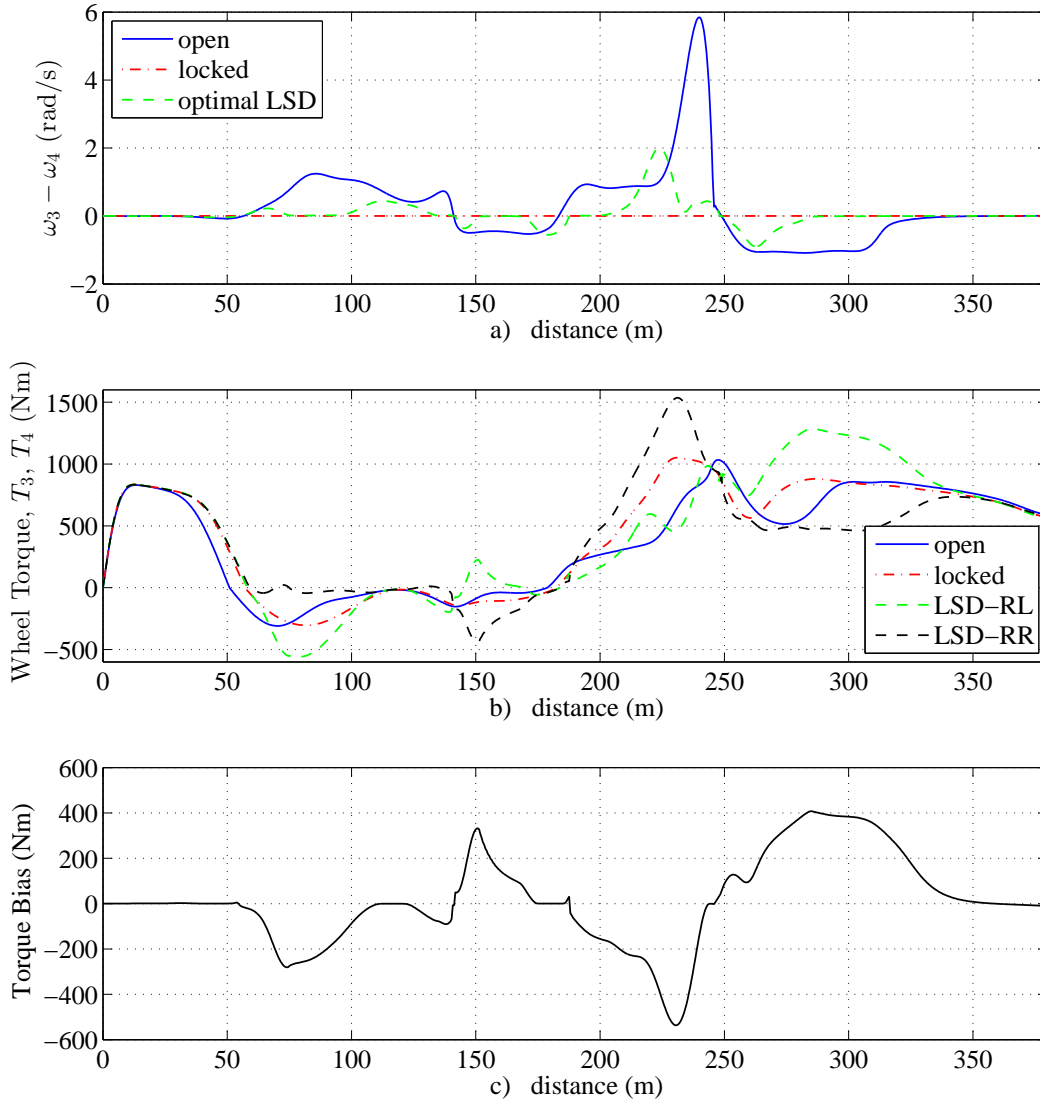


Figure 7.10: a) driven wheel speed difference ($\omega_3 - \omega_4$) b) rear wheel torque T_3, T_4
 c) torque bias $T_{lock} = \frac{1}{2}(T_3 - T_4)$ (LSD only)

The only surprising result is the optimal LSD tyre wear (see Table 7.3). At 33.7kJ, the LSD is shown to generate over 6.5% more wear energy than the locked configuration, by the end of lane change. Inspection of the wear energy history in Figure 7.11 reveals that up until 225m, the locked differential actually generated the most wear. At this point, excessive longitudinal slip on the inside wheel (see Figure 7.12a) has caused a dramatic rise in wear energy. This event would not normally have such a dominant influence, since according to Equation 7.40, the normal load on this tyre should be very low. However, because of the left-right direction change, the normal load is more significant than would otherwise be the case (for a 90° bend for example).

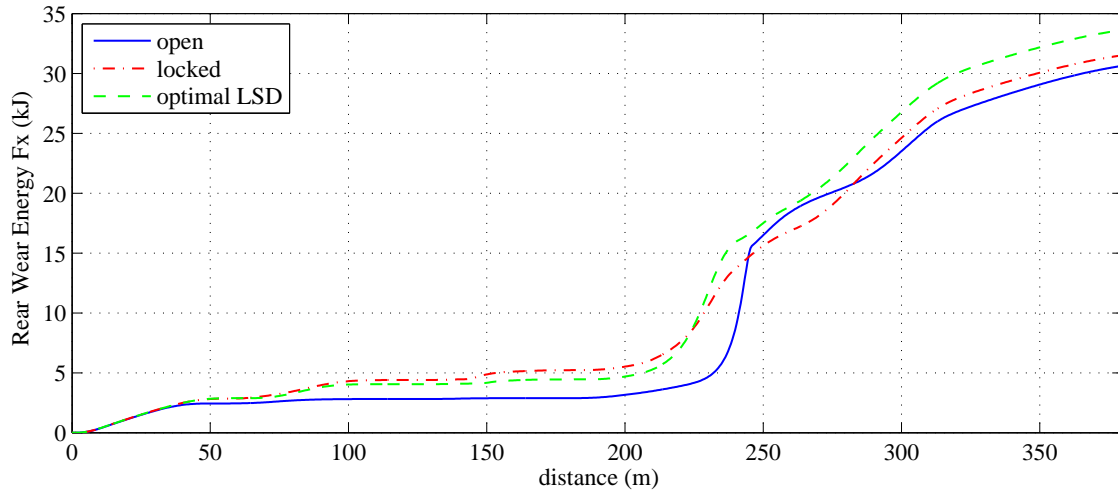
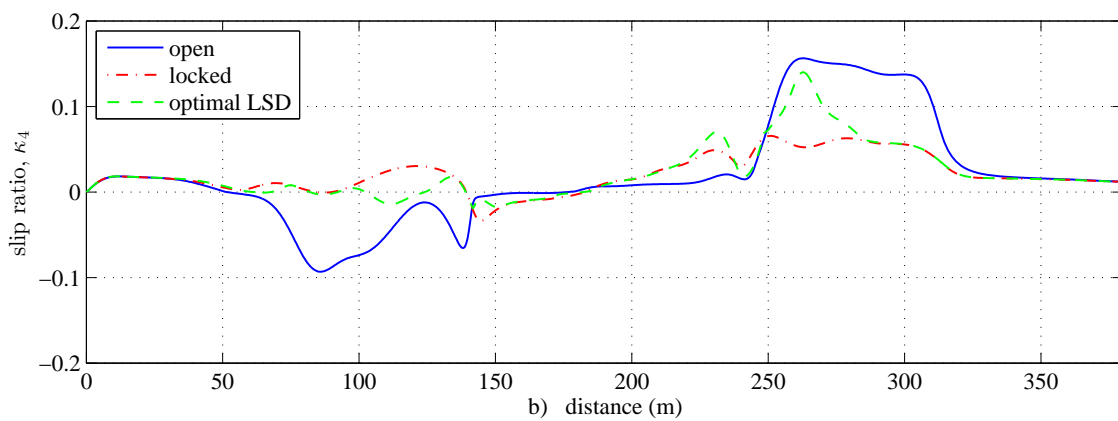
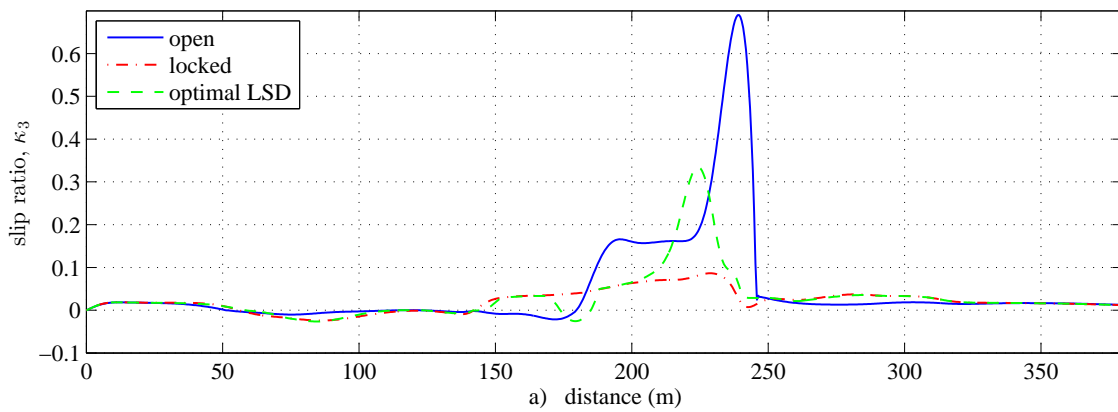


Figure 7.11: Total driven wheel tyre wear energy - longitudinal slip only

Figure 7.12: a) rear left slip ratio κ_3 b) rear right slip ratio κ_4

7.3 Optimal Passive LSD

The optimal torque bias profile presented in previous sections can either be used as the basis of a control algorithm for an active LSD, or give further insight into passive LSD characteristics. In a similar manner to the QSS solutions presented in Section 5.7.1, the torque bias history can be plotted against propulsive and braking torques, to demonstrate optimal plate LSD setup parameters. The torque bias history from the 90° bend manoeuvre (see Section 7.2.1) is used in this example, with the results illustrated in Figure 7.13. The fitted characteristics of the plate LSD model (see Section 3.1) are also shown, in addition to being summarised in Table 7.4.

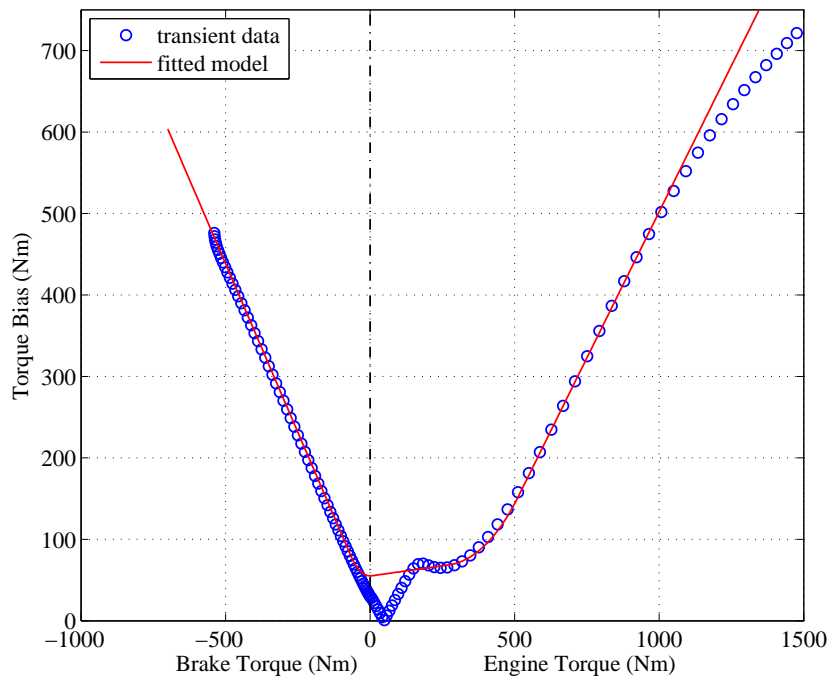


Figure 7.13: Passive torque sensing LSD data fit

Table 7.4: Fitted plate differential setup parameters

Parameter	Value
Drive ramp angle	37°
Coast ramp angle	33°
Number of friction faces	16
Static positive preload	55Nm
Drive negative preload	270Nm
Coast negative preload	-50Nm

Compared to the QSS solution shown in Figure 5.24 and Table 5.6, the drive and ramp angles are very similar. The drive angle is within one degree and the coast angle is only three degrees larger. A potential explanation for this reduced locking on coast, is that although a smaller understeer moment will be generated under braking, the vehicle

will be able to turn-in faster due to an increased yaw response (it is acknowledged that vehicle will also be more unstable as a result). Since the QSS method relies on a GG diagram description, it is essentially track independent. A disadvantage of this of course, is that potential gains from a different racing line, possible with a more agile car, cannot be quantified in terms of lap time.

The level of negative preload on drive is 10Nm larger than the 260Nm predicted by the QSS solution at 60m/s. Coast negative preload is very similar to the high speed (60m/s) QSS solution at -50Nm.

7.3.1 Road Friction

To investigate the effect of varying friction levels on track, the same 90° bend simulation was conducted with the longitudinal and lateral tyre forces scaled down by 15% and 30%. The intention was to replicate intermediate (greasy) and totally wet track conditions. The resulting control and torque bias histories are shown in Figure 7.14a-d.

As one might expect, the speed histories (Figure 7.14a) show that as track conditions deteriorate, the vehicle must brake sooner and reduce its associated minimum apex speed. Interestingly, at a 70% grip level, the torque bias increases under braking, but decreases under acceleration. This indicates that stabilising understeer moments are encouraged under braking, but the (de-stabilising) oversteer moment typically seen under acceleration is reduced. This agrees with typical driver convention, which dictates that stability is maintained in wet conditions at all costs - even to the detriment of agility.

These datasets were again used to plot optimal plate LSD characteristics, and are depicted in Figure 7.15. The equivalent setup parameters are summarised in Table 7.5.

Table 7.5: Plate differential setup parameters - variable road friction

Parameter	100%	85%	70%
Drive ramp angle (°)	37	36	47
Coast ramp angle (°)	33	41	43
Number of friction faces	16	16	16
Static positive preload (Nm)	55	0	0
Drive negative preload (Nm)	270	270	270
Coast negative preload (Nm)	-30	-160	-275

The results show that the drive ramp angles are similar for 100% and 85% grip conditions. It is only when grip levels reduces to 70% that a much more significant increase in ramp angle is seen, up to 47°. This confirms the drop in bias torque seen under acceleration. Under braking conditions, the coast ramp angle is actually seen to increase, indicating lower levels of torque bias. This is unexpected, but on closer inspection of the braking torque history (see Figure 7.14c) it is apparent that the vehicle is having to brake harder and sooner to slow the vehicle down for the corner. This is reflected in the minimum apex speed which reduces from 29m/s at 100% grip

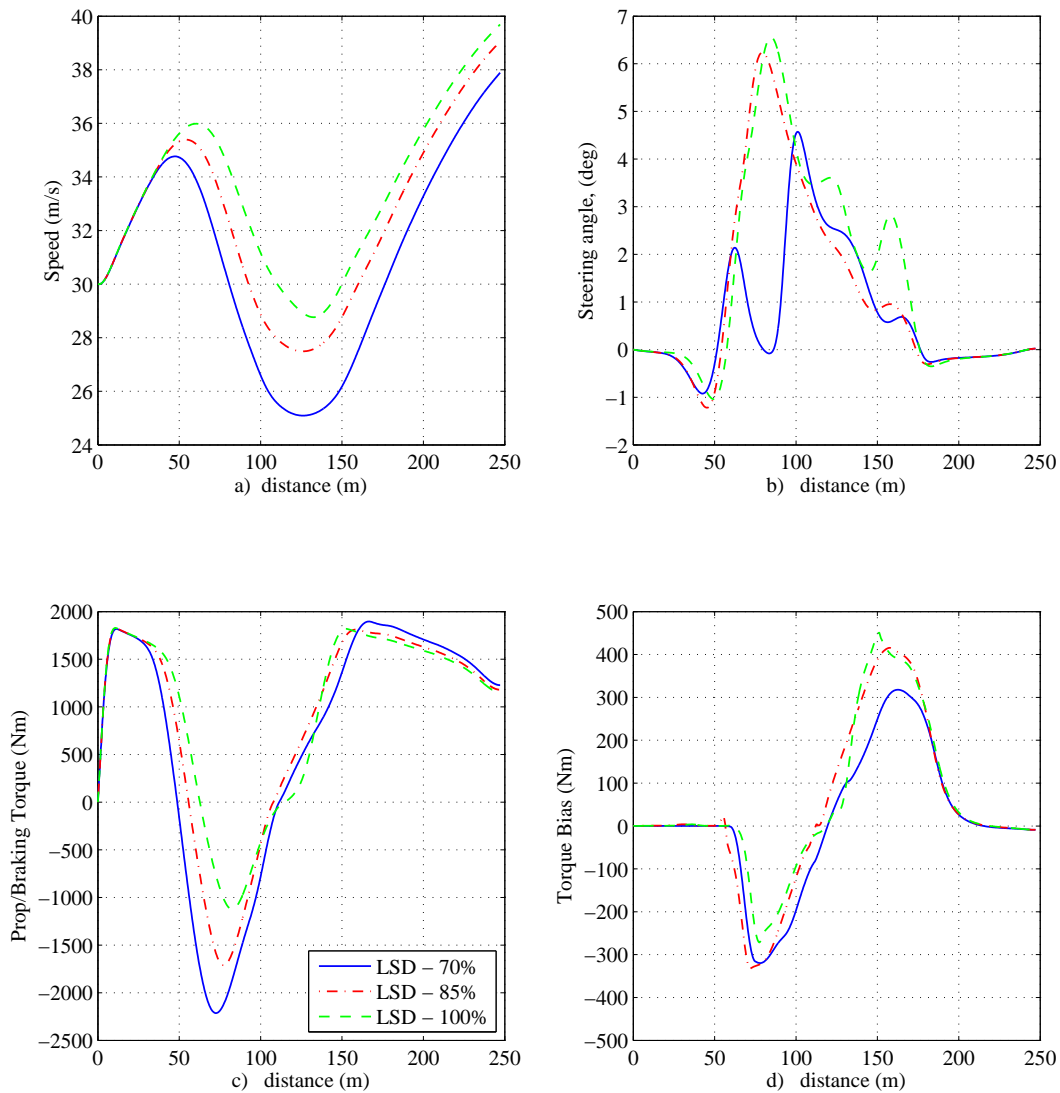


Figure 7.14: a) absolute speed ($\sqrt{U^2 + V^2}$) b) steering wheel angle (δ_{rw}),
 c) total propulsive ($\gamma_t > 0$) and braking ($\gamma_t < 0$) torque,
 d) optimal torque bias $T_{lock} = \frac{1}{2}(T_3 - T_4)$

level, to 25m/s at the 70% grip level. This means, comparatively speaking, there is more brake torque being generated. As a result, even though the optimal bias torque has increased, this is not enough to outweigh the increase in brake torque required to generate it.

The levels of drive-side negative preload remain consistent throughout varying grip levels, at 270Nm, which again agrees with earlier QSS results. Under coast conditions, the ‘deadband’ region in which no torque bias occurs, reduces with grip. This corresponds to a negative preload on the coast side which shifts from -30Nm at 100%, to -275Nm at 70% grip. This simply allows a greater bias torque to occur, when input torque levels are low (in this case 0 - 250Nm of engine input torque). This corresponds to the cornering phase just before the apex, where car is transitioning from off to on-throttle, and the initial portion of positive engine torque is used to overcome longitudinal drag.

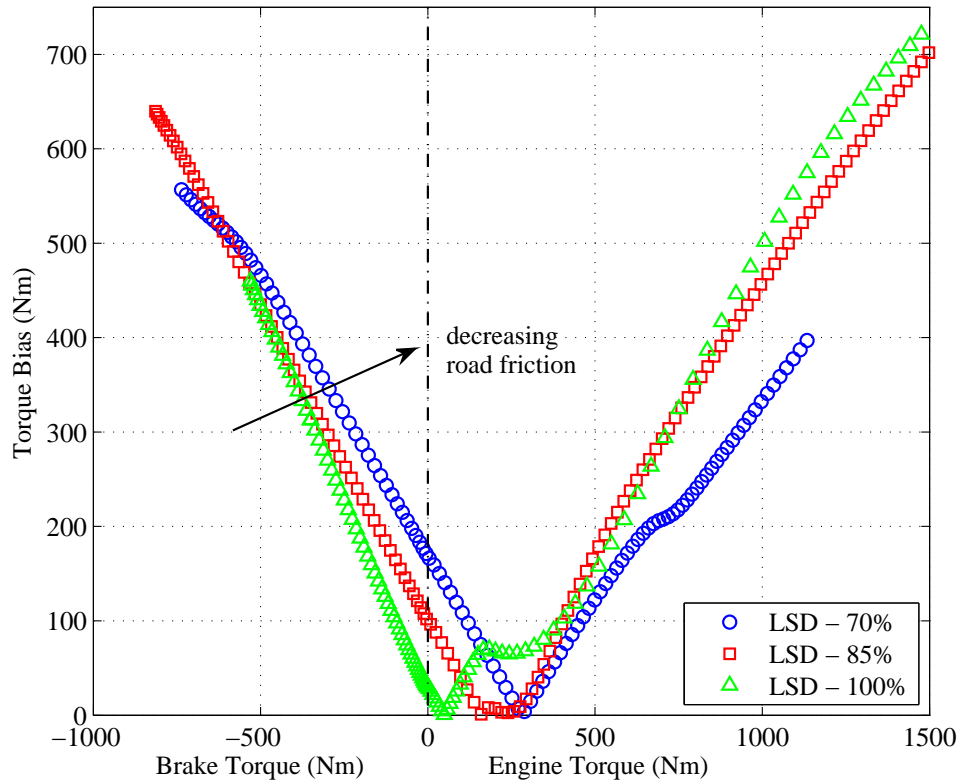


Figure 7.15: Passive torque sensing LSD data fit - variable road friction

7.4 Conclusions

A dynamic optimisation routine has been implemented to investigate how the optimal torque bias profile changes with manoeuvre type, and if this influences the ideal racing line that a racing driver should use.

For the two manoeuvres considered (a 90° bend and lane change), a significant difference was seen between open and locked configurations. This was in the order of tenths of seconds, which over a lap distance would run into seconds of lap time advantage. The difference between optimal LSD and locked configurations however, was more variable. For the 90° bend, the difference was negligible (in the order of thousandths of seconds). Conversely, for the lane change manoeuvre, a more significant time gain of 0.01s over an 11s total manoeuvre time was seen. The performance gain correlated to the points on track where the vehicle was having to change direction during cornering. This can be explained by the better overall yaw response of vehicles fitted with an LSD (when compared to locked differentials). In this instance, it was used to turn the vehicle into the next corner more easily. In practice, the number of corners requiring such a direction change will vary from track to track. However at some circuits, this advantage will approach the tenths of a second over a lap distance, which is a gain many racing teams would pursue.

Optimal torque bias histories were fitted against the torque sensing model presented in Section 3.1. The resulting passive configuration parameters were similar to that found with the QSS method discussed in Section 5.7.1. The drive side negative preload

was within 10Nm of the QSS equivalent, confirming that an x-axis shift in the locking ‘V’ profile is necessary to extract the most from the tyres. The drive ramp angle was within one degree, with the coast ramp overestimated by 3°. In this instance, it is thought that some torque bias under braking has been sacrificed, to allow the vehicle to turn in into the corner more quickly (i.e. an increased yaw response). Of course, this highlights one of the limitations of QSS methods, in that potential benefits from improved yaw response, or alternative racing lines cannot be quantified. Furthermore, the differences seen in the position of the apex between open and locked configurations (up to 10m later in the open case) also shows how critical this boundary condition will be in influencing QSS derived lap times. One of the main reasons why the open configuration apexes later is driven by the need to minimise curvature at all costs. In the lane change study, the entry into the first right hand bend was compromised so that a smaller curvature could be maintained through the following corner. Essentially, due to its inherent traction limitation, racing lines which prevent lateral load transfer, will be more dominant than in the locked and optimal LSD case.

The torque bias characteristics under reduced grip conditions were shown to promote understeer-moment generating locking torque under braking, whilst reducing oversteer moments under acceleration. Maximising the stability of the vehicle at the cost of vehicle agility is a known trade-off, which race drivers are happy to accept in the knowledge that the vehicle will be more driveable in such extreme conditions. The associated passive plate LSD locking characteristics reflect this behaviour under acceleration, with a decrease in the associated locking gradient. Counter-intuitively however, under braking, the locking gradient was shown to decrease. This is due to the fact that as grip levels deteriorate, the vehicle had to brake harder and sooner into the corner. Although the optimal torque bias profile increases under braking due to this increase in braking effort, the relative proportion of brake torque to locking torque actually decreased. This underlines the importance of considering how the vehicle is driven when finding optimal passive LSD setup parameters.

Chapter 8

Conclusions and Further Work

This research investigates the influence of highly adjustable motorsport differentials on ultimate vehicle performance and handling behaviour. The main aim of the work was to develop methods to optimise motorsport differential configuration parameters. This was addressed in three key areas: i) the creation of a range of comprehensive LSD models ii) the development of QSS and dynamic time optimal methods and iii) the creation of a methodology to determine the associated stability and agility contours of the vehicle. This chapter discusses the main findings in each of these areas with regard to the objectives described in Section 1.5 and outlines the scope for future work.

8.1 Differential Modelling

The literature review in Chapter 2 demonstrated that the body of work which surrounds the study of LSD influence on ultimate performance is substantial. However, the adjustable LSD models required to provide a comprehensive performance analysis did not exist. Furthermore, only in a limited number of cases were these models validated against experimental data. Of those which were, significant errors were seen in the locking torque calculating, which brings into question the validity of any associated vehicle handling studies. At the time of writing, none of these models however, had been validated in the parent vehicle system, against on-board vehicle measurements.

Three comprehensive LSD models were presented, which included a torque sensing plate type (Salisbury), a speed sensing VC and a hybrid VCP which combined both speed and torque sensing elements. The plate LSD torque bias characteristics were evaluated from a semi-empirical model which defined three torque bias regions: a linear positive preload at low input torque levels (0-250Nm) and a much more aggressive ramp locking region at higher input torque levels (250Nm+). These were separated by a nonlinear transition, which was proportional to the magnitude of applied positive and negative preload. The resulting model allowed the evaluation of changes in drive and coast ramp angle, the number of friction faces and positive/negative preload. A bespoke differential test rig was developed for validation purposes, which allowed both steady state and transient tests to be conducted. The steady state validations for each configuration parameter reduced the associated NMSE error originally presented by Dickason [24] from over 40%, to less than 15%. In the majority of cases the NMSE was below 5%.

The steady state model was shown to provide a good approximation of transient behaviour in step response QTDTR rig tests. Correlation was improved through the use of a first order lag function. The resulting model was able to replicate the dynamic torque biasing behaviour of a typical off/on throttle input torque event.

However, one of the limitations of using the QTDTR test rig for validation purposes, was that the LSD had to be tested in its ‘slipping’ state. This means that for plate and VCP LSD types, the conditions under which they are able to lock and unlock could not be verified on the QTDTR. As a result, a secondary validation was carried out, in which in-car wheel speed data around the Snetterton race circuit was used to verify the lock/unlock points around multiple corners. Two very different plate LSD setups were tested and demonstrated a good level of model agreement. This gives confidence that the LSD models are capable of demonstrating realistic behaviour and that the dominant interactions with other vehicle subsystems (like the tyre and engine models) have been captured.

The modelling of a speed sensitive VC LSD proved to be more challenging due to the highly influential thermal characteristics of the shear fluid. An adiabatic thermal model was used, with the critical relationships between shear rate, temperature and fluid viscosity established from empirical test data. The resulting modelling errors gave an NMSE of less than 1%, although it should be noted that test durations above 10s are likely to yield larger errors.

8.2 QSS Time Optimal Methods

Although a number of nonlinear simulations were carried out to validate LSD and vehicle models, these cannot provide a true time optimal solution. Any differences in manoeuvre time could potentially arise from either the performance improvement of the vehicle itself, or the performance of the associated steering and throttle controllers. The inability to distinguish between these factors meant that alternative methods were required to find solutions closer to the optimum. The first way this was addressed was with the use of a QSS methodology, which allowed the acceleration limits of the vehicle to be found using nonlinear constrained optimisation. The resulting GG envelopes were defined at multiple vehicle speeds and a lap time derived using an interpolation scheme. This predicted the lap time of a RWD saloon racing vehicle around the Snetterton 300 circuit to within 1.3% (it should be noted that in this instance, tyre forces were scaled by -5% to replicate on-track friction levels more closely).

A number of sensitivity studies were conducted to assess the influence of typical speed and torque sensitive LSD setup parameters on lap time. The key findings were:

- Drive and coast ramp angles were the most dominant setup parameters of a torque sensing plate type LSD. Lower coast ramp angles led to reduced lap times universally. In the positive acceleration case, lap time improvements saturated at drive angles below 40°. A ramp angle combination of D36/C30 gave the quickest lap time for the RWD saloon racing vehicle considered.

- For D45/C45 and D60/C75 ramp combinations, positive preload reduced lap times in all cases, although negative preload was seen to be detrimental at lower speeds (below 30m/s). In the case of more aggressive locking gradients generated by a D30/C45 base ramp setup, negative preload provided a marginal improvement of 0.007s at an optimum negative preload of 140Nm.
- The speed sensitive VC and VCP types were shown to have a more significant influence at higher lateral accelerations, where the driven wheel speed difference is greatest. Lap time improvements saturated once a threshold amount of bias torque had been reached.

An active LSD model was used to illustrate how the optimal torque bias should vary around the GG edge. Under large longitudinal accelerations, higher levels of torque bias were encouraged. Under large lateral accelerations however, torque bias levels were shown to reduce. These characteristics are more typical of torque sensing devices than speed sensing ones, which may explain the current dominance of torque sensing devices in motorsport. The lap time advantage for adopting this strategy was 0.1s faster than a locked differential (for the RWD saloon racing vehicle considered). The optimal torque bias profile was related to equivalent passive plate LSD characteristics to provide a robust means of finding optimal setup parameters. This was then used to propose a novel plate LSD device which allows positive and negative preload to be varied with vehicle speed.

8.3 Dynamic Time Optimal Methods

One of the limitations of QSS methods identified in literature, is that potential gains from changes in the racing line, or in the dynamic yaw response of the vehicle cannot be quantified in real terms. The system dynamics are also important in representing realistic vehicle behaviour and practical driver and torque bias rate related limitations. To that end, a dynamic optimisation method was implemented, which used nonlinear optimal control theory to predict the associated minimum manoeuvre time of the continuous vehicle system.

For the two manoeuvres considered (a 90° bend and a lane change), the time difference between open and locked configurations was approximately 0.1s per corner. The time differences between locked and optimal LSD profiles however, were shown to be more variable. For the 90° bend, the difference was in the order of thousandths of seconds. Conversely, for the lane change manoeuvre, a more significant time gain of 0.01s was seen. The points at which the optimal LSD vehicle was faster correlated to the points on track where the vehicle was having to change direction during cornering. This demonstrated that the cost of running overly aggressive setups (i.e. setups which promote high levels of locking) will be felt most acutely at tight twisty circuits with multiple direction changes.

Differences in the racing line between locked and optimal LSD configurations were minimal. An open differential promoted lines which maximise the radius of curvature over the largest proportion of the manoeuvre (even if this means taking a much tighter line in an earlier corner). This is due to the inherent reduction in lateral load transfer

that comes with a straightening of the racing line. In the open differential case, this influence is particularly dominant, since traction is so severely compromised when compared to its LSD and locked counterparts. Maintaining apex speed is therefore crucial in getting the most from an open differential. The optimal control histories also highlighted the need for drivers to be less aggressive with brake and throttle inputs when driving with an open differential.

The optimal torque bias profile was again used to predict passive plate LSD locking gradients. The results were in close agreement with those generated from QSS methods. This gives confidence that both methodologies are robust ways of finding optimal LSD setup parameters.

Optimal locking characteristics under reduced grip conditions encouraged understeer-moment generating torque bias under braking, whilst reducing oversteer moments under acceleration. The associated passive plate LSD locking characteristics reflected this behaviour with a decrease in the locking gradient under drive conditions. Counter-intuitively however, under braking, the locking gradient was shown to decrease. This was due to a more fundamental change in the way the car was being driven on the limit. The resulting control histories suggested that as grip levels deteriorate, the vehicle must brake sooner and harder into the corner, to maintain the associated reduction in apex speed. Although the optimal torque bias actually increased under braking due to this increase in braking effort, the relative proportion of brake torque to locking torque decreased. This demonstrates that the way in which the car is driven on the limit significantly influences optimal LSD setup parameters.

8.4 QSS Handling Methods

Investigations which have dealt with finding optimal race vehicle setup parameters, have traditionally considered the minimum manoeuvre time as the main performance index. Whilst this is of course significant, experience has shown that the balance of the vehicle and more specifically, how this changes throughout the operating envelope, alters the drivers innate ability to approach the GG limit, and be comfortable operating there. To address these concerns, a more extensive QSS framework was developed to find not only the GG outer edge, but also information regarding how the vehicle states were changing within a so-called feasibility region.

This framework was used to demonstrate how LSD yaw moments of speed and torque sensing types varied throughout the envelope. Torque sensing, plate LSDs were highly dependant on longitudinal acceleration, generating their peak yaw moments in the corner entry and exit phase points on the GG map. Conversely, speed sensing LSDs provided a greater yaw moment closer to the corner apex, where peak lateral acceleration occurs on the GG map. As expected, the speed and torque sensing VCP was shown to have a combination of the yaw moment contours generated by each separate speed and torque sensing element.

The most useful application of the feasibility region framework however, was its ability to show driveability metrics throughout the GG envelope. Linearisation of the

vehicle model over multiple operating points allowed stability and agility metrics to be extracted. These took the form of the dominant system eigenvalues and a normalised yaw rate response bandwidth. The resulting contours qualitatively represented behaviour well known to race drivers, namely: i) a decrease in stability under braking but a greater potential to turn the car into a corner and ii) greater instability at the peak lateral acceleration limit and a reduced ability to turn the vehicle. The method was used to compare three different plate LSD setups. The results were again consistent with behaviour known to exist, in the form of increased stability under braking with higher locking levels, but an increased likelihood for instability during the corner exit at higher vehicle speeds.

An active LSD model was used to show how optimal torque bias characteristics could be used to promote agility below the limit, then progressively stabilise the vehicle as the lateral acceleration limit is approached. This ultimately lays the foundation for using the differential to tailor the specific stability and agility contours to suit different driving styles and vehicle types. The methodology can be applied to both passive LSDs and in the implementation of new active control strategies.

8.5 Contribution

This work has generated a number of novel contributions in its associated research field. Firstly, the creation of a range of state-of-the-art motorsport LSD models, validated under a number of operating conditions. Secondly, the methodologies used to optimise LSD setup parameters, the results from which, have themselves provided the basis of a novel, vehicle speed dependent LSD device. Finally, a more practical and intuitive way to evaluate vehicle stability and agility at different cornering phases. This has laid the foundations of a procedure which not only maximises performance, but also allows the vehicle behaviour to be tailored to suit individual driver preferences

8.6 Future Work

With regard to the differential modelling aspects of this research, a range of comprehensive models have been created and validated. An in-car validation was carried out over a lap distance which identified that the models were capable of replicating the highly transient locking behaviour associated with passive plate LSDs. Under braking conditions however, a number of supporting assumptions were made about the resistance of the engine seen by the differential during braking phases, and that the LSD does indeed use its coast ramp for the majority of the braking phase. This assumption is highly dependent on engine overrun characteristics and warrants further investigation. Ultimately, the torque delivered to each driven wheel and the engine input torque, must be validated under the transient brake to on-throttle scenario, typically associated with corner apex conditions. For this to be achieved, torque sensors fitted to the driveshafts and gearbox output shaft are required. These are not standard fitment on many race cars due to the cost and complexity involved in their implementation. However, their use would provide supporting evidence of the precise torque bias levels which cause a plate LSD to lock, and allow the transition

between drive and coast conditions to be studied in more rigorous detail.

In reference to the vehicle dynamics aspects of this work, the greatest potential for future research lies in the quantitative validation of stability and agility contours with subjective driver assessments. Of course, the scope of this task is vast, but ultimately would allow a vehicle to be optimised not only for out-and-out acceleration performance, but also for driveability. It is intended that the work presented in this thesis lays the foundation of a formal methodology to achieve this elusive goal.

Publications

A. Tremlett, D. Purdy, N. Vaughan, F. Assadian, A. Moore and M. Halley. The Influence of Torque and Speed Sensitive Differential Characteristics in a Front Wheel Drive Vehicle During On-Limit Manoeuvres, *Proceedings of the FISITA 2012 World Automotive Congress*, Lecture Notes in Electrical Engineering, Volume 193, pp. 79-91, 2012.

A. Tremlett, F. Assadian, D. Purdy, N. Vaughan, A. Moore and M. Halley. The Control Authority of Passive and Active Torque Vectoring Differentials for Motorsport Applications, *Proceedings of the FISITA 2012 World Automotive Congress*, Lecture Notes in Electrical Engineering, Volume 193, pp. 335-347, 2012.

A. Tremlett, F. Assadian, D. Purdy, N. Vaughan, A. Moore and M. Halley. Quasi-steady-state linearisation of the racing vehicle acceleration envelope: a limited slip differential example, *Vehicle System Dynamics*, Volume 52, pp. 1416-1442, 2014.

A. Tremlett, M. Massaro, D. Purdy, E. Velenis, F. Assadian and A. Moore. Optimal control of motorsport differentials, *Vehicle System Dynamics*, (accepted for publication).

References

- [1] M. Abe and W. Manning. *Vehicle Handling Dynamics, Theory and Application*. Elsevier, 2009.
- [2] J. Allen. Computer optimisation of cornering line. Master's thesis, School of Engineering, Cranfield University, 1997.
- [3] E. Bertolazzi, F. Biral, and M. Da Lio. Symbolic-numeric efficient solution of optimal control problems for multibody systems. *Journal of Computational and Applied Mathematics*, 185(2):404–421, 2006.
- [4] M.C. Best and T.J. Gordon. A sequential dual model approach to lap optimisation. *Proceedings of the 6th International Symposium on Advanced Vehicle Control*, 2002.
- [5] M.C. Best and T.J. Gordon. Simultaneous optimisation of vehicle parameter and control action to examine validity of handling control assumptions. *Proceedings of the 6th International Symposium on Advanced Vehicle Control*, pages 87–92, 2002.
- [6] M.C. Best and T.J. Gordon. On the synthesis of driver inputs for the simulation of closed-loop handling manoeuvres. *Int. J. of Vehicle Design*, 40:52–76, 2006.
- [7] J.T. Betts. *Practical Methods for Optimal Control Using Nonlinear Programming*. Society for Industrial and Applied Mathematics, 1987.
- [8] J.R. Blasco-Figueroa. Minimum time manoeuvre based on the GG speed envelope. Master's thesis, School of Engineering, Cranfield University, 2000.
- [9] H.G. Bock and K.J. Plitt. A multiple shooting algorithm for direct solution of optimal control problems. *Proceedings of the 9th IFAC World Congress*, 1984. Budapest.
- [10] D. Brayshaw. *The use of numerical optimisation to determine on-limit handling behaviour of race cars*. PhD thesis, Department of Automotive, Mechanical and Structural Engineering, Cranfield University, 2004.
- [11] A.E. Bryson and Y. Ho. *Applied Optimal Control: Optimization, Estimation and Control*. Taylor and Francis, 1975.
- [12] L.R. Buckendale and L.G. Boughner. Automotive differentials. *SAE Paper Number: 510197*, 1951.

-
- [13] S. Cafferty. *Characterisation of Automotive Shock Absorbers Using Time and Frequency Domain Techniques*. PhD thesis, School of Engineering, University of Manchester, 1996.
- [14] A. Candelpergher, M. Gadola, and D Vetturi. Developments of a method for lap time simulation. *Proceedings of the 2000 SAE Motorsport Engineering Conference and Exposition*, 2000. SAE Technical Paper 2000-01-3562.
- [15] D. Casanova. *On Minimum Time Vehicle Manoeuvring: The Theoretical Optimum Lap*. PhD thesis, School Of Engineering, Cranfield University, 2000.
- [16] B.C. Chachuat. *Nonlinear and dynamic optimisation, from theory to practice*. Ecole Polytechnique Federale de Lausanne, 2009.
- [17] F. Cheli, M. Pedrinelli, F. Resta, G. Travaglio, M. Zanchetta, and A. Zorzutti. Development of a new control strategy for a semi-active differential for a high-performance vehicle. *Vehicle System Dynamics*, 44(1):202–215, 2006.
- [18] S. Chockolek. The development of a differential for the improvement of traction control. In *Traction control and anti-wheel-spin systems for road vehicles*. IMechE, 1988.
- [19] M. Croft-White and M. Harrison. Study of torque vectoring for all-wheel-drive vehicles. *Vehicle System Dynamics: International Journal of Vehicle Mechanics and Mobility*, 44(1):313–320, 2006.
- [20] D.A. Crolla. Introduction to vehicle dynamics. Cranfield University CPD course, 2010.
- [21] M.M. Da Silva, R.H. Cunha, and A. C. Neto. A simplified model for evaluating tire wear during conceptual design. *International Journal of Automotive Technology*, 13(6):915–922, 2012.
- [22] J. Deur, M. Hancock, and F. Assadian. Bond graph modeling and analysis of active differential kinematics. In *Proceedings of the ASME Dynamic Systems and Control Conference*, pages (Part A) 229–236, 2008.
- [23] J. Deur, V. Ivanovic, M. Hancock, and F. Assadian. Modeling and analysis of active differential dynamics. *Journal of Dynamic Systems, Measurement, and Control*, 132(6), November 2010.
- [24] I. Dickason. Development of a theoretical locking model for a motorsport mechanical plate differential. Master’s thesis, School of Engineering, Cranfield University, 2008.
- [25] J.C. Dixon. *Tyres, Suspension, and Handling*. Cambridge University Press, 2nd edition, 1991.
- [26] S. Evangelou, D. Limebeer, and R. Sharp. The stability of motorcycles under acceleration and braking. *Proceedings of the Institution of Mechanical Engineers, Part C: Journal of Mechanical Engineering Science*, 215(9):1095–1109, 2001.

- [27] E. Evans and J. Whittle. Friction in wet clutches. *Proceedings of the Institution of Mechanical Engineers*, Volume 182(3N):132–138, 1967.
- [28] FIA. www.fia.com/regulations. accessed June 2013.
- [29] S. Forth and M. Mdvall. *User Guide for MAD - MATLAB Automatic Differentiation Toolbox TOMLAB/ MAD, Version 1.1 The Forward Mode*. TOMLAB Optimisation Inc., 855 Beech St 12, San Diego, CA 92101, USA, 2004.
- [30] B. Freidland. *Control System Design: An Introduction to State Space Methods*. McGraw-Hill, 1986.
- [31] D. Frey, E. Ast, and E. Brugel. European test procedures and test equipment for slip-controlled wet disc clutches. 1998. SAE Technical Paper 982258.
- [32] T. Fujioka and T. Kimura. Numerical simulation of minimum-time cornering behaviour. *JSAE Review*, 13(1):44–51, 1992.
- [33] T. Gassmann and J. Barlage. Visco-lok: A speed-sensing limited-slip device with high-torque progressive engagement. *SAE Technical Paper 960718*, 1996.
- [34] R. H. Haas and R. C. Manwaring. Development of a limited slip differential. *SAE Paper Number: 710610*, 1971.
- [35] D. Hales. Lateral stability problems of simply articulated vehicles. *Proceedings of IUTAM Symposium on Recent Progress in Linear Mechanical Vibrations*, page 1734, 1965.
- [36] M. Hancock. *Vehicle Handling Control Using Active Differentials*. PhD thesis, University of Loughborough, 2006.
- [37] M. J. Hancock, R. A. Williams, T. J. Gordon, and M. C. Best. A comparison of braking and differential control of road vehicle yaw-sideslip dynamics. *Journal Proceedings of the Institution of Mechanical Engineers, Part D: Journal of Automobile Engineering*, 219(3), 2005.
- [38] J. Hannah and R. Stephens. *Mechanics of Machines: Elementary Theory and Examples*. Arnold, 4th edition, 1984.
- [39] J. He, D.A. Crolla, M.C. Levesley, and W.J. Manning. Coordination of active steering, driveline, and braking for integrated vehicle dynamics control. *Proceedings of the Institution of Mechanical Engineers, Part D: Journal of Automobile Engineering*, 220(10):1401–1420, 2006.
- [40] J.P.M. Hendriks, T.J.J. Meijlink, and R.F.C Kriens. Application of optimal control theory to inverse simulation of car handling. *Vehicle System Dynamics*, 26:449–462, 1996.
- [41] R. Hoffman, J. Stein, L. Louca, and K. Huh. Using the Milliken Moment Method and dynamic simulation to evaluate vehicle stability and controllability. *Int. J. of Vehicle Design*, 48(1/2):132–148, 2008.

-
- [42] R.K. Holzwarth and K.A. May. Analysis of traction control systems augmented by limited slip differentials. *SAE Electronic braking, traction and stability control*, 76:277–285, 1994. Paper Number: 940831.
- [43] International Standards Organisation (ISO). Road vehicles - lateral transient response test methods - open-loop test methods, ISO 7401:2011. 2011.
- [44] V. Ivanovic, J. Deur, Z. Herold, M. Hancock, and F. Assadian. Experimental Setups for Active Limited Slip Differential Dynamics Research. *SAE World Congress and Exhibition*, (2008-01-0302), April 2008.
- [45] A. James. Predictive modelling techniques for the Xtrac Differential Test Rig. Master’s thesis, University of Hertfordshire, 2008.
- [46] J.Y. Jang and M.M. Khonsari. Thermal characteristics of a wet clutch. *Journal of Tribology*, 121(3):610–617, July 1999.
- [47] D.P. Kelly. *Lap time simulation with transient vehicle and tyre dynamics*. PhD thesis, Cranfield University School of Engineering Automotive Studies Group, 2008.
- [48] D.E. Kirk. *Optimal Control Theory: An Introduction*. Dover Books on Electrical Engineering, 1970.
- [49] S. Knisley. A correlation between rolling tire contact friction energy and indoor tread wear. *Tire Science and Technology*, 30(2):83–99, 2002.
- [50] P. Kopf, M. Escher, U. Gazyakan, and M. Oberhauser. Optimization of traction and driving stability in 2-wheel drive cars by means of electro-hydraulic limited-slip differentials. *SAE paper 905108*, 1990.
- [51] R.P. Lewis and L.J. O’Brien. Limited slip differentials. *SAE Transactions, Paper Number: 590028*, 67:203–211, 1959.
- [52] D. Liaw, H. Chiang, and T. Lee. Elucidating vehicle lateral dynamics using a bifurcation analysis. *Intelligent Transportation Systems, IEEE Transactions*, 8(1), 2007.
- [53] R. Maki. New demands driving new technology; a literature review of research into the behaviour and performance of wet clutches. Technical report, Lulea University of Technology, 2005.
- [54] R. Maki. *Wet Clutch Tribology*. PhD thesis, Lulea University of Technology, Department of Applied Physics and Mechanical Engineering, 2005.
- [55] S. Mammari and D. Koenig. Vehicle handling improvement by active steering. *Vehicle System Dynamics*, 38(3):211–242, 2002.
- [56] Maple. Maple User Manual: Maplesoft, a division of Waterloo Maple Inc., 2005-2013.
- [57] P. Marklund, R. Maki, R. Larsson, E. Hoglund, M. Khonsari, and J. Jang. Thermal influence on torque transfer of wet clutches in limited slip differential applications. *Tribology International*, 40(5):876–884, 2007.

- [58] P. Marklund, F. Sahlin, and R. Larsson. Modelling and simulation of thermal effects in wet clutches operating under boundary lubrication conditions. *Journal Proceedings of the Institution of Mechanical Engineers, Part J: Journal of Engineering Tribology*, 223(8):1129–1141, 2009.
- [59] G. Mastinu and E. Battistini. The influence of limited-slip differentials on the stability of rear-wheel-drive automobiles running on even road with dry surface. *International Journal of Vehicle Design*, 14(2/3):166–183, 1993.
- [60] Matlab. Matlab Symbolic and Optimisation Toolboxes, The MathWorks Inc., 2014.
- [61] D.T. Mcruer and E.S. Krendel. The man-machine system concept. *Proceedings of the IRE*, 50(5):1117–1123, May 1962.
- [62] W. F. Milliken and D. L. Milliken. *Race Car Vehicle Dynamics*. SAE, 1995.
- [63] T. Mimuro, M. Ohsaki, H. Yasunaga, and K. Satohm. Four parameter evaluation method of lateral transient response. 1990. SAE Technical Paper 901734.
- [64] S. K. Mohan, A. Sharma, R. Mizon, and T. Burns. Torque vectoring systems: architecture, stability performance and efficiency considerations. In *Proceedings of the Sixth All-Wheel Drive Congress*, pages 166–180, Graz, Austria, 2005.
- [65] S.K. Mohan and B.V. Ramarao. A comprehensive study of self-induced torque amplification in rotary viscous couplings. *Journal of Tribology*, 125(1):110–120, 2003.
- [66] R. Morselli, R. Zanasi, and G. Sandoni. Detailed and reduced dynamic models of passive and active limited-slip car differentials. *Mathematical and Computer Modelling of Dynamical Systems*, 12(4):347–362, 2006.
- [67] S. Moss and L. Pomeroy. *Design and Behaviour of the Racing Car*. William Kimber, London, 1963.
- [68] J. Nocedal and S. Wright. *Numerical Optimization*. Springer series in operational research, Springer-Verlag, 1999.
- [69] H. B. Pacejka. *Tyre and Vehicle Dynamics*. 2nd edition Butterworth-Heinemann, 2006.
- [70] H. B. Pacejka and I.J.M. Besselink. Magic formula tyre model with transient properties. *Vehicle System Dynamics*, 27(1):234–249, 1997.
- [71] J. Park, J. Dutkiewicz, and K. Cooper. Simulation and control of Dana’s active limited-slip differential e-diff. *SAE 2005 World Congress & Exhibition*, April 2005. Paper Number: 2005-01-0409.
- [72] C. Patton. *Development of Vehicle Dynamics Tools for Motorsports*. PhD thesis, Oregon State University, 2013.
- [73] G. Perantoni and D.J. Limebeer. Optimal control for a formula one car with variable parameters. *Vehicle System Dynamics*, 52(5):653–678, 2014.

- [74] W. Peschke. A viscous coupling in the drive train of an all-wheel-drive vehicle. *SAE Technical Paper Series 860386*, 1986.
- [75] D. Piyabongkarn, J.Y. Lew, R. Rajamani, and J.A. Grogg. Active driveline torque-management systems. *IEEE Control Systems Magazine*, 30(4):86 – 102, August 2010.
- [76] D. Piyabongkarn, R. Rajamani, J.Y. Lew, and H. Yu. On the use of torque-biasing devices for vehicle stability control. In *Proceedings of the American Control Conference*, pages 5360–5365, 2006.
- [77] P. Piyabongkarn, J. Grogg, Q. Yuan, J. Lew, and R. Rajamani. Dynamic modeling of torque-biasing devices for vehicle yaw control. In *SAE Automotive Dynamics, Stability and Controls Conference and Exhibition*, 2006. 2006-01-1963.
- [78] L.S. Pontryagin, V.G. Boltyanski, R.S. Gamkrelidze, and E.F. Mishchenko. *The Mathematical Theory of Optimal Processes*. Interscience, 1962.
- [79] W.H. Press, S. A. Teukolsky, W. T. Vetterling, and B.P. Flannery. *Numerical recipes in C: the art of scientific computing*. Cambridge University Press, 2nd edition edition, 1992.
- [80] G. Prokop. Modeling human vehicle driving by model predictive online optimization. *Vehicle System Dynamics: International Journal of Vehicle Mechanics and Mobility*, 35(1):19–53, 2001.
- [81] H. Radt and D. Van Dis. Vehicle handling responses using stability derivatives. *SAE Technical Paper 960483*, 1996.
- [82] H. Rothbart and T. Brown. *Mechanical Design Handbook*. McGraw Hill, 2nd edition, 2006.
- [83] H. Sasaki, G. Naitou, Y. Eto, J. Okuda, H. Kusukawa, and S. Sekiguchi. Development of an electronically controlled limited slip differential system. *JSAE review*, 15(4):341–365, October 1994.
- [84] K. Sawase. Left/right drive torque adjusting apparatus for vehicle and left/right drive torque adjusting method for vehicle. United States Patent, 1994.
- [85] K. Sawase and K. Inoue. Classification and analysis of lateral torque-vectoring differentials using velocity diagrams. *Journal Proceedings of the Institution of Mechanical Engineers, Part D: Journal of Automobile Engineering*, 222(9):1527–1541, 2008.
- [86] K. Sawase and Y. Sano. Application of active yaw control to vehicle dynamics by utilizing driving/breaking force. *JSAE Review*, 20(2):289–295, 1999.
- [87] K. Sawase, Y. Ushiroda, and T. Miura. Left-right torque vectoring technology as the core of super all wheel control (S-AWC). *Mitsubishi Motors Technical Review*, 18:18–24, 2006.
- [88] M.W. Sayers. *Introductory guide to AUTOSIM Version 2.0*. The Regents of the University of Michigan, 1992.

- [89] L. Segel. Theoretical prediction and experimental substantiation of the response of the automobile to steering control. *Proceedings of the Institution of Mechanical Engineers, Automobile Division 1947-1970*, pages 310–330, 1956.
- [90] R. Sharp. The stability of motorcycles in acceleration and deceleration. *Inst. Mech. Eng. Conference Proceedings on Braking of Road Vehicles*, page 4550, 1976.
- [91] R. Sharp. *Motorsport Vehicle Dynamic Analysis*. MSc Lecture Notes, 2001. Cranfield University.
- [92] R. Sharp, D. Casanova, and P. Symonds. Mathematical model for driver steering control, with design, tuning and performance results. *Vehicle System Dynamics*, 33(5):289–326, 2000.
- [93] Y. Shibahata, N. Kuriki, K. Kitamura, K. Honda, K. Wada, H. Kajiwara, A. Nori, K. Kuwahara, and S. Okuma. Development of left-right torque distribution system. *Honda R&D Technical Review*, 9:166–180, 1997.
- [94] B. Siegler. *Lap time simulation for racing car design*. PhD thesis, University of Leeds, 2002.
- [95] R. Skoog and C. Lau. Instability of slowly varying systems. *IEEE Trans Auto Control*, AC-17(1):8692, 1972.
- [96] J. Slotine and W. Li. *Applied Nonlinear Control*. Prentice Hall, 1990.
- [97] C. Smith. Race car special report: The racing differential, 1994.
- [98] E. Stall, J. Botterill, and R. Rickell. Electronically controlled traction systems with electric motor actuation. In *Proceedings of FISITA 1992 Congress*, pages 123–134, 1992. Technical Paper C389/467.
- [99] T. Takemura and Y. Niikura. An analysis of viscous coupling torque transmission characteristics and hump phenomenon. *SAE Technical Paper 900558*, 1990.
- [100] I. Taureg and J. Horst. Induced torque amplification in viscous couplings. *SAE Technical Paper 900557*, 1990.
- [101] M. Teraoka. Development of the electro-magnetic controlled limited slip differential unit (EMCD). In *SAE International Congress & Exposition*, March 1993.
- [102] M.P. Thommypillai. *Optimal path-tracking of virtual race-cars using gain-scheduled preview control*. PhD thesis, Imperial College London, 2010.
- [103] J.P. Timings and D. Cole. Minimum manoeuvre time calculation using convex optimization. *Journal of Dynamic Systems, Measurement and Control*, 135(3), 2013.
- [104] J.P. Timings and D. Cole. Robust lap time simulation. In *Vehicle Dynamics and Control Conference*. Cambridge University, 2013.

-
- [105] L.L. Ting. Engagement behaviour of lubricated porous annular disks. part i: squeeze film phase surface roughness and elastic deformation effects. *Wear*, 34(2):159–172, September 1975.
- [106] P. Tsiotras and E. Velenis. Minimum time vs maximum exit velocity path optimization during cornering. *Proceedings of the IEEE International Symposium on Industrial Electronics*, 2005.
- [107] P. Tsiotras and E. Velenis. Optimal velocity profile for given acceleration limits: Receding horizon implementation. *Proceedings of the American Control Conference*, 3:2417–2152, 2005.
- [108] P. Tsiotras and E. Velenis. Optimal velocity profile for given acceleration limits: The half-car model case. *Proceedings of the IEEE International Symposium on Industrial Electronics*, 1:361–366, 2005.
- [109] P. Tsiotras and E. Velenis. Optimal velocity profile for given acceleration limits: Theoretical analysis. *Proceedings of the American Control Conference*, 2:1478–1483, 2005.
- [110] O. van Stryk and R. Bulirsch. Direct and indirect methods for trajectory optimization. *Annals of Operations Research*, 37(1):357–373, 1992.
- [111] A. van Zanten. Bosch ESP systems: 5 years of experience. In *SAE Automotive Dynamics and Stability Conference*. SAE, 2000. Paper Number: 2000-01-1633.
- [112] A. van Zanten, R. Erhardt, and G. Pfaff. VDC, the vehicle dynamics control system of Bosch. *SAE Transactions Journal of Passenger Cars*, 104(1), 1995. SAE-950759.
- [113] A. G. Veith. The most complex tire-pavement interaction: Tire wear. *ASTM Special Technical Publication*, 929:125–158, 1986.
- [114] T. Volkl, M. Muehlmeier, and H. Winner. Extended steady state lap time simulation for analysing transient vehicle behaviour. *SAE Int. J. Passeng. Cars - Mech. Syst.*, 6(1):283–292, 2013. Paper Number: 2013-01-0806.
- [115] F1 Technical website. www.f1technical.com, accessed Decemeber 2013.
- [116] D. Weir and R. DiMarco. Correlation and evaluation of driver/vehicle directional handling data. *SAE Technical Paper 780010*, 1978.
- [117] J.C. Wheals and R. Donin. SUV demonstration of a torque vectoring driveline and new concepts for practical actuation technologies. In *Proceedings JSAE Annual Congress*, 2005.
- [118] K. Worden. Data processing and experiment design for the restoring force surface method, part i: integration and differentiation of measured time data. *Mechanical Systems and Signal Processing*, 4(4):295–319, July 1990.
- [119] P. Wright. *Formula One Technology*. SAE, 2001.

REFERENCES

- [120] Hai Wu. An analysis of the engagement of wet-clutch plates. *Wear*, 24(1):23–33, April 1973.
- [121] Xtrac. Xtrac Limited, Kennet Park, Gables Way, Thatcham, Berkshire, RG19 4ZA. www.xtrac.com.
- [122] J. Yi, J. Li, J. Lu, and Z. Liu. On the stability and agility of aggressive vehicle manoeuvres: A pendulum-turn manoeuvre example. *Control Systems Technology, IEEE Transactions*, 20(3), 2012.

Appendix A

QTDTR Sensor Calibration Certificates

		
Kalibrierschein in Anlehnung an DIN EN ISO 10012 <i>Calibration Certificate with reference to ISO 10012</i>		MK967
(Werkskalibrierschein / Working standard calibration certificate)		HBM
		2008-11
Gegenstand <i>Object</i>	Drehmomentaufnehmer	
Hersteller <i>Manufacturer</i>	Hottinger Baldwin Messtechnik, Darmstadt	
Typ <i>Type</i>	T10F/3kN·m	
Fabrikate/Serien-Nr. <i>Serial number</i>	032430123	
Auftraggeber <i>Customer</i>	Xtrac Ltd.; GB - Thatcham Berkshire RG 19 4ZA	
Auftragsnummer <i>Order No.</i>	3609000179A	
Anzahl der Seiten des Kalibrierscheines <i>Number of pages of the certificate</i>	3	
Die Kalibrierung erfolgte unter Berücksichtigung der Anforderungen der DIN EN ISO/IEC 17025 mit Messmitteln, die im Sinne der DIN EN ISO 9001 und DIN EN ISO 10012 auf Nationale Normale rückführbar sind.		
<i>The calibration was performed respecting the requirements of ISO/IEC 17025 using calibration equipment traceable to National Standards according to ISO 9001 and ISO 10012.</i>		
Prüfer <i>Tester</i>	Stahlecker	Abnahme <i>Release</i>
Datum <i>Date</i>	2008-11-19	
<small>0402/01-01/0008</small>		
<small>QV1061F1.06 - 11/07</small>		<small>Seite / page 1</small>
<small>Hottinger Baldwin Messtechnik GmbH Im Tiefen See 45 · D-64293 Darmstadt · Germany · Tel. +49 6151 803 436 · Fax +49 6151 803 590 · Email: dkdc@hbm.com · www.hbm.com</small>		
<small>Zertifiziert nach ISO 9001 und ISO 14001 (DQS-000001) Akkreditiert als DKD-Kalibrierlab. (DKD-K-00101) Akkreditiert als EMV-Prüflab. (DAT-P-012/ DAT-P-006) Certified acc. to ISO 9001 and ISO 14001 by DQS Accredited as calibration laboratory by DKD Accredited as EMC testing laboratory by DATech</small>		

Figure A.1: QTDTR torque and speed sensor calibration certificate - page 1

```

Page 2 of the calibration dated 19.11.2008

The transducer was calibrated on a 20 kN·m torque reference
standard measuring unit which produces torque loading by means
of weights attached to a double ended lever.

Uncertainty of the calibration method from the torque reference
Standard measuring unit confirmed by the Physikalisch-Technischen
Bundesanstalt with the reference No. 8.32-21980/93 is :

from 0 N·m to 200 N·m 0.04% of the torque applied
from 250 N·m to 20000 N·m 0.02% of the torque applied

The calibration is only valid if the signal conditioner of the same
type as described below are used.

-----
Ambient temperature : 22 Grad C
Environmental humidity: 45 %
-----
Transducer data
Type : T10F/3 kN·m Serial. No : 032430123
Zero signal: 9996,8 Hz Mounting parts : HBM-Standard
Calibration range : 3000 N·m Calibration accessories : ****
-----
Cable data
Length (fixed) : **** Extension : 6 m
Version : 6 - core
Connection of amplifier : 6 - lead
-----
Signal conditioner data
Amplifier type : HBM-ML60B Serial No : DKD62
Bridge excitation : 5 VDC Filter : 0,1 Hz Bessel
(volt., frequ., form)
Type of connection : 6 - lead Check signal: 2825,1 Hz
Measuring point : Channel 3 Measuring range : 20000,0 Hz
-----
Indicator data
Indicator type : HBM-AB22A Serial No : 500000201
Indicator matching : ****
Accessories : Customer owned Stator

The Signal conditioner and indicator is owned by HBM.
+-----+
: MK967 :
+-----+
: HBM :
: :
+-----+
: 2008-11 :
+-----+

```

Figure A.2: QTDTR torque and speed sensor calibration certificate - page 2


```

+-----+
: MK967 :
+-----+
: HBM :
: :
+-----+
: 2008-11 :
+-----+
  
```

calibration modes : alternating torque:

Measured values : Hz


Load in N·m	reading at clockwise torque		reading at anticlockwise torque	
	increasing load	decreasing load	increasing load	decreasing load
	3000	5003,7	-----	
2500	4169,2	4169,1		
2000	3334,8	3334,5		
1600	2667,3	2667,0		
1200	2000,3	1999,9		
600	1000,2	999,8		
0	0,0	0,0	-----	0,4
- 600			- 1000,0	- 999,3
- 1200			- 1999,8	- 1999,1
- 1600			- 2666,1	- 2665,7
- 2000			- 3332,6	- 3332,2
- 2500			- 4165,9	- 4165,5
- 3000			- 4999,2	-----

Figure A.3: QTDTR torque and speed sensor calibration certificate - page 3

41111 N
5725

Prüfprotokoll

test certificate / protocole d'essai



Typ: type / type	U10M/25kN	Auftrag: order no / commission	3600005808/10
Justiermessbereich [kN] Adjusted range / étendue de mesure	25.00	Prüfer: examiner / contrôleur	Arras
IdentNr: serial no / N°-ident	015402S	Datum: test date / date d'essai	2012-06-01

Prüfergebnisse:
test results / résultats d'essai

Eingangsgröße des Messbereichs [kN] input quantity / échelle d'essai	Ausgangsgröße [mV/V] output quantity / résultats	
	Zug tension / traction	Druck compression / compression
0	0.0000	0.0000
5	0.4177	-0.4177
10	0.8354	-0.8354
15	1.2531	-1.2532
20	1.6709	-1.6711
25	2.0886	-2.0888
10	0.8355	-0.8355
0	0.0001	0.0000

Aus den Prüfergebnissen berechnete messtechnische Kenngrößen:
Metrological characteristic quantities computed from the test results:
Grandeurs caractéristiques de mesure calculées à partir des résultats d'essai :

Kennwert C [mV/V] sensitivity / sensibilité	2.0886	-2.0888
Linearitätsabweichung [%vC] linearity deviation / linéarité (Abweichung von der bestpassenden Geraden durch das Nullsignal) (deviation from bestfit through zero / écart par rapport à la meilleure droite passant par le zéro)	0.002	0.005
Relative Umkehrspanne 0,4 F _{nom} relative hysteresis / hystérésis relatif		
in % vom Istwert in % of reading / en % de lecture	0.014	0.012
in % vom Kennwert C in % of sensitivity / en % de sensibilité	0.006	0.005

Alle aus den Messergebnissen ermittelten Kenngrößen entsprechen den Spezifikationen gemäß Datenblatt.
All characteristic quantities determined from the measurement results correspond to the specifications per datasheet.
Toutes les grandeurs caractéristiques déterminées à partir des résultats de mesure correspondent aux spécifications selon les caractéristiques techniques.

Allgemeine Zusatzinformationen:
general information / informations complémentaires

Alle weiteren messtechnischen Eigenschaften des Aufnehmers sind durch Typprüfungen und laufende Produktaudits des Qualitätswesens abgesichert.
All other metrological characteristics of the transducer are verified by type testing and regular product audits of the quality department.
Toutes les autres caractéristiques techniques du capteur sont garanties par le Service Qualité, au moyen d'essais et d'audits suivis sur le produit.

Hottinger Baldwin Messtechnik GmbH, Im Tiefen See 45, 64293 Darmstadt, Germany | www.hbm.com
Registered as GmbH (German limited liability corporation) in the commercial register at the local court of Darmstadt, HRB 1147
Company domiciled in Darmstadt | CEO: Andreas Hüllhorst | Chairman of the board: James Charles Webster

Zertifiziert nach ISO 9001 und ISO 14001 / ISO 9001 and ISO 14001 certified / Certification selon ISO 9001 et ISO 14001
Akkreditierungen gemäß ISO 17025 / Accreditations per ISO 17025 / Accréditations selon ISO 17025

Nr: 236 V4.0/SC-T/01.12 Seite / Page 1 (1)

Figure A.4: QTDTR rack load cell calibration certificate

Appendix B

Plate LSD Step Response Data

In Section 3.4.1, a plate LSD model was validated against a transient input torque profile. This test consisted of a step input torque of +1000Nm, whilst keeping the LSD at a constant +40rpm differential speed. Figure B.1 illustrates the locking torque history from this same test (Figure B.1c), but also at 20, 30 and 50rpm differential speeds. The time taken to reach the steady state is some 0.2-0.3s quicker at 50rpm (Figure B.1d) than at the slowest speed of 20rpm (Figure B.1a).

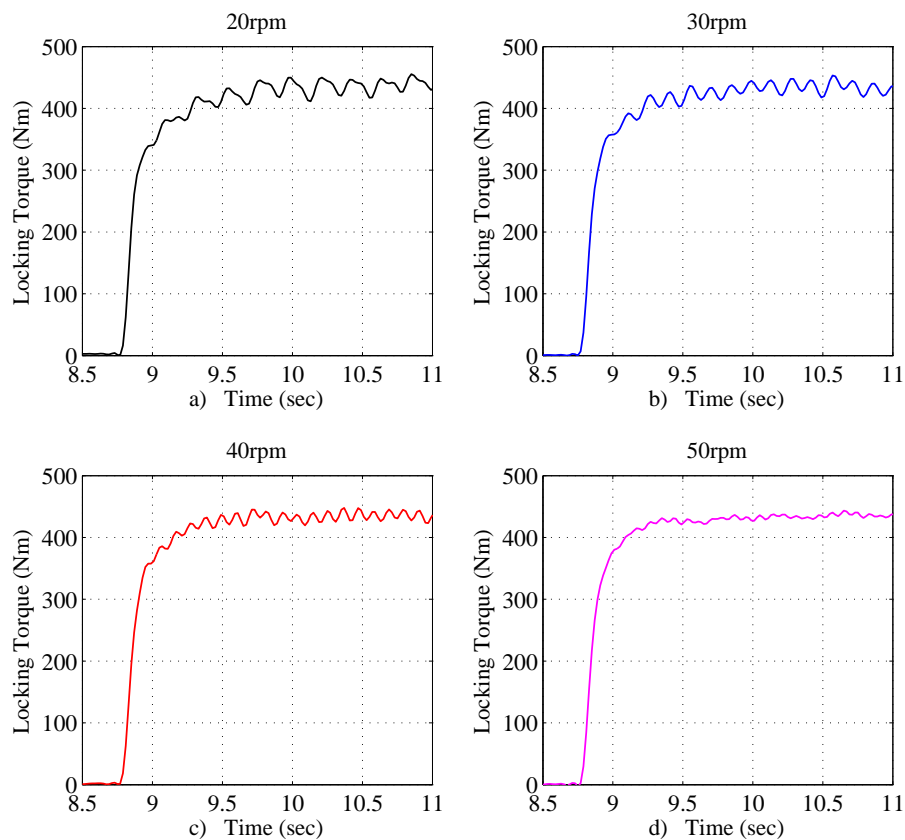


Figure B.1: Transient step response at a) 20rpm, b) 30rpm, c) 40rpm and d) 50rpm for 1000Nm input torque at $t = 8.75s$, drive ramp $\theta_r = 60$, friction faces $z_f = 12$, bulk oil temperature $80^\circ C$

Appendix C

Clutch Pack Transducer

Previous literature [24, 44] and findings during this research, have shown that plate LSD model fidelity largely depends on accurate assessment of friction coefficients, both at the clutch contact and at the ramp-crosspin interface. To supplement this process, a bespoke transducer was designed and developed to measure the ramp clamping loads directly. Due to its narrow profile, it could be installed within the clutch pack assembly, so that the relative magnitude of clutch and ramp friction coefficients could be evaluated more robustly. One limitation of its use was that no more than 12 friction faces could be tested, due to the additional space required to house the sensor. A CAD image of the installation, as well as detail views of the transducer are shown in Figures C.1, C.2 and C.5.

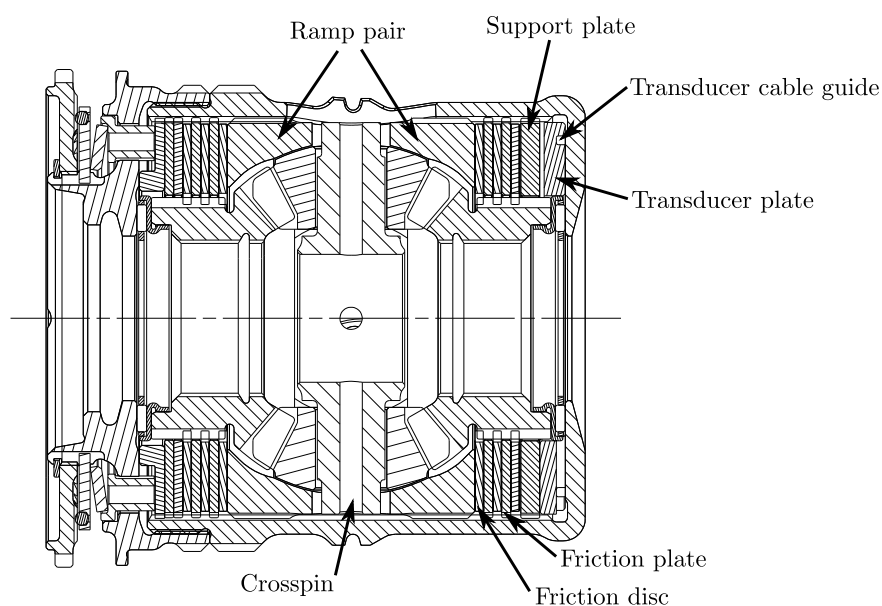


Figure C.1: Transducer plate installation within LSD cassette assembly

The transducer measured axial load through three raised pressure pads located on its surface. Four strain gauges were located behind each pad (see Figure C.3), in cutouts designed to deform locally during compression. The voltage signals from each of the pads were averaged and calibrated against an applied load to give a resultant clamp force. Each of the three sets of strain gauges were temperature compensated, to counter varying material expansion rates across the plate surface. Tooling which

allowed the plate to be calibrated within the differential case was also used to replicate the stiffness of the surrounding differential case material. This was shown to be an important consideration in ensuring calibration repeatability and in the minimisation of hysteresis. The assembly was held within an oven at an operating temperature of 80 °C throughout the process. The load was applied on a separate hydraulic test rig which ramped to a load of 10kN and back down to zero in 2s. The resultant linear calibration is shown in Figure C.4, and the tooling assembly used in the process in Figure C.6.

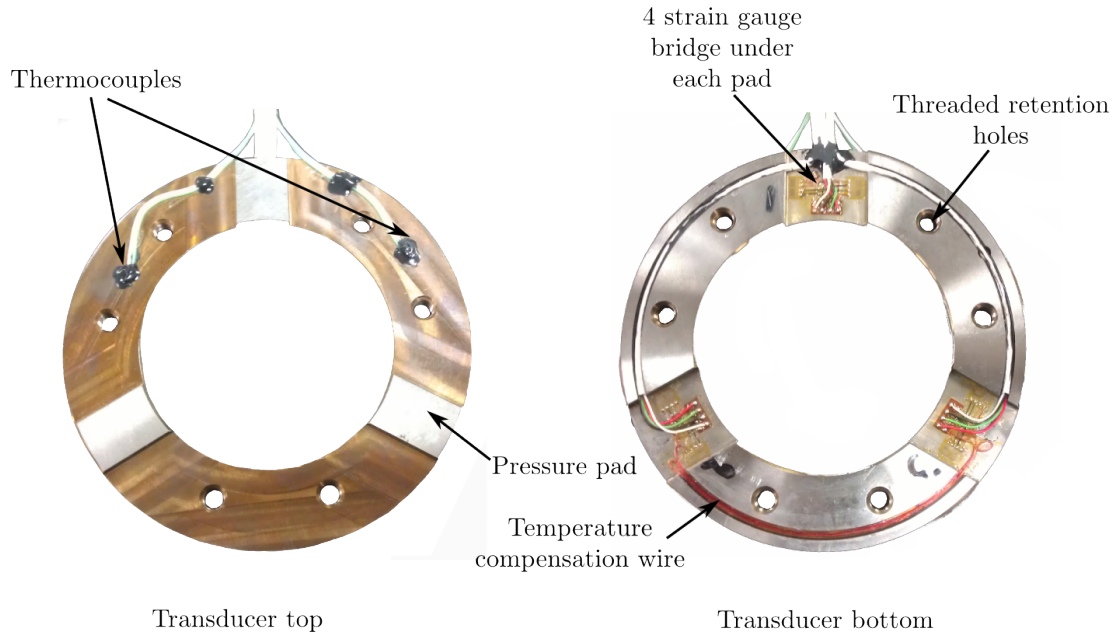


Figure C.2: Strain gauged transducer - top and bottom views

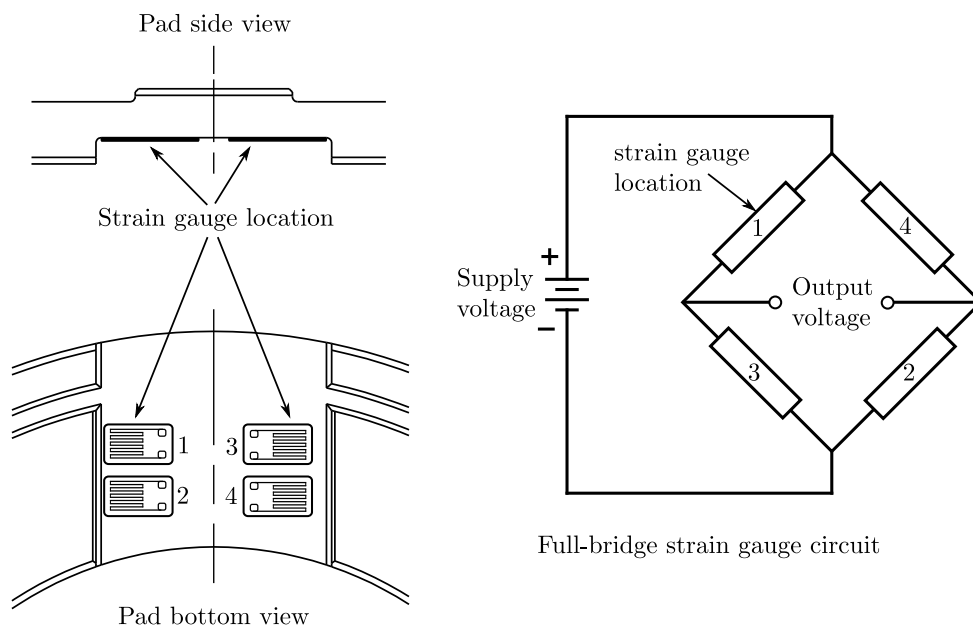


Figure C.3: Strain gauged transducer - bridge configuration

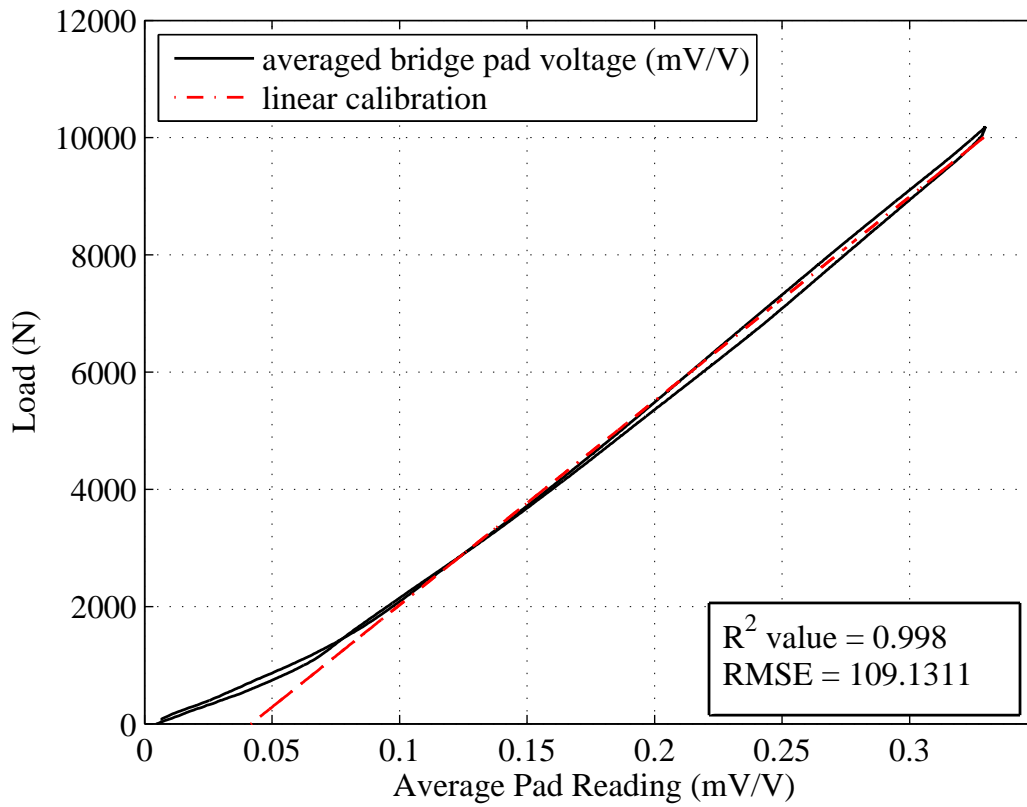


Figure C.4: Transducer calibration, 80°C differential casing temperature

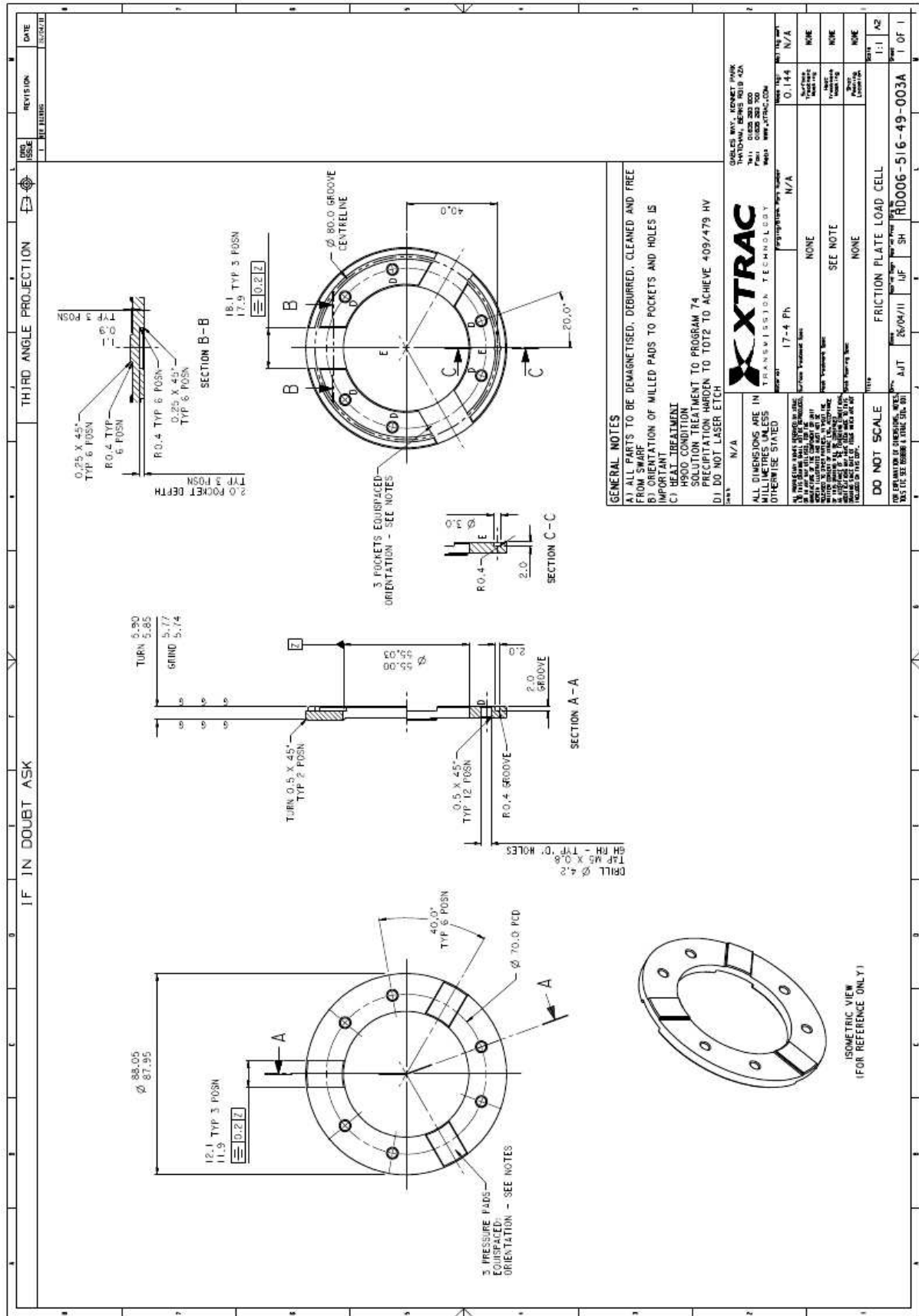


Figure C.5: Transducer pressure plate

APPENDIX C. CLUTCH PACK TRANSDUCER

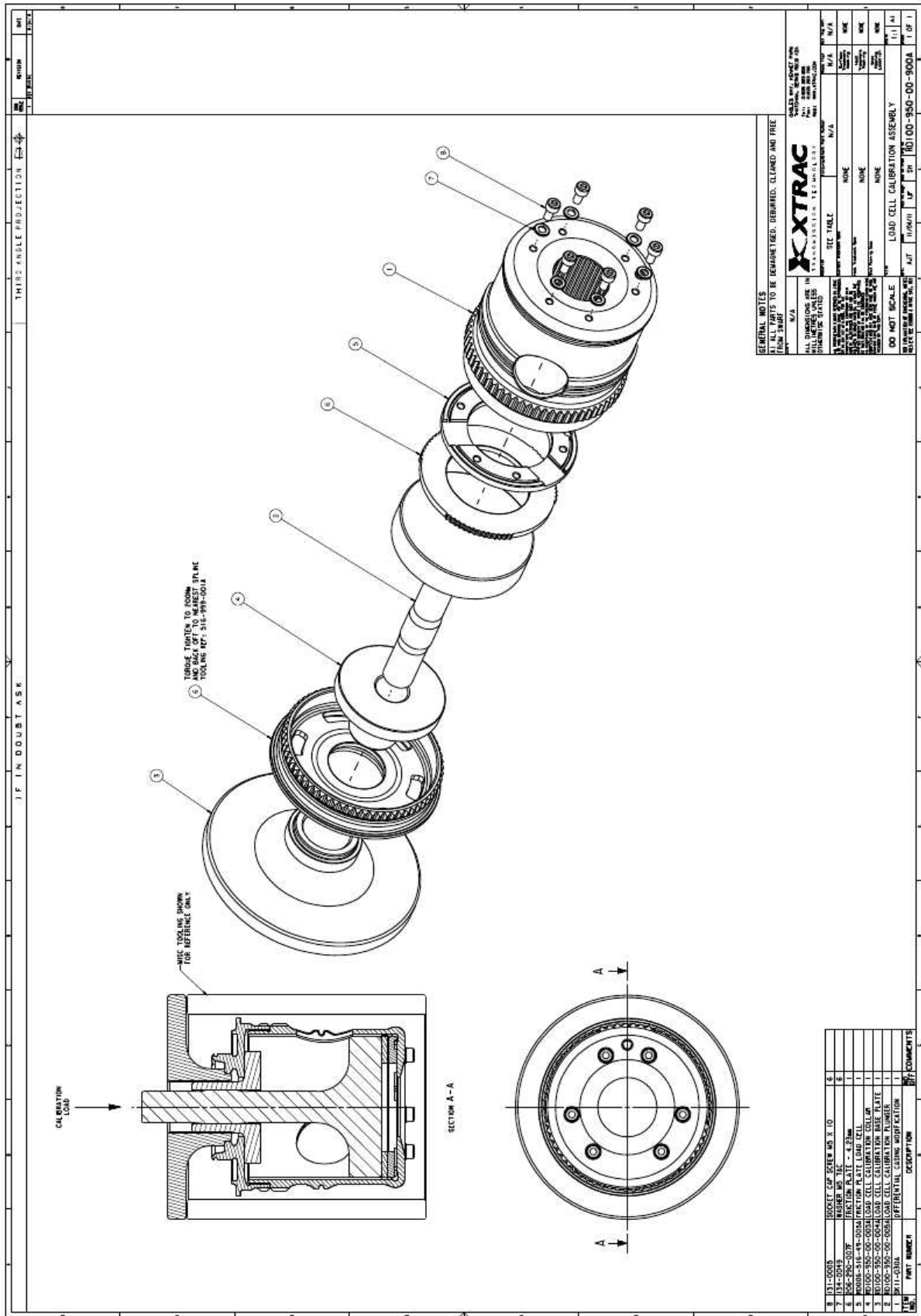


Figure C.6: Transducer calibration tooling

Appendix D

Vehicle Parameters

The vehicle parameters used in the 7DOF vehicle model are detailed below and are representative of the FWD and RWD Touring Car test vehicles used in this thesis.

Table D.1: FWD Touring Car vehicle parameters

Parameter	Symbol	Value	Unit
front wheel centre to CG position	a	1.022	m
rear wheel centre to CG position	b	1.620	m
wheelbase	l	2.642	m
front track	t_f	1.55	m
rear track	t_r	1.50	m
CG height	h_g	0.45	m
front roll centre height	h_{rf}	0.06	m
rear roll centre height	h_{rr}	0.15	m
front roll distribution factor	R_{sf}	0.55	-
rear roll distribution factor	R_{sr}	0.45	-
wheel diameter	R_f, R_r	0.6	m
total vehicle mass	m	1200	kg
wheel rotational inertia	J_w	1.75	kg m ²
vehicle yaw inertia	I_{zz}	1700	kg m ²
engine rotational inertia	J_e	0.05	kg m ²
drag coefficient	C_d	0.35	-
frontal area	A_f	2.4	m ²
maximum brake torque	$T_{b_{max}}$	5000	Nm
front brake bias ratio	B_f	0.65	-

Table D.2: RWD Touring Car vehicle parameters

Parameter	Symbol	Value	Unit
front wheel centre to CG position	a	1.35	m
rear wheel centre to CG position	b	1.40	m
wheelbase	l	2.75	m
front track	t_f	1.65	m
rear track	t_r	1.65	m
CG height	h_g	0.45	m
front roll centre height	h_{rf}	0.02	m
rear roll centre height	h_{rr}	0.09	m
front roll distribution factor	R_{sf}	0.6	-
rear roll distribution factor	R_{sr}	0.4	-
wheel diameter	R_f, R_r	0.6	m
total vehicle mass	m	1200	kg
wheel rotational inertia	J_w	1.75	kg m ²
vehicle yaw inertia	I_{zz}	1700	kg m ²
engine rotational inertia	J_e	0.05	kg m ²
drag coefficient	C_d	0.36	-
frontal area	A_f	2.4	m ²
maximum brake torque	$T_{b_{\max}}$	5000	Nm
front brake bias ratio	B_f	0.65	-

Appendix E

Vehicle Model Linearisation

In Chapter 6, Section 6.3.1, the nonlinear vehicle model was linearised about multiple QSS operating points to provide a linear model description within the GG envelope. This allowed stability and yaw rate response information to be extracted for varying combinations of longitudinal and lateral acceleration. The following Appendix details the linearisation process used in this analysis. The vehicle model can be expressed as a series of differential equations of the form:

$$\dot{\mathbf{x}}(t) = \mathbf{f}(\mathbf{x}(t), \mathbf{u}(t)) \quad (\text{E.1})$$

$$\mathbf{y}(t) = \mathbf{g}(\mathbf{x}(t), \mathbf{u}(t)) \quad (\text{E.2})$$

where $\mathbf{x}(t)$ is the state variable vector, $\mathbf{u}(t)$ the input vector and $\mathbf{y}(t)$ the output vector. The vector expression $\mathbf{f}(\mathbf{x}(t), \mathbf{u}(t))$ can be decomposed into its constituent equations of motion, and in this case the lateral, yaw and four wheel motions have been considered. These are described in Equations 4.2 - 4.3, 4.25 - 4.26 and 4.32 - 4.33 and can be expressed as functions of the state variables:

$$\frac{dV}{dt} = f_1(U, V, r, \omega_1, \omega_2, \omega_3, \omega_4, \delta_{rw}, T_3, T_4, T_{bf}, T_{br}) \quad (\text{E.3})$$

$$\frac{dr}{dt} = f_2(U, V, r, \omega_1, \omega_2, \omega_3, \omega_4, \delta_{rw}, T_3, T_4, T_{bf}, T_{br}) \quad (\text{E.4})$$

$$\frac{d\omega_n}{dt} = f_{2+n}(U, V, r, \omega_1, \omega_2, \omega_3, \omega_4, \delta_{rw}, T_3, T_4, T_{bf}, T_{br}), \quad n = 1...4 \quad (\text{E.5})$$

It should be noted that U is considered constant during the linearisation process. These equations can be put into standard state space matrix form:

$$\dot{\mathbf{X}} = \mathbf{A}\mathbf{X} + \mathbf{B}\mathbf{U} \quad (\text{E.6})$$

$$\mathbf{Y} = \mathbf{C}\mathbf{X} \quad (\text{E.7})$$

where \mathbf{X} and \mathbf{U} are the state and input vectors and \mathbf{C} the output matrix of the system:

$$\mathbf{X} = \begin{bmatrix} V \\ r \\ \omega_1 \\ \omega_2 \\ \omega_3 \\ \omega_4 \end{bmatrix}, \quad \mathbf{U} = \begin{bmatrix} \delta_{rw} \\ T_3 \\ T_4 \\ T_{bf} \\ T_{br} \end{bmatrix}, \quad \mathbf{C} = \mathbf{I}^{6 \times 6} \quad (\text{E.8})$$

The system inputs consist of steering angle δ_{rw} , positive torque delivered to the rear wheels T_3 , T_4 , and the brake torque generated at the front and rear axles T_{bf} , T_{br} . The tyre force terms are included through the longitudinal and lateral slip equations (Equations 4.42 - 4.45) and the Magic Formula tyre model described by Pacejka [69]. The resulting tyre force expressions include many nonlinear terms which must be linearised. This process (described in Section 6.3.1) allows the tyre forces to be described by the linearised tyre force gradients $C_{\alpha 1..4_0}$, $C_{\kappa 1..4_0}$, and the vehicle states. By using a first order Taylor series expansion, the response of the system to small perturbations in states and inputs can then be described by:

$$\delta \dot{\mathbf{X}} = \mathbf{A}_j \delta \mathbf{X} + \mathbf{B}_j \delta \mathbf{U} \quad (\text{E.9})$$

$$\delta \mathbf{Y} = \mathbf{C}_j \delta \mathbf{X} \quad (\text{E.10})$$

Where $\delta \mathbf{X}$ and $\delta \mathbf{U}$ represent small changes in the state and input vectors:

$$\delta \mathbf{X} = \begin{bmatrix} V - V_0 \\ r - r_0 \\ \omega_1 - \omega_{1_0} \\ \omega_2 - \omega_{2_0} \\ \omega_3 - \omega_{3_0} \\ \omega_4 - \omega_{4_0} \end{bmatrix}, \quad \delta \mathbf{U} = \begin{bmatrix} \delta_{rw} - \delta_{rw_0} \\ T_3 - T_{3_0} \\ T_4 - T_{4_0} \\ T_{bf} - T_{bf_0} \\ T_{br} - T_{br_0} \end{bmatrix} \quad (\text{E.11})$$

and \mathbf{A}_j , \mathbf{B}_j and \mathbf{C}_j are the jacobian of the state, input and output matrices:

$$\mathbf{A}_j = \left(\frac{\partial \mathbf{f}}{\partial \mathbf{x}} \right)_{\substack{x=x_0 \\ u=u_0}}, \quad \mathbf{B}_j = \left(\frac{\partial \mathbf{f}}{\partial \mathbf{u}} \right)_{\substack{x=x_0 \\ u=u_0}}, \quad \mathbf{C}_j = \left(\frac{\partial \mathbf{g}}{\partial \mathbf{x}} \right)_{\substack{x=x_0 \\ u=u_0}} = \mathbf{I}^{6 \times 6} \quad (\text{E.12})$$

where \mathbf{x}_0 is the vector of vehicle states at the QSS operating point V_0 , r_0 , $\omega_{1..4_0}$, and \mathbf{u}_0 is the vector of control inputs δ_{rw_0} , T_{3_0} , T_{4_0} , T_{bf_0} , T_{br_0} . The constant longitudinal velocity value used at the linearisation point is denoted by U_0 . The derivation of the \mathbf{A}_j and \mathbf{B}_j matrices is complex and as a result, were derived symbolically using the Matlab Symbolic Toolbox [60] to yield the following matrices:

$$\mathbf{A}_j = \begin{bmatrix} a_{11} & a_{12} & 0 & 0 & 0 & 0 \\ a_{21} & a_{22} & \frac{C_{\kappa 10} R_f t_f}{2I_{zz} A_{j8}} & -\frac{C_{\kappa 20} R_f t_f}{2I_{zz} A_{j7}} & \frac{C_{\kappa 30} R_r t_r}{2I_{zz} A_{j2}} & -\frac{C_{\kappa 40} R_r t_r}{2I_{zz} A_{j1}} \\ 0 & \frac{C_{\kappa 10} R_f^2 \omega_{1,0} t_f}{2J_w A_{j8}^2} & -\frac{C_{\kappa 10} R_f^2}{J_w A_{j8}} & 0 & 0 & 0 \\ 0 & -\frac{C_{\kappa 20} R_f^2 \omega_{2,0} t_f}{2J_w A_{j7}^2} & 0 & -\frac{C_{\kappa 20} R_f^2}{J_w A_{j7}} & 0 & 0 \\ 0 & \frac{C_{\kappa 30} R_r^2 \omega_{3,0} t_r}{2J_w A_{j2}^2} & 0 & 0 & -\frac{C_{\kappa 30} R_r^2}{J_w A_{j2}} & 0 \\ 0 & -\frac{C_{\kappa 40} R_r^2 \omega_{4,0} t_r}{2J_w A_{j1}^2} & 0 & 0 & 0 & -\frac{C_{\kappa 40} R_r^2}{J_w A_{j1}} \end{bmatrix}$$

$$\mathbf{B}_j = \begin{bmatrix} \frac{C_{\alpha 10} + C_{\alpha 20}}{m} & 0 & 0 & 0 & 0 \\ a \frac{C_{\alpha 10} + C_{\alpha 20}}{I_{zz}} & 0 & 0 & 0 & 0 \\ 0 & 0 & 0 & -\frac{1}{2J_w} & 0 \\ 0 & 0 & 0 & -\frac{1}{2J_w} & 0 \\ 0 & \frac{1}{J_w} & 0 & 0 & -\frac{1}{2J_w} \\ 0 & 0 & \frac{1}{J_w} & 0 & -\frac{1}{2J_w} \end{bmatrix}$$

where:

$$a_{11} = -\left(\frac{C_{\alpha 10}}{A_{j8}} + \frac{C_{\alpha 20}}{A_{j7}} + \frac{C_{\alpha 30}}{A_{j2}} + \frac{C_{\alpha 40}}{A_{j1}}\right) / m \quad (\text{E.13})$$

$$a_{12} = \frac{C_{\alpha 30} b}{m A_{j2}} - \frac{(A_{j6} + A_{j5})}{m} + \frac{C_{\alpha 40} b}{m A_{j1}} + \frac{A_{j4}}{2m A_{j2}^2} - \frac{A_{j3}}{2m A_{j1}^2} - U_0 \quad (\text{E.14})$$

$$a_{21} = b \left(\frac{C_{\alpha 30}}{A_{j2}} + \frac{C_{\alpha 40}}{A_{j1}}\right) / I_{zz} - a \left(\frac{C_{\alpha 10}}{A_{j8}} + \frac{C_{\alpha 20}}{A_{j7}}\right) / I_{zz} \quad (\text{E.15})$$

$$\begin{aligned}
 a_{22} = & -\frac{a(A_{j6} + A_{j5})}{I_{zz}} - b \left(\frac{C_{\alpha 30} b}{A_{j2}} + \frac{C_{\alpha 40} b}{A_{j1}} + \frac{A_{j4}}{2A_{j2}^2} - \frac{A_{j3}}{2A_{j1}^2} \right) / I_{zz} \quad (\text{E.16}) \\
 & - \left(\frac{C_{\kappa 10} R_f \omega_{1,0} t_f^2}{2A_{j8}^2} + \frac{C_{\kappa 20} R_f \omega_{2,0} t_f^2}{2A_{j7}^2} \right) / 2I_{zz} \\
 & - \left(\frac{C_{\kappa 30} R_r \omega_{3,0} t_r^2}{2A_{j2}^2} + \frac{C_{\kappa 40} R_r \omega_{4,0} t_r^2}{2A_{j1}^2} \right) / 2I_{zz}
 \end{aligned}$$

$$A_{j1} = U_0 - \frac{t_r r_0}{2} \quad (\text{E.17})$$

$$A_{j2} = U_0 + \frac{t_r r_0}{2} \quad (\text{E.18})$$

$$A_{j3} = C_{\alpha 40} t_r (V_0 - b r_0) \quad (\text{E.19})$$

$$A_{j4} = C_{\alpha 30} t_r (V_0 - b r_0) \quad (\text{E.20})$$

$$A_{j5} = C_{\alpha 20} \left(\frac{a}{A_{j7}} + \frac{A_{j9}}{2A_{j7}^2} \right) \quad (\text{E.21})$$

$$A_{j6} = C_{\alpha 10} \left(\frac{a}{A_{j8}} + \frac{A_{j9}}{2A_{j8}^2} \right) \quad (\text{E.22})$$

$$A_{j7} = U_0 - \frac{t_f r_0}{2} \quad (\text{E.23})$$

$$A_{j8} = U_0 + \frac{t_f r_0}{2} \quad (\text{E.24})$$

$$A_{j9} = t_f (V_0 + a r_0) \quad (\text{E.25})$$

$$(\text{E.26})$$

Appendix F

Simplified Pacejka Tyre Model

The tyre forces required throughout Chapters 4 - 6 were generated using a 1996 Pacejka Magic Formula model [69] for a 235/610R17 racing slick tyre. This required over 50 parameters to describe the resultant longitudinal and lateral tyre forces as a function of slip angle α_n , slip ratio κ_n , normal load F_{zn} and camber angle γ_n . Due to the complexity of the optimal control method presented in Chapter 7, the model was simplified to increase robustness and reduce simulation run times. The aspects of the tyre model which dominate tyre force properties are retained with the use of only 13 parameters and are detailed in Table F.1.

Table F.1: Simplified Pacejka model coefficients

Symbol	Description
F_{z0}	reference normal load where $df = 0$ (N)
pK_{x1}	max longitudinal stiffness coefficient
pK_{y1}	max cornering stiffness coefficient
pK_{x3}	max longitudinal stiffness coefficient
pK_{y2}	max cornering stiffness coefficient
pC_{x1}	longitudinal shape factor
pC_{y1}	lateral shape factor
pD_{x1}	max longitudinal friction coefficient
pD_{y1}	max lateral friction coefficient
pD_{x2}	longitudinal friction load dependency factor
pD_{y2}	lateral friction load dependency factor
pE_{x1}	longitudinal curvature factor
pE_{y1}	lateral curvature factor

The three dominant behaviours retained from the full Pacejka model (considered essential for realistic results) were:

- i) A decrease in the longitudinal and lateral friction coefficients with normal load.
- ii) Variation in the slip angle and slip ratio at which peak lateral and longitudinal forces are generated.
- iii) Nonlinear reduction in the longitudinal and lateral slip stiffness with normal load.

It should be noted that the current dynamic optimisation routines available [73, 103] only capture the first of these two characteristics. The variation of slip stiffness is crucial however, in determining the overall understeer/oversteer balance of the vehicle.

The derivation presented below is taken from Chapter 4 of Pacejka [69]. The coupling between longitudinal and lateral forces is included through the use of the friction circle concept. The theoretical longitudinal slip σ_x , lateral slip σ_y and equivalent slip σ values can be evaluated from the practical slip values κ and α using:

$$\sigma_x = \frac{\kappa}{1 + \kappa} \quad \sigma_y = \frac{\tan \alpha}{1 + \kappa} \quad \sigma = \sqrt{\sigma_x^2 + \sigma_y^2} \quad (\text{F.1})$$

The resulting longitudinal F_x and lateral F_y forces can then be found using the traditional Magic Formula expressions:

$$F_x = \frac{\sigma_x}{\sigma} D_x \sin(C_x \arctan(B_x \sigma - E_x(B_x \sigma - \arctan(B_x \sigma)))) F_z \quad (\text{F.2})$$

$$F_y = \frac{\sigma_y}{\sigma} D_y \sin(C_y \arctan(B_y \sigma - E_y(B_y \sigma - \arctan(B_y \sigma)))) F_z \quad (\text{F.3})$$

The parameters $B_{x,y}$, $C_{x,y}$, $D_{x,y}$, $E_{x,y}$ are defined at a particular reference tyre load F_{z0} , and the normalized change in vertical load is employed to linearly scale the peak friction coefficient $D_{x,y}$ parameter:

$$df_z = \frac{F_z - F_{z0}}{F_{z0}} \quad (\text{F.4})$$

For longitudinal tyre forces, the slip stiffness (gradient at $\alpha = 0$) is defined by:

$$K_x = F_z pK_{x1} \exp(pK_{x3} df_z) \quad (\text{F.5})$$

where the parameters B_x , C_x and D_x are:

$$E_x = pE_{x1} \quad (\text{F.6})$$

$$D_x = (pD_{x1} + pD_{x2} df_z) \lambda_{\mu,x} \quad (\text{F.7})$$

$$C_x = pC_{x1} \quad (\text{F.8})$$

$$B_x = \frac{K_x}{C_x D_x F_z} \quad (\text{F.9})$$

The scaling factor $\lambda_{\mu,x}$ was used to provide a means to reduce friction levels for the analysis presented in Section 7.3.1.

Similarly, for lateral tyre forces the slip stiffness can be described by:

$$K_y = pK_{y1} F_{z0} \sin\left(2 \arctan \frac{F_z}{pK_{y2} F_{z0}}\right) \quad (\text{F.10})$$

where B_y , C_y and D_y are:

$$E_y = pE_{y1} \quad (\text{F.11})$$

$$D_y = (pD_{y1} + pD_{y2} df_z) \lambda_{\mu,y} \quad (\text{F.12})$$

$$C_y = pC_{y1} \quad (\text{F.13})$$

$$B_y = \frac{K_y}{C_y D_y F_z} \quad (\text{F.14})$$

$\lambda_{\mu,y}$ is again the appropriate scaling factor in the lateral direction. The normalised longitudinal and lateral force curves are shown in Figures F.1 and F.2. The maximum friction coefficients reduce significantly as the load increases from 2kN to 5kN, in both longitudinal and lateral directions. The position of the peak longitudinal friction moves towards larger slip ratios as the normal load increases, while the peak lateral friction moves towards smaller slip angles. Crucially, for both longitudinal and lateral forces, the slip stiffness (slope of the curves at the origin) reduce as the normal load increases.

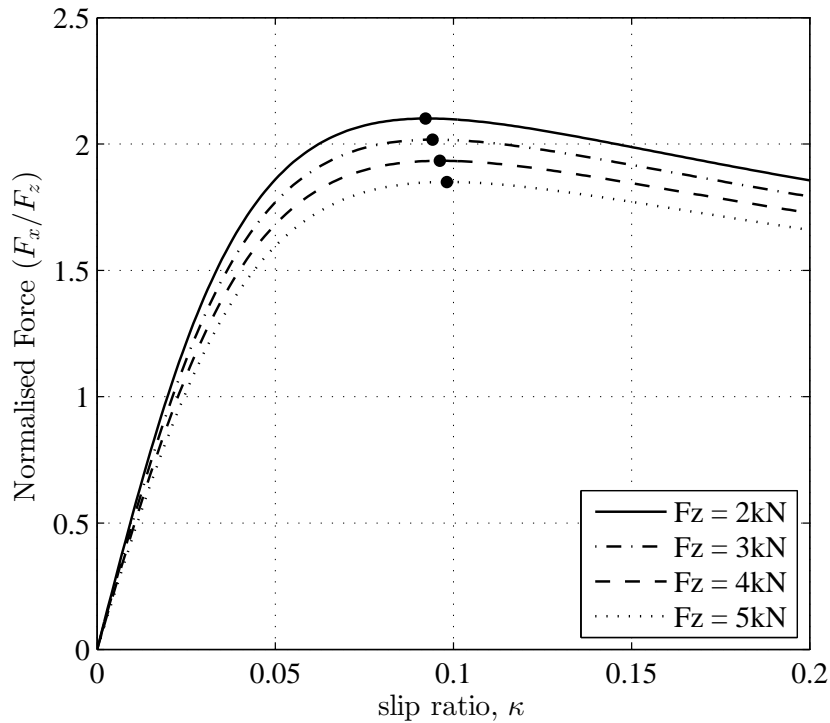


Figure F.1: Normalised longitudinal tyre forces (pure longitudinal slip)

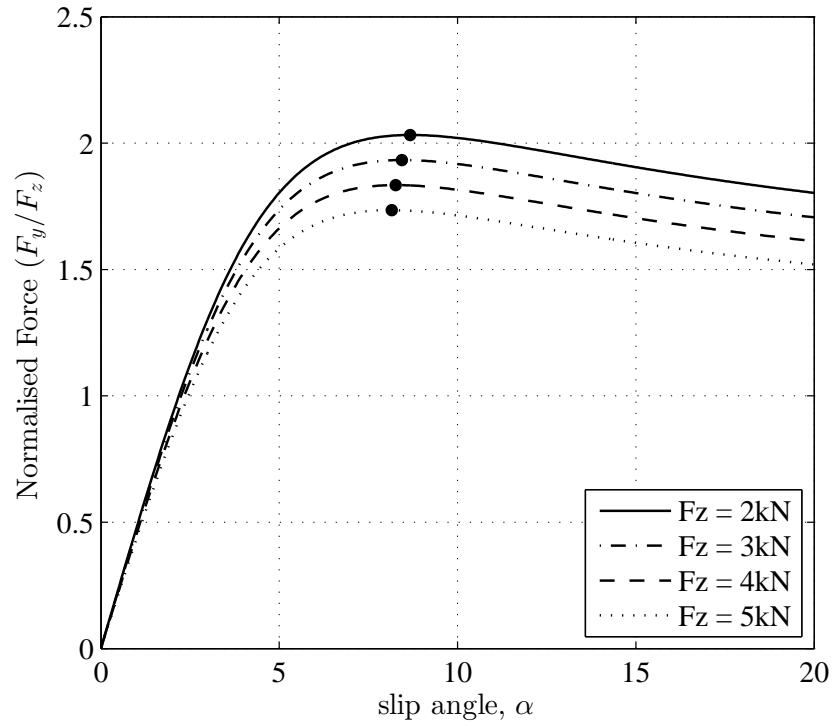


Figure F.2: Normalised lateral tyre forces (pure lateral slip)